CONTROLLED INJECTION AND HYBRID STAGING IN PLASMA WAKEFIELD ACCELERATORS

by

THOMAS HEINEMANN

A thesis presented for the degree of
Doctor of Philosophy in Physics

University of Strathclyde

Department of Physics

2025

SUPERVISORS:
Bernhard Hidding
Zheng-Ming Sheng
Ralph W. Aßmann

Thomas Heinemann
Controlled Injection and Hybrid Staging in Plasma Wakefield Accelerators
A thesis presented for the degree of Doctor of Philosophy in Physics

DECLARATION

This thesis is the result of the author's original research. It has been composed by the author and has not been previously submitted for examination which has led to the award of a degree.

Signed: Thomas Heinemann

Date: December 2025

"It's *significant*!"

— O. S. Karger

"Ach was soll's, ich bau mir jetzt 'ne Zielscheibe!"

— A. Knetsch (paraphrased)

"Rotate!"

— J. P. Couperus Cabadağ

"Fledermäuse!"

— T. Kurz

ABSTRACT

Plasma wakefields, driven by either a short, highly intense laser pulse or a short and dense, highly relativistic charged-particle beam, can provide electric field strengths orders of magnitude beyond what is in reach with conventional accelerator technology. They could therefore drastically reduce the size and costs of particle accelerators and, accordingly, their applications. Prospects for miniaturised light sources based on electron beams delivered by compact plasma wakefield accelerators are particularly attractive, however, require substantial improvements in beam quality.

An important compound quality parameter is the beam brightness. The beam brightness attainable in plasma wakefield accelerators is largely determined by the mechanism through which the electrons are injected into the accelerating wakefield. A particularly promising method is the plasma photocathode, which utilises a comparatively low-intensity laser pulse to release electrons at precisely controlled locations directly inside the wake structure. Plasma photocathodes offer a pathway for generating electron beams of highest brightness, and unfold their full potential in particle beam-driven plasma wakefield accelerators (PWFAs).

However, establishing wakefield conditions suitable for plasma photocathode injection requires particularly strong drivers with high peak-currents. Such drivers are challenging to produce, and could thus far only be delivered by a kilometre-scale conventional accelerator. Meanwhile, laser-driven wakefield accelerators (LWFAs) are realised in many comparatively small-scale high-power laser facilities all over the world. Compact LWFAs nowadays excel in generating short, high peak-current electron beams that may provide superb drivers for a subsequent PWFA stage. Such a hybrid LWFA-PWFA staging concept (LPWFA) thus offers to combine and exploit the individual advantages of both laser- and particle beam-driven methods.

This thesis explores these two approaches – plasma photocathode injection and hybrid staging – conceptually and experimentally.

The first part of this thesis introduces fundamental concepts of plasma wakefield accelerators, briefly discusses differences in LWFA and PWFA approaches, and provides an overview of common injection methods. The second part of this thesis focuses on plasma photocathode injection and presents a first proof-of-principle experiment conducted at the Facility for Advanced Accelerator Tests at the SLAC National Labor-

atory (USA), utilising its ∼2 km long conventional accelerator to provide electron drive beams. While this experiment was not yet designed for delivering highest output beam quality, it demonstrates the feasibility of plasma photocathode injection, showcases the production of electron beams with substantially better emittance compared to the original driver, and provides valuable insights for further implementations. The third part of this thesis discusses prospects of the hybrid staging concept and presents a first experimental realisation of a hybrid plasma wakefield accelerator prototype. This experiment was conducted at the DRACO laser facility at the Helmholtz-Zentrum Dresden–Rossendorf (Germany), utilising a ∼3 mm long LWFA stage powered by a ∼150 TW laser pulse to generate electron drivers for the subsequent PWFA stage. The main result of this experiment is the acceleration of electrons up to ∼130 MeV in a discrete, ∼1.5 mm long PWFA section. This achievement constitutes the first demonstration of electron acceleration in a separate PWFA stage powered by LWFA-generated electron drivers.

The results presented in this thesis demonstrate the feasibility of plasma photocathodes and establish hybrid LPWFA systems as novel accelerator platform. In the future, a variety of PWFA concepts can therefore be explored and further developed at widely accessible, compact LWFA systems, including advanced injection schemes such as the plasma photocathode. Ultimately, the combination of hybrid staging and plasma photocathodes may lead to a new class of truly compact accelerator systems delivering electron beams of unprecedented brightness.

PUBLICATIONS

The author has produced or contributed to the following publications over the course of this study[1]:

[p1] G. G. Manahan et al. 'Hot spots and dark current in advanced plasma wakefield accelerators'. In: *Physical Review Accelerators and Beams* 19.1 (Jan. 2016), p. 011303. DOI: 10.1103/physrevaccelbeams.19.011303.

[p2] S. Kuschel et al. 'Demonstration of passive plasma lensing of a laser wakefield accelerated electron bunch'. In: *Physical Review Accelerators and Beams* 19.7 (July 2016), p. 071301. DOI: 10.1103/physrevaccelbeams.19.071301.

[p3] T. Heinemann et al. 'Investigating the Key Parameters of a Staged Laser- and Particle Driven Plasma Wakefield Accelerator Experiment'. In: *Proceedings of the 8th Int. Particle Accelerator Conf.* IPAC2017. JACoW, Geneva, Switzerland, 2017. DOI: 10.18429/JACOW-IPAC2017-TUPIK010.

[p4] B. Hidding et al. 'First Measurements of Trojan Horse Injection in a Plasma Wakefield Accelerator'. In: *Proceedings of the 8th Int. Particle Accelerator Conf.* IPAC2017 (Denmark). JACoW, Geneva, Switzerland, 2017. DOI: 10.18429/JACOW-IPAC2017-TUYB1.

[p5] G. G. Manahan et al. 'Single-stage plasma-based correlated energy spread compensation for ultrahigh 6D brightness electron beams'. In: *Nature Communications* 8.1 (June 2017). DOI: 10.1038/ncomms15705.

[p6] E. N. Svystun et al. 'Two-stage laser-driven plasma acceleration with external injection for EuPRAXIA'. In: *Journal of Physics: Conference Series* 1067 (Sept. 2018), p. 042011. DOI: 10.1088/1742-6596/1067/4/042011.

[p7] E. Svystun et al. 'Beam quality preservation studies in a laser-plasma accelerator with external injection for EuPRAXIA'. In: *Nuclear Instruments and Methods in Physics Research Section A: Accelerators, Spectrometers, Detectors and Associated Equipment* 909 (Nov. 2018), pp. 90–94. DOI: 10.1016/j.nima.2018.02.060.

1 Throughout this thesis, in-line references with contributions from the author are highlighted in red colour.

[p8] M. F. Gilljohann et al. 'Direct Observation of Plasma Waves and Dynamics Induced by Laser-Accelerated Electron Beams'. In: *Physical Review X* 9.1 (Mar. 2019), p. 011046. DOI: 10.1103/physrevx.9.011046.

[p9] B. Hidding et al. 'Fundamentals and Applications of Hybrid LWFA-PWFA'. In: *Applied Sciences* 9.13 (June 2019), p. 2626. DOI: 10.3390/app9132626.

[p10] A. Martinez de la Ossa et al. 'Hybrid LWFA–PWFA staging as a beam energy and brightness transformer: conceptual design and simulations'. In: *Philosophical Transactions of the Royal Society A: Mathematical, Physical and Engineering Sciences* 377.2151 (June 2019), p. 20180175. DOI: 10.1098/rsta.2018.0175.

[p11] G. G. Manahan et al. 'Advanced schemes for underdense plasma photocathode wakefield accelerators: pathways towards ultrahigh brightness electron beams'. In: *Philosophical Transactions of the Royal Society A: Mathematical, Physical and Engineering Sciences* 377.2151 (June 2019), p. 20180182. DOI: 10.1098/rsta.2018.0182.

[p12] A. Deng et al. 'Generation and acceleration of electron bunches from a plasma photocathode'. In: *Nature Physics* 15.11 (Aug. 2019), pp. 1156–1160. DOI: 10.1038/s41567-019-0610-9. A. Deng and O. S. Karger contributed equally to this work.

[p13] F. Habib et al. 'Plasma accelerator-based ultrabright x-ray beams from ultrabright electron beams'. In: *Advances in Laboratory-based X-Ray Sources, Optics, and Applications VII*. Ed. by A. Murokh and D. Spiga. SPIE, Sept. 2019. DOI: 10.1117/12.2530976.

[p14] M. B. Schwab et al. 'Visualization of relativistic laser pulses in underdense plasma'. In: *Physical Review Accelerators and Beams* 23.3 (Mar. 2020), p. 032801. ISSN: 2469-9888. DOI: 10.1103/physrevaccelbeams.23.032801.

[p15] G. Raj et al. 'Probing ultrafast magnetic-field generation by current filamentation instability in femtosecond relativistic laser-matter interactions'. In: *Physical Review Research* 2.2 (May 2020), p. 023123. DOI: 10.1103/physrevresearch.2.023123.

[p16] R. W. Assmann et al. 'EuPRAXIA Conceptual Design Report'. In: *The European Physical Journal Special Topics* 229.24 (Dec. 2020), pp. 3675–4284. DOI: 10.1140/epjst/e2020-000127-8.

[p17] T. Kurz et al. 'Demonstration of a compact plasma accelerator powered by laser-accelerated electron beams'. In: *Nature Communications* 12.1 (May 2021). DOI: 10.1038/s41467-021-23000-7. T. Kurz and T. Heinemann contributed equally to this work.

[p18] J. P. Couperus Cabadağ et al. 'Gas-dynamic density downramp injection in a beam-driven plasma wakefield accelerator'. In: *Physical Review Research* 3.4 (Oct. 2021), p. l042005. DOI: 10.1103/physrevresearch.3.l042005.

[p19] D. Ullmann et al. 'All-optical density downramp injection in electron-driven plasma wakefield accelerators'. In: *Physical Review Research* 3.4 (Dec. 2021), p. 043163. DOI: 10.1103/physrevresearch.3.043163.

[p20] P. Scherkl et al. 'Plasma photonic spatiotemporal synchronization of relativistic electron and laser beams'. In: *Physical Review Accelerators and Beams* 25.5 (May 2022), p. 052803. ISSN: 2469-9888. DOI: 10.1103/physrevaccelbeams.25.052803.

[p21] S. Schöbel et al. 'Effect of driver charge on wakefield characteristics in a plasma accelerator probed by femtosecond shadowgraphy'. In: *New Journal of Physics* 24.8 (Aug. 2022), p. 083034. DOI: 10.1088/1367-2630/ac87c9.

[p22] F. M. Foerster et al. 'Stable and High-Quality Electron Beams from Staged Laser and Plasma Wakefield Accelerators'. In: *Physical Review X* 12.4 (Nov. 2022), p. 041016. DOI: 10.1103/physrevx.12.041016.

[p23] B. Hidding et al. 'Progress in Hybrid Plasma Wakefield Acceleration'. In: *Photonics* 10.2 (Jan. 2023), p. 99. DOI: 10.3390/photonics10020099.

[p24] A. F. Habib et al. 'Attosecond-Angstrom free-electron-laser towards the cold beam limit'. In: *Nature Communications* 14.1 (Feb. 2023). DOI: 10.1038/s41467-023-36592-z.

[p25] A. F. Habib et al. 'Plasma Photocathodes'. In: *Annalen der Physik* 535.10 (Sept. 2023). ISSN: 1521-3889. DOI: 10.1002/andp.202200655. A. F. Habib, T. Heinemann and B. Hidding contributed equally to this work.

CONTENTS

Summary & Outlook

Appendix

INTRODUCTION

Over the past century, the acceleration of sub-atomic particles to highly relativistic kinetic energies has become one of the most powerful tools of scientific discovery. Continuously pushing the energy frontier resulted in ever increasing capabilities to test and establish fundamental physics theories. The corresponding technological advancements of particle accelerator machines have also brought forth a broad range of applications beyond fundamental physics. Particle accelerators have become indispensable for modern society, delivering a variety of particle types at various energies for many purposes. For example, they enable photon science applications, facilitate the engineering of novel materials and medications, provide medical diagnostics and treatments, contribute to the development of sustainable energy sources and are applied in numerous industrial processes [1, 2].

Depending on their purpose, today's particle accelerators tend to be quite large and rely on complex infrastructures. They are therefore costly to build and to operate. The development of new accelerator technologies, aiming for substantially smaller and more affordable devices, is therefore highly desired and of strong socio-economic interest.

MODERN PARTICLE ACCELERATORS AND LIGHT SOURCES

The basic principle of particle accelerators is to generate a strong electric field to propel charged matter constituents along a defined direction. Modern accelerator modules utilise radio-frequency (RF) electromagnetic waves in metallic resonator cavities to provide such directional accelerating electric field gradients. The size of these cavities is thus typically on the order of a few centimetres to a metre. Magnetic structures between the accelerator modules are used to steer and manipulate the resulting particle beams. The final energy that these machines can impart to an ensemble of particles is therefore, in its simplest approximation, the product of the accelerating field strength and the combined length of the accelerator modules.

After nearly a century of continuous refinements [3], current RF-based accelerator technology seems to approach a fundamental limit in the maximum field strength that can be supported before the cavity material breaks down. This threshold is

reached upon an electric field on the order of ~100 MV/m , and modern accelerator modules are typically operated at substantially lower field strengths. To increase the particle energies to levels desired for future high-energy physics experiments (several hundreds to thousands of GeV for lepton colliders), a linear accelerator (linac) would consequently need to become as long as tens of kilometres, and twice that when aiming for a head-on particle collider. Synchrotron machines, instead, steer the particles along a closed circular path so they can pass the accelerating structures many times and gain additional energy upon each turn. The particle energy that can be reached in a circular accelerator machine with a fixed circumference is nevertheless limited, by either the strength of the bending magnets (for heavy particles, such as protons) or due to synchrotron radiation (for lightweight particles, such as electrons). This synchrotron radiation is emitted whenever a charged particle is forced on a curved trajectory, and carries energy away from the particle. The amount of energy converted into synchrotron radiation upon one turn in a circular machine increases with the fourth power of the ratio between the particle's kinetic energy and its rest mass, and decreases for a softer bending radius. Ultimately, the particle energy can therefore only be increased by also increasing the machine circumference. Whether using circular machines or linear accelerators based on current technology, accelerating particles beyond a certain energy thus requires big and costly machines. The financial investments required for future particle colliders based on linear [4, 5] and circular [6, 7] accelerator designs is estimated to be on the order of ten billion £ or more, and their construction might be associated with a substantial impact on the environment.

While detrimental for reaching higher energies in a circular accelerator, synchrotron radiation has unique characteristics that sparked a new era of particle accelerator-based light sources. Both circular accelerators and linacs are nowadays re-purposed or directly designed to deliberately generate synchrotron radiation. The latest generation of these accelerator-based light sources are free electron lasers (FELs) [8–12]. FELs utilise alternating magnetic structures, so-called undulators, to force electrons on an oscillating trajectory. This allows the electrons to interact with the emitted radiation, which, under appropriate conditions, results in a resonant amplification process. Free electron lasers are thereby capable of generating short and intense pulses of coherent radiation across a broad range of wavelengths, including soft and hard X-rays. State-of-the-art FELs deliver sub-femtosecond, coherent flashes of hard X-ray radiation which can resolve extremely fast and tiny processes. X-ray FELs therefore provide unique tools, for example, for probing molecular systems and biological processes on their natural scales, as well as studying nano-materials and exotic states of matter.

They therefore enable new research perspectives across biochemistry, material science, pharmacology and beyond.

Powering these formidable machines, however, requires short and highly relativistic electron beams of exceptionally high quality. An important compound quality parameter combining several desired beam characteristics is the electron beam brightness. Prominent examples for hard X-ray FELs, such as LCLS [13], the European XFEL [14] and the most recent LCLS-II [15] rely on sophisticated kilometre-scale linacs to deliver high-brightness beams with energies on the order of $\sim 10\,\mathrm{GeV}$. While not as excessively expensive as colliders, constructing these facilities breached the billion-£ threshold. Consequently, only a handful of X-ray FELs are available to users, which imposes severe limitations on research capacities. The development of novel accelerator concepts that could drastically reduce the spatial and economic footprint of future light sources is therefore highly desired.

PLASMA-BASED PARTICLE ACCELERATORS

A plasma consists of already unbound, negatively charged electrons and positively charged ions. Utilising plasma as an accelerator medium hence circumvents the material breakdown issues of conventional metallic cavities. Plasma-based particle accelerators can therefore provide and sustain electromagnetic field strengths orders of magnitude beyond the limit of conventional accelerator technology. Accelerating structures with a size of tens to hundreds of micrometres, associated with electric field gradients on the order of $\sim 100\,\mathrm{GV/m}$, can be efficiently generated when a sufficiently short, highly intense laser pulse [16] or a high-current, highly relativistic charged-particle beam [17, 18] is sent through the plasma. Upon traversing the plasma with nearly the speed of light, this laser- or particle-"driver" transiently separates the plasma electrons from the substantially heavier ions and thereby induces collective charge-density oscillations. The emerging plasma wave structure in the wake of the driver is associated with strong electromagnetic fields, in both longitudinal and transverse dimensions with respect to the driver propagation direction. These wakefields thus trail the driver and can be harnessed to rapidly accelerate charged particles, while also providing enormous focusing forces. The plasma can therefore be utilised as a medium to transfer energy from the driver to an ensemble of charged particles located at an appropriate co-moving position inside the wake structure.

Plasma wakefield accelerators are particularly well-suited to accelerate electrons, which makes them especially attractive for powering future compact and economic

light sources [19–21]. Realising X-ray free electron lasers based on compact plasma wakefield accelerators could crucially enhance the capacities and accessibility of photon science applications. Such plasma-based X-ray FELs are furthermore regarded as a bridge technology towards a potential high-energy physics linear collider (partially) based on plasma wakefield accelerator stages [22].

However, the reproducibility and attainable electron beam quality of plasma-based accelerators are not yet on par with state-of-the-art conventional linacs. One of the challenges is that the accelerating wake structure is not a manufactured device such as RF cavities, but dynamically generated by the driver as it traverses the plasma. The shape, stability and evolution of the wake, and correspondingly control over the acceleration process, is hence colligated with the driver-plasma interaction. Another key challenge is the development of mechanisms to precisely position electrons into the accelerating wakefield. This electron injection process is critical, as it largely predetermines the final electron beam characteristics and brightness.

Nevertheless, continuous innovations and refinements of experimental techniques alongside substantial advancements in understanding and modelling the underlying fundamental mechanisms have resulted in steady progress [23–27] towards achieving technological maturity, including the development of plasma-based beam manipulation techniques and sophisticated diagnostic tools. Multi-gigaelectronvolt electron energy gains over tens of centimetres obtained within a single plasma accelerator module have nowadays been demonstrated in both laser- and particle-driven scenarios [28–30]. Moreover, recent experiments have shown first indications of a free electron lasing, albeit at wavelengths above the X-ray regime [31]. Plans for a plasma-based FEL user facility are actively being developed, for example within the EuPRAXIA project [32].

Further advancing the capabilities of plasma wakefield accelerators to reliably deliver electron beams compatible with the stringent quality demands of X-ray FELs is therefore a prime objective of current research [31, 33].

ABOUT THIS THESIS

Laser-driven wakefield accelerators (LWFAs) and particle beam-driven wakefield accelerators (PWFAs) share the same fundamental working principle, but substantially differ in the driver-plasma interaction dynamics. Another important difference lies in the availability of adequate drivers.

Continuous advancements in laser technology, most prominently the chirped pulse amplification technique [34] at infrared laser wavelengths, have lead to an ever in-

creasing dissemination of high-power laser systems with infrastructures much smaller and more economic compared to large-scale conventional accelerator facilities. The first experimental demonstration of laser-driven plasma wakefield accelerators generating electron beams with a controlled energy distribution was reported in a series of independent publications in 2004 [35–37], which is nowadays considered as the breakthrough that lead to many subsequent advancements in LWFA research. As a result of this development, compact LWFAs are nowadays commonly realised in many university-scale laboratories worldwide.

In contrast, the development of advanced PWFA concepts relies on highly relativistic particle drivers with sufficient charge density, and has thus far been restricted to a few comparatively large-scale conventional accelerator facilities. Nonetheless, particle beam-driven wakefields offer significant advantages compared to laser-driven scenarios. PWFAs can, in principle, provide consistent accelerating conditions over longer distances and hence enable higher energy gains. Electron-driven wakefields, in particular, can be operated in a regime exhibiting enhanced resilience against the driver evolution throughout the plasma. This further facilitates preserving the quality of injected electron beams during acceleration. Moreover, PWFAs can provide a favourable environment for realising advanced ionisation-based injection schemes that promise to generate electron beams of highest brightness.

One particularly promising method is the so-called ultracold underdense plasma photocathode, also known as Trojan Horse injection [38, 39]. Plasma photocathodes utilise a comparatively low-power, tightly focused laser pulse to release electrons at precisely controlled locations directly inside the plasma wake structure. Provided a sufficiently strong wakefield, the released electron distribution is subsequently compressed, captured and rapidly accelerated by the plasma wave. The plasma photocathode method therefore enables enhanced control over the injection process and provides a pathway for the production of extremely short, sub-femtosecond-duration electron beams with exceptionally high brightness values that may largely surpass the capabilities of state-of-the-art conventional linacs.

A first proof-of-principle experiment demonstrating plasma photocathode injection is presented in this thesis. These results were obtained during the "E-210" programme at the Facility for Advanced Accelerator Tests (FACET) at the SLAC National Accelerator Laboratory located in the USA. The author has been involved in the iterative design process of the experiment and joined the experimental team on-site for the final three months of the E-210 campaign, during which the experimental setup was finalised and the main part of the experiment was conducted. Thereafter, the author

assisted in analysing the recorded measurements and contributed extensively to the accompanying simulations that provided further insights on the wakefield and injection dynamics specific to this experiment. The author further contributed extensively to writing the corresponding manuscript [40].

Generating wakefield conditions adequate for plasma photocathode injection, in turn, requires sufficiently short electron beam drivers with particularly high peak-current. Such electron drivers, however, are very challenging to produce in conventional accelerators, and plasma photocathode injection could thus far only be explored at the FACET facility utilising its ~2 km long linac.

Meanwhile, recent advancements in laser-wakefield accelerators may offer an alternative approach. LWFAs have nowadays shown a remarkable aptitude for generating a unique class of short, high peak-current electron beams that are particularly attractive to be utilised as PWFA drivers. The second strategy followed in this thesis is therefore to explore a staged system consisting of a compact laser-driven plasma wakefield accelerator followed by a separate electron-driven plasma wakefield accelerator. This hybrid LWFA-PWFA staging concept thus aims to combine and exploit the advantages and capabilities unique to each method. Preliminary experimental explorations of such hybrid LWFA-driven PWFA (LPWFA) setups showed encouraging results, however, did not achieve electron acceleration in a separate PWFA stage.

The second experiment presented in this thesis demonstrates, for the first time, electron acceleration in a discrete PWFA stage driven by LWFA-generated electron beams. This hybrid LPWFA experiment was conducted at the DRACO laser facility at the Helmholtz-Zentrum Dresden–Rossendorf in Germany, and largely built upon previously established LWFA capabilities reported and discussed, for example, in [41–43]. A compact, ~3 mm long LWFA stage powered by a ~150 TW laser pulse provided electron drivers for the PWFA stage, in which electrons were accelerated up to ~130 MeV with gradients of at least ~50 GV/m . The author has been a primary contributor to the hybrid LPWFA experiment throughout the entire project, from its conception to developing the experimental design, realising and optimising the experimental setup, performing the measurements and subsequently analysing and interpreting the obtained data. Many aspects of this work were realised together with Thomas Kurz as a joint Ph.D. project [44]. Thomas Kurz and the author jointly lead the writing of the corresponding manuscript [45].

This first realisation of a functional LPWFA prototype enables the exploration and development of various PWFA concepts at numerous small-scale LWFA systems,

including advanced injection schemes such as the plasma photocathode. Hybrid LWFA-PWFA staging and plasma photocathodes are a particularly promising combination that raises prospects for a new class of miniaturised accelerator systems delivering electron beams of unprecedentedly high brightness. Such LPWFA plasma photocathodes could therefore enable particularly compact future light sources compatible with the infrastructure resources of university-scale laboratories, including soft X-ray and hard X-ray free electron lasers.

This thesis is structured into three main parts. The first part introduces fundamental concepts of plasma-based particle accelerators. Essential characteristics of plasmas are briefly discussed in chapter 1, followed by a description of plasma generation via laser pulses and strong electric fields in chapter 2. Basic aspects of plasma wakefields driven by intense laser pulses and electron beams are discussed in chapter 3. Chapter 4 introduces essential beam quality parameters and briefly discusses basic electron dynamics inside plasma wakefields. Characteristic differences between laser- and electron-driven plasma wakefield accelerators are discussed in chapter 5. Chapter 6 provides an overview of electron injection concepts in both LWFA and PWFA scenarios. In the second part of this thesis, methods of laser-induced injection in PWFAs are addressed in more detail, whereafter the E-210 experiment is presented. The basic principle and prospects of plasma photocathodes for generating high-brightness electron beams are addressed in chapter 7. Another injection method was realised in the E-210 experiment, and exploited to access the plasma photocathode regime. This plasma torch injection method is introduced in chapter 8. The E-210 experiment itself is presented and discussed in chapter 9. The third part of this thesis addresses hybrid LWFA-PWFA staging. An overview of the hybrid staging concept, its motivation and prospects is provided in chapter 10. Chapter 11 discusses the current status and potential future developments of hybrid LPWFAs. The experimental realisation of a first functional LPWFA prototype is presented and discussed in chapter 12. The final part concludes with a brief summary of the concepts and results presented in this thesis and offers an outlook into the future.

FUNDAMENTALS OF PLASMA WAKEFIELD ACCELERATORS

1

PLASMA PARAMETERS

Plasmas are a particularly astonishing form of matter, found in numerous natural terrestrial phenomena, in technological applications and in its more exotic forms at the very basis of fundamental physics. As such, a plasma can be formed whenever electrons are detached from their atomic or molecular shells, a process known as ionisation. In fact, most of the ordinary matter throughout the observable universe exists in an ionised state, abundant in stars, the interstellar and even the intergalactic medium. Plasmas are thus associated with a remarkable variety of physical phenomena, owing the wide range of densities and temperatures at which they occur. All plasmas have in common that they consist of a large number of unbound positive and negative charge carriers. It is in this context that the term plasma was first introduced in physics by Nobel laureate Irving Langmuir, one of the pioneering scientists who studied the properties of ionised gases:

> "We shall use the name *plasma* to describe this region containing balanced charges of ions and electrons." [46]

According to Harold M. Mott-Smith [47], Langmuir was inspired by medical science, referring to a similarity he saw in the way erythrocytes and leukocytes are embedded in blood plasma. Although there is no such underlying fluid medium in an ionised gas, the analogy describes how a large number of microscopic constituents and their mutual dynamics define the characteristics of a macroscopic substance. Not all ionised matter can thus be considered a plasma per se. Instead, a plasma is commonly defined as a quasi-neutral medium that comprises unbound charged particles and exhibits collective behaviour [48]. This implies that plasmas are governed by cooperative Coulomb interactions of a large number of particles rather than individual collisions of its constituents, resulting in a variety of complex dynamics with characteristic length and time scales. This chapter provides a basic overview of fundamental plasma concepts and parameters, following references [48–51].

1.1 PLASMA SHIELDING

Ionisation of a neutral gas releases a balanced amount of negatively charged electrons and positively charged ions, and the resulting medium hence appears overall neutral. One of the defining properties of plasma is that this remains true even if a local imbalance in charge is introduced artificially.

In vacuum, a point-like charge Q gives rise to a Coulomb potential ϕ_0 that scales inversely with distance r

$$\phi_0(r) = \frac{Q}{4\pi\,\epsilon_0\,r} \ , \tag{1.1}$$

where ϵ_0 is the vacuum permittivity. In a plasma with mobile charged constituents, however, such potential evokes a spatial re-arrangement of the surrounding particles, effectively shielding the local perturbation in charge density. Consequently, the corresponding electrostatic potential is screened exponentially:

$$\phi(r) = \phi_0(r)\ e^{-r/\lambda_D} \ . \tag{1.2}$$

The characteristic shielding distance λ_D is the electron Debye length[1]

$$\lambda_D = \sqrt{\frac{\epsilon_0\,k_B\,T}{n_e\,e^2}} \ , \tag{1.3}$$

which depends on the electron temperature T and the unperturbed electron number density n_e, where k_B and e are the Boltzmann constant and elementary charge, respectively. The Debye length thus defines the radius over which an electrostatic potential arising from a local charge perturbation is attenuated by a factor of $1/e$, the reciprocal of Euler's number. For a plasma in thermal equilibrium, this corresponds to the distance from the perturbation at which the potential energy equals the thermal energy of the electrons.

A prerequisite for efficient Debye shielding is that a large number of charged particles is in range of the perturbation, which necessitates that the population of the Debye sphere,

$$N_D = n_e\,\frac{4}{3}\pi\lambda_D^3 \ , \tag{1.4}$$

1 A similar Debye length including the ion response can be defined, though the contribution of ions is typically neglected for processes on short time scales due to their substantially larger inertia.

largely exceeds unity. In this case, the plasma dynamics are governed by mutual Coulomb interaction rather than binary collisions. The scaling of N_D with plasma density and temperature is visualised in Figure 1.1 for parameter ranges relevant for plasma-based accelerators.

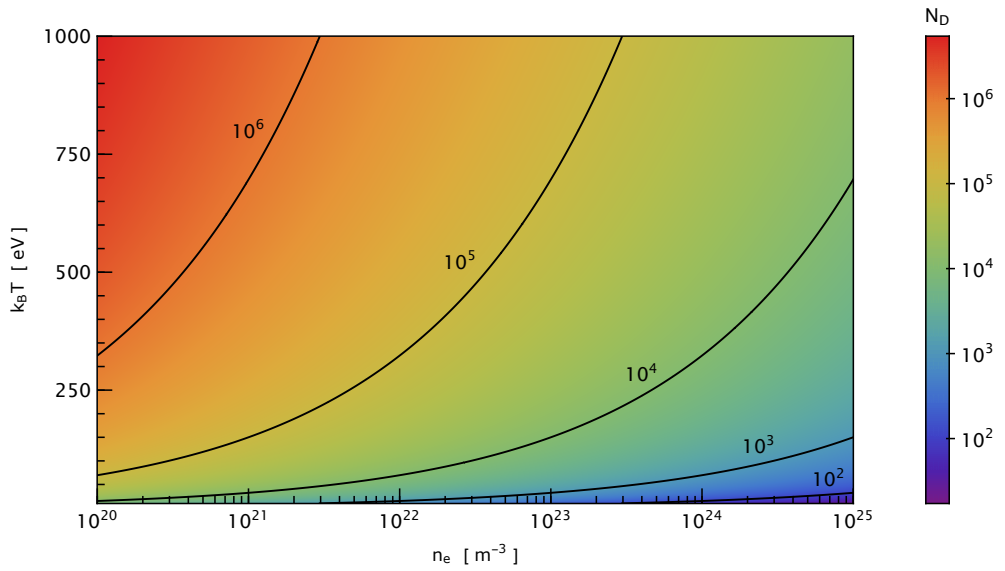

Figure 1.1: **Electron population of the Debye sphere.** The number of electrons that can interact via their mutual Coulomb force depends on electron temperature and the unperturbed electron density. Efficient Debye shielding necessitates $N_D \gg 1$.

The shielding response of plasma on the microscopic scale, consequently, preserves its neutral appearance on macroscopic scales $\gg \lambda_D$. There, the electron density n_e and ion density n_i can be considered homogeneous and equal to the unperturbed plasma density n_0 to a good approximation:

$$n_0 \simeq n_e \simeq n_i = \sum_j Z_j n_j \ , \tag{1.5}$$

with Z_j and n_j indicating the charge number and density of individual ion species, respectively. This quasi-neutrality, together with the predominance of cooperative electrostatic interactions over collisions are defining characteristics of an ideal plasma. Such plasmas with an extent much larger than the Debye length and a densely populated Debye sphere ($N_D \gg 1$) exhibit a wide range of collective phenomena, including plasma waves capable of rapidly accelerating charged particles.

1.2 PLASMA FREQUENCY

The ability of plasma to screen local charge imbalances results in an equilibrium state absent of strong electrostatic potentials beyond the Debye length. Any transient perturbation of charge neutrality, however, evokes a dynamic plasma response on a characteristic time scale corresponding to the plasma frequency

$$\omega_p = \sqrt{\frac{e^2\, n_0}{m_e\, \epsilon_0}} \quad . \tag{1.6}$$

In contrast to the electron Debye length, the plasma frequency does not depend on temperature, but on the electron mass m_e. The plasma frequency is thus, strictly speaking, the characteristic frequency of the plasma electrons, that is, the angular eigenfrequency of a an electron sheath performing harmonic oscillations after being displaced against a homogeneous and static ion background. However, an artificially induced charge separation in plasma, for example, by a transient electromagnetic pulse or electron beam, manifests itself predominantly in the displacement of the far more mobile electrons, and the ions are typically assumed to remain stationary on time scales $t \sim 2\pi/\omega_p$.

1.3 PLASMA DISPERSION

The finite response time of plasma electrons gives rise to a non-zero current density upon interaction with oscillating electromagnetic fields, which implies a frequency-dependent relative permittivity. Consequently, the propagation of light in plasma deviates from the vacuum case. This is expressed by the non-linear dispersion relation for plane electromagnetic waves in plasma

$$\omega_l^2 = c^2\, k^2 + \omega_p^2 \quad , \tag{1.7}$$

where ω_l is the frequency of the light wave, $k = 2\pi/\lambda_l$ is the wavenumber associated with its wavelength λ_l in plasma, and c is the vacuum speed of light. The corresponding refractive index arising in plasma is thus given by

$$\eta \equiv c\,\frac{k}{\omega_l} = \sqrt{\frac{\omega_l^2 - \omega_p^2}{\omega_l^2}} = \sqrt{1 - \frac{\omega_p^2}{\omega_l^2}} \quad . \tag{1.8}$$

It follows that $\eta \leqslant 1$ for all $\omega_l \geqslant \omega_p$ and the plasma appears transparent, whereas the refractive index becomes imaginary for all $\omega_l < \omega_p$. The latter is equivalent to the wave number k becoming imaginary, which implies the absence of a wave-like solution inside the plasma. Instead, the incident wave will be totally reflected at the plasma boundary, with an exponentially decaying evanescent field penetrating the plasma. The characteristic decay length is the plasma skin depth

$$k_p^{-1} = \frac{c}{\sqrt{\omega_p^2 - \omega_l^2}} \ , \tag{1.9}$$

which, for $\omega_l \ll \omega_p$, reduces to $k_p^{-1} \approx c/\omega_p$. The Brillouin diagram visualising the plasma dispersion relation and the resulting cut-off between a transparent and a reflecting plasma at $\omega_l = \omega_p$ is shown in Figure 1.2.

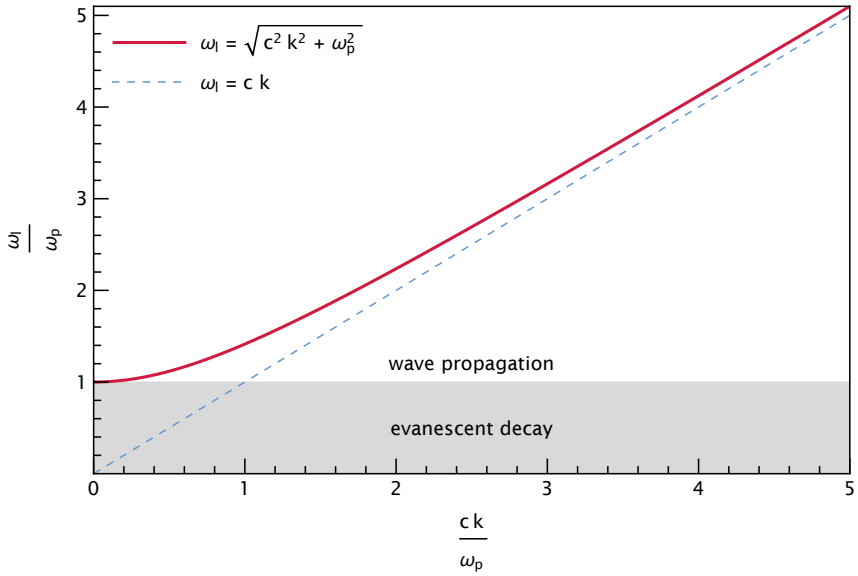

Figure 1.2: **Plasma dispersion relation.** The solid red line illustrates the dispersion relation of plane electromagnetic waves in plasma. The plasma appears transparent for electromagnetic radiation with $\omega_l > \omega_p$, and asymptotically approaches the vacuum dispersion (blue dashed line) with increasing ω_l. Electromagnetic waves with frequency below the plasma frequency, in contrast, are unable to traverse the plasma and are totally reflected, with an evanescent field inside the plasma.

On a microscopic level, this behaviour can be interpreted in terms of the rapidness of the plasma response compared to an external perturbation. When the period of the incident wave exceeds the plasma response time, the plasma is able to adiabatically shield the electric field of the radiation, thus effectively forming a reflecting boundary.

Since the plasma frequency is directly linked to the plasma density, the cut-off condition $\omega_l = \omega_p$ can also be expressed in terms of a critical plasma density, above which reflection occurs:

$$n_{crit.} = \frac{\omega_l^2 \, \epsilon_0 \, m_e}{e^2} \quad . \tag{1.10}$$

A transparent plasma with $n_0 < n_{crit.}$ is thus termed underdense with respect to electromagnetic radiation, a reflecting plasma with $n_0 > n_{crit.}$ is, correspondingly, called overdense[2].

2 Such overdense plasma mirrors [52, 53] have been successfully utilised in plasma-based particle accelerator experiments, for example, as a method for coupling a high-intensity laser pulse into [54, 55] or out of [56][57] the accelerator section.

2

PLASMA GENERATION

The plasma parameters, especially the plasma density profile, largely define the characteristics and operational states of plasma-based particle accelerators. To utilize plasmas as accelerator medium, however, they have to be generated artificially in a laboratory environment, typically by ionising a gaseous substance inside a vacuum chamber. One of the most prevalent techniques of plasma generation for particle accelerators is ionisation via laser pulses. The virtue of this method lies in its ability to generate comparatively cold plasmas over a wide range of sub-atmospheric pressures [58–60], in conjunction with the potential to selectively access distinct ionisation levels of individual atomic or molecular species. These ionisation levels are characterised by the electrostatic potential energy ξ_i binding electrons to their respective atomic or molecular shell, and thus depend on the specific electron configuration and effective nuclear charge. The process of ionisation overcomes this binding energy and transitions an electron from its bound state into an unbound continuum state. The inverse process to ionisation is recombination, which is in turn associated with emission of light [61, 62].

The underlying mechanisms of ionisation by means of intense laser light are multifaceted, yet may be interpreted as energy transfer via direct absorption of one or multiple photons, or, in the strong field regime, a distortion of the electrostatic binding potential. In his seminal publication on strong-field ionisation [63], Leonid Keldysh derived a parameter to identify the dominant ionisation process. In a broad classification, the Keldysh adiabaticity parameter [64]

$$\gamma_K = \frac{\omega_l}{E_0} \sqrt{2 \frac{m_e}{e^2} |\xi_i|} \tag{2.1}$$

distinguishes between the regimes of photoionisation for $\gamma_K \gg 1$ and strong-field ionisation for $\gamma_K \ll 1$, that is, whether ionisation processes are dominated by the frequency or the electric field amplitude E_0 of the laser. More specifically, γ_K relates the ionisation energy $|\xi_i|$ to the ponderomotive energy [50]

$$U_p = \frac{e^2 E_0^2}{4 m_e \omega_l^2} \ , \tag{2.2}$$

which is the average quiver energy of an electron in an oscillating electromangetic field. The Keldysh parameter can thus be equally expressed as

$$\gamma_K = \sqrt{\frac{|\xi_i|}{2\,U_p}} \quad . \tag{2.3}$$

Alongside the binding energy and the ponderomotive energy, the third fundamental energy scale relevant for ionisation is the energy carried by a single photon, $\hbar\omega_l$, where $\hbar$ is the reduced Planck constant. By relating $|\xi_i|$ to U_p and $\hbar\omega_l$, the classification of ionisation mechanisms can be further detailed [65].

2.1 PHOTOIONISATION

When the ponderomotive energy is negligible, then $\gamma_K \to \infty$, and the interaction of bound electrons with electromagnetic fields can be reduced to a simplified picture of individual photon absorption. In this low-intensity, high-frequency regime, a single photon may carry sufficient energy to directly release an electron from its binding potential. Such single-photon ionisation, characterised by $\hbar\omega_l \geqslant |\xi_i| \gg U_p$, is illustrated schematically in Figure 2.1a. The transition from a bound state into an ionised continuum state may also be achieved by the interaction of multiple photons via (virtual) excitation states, as sketched in Figure 2.1b. In this case, the energy of a single photon can be below the ionisation energy, such that $|\xi_i| > \hbar\omega_l \gg U_p$.

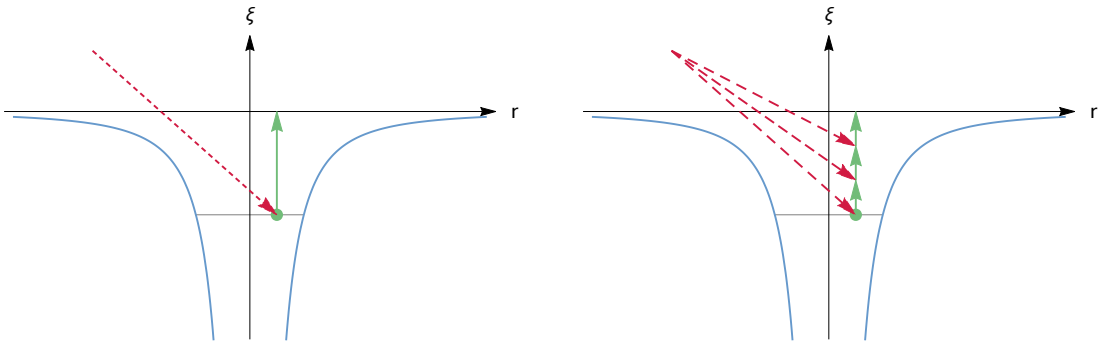

(a) single-photon ionisation (b) multi-photon ionisation

Figure 2.1: **Photionisation process.** The energy transferred by (a) a single photon (red, dashed) or (b) multiple photons is sufficient to liberate an electron (green) beyond the atomic potential well (blue).

While photoionisation is the conceptually simplest ionisation mechanism, it relies on high photon frequency, and thus necessitates lasers with sufficiently short wavelength. The most prevalent short-pulse, high-intensity laser systems to date are Ti:sapphire lasers with a typical central wavelength of 800 nm. However, accessing the single-photon regime for the first ionisation level of helium, with ionisation energy of $\approx 24.6\,\mathrm{eV}$, would require a laser wavelength below $\sim 50\,\mathrm{nm}$. Similarly, the wavelength threshold for ionising atomic hydrogen with an ionisation energy of $\approx 13.6\,\mathrm{eV}$ already lies at $\sim 91\,\mathrm{nm}$. Such wavelengths in the extreme ultraviolet spectrum are far below what is in reach of current laser technology for plasma wakefield accelerators. Even considering multi-photon interactions, the number of photons that need to coincide with an individual electron is substantial. At that point, the required photon density, and hence laser intensity, implies that the ponderomotive energy can no longer be neglected. This highly complex multi-photon regime [65, 66], where $|\xi_i| \sim U_p > \hbar\omega_l$, marks the transition to the strong-field regime of ionisation.

2.2 STRONG-FIELD IONISATION

For further increased field strength at low photon energy, the ponderomotive energy becomes increasingly dominant, until $U_p > |\xi_i| \gg \hbar\omega_l$, which represents the high-intensity, long-wavelength regime typically encountered in plasma wakefield accelerators. Under this condition, the atomic binding potential is substantially distorted by the superimposed external electric field, such that the potential barrier is lowered and shortened. Consequently, a non-zero amplitude of the electron's quantum-mechanical probability density function arises beyond the barrier, which allows the electron to tunnel through the remaining potential well into an unbound continuum state. This tunnel ionisation process is illustrated in Figure 2.2a. Lowering the potential barrier even further, as shown in Figure 2.2b, may ultimately allow the electron to escape its binding potential classically.

Moreover, as $\gamma_K \to 0$, these strong-field ionisation processes become adiabatically independent of the laser frequency [63]. In other words, the electron then escapes the atomic barrier within a fraction of a laser cycle [64], and the effective potential deformation can be treated as quasi-static. One of the most widely used approaches for modelling tunnel ionisation rates in this quasi-static limit has been formulated by Ammosov, Delone and Krainov [67], based on the seminal ideas of Keldysh and extensive previous work, for example by Perelmov, Popov and Terent'ev [68].

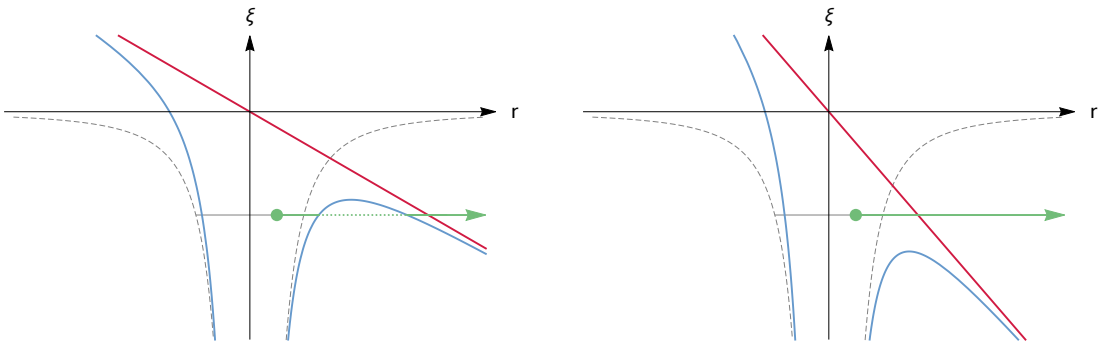

(a) tunnel ionisation (b) barrier-suppression ionisation

Figure 2.2: **Ionisation in the strong-field regime.** In the presence of a strong, quasistatic electric potential (red), the atomic potential barrier (blue) is deformed compared to the unperturbed potential (grey, dashed). An electron (green) may thus (a) tunnel through the remaining barrier or (b) escape directly when the barrier is sufficiently suppressed.

Insightful reviews summarising the historical development and variations of tunnel ionisation models are provided, for example, by Bauer and Mulser [69] or Popov [70].

Deriving numerical values of tunnel ionisation rates ω_{ti} is largely facilitated by utilising atomic units, according to:

$$\text{Hartree energy:} \quad U_H = \frac{m_e\, e^4}{(4\pi\,\epsilon_0\,\hbar)^2} \approx 4.36 \times 10^{-18}\,\text{J} \approx 27.21\,\text{eV} \tag{2.4a}$$

$$\text{time:} \quad \tau_{au} = \frac{\hbar}{U_H} = (4\pi\,\epsilon_0)^2\,\frac{\hbar^3}{m_e\, e^4} \approx 2.42 \times 10^{-17}\,\text{s} \tag{2.4b}$$

$$\text{Bohr radius:} \quad \delta_{au} = \frac{4\pi\,\epsilon_0\,\hbar^2}{m_e\, e^2} \approx 5.29 \times 10^{-11}\,\text{m} \tag{2.4c}$$

$$\text{electric field:} \quad E_{au} = \frac{U_H}{e\,\delta_{au}} = \frac{m_e^2\, e^5}{64\pi^3\,\epsilon_0^3\,\hbar^4} \approx 5.14 \times 10^{11}\,\text{V/m}\ . \tag{2.4d}$$

Conversion between atomic and SI units thus follows the relations $\hat{\omega}_{ti} = \omega_{ti}\,\tau_{au}$, $\hat{E}_0 = E_0/E_{au}$, and $\hat{\xi}_i = |\xi_i|/U_H$. The tunnel ionisation rate for complex atoms or ions in the quasi-static limit [67–71] can then be expressed in atomic units as

$$\hat{\omega}_{ti} = C^2_{n^*\ell^*}\, f(\ell, m)\ \hat{\xi}_i \left(2\,\frac{(2\,\hat{\xi}_i)^{\frac{3}{2}}}{\hat{E}_0}\right)^{2n^*-|m|-1} \times \exp\left(-\frac{2}{3}\,\frac{(2\,\hat{\xi}_i)^{\frac{3}{2}}}{\hat{E}_0}\right)\ . \tag{2.5}$$

The orbital of the electron is considered in the tunnel ionisation rate via

$$f(\ell, m) = \frac{(2\ell+1)\,(\ell+|m|)!}{2^{|m|}\;|m|!\;(\ell-|m|)!}\;, \tag{2.6}$$

where ℓ and m are the angular and magnetic quantum numbers, respectively. Furthermore, the electron energy state is characterised by the coefficient

$$C^2_{n^*\ell^*} = \frac{2^{2n^*}}{n^*\,\Gamma(n^*+\ell^*+1)\;\Gamma(n^*-\ell^*)}\;. \tag{2.7}$$

Here, utilising the effective principle quantum number n^* and effective angular quantum number ℓ^* of an electron state in an arbitrary atom or ion forms the central substitution in the Ammosov-Delone-Krainov (ADK) model [67, 72]. The effective principle quantum number can be expressed in terms of the ionisation energy as

$$n^* = \frac{Z}{\sqrt{2\hat{\xi}_i}} \approx Z\sqrt{\frac{13.6}{\xi_i\;[\mathrm{eV}]}}\;, \tag{2.8}$$

with Z indicating the integer charge number of the atomic residue after ionisation. Accordingly, the effective angular quantum number is defined as $\ell^* = n^*_0 - 1$, with n^*_0 corresponding to the ground state. The Gamma function $\Gamma(n) = \int_0^\infty \zeta^{n-1} e^{-\zeta}\,d\zeta$ is introduced to interpolate between non-integer factorials arising for complex atoms other than hydrogen. Substituting expression 2.8 into equation 2.5, an equivalent formulation [67] of the tunnel ionisation rate reads

$$\hat{\omega}_{ti} = C^2_{n^*\ell^*}\,f(\ell, m)\;\frac{(Z/n^*)^2}{2}\;\left(2\,\frac{(Z/n^*)^3}{\hat{E}_0}\right)^{2n^*-|m|-1} \times \exp\left(-\frac{2}{3}\,\frac{(Z/n^*)^3}{\hat{E}_0}\right)\;. \tag{2.9}$$

The ADK rate in this form considers a quasi-static electric field. It can thus be directly applied for circularly polarised lasers, or the electric space-charge field of a charged-particle beam. In case of a linearly polarised laser field with an oscillating electric field strength, the effective ionisation rate $\bar{\hat{\omega}}_{ti}$ is found by averaging $\hat{\omega}_{ti}$ over one laser cycle [63, 67, 71], resulting in

$$\bar{\hat{\omega}}_{ti} = \hat{\omega}_{ti}\sqrt{\frac{3}{\pi}\,\frac{\hat{E}_0}{\left(2\,\hat{\xi}_i\right)^{\frac{3}{2}}}} = \hat{\omega}_{ti}\sqrt{\frac{3}{\pi}\,\frac{\hat{E}_0}{(Z/n^*)^3}}\;. \tag{2.10}$$

A few further practical approximations can be made to facilitate the numerical derivation of the tunnel ionisation rate. A simplified expression for the coefficient $C^2_{n^*\ell^*}$ can be found using Stirling's approximation for factorials, which, in the limit of $\ell^* \ll n^*$, reduces[1] to [67, 71, 72]

$$\lim_{\ell^* \ll n^*} C^2_{n^*\ell^*} \approx C^2_{n^*} \approx \frac{1}{2\pi n^*} \left(\frac{2e}{n^*}\right)^{2n^*} \quad , \tag{2.11}$$

where e denotes Euler's number. Besides the effective principal quantum number, the exact ionisation rate depends on the specific orbital quantum numbers ℓ and m via the parameter $f(\ell, m)$. However, ionisation rates for electron states $m \neq 0$ are substantially reduced [72], due to the exponential scaling with $-|m|$ in equation 2.5 or 2.9. When considering only the dominant ionisation process of levels with $m = 0$, the parameter $f(\ell, m)$ stated in equation 2.6 simplifies to

$$f(\ell, 0) = 2\ell + 1 \quad . \tag{2.12}$$

A reduced expression to approximate the averaged ADK ionisation rate can thus be stated in SI units as

$$\overline{\omega}_{ti}^{m=0} \approx \frac{\sqrt{3}}{\tau_{au}} \left(\frac{e}{\pi}\right)^{3/2} (2\ell+1) \frac{Z^2}{n^{*9/2}} \left(4e \frac{E_{au}}{E_0} \frac{Z^3}{n^{*4}}\right)^{2n^*-3/2} \times \exp\left(-\frac{2}{3} \frac{E_{au}}{E_0} \frac{Z^3}{n^{*3}}\right) \quad . \tag{2.13}$$

The ADK model is, however, strictly valid solely in the pure tunnel ionisation regime. It is thus only applicable up to a maximum field strength above which the Coulomb binding potential barrier is suppressed below the energy level of the respective electron. Transition from tunnel ionisation to barrier-suppression ionisation [72, 74] occurs at the threshold field strength

$$\hat{E}_{BSI} = \frac{\hat{\xi}_i^{\,2}}{4Z} = \frac{Z^3}{16 n^{*4}} \quad , \tag{2.14}$$

or, for hydrogen-like atoms and ions with a single valence electron [73, 75], at

$$\hat{E}_{BSI,\,H\text{-like}} = \hat{\xi}_i^{\,3/2} \left(\sqrt{2} - 1\right) \quad . \tag{2.15}$$

1 Although it has been noted that this approximation is often not particularly accurate, which has been discussed, for example, in [70, 72, 73].

A selection of cycle-averaged ADK ionisation rates for various gases and their respective barrier-suppression ionisation thresholds is shown in Figure 2.3. The

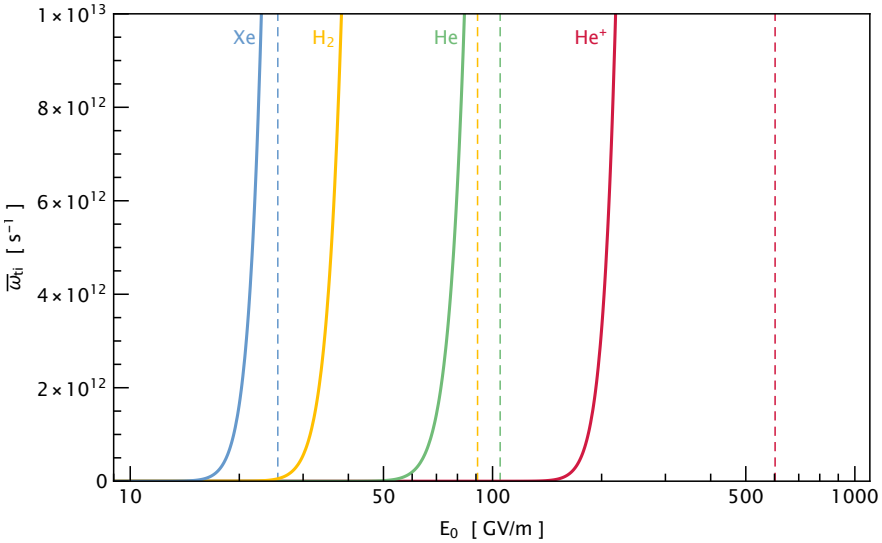

Figure 2.3: **Cycle-averaged tunnel ionisation rates for various gas species.** Above a species-specific onset, the ionisation rates (solid lines) increase rapidly with electric field strength. The resulting separation of tunnel ionisation windows enables species-selective ionisation control. Respective barrier-suppression thresholds are indicated as dashed vertical lines.

individual ionisation rates show a similar shape but differ in the onset electric field strength, owing the specific electron configuration and ionisation energy of their respective atom or ion species. Beyond the onset, the ionisation rates are highly sensitive to small increases in electric field strength. The tunnel ionisation regime is thus restricted to a narrow, species-specific window of laser intensity. A careful choice of laser parameters, therefore, enables selective ionisation of individual constituents in a gas mixture, or to access specific ionisation levels of the same gas species at different times and locations. The scenario in which some species are fully ionised, whereas others remain unaffected by the ionising laser pulse may be realised by targeting sufficiently separated ionisation levels. Such ionisation control, in conjunction with the release of comparatively cold electrons, renders tunnel ionisation via short laser pulses a highly attractive method for plasma-based diagnostics and controlled injection schemes in plasma wakefield accelerators.

Predicting tunnel ionisation rates from the cycle-averaged ADK approach is appropriate under the assumption that the electric field amplitude E_0 remains approximately constant over many laser periods and that the electric field strength during one laser

cycle can still be treated as adiabatic, that is, for $|\xi_i| \gg \hbar\omega_l$ and $\gamma_K \ll 1$. A comparison of theoretical predictions with experimental data [72] suggests that reasonable accuracy is maintained up to $\gamma_K \lesssim 0.5$. Adiabaticity is, however, not rigorously fulfilled in the intermediate regime of $\gamma_K \sim 1$. The quasi-static assumption is likewise not maintained for extremely short few-cycle laser pulses where the envelope of the electric field strength varies substantially on the time scale of one laser period. For such cases, Yudin and Ivanov [76] suggested a model for sub-cycle ionisation dynamics that specifically includes the instantaneous phase of the oscillating laser field. Further adaptions to the ADK model have been proposed since its original formulation, including extensions into the barrier-suppression regime [69, 77, 78] and for diatomic molecules [79].

3

PLASMA WAKEFIELDS

Particle accelerators employ controlled electromagnetic fields to propel sub-atomic charged particles to relativistic energies. Conventional particle accelerator modules achieve this typically by generating resonant electromagnetic standing or travelling waves in the radio-frequency (RF) range inside a sequence of metallic cavities [80]. A charged particle then gains kinetic energy when it passes each cavity at the appropriate phase of the resonant wave. The physical dimensions of such accelerating structures are largely determined by their operating frequency, usually resulting in centimetre- to metre-scale devices. While modern RF structures have reached a remarkable level of sophistication, their attainable peak accelerating gradient is limited to $\sim 100\,\mathrm{MV/m}$, due to the onset of field emission at higher RF power and, ultimately, electrical or thermal breakdown of the cavity material [81–85].

In comparison, a plasma can provide and sustain much larger field strengths. Utilising plasmas as accelerator medium is thus a compelling alternative to conventional accelerator technology. In contrast to resonant RF waves in a metallic cavity, the generation of an accelerating field configuration in plasma-based accelerators rests upon the deliberate excitation of longitudinal plasma waves. This is achieved by utilising a highly intense laser pulse or a strongly relativistic charged-particle beam to continuously drive a dynamic charge-density perturbation inside a plasma. Thereby, a sufficiently short driver rapidly displaces the plasma electrons against the virtually stationary ion background. This initial charge separation induces subsequent plasma electron oscillations, forming a longitudinal travelling electron density wave trailing the driver. The wave number associated with such a plasma wave is thus the relation of the plasma electron frequency to the velocity v_d of the driving perturbation

$$k_p = \frac{\omega_p}{v_d} \ , \tag{3.1}$$

with an associated plasma wavelength

$$\lambda_p = \frac{2\pi}{k_p} \ . \tag{3.2}$$

The plasma wavelength determines the characteristic length scale of an accelerating structure in plasma-based accelerators. The term nominal plasma wavelength refers to the limit of driver velocities approaching the speed of light, while disregarding relativistic effects of the expelled plasma electrons on the plasma frequency. The nominal plasma wavelength, therefore, depends only on the plasma density, according to:

$$\begin{aligned} \lim_{v_d \to c} \lambda_p &= 2\pi c \sqrt{\frac{\epsilon_0 m_e}{e^2 n_0}} \\ &\approx 33.4\,\mu m \left(\frac{n_0}{10^{18}\,cm^{-3}}\right)^{-1/2} . \end{aligned} \tag{3.3}$$

Plasma-based accelerators are typically operated at plasma densities in the range of $10^{16} - 10^{18}\,cm^{-3}$, with corresponding plasma frequencies several orders of magnitude beyond the operating frequencies of RF-powered devices. Accordingly, typical plasma wavelengths are on the order of $\sim 100\,\mu m$, in turn substantially smaller than conventional metallic accelerator cavities. The longitudinal electron density modulation within such short plasma wave periods gives rise to a strong electrostatic potential that is accompanied by a large-amplitude electric field gradient, forming a periodic accelerating structure in the wake of the driver. These wakefields can provide extreme accelerating gradients far beyond the capabilities of conventional metallic cavities, on the order of the cold, non-relativistic wave breaking field[1] [86, 87]

$$\begin{aligned} E_{wb} &= \omega_p \frac{m_e c}{e} \\ &\approx 96\,GV/m \sqrt{\frac{n_0}{10^{18}\,cm^{-3}}} . \end{aligned} \tag{3.4}$$

These considerations summarise the key qualities that render plasma-based approaches highly attractive for a new generation of miniaturised particle accelerators. Plasma wakefields have been proven to be particularly well-suited for the acceleration of electrons, and the remainder of this thesis will be discussed in this context. The capabilities of plasma-based accelerators for generating highly relativistic positron beams are also actively explored [88, 89], but differ conceptually.

1 The phenomenon of wave breaking is further discussed in chapter 6.2.1 .

3.1 INTENSE LASER AND ELECTRON DRIVERS

The two main classes of plasma-based accelerators are laser-driven wakefield accelerators (LWFAs) and particle beam-driven wakefield accelerators (PWFAs). Laser wakefield accelerators were conceptualised by Tajima and Dawson in 1979 [16]. First ideas about using plasma wakefields generated by a charged-particle beam to accelerate electrons were expressed by Veksler in 1956/1957 [90, 91], yet were explicitly formulated in 1984/1985 by Chen et al. [17, 18] and further examined by Ruth et al. [92] and Keinigs & Jones [93]. The majority of PWFA concepts rely on electron-beam drivers to excite a plasma wave, however, other variants driven by protons [94, 95] or positrons [88, 89, 96] are being investigated. This thesis focuses on plasma wakefields generated by short and intense laser pulses or compact electron bunches.

3.1.1 *Laser drivers*

A simplified mathematical description of laser drivers may be obtained by starting from a linearly polarised, monochromatic electromagnetic wave. The electric and magnetic field components of such a plane wave can be expressed in terms of the scalar potential ϕ and vector potential $\vec{A}$, according to

$$\vec{E} = -\nabla\phi - \frac{\partial}{\partial t}\vec{A} \tag{3.5a}$$

$$\vec{B} = \nabla \times \vec{A} \ . \tag{3.5b}$$

A linearly polarised wave propagating in z-direction in vacuum is characterised by the vector potential [49]

$$\vec{A}(z,t) = \vec{A}_0 \cos(k_l z - \omega_l t) \ , \tag{3.6}$$

where k_l and ω_l are the wave number and frequency of the wave, respectively. As the derivatives of the scalar potential ϕ vanish in vacuum, the associated electric and magnetic fields are obtained as

$$\vec{E}(z,t) = \vec{E}_0 \sin(k_l z - \omega_l t) \tag{3.7a}$$

$$\vec{B}(z,t) = \vec{B}_0 \sin(k_l z - \omega_l t) \ , \tag{3.7b}$$

with $E_0 = c\,B_0 = \omega_l\,A_0$ and $\vec{E} \parallel \vec{A} \perp \vec{B}$.

The energy flux density carried by the oscillating electromagnetic fields is expressed by the Poynting vector

$$\vec{S} = \epsilon_0 \, c^2 \left(\vec{E} \times \vec{B} \right) \quad . \tag{3.8}$$

The corresponding intensity I_0, that is, the power per unit area, is a scalar quantity equivalent to the cycle-averaged norm of the Poynting vector

$$I_0 \equiv \left\langle \left| \vec{S} \right| \right\rangle = \epsilon_0 \, c^2 \left\langle \left| \vec{E} \times \vec{B} \right| \right\rangle = \frac{1}{2} \, \epsilon_0 \, c \, E_0^2 \quad . \tag{3.9}$$

Even though a plane electromagnetic wave has the ability to transport energy, it is not capable of driving a plasma wave. This is elaborated on by the Lawson-Woodward theorem [87, 97, 98], which states that a single electron interacting with a plane electromagnetic wave, albeit undergoing harmonic oscillations, receives no net energy gain. The average energy associated with the quiver motion of such an electron in an oscillating electromagnetic field is the ponderomotive energy, which was introduced in equation 2.2. This kinetic energy is associated with an equivalent ponderomotive potential [50]

$$\phi_{\text{pond.}} = U_p = \frac{e^2}{4 \, m_e \, \omega_l^2} \, E_0^2 \quad . \tag{3.10}$$

In a plane electromagnetic wave, $\nabla \phi_{\text{pond.}} = 0$ and no work is done on the electron over one oscillation period, as implied by the Lawson-Woodward theorem. The conditions leading to this finding, however, are not fulfilled in case of tightly focused laser pulses with finite duration. Such laser pulses are employed for driving laser-wakefield accelerators. Close to their focus, they are typically well-approximated by a Gaussian intensity envelope following the form [99]

$$I(z, r, t) = I_0 \left(\frac{w_0}{w(z)} \right)^2 \exp\left(-\frac{2r^2}{w(z)^2} \right) \exp\left(-\frac{1}{2} \frac{(z - c\,t)^2}{(c\,\sigma_t)^2} \right) \quad , \tag{3.11}$$

with peak intensity I_0. The temporal shape of Gaussian pulses is thus characterised by the root-mean-square (rms) pulse duration σ_t. Another commonly used characterisation of the pulse length is its full-width-at-half-maximum (FWHM) duration $\tau_{\text{FWHM}} = 2\sqrt{2 \ln(2)} \, \sigma_t$. The transverse intensity distribution is described by the beam waist $w(z)$, defined as the $1/e^2$-radius of intensity, with w_0 denoting the focus spot size. The peak intensity for perfectly Gaussian laser pulses is thus related to the peak

power P_0 and total energy W_{laser} contained in the pulse via $I_0 = 2P_0/(\pi w_0^2)$ and $P_0 = W_{\text{laser}}/(\sqrt{2\pi}\,\sigma_t)$. The beam waist thereby increases with longitudinal distance from the focus position z_0, according to

$$w(z) = w_0 \sqrt{1 + \left(\frac{z - z_0}{z_R}\right)^2} \quad , \quad \text{with} \quad z_R = \pi \frac{w_0^2}{\lambda_l} \quad . \tag{3.12}$$

The characteristic diffraction scale z_R is known as the Rayleigh length and corresponds to the distance at which $w(z_R) = \sqrt{2}\,w_0$ and $I(z_R) = I_0/2$.

The intensity profile thus exhibits a transverse and longitudinal gradient, which is largest at focus. This gives rise to a conservative net force [50]

$$\begin{aligned} \vec{F}_{\text{pond.}} = -\nabla\phi_{\text{pond.}} &= -\frac{1}{2}\frac{e^2}{m_e\,\omega_l^2\,\epsilon_0\,c}\,\nabla I \\ &= -\frac{1}{2}\frac{e^2}{m_e\,\omega_l^2}\,\nabla\left\langle\left|\vec{E}\right|^2\right\rangle \\ &= -\frac{1}{2}\,m_e\,c^2\,\nabla\left\langle|\vec{a}|^2\right\rangle \quad , \end{aligned} \tag{3.13}$$

the so-called ponderomotive force. As a direct consequence, an electron in the vicinity of a laser pulse experiences an average drift superimposed on its fast quiver motion in the oscillating electromagnetic field. The direction of the drift motion follows the intensity gradient, such that electrons are effectively driven out of the central region of the laser pulse. The ponderomotive force is thus the key mechanism to induce the electron density modulations which form a laser-driven plasma wave.

An important parameter to quantify the interaction strength of a laser pulse with the plasma electrons is the peak amplitude a_0 of the normalised vector potential $\vec{a}$ introduced in equation 3.13, defined as

$$a_0 \equiv \frac{e\,A_0}{m_e\,c} = \frac{e\,E_0}{m_e\,\omega_l\,c} = \frac{e}{m_e\,\omega_l\,c}\sqrt{\frac{2I_0}{\epsilon_0\,c}} \quad . \tag{3.14}$$

In the limit of low laser amplitudes, $a_0\,c = e\,E_0/(m_e\,\omega_l)$ denotes the maximum electron quiver velocity, and the ponderomotive force scales linearly with the peak intensity, or a_0^2. Clearly, this classical interpretation fails when $a_0 \sim 1$ and relativistic corrections have to be applied to the electron dynamics [50, 87, 100–102]. The normalised vector potential is thus an important parameter to differentiate between the linear regime $a_0 \ll 1$ and the non-linear regime $a_0 \gtrsim 1$ of laser-plasma interaction.

3.1.2 *Electron drivers*

The mechanism of generating a plasma wave by means of a highly relativistic electron bunch differs fundamentally from laser drivers. Such electron drivers constitute a transient charge imbalance in the plasma and thus prompt a direct shielding response by the plasma electrons. Therefore, the driver-plasma interaction is largely defined by the ratio of the beam density n_b to the unperturbed plasma density n_0, whereby the plasma is termed overdense for $n_b/n_0 < 1$, and underdense for $n_b/n_0 > 1$. Similar to laser pulses, an electron beam driver may be characterised by a Gaussian density distribution

$$n_b(z, r, t) = n_{b,0} \exp\left(-\frac{(z - v_d\, t)^2}{2\sigma_z^2}\right) \exp\left(-\frac{r^2}{2\sigma_r^2}\right) \quad , \tag{3.15}$$

with peak density

$$n_{b,0} = \frac{Q/e}{(2\pi)^{3/2}\ \sigma_z\, \sigma_r^2} \tag{3.16}$$

and peak current

$$J_p = v_d \frac{Q}{\sqrt{2\pi}\, \sigma_z} \tag{3.17}$$

depending on the total driver charge Q.

The electric field of a point charge q moving uniformly with velocity v is given by [49, 103]

$$\vec{E} = \frac{q}{4\pi\, \epsilon_0} \frac{\vec{r}_o}{r_o^3} \frac{1 - \frac{v^2}{c^2}}{\left(1 - \frac{v^2}{c^2}\ \sin^2(\theta)\right)^{3/2}} \quad , \tag{3.18}$$

where r_o is the distance from the charge to an observer, and θ is the angle between the observation vector $\vec{r}_o$ and the velocity vector $\vec{v}$. Compared to a charge at rest, the electric field in the direction perpendicular to the propagation axis is enhanced by a factor of $1/\sqrt{1 - v^2/c^2}$, whereas the electric field along the propagation axis is suppressed by a factor of $\left(1 - v^2/c^2\right)$ and asymptotically vanishes for $v \to c$. The electric field of a uniformly moving charge approaching the speed of light is thus

effectively confined to the transverse plane[2]. This effect can be generalised to any charge distribution moving with constant, relativistic velocity [103]. For a Gaussian electron distribution, the transverse electric space-charge field is [106]

$$E_{b\perp}(z,r,t) = \begin{cases} 0 & \text{for } r = 0 \\ -\dfrac{e\,\sigma_r^2}{\epsilon_0\,r}\,n_{b,0}\,\exp\left(-\dfrac{(z-v_d\,t)}{2\sigma_z^2}\right)\times\left(1-\exp\left(-\dfrac{r^2}{2\sigma_r^2}\right)\right) & \text{for } r \neq 0 \end{cases} . \tag{3.19}$$

In contrast to a laser pulse, the transverse electric field of a Gaussian electron driver is thus zero on axis[3], with a peak value of $E_{b,0} \approx 0.451\,\frac{n_{b,0}\,e\,\sigma_r}{\epsilon_0}$ located at a distance $r \approx 1.585\,\sigma_r$ from its centre. The current density of the electron beam further generates an azimuthal magnetic field, which is related to the electric space-charge field via [49, 103]

$$B_{b,\theta} = \frac{v_d}{c^2}\,E_{b\perp} \quad . \tag{3.20}$$

The nature of the driver-plasma interaction depends on whether the driver traverses an overdense or underdense plasma. When $n_{b,0}/n_0 \ll 1$, the electron beam imposes only a small perturbation to the plasma density and the driver charge is rapidly shielded by the plasma electrons. The resulting plasma density modulation trailing the driver then forms the plasma wave, with wake amplitudes linearly scaling with $n_{b,0}/n_0$. As the driver density increases and $n_{b,0}/n_0 \lesssim 1$, however, the plasma density modulation is no longer small compared to n_0 and the interaction becomes non-linear [107]. In case of a driver traversing an underdense plasma with $n_{b,0}/n_0 > 1$, the number of plasma electrons is insufficient to shield the driver entirely and all plasma electrons are rapidly expelled from the driver region [108]. The plasma response is then governed by the electric space-charge field and magnetic field of the driver.

The shielding efficiency thus depends on the number of plasma electrons in the vicinity of the driver, whereby the characteristic interaction length is then the plasma

2 Note that this effect arises naturally in classical electrodynamics as a consequence of a finite speed of light. Equation 3.18 has been first noted by Heaviside in 1888 [104] (see also [105]). A thorough derivation can be found, for example, in [49] (chapter 10.3 therein) or in [103]. In the framework of special relativity, the Lorentz transformations of electromagnetic fields and spacetime coordinates provide a straight-forward method to arrive at the same result (see, for example, [49] (chapter 12.3 therein)).

3 Which is, of course, true for any radially symmetric charge distribution.

skin depth. A measure of (non-)linearity can thus be found upon normalising the beam dimensions to the skin depth [109, 110], such that

$$\frac{n_{b,0}}{n_0} = \frac{\tilde{Q}}{(2\pi)^{3/2}\, k_p \sigma_z \,\left(k_p \sigma_r\right)^2} \quad , \tag{3.21}$$

with

$$\tilde{Q} = \frac{Q\, k_p^3}{e\, n_0} \quad . \tag{3.22}$$

The parameter $\tilde{Q}$ corresponds to the number of driver electrons in a volume of cubic skin depth and can be interpreted as normalised beam charge. Similar to the a_0 parameter for laser drivers, it serves to distinguish between the linear regime for $\tilde{Q} \ll 1$ and the non-linear regime for $\tilde{Q} \gtrsim 1$.

3.2 1D COLD FLUID APPROXIMATION

The microscopic dynamics inside a plasma usually involves a huge number of particles; at a plasma density of $n_0 = 10^{18}\,\mathrm{cm}^{-3}$, a volume of $100\,\mu\mathrm{m}^{-3}$ contains 10^{12} electrons. A rigorous derivation of all individual particle motions and their mutual interactions is therefore extremely challenging. However, when the plasma dynamics are dominated by collective effects, an approximative macroscopic description can be found under certain assumptions.

The first prerequisite is that the driver traverses a homogeneous, unperturbed plasma environment. The plasma response to the driver is then further assumed to be governed solely by collective electron dynamics, implying that the ions form a static background and collisions can be neglected on the time scale of the driver-plasma interaction. In addition, the contribution of thermal velocities are assumed to be negligible for the collective electron motion.

These preconditions result in the simplified cold electron fluid model [87, 100, 111, 112], which formulates the plasma dynamics in terms of a laminar flow with associated fluid momenta, plasma densities and electrostatic potentials. A key element in this picture is the quasi-static or frozen-field approximation. It implies that the driver evolves on time scales much larger than $1/\omega_p$, and can hence be regarded as being rigid during a plasma electron oscillation period. This results in a convenient

simplification of temporal derivatives when applying a Galilean coordinate transform into the co-moving frame of the driver traversing with v_d in z-direction,

$$\zeta = z - v_d t \tag{3.23a}$$

$$\tau = t \tag{3.23b}$$

$$\frac{\partial}{\partial t} = \frac{\partial}{\partial \tau} - v_d \frac{\partial}{\partial \zeta} \ , \tag{3.23c}$$

as the derivative with respect to τ vanishes upon applying the quasi-static approximation. In the limit of driver velocities approaching the speed of light, temporal derivatives thus translate into 1D spatial derivatives

$$\frac{\partial}{\partial t} \simeq -c \frac{\partial}{\partial \zeta} \ , \tag{3.24}$$

implying that the electromagnetic fields, charge currents, and plasma density variations are frozen in the speed-of-light frame. The plasma wake is then fully characterised by its electrostatic 1D potential ϕ, which is typically treated in its normalised form

$$\varphi = \frac{e}{m_e c^2} \phi \ . \tag{3.25}$$

The normalised electrostatic plasma wake potential in the cold 1D fluid model obeys the differential equation [87, 100, 111, 112]

$$\frac{\partial^2 \varphi(\zeta)}{\partial \zeta^2} = k_p^2 \left(\frac{1 + a^2(\zeta)}{2\,(1 + \varphi(\zeta))^2} + \frac{n_b(\zeta)}{n_0} - \frac{1}{2} \right) \ , \tag{3.26}$$

where the a and n_b terms correspond to laser and electron-beam drivers, respectively. It describes how the longitudinal shape of the driver determines the emerging plasma wake structure. Finding solutions to this equation for arbitrary driver profiles generally requires numerical methods with suitable boundary conditions reflecting the initially unperturbed state of the plasma. Once φ has been derived, the longitudinal electric field associated with the electrostatic wake potential follows directly from

$$\frac{E_z(\zeta)}{E_{wb}} = -k_p^{-1} \frac{\partial \varphi(\zeta)}{\partial \zeta} \ , \tag{3.27}$$

whereas the electron density variation is recovered according to

$$\frac{\Delta n(\zeta)}{n_0} = \frac{n(\zeta) - n_0}{n_0} = k_p^{-2} \frac{\partial \varphi^2(\zeta)}{\partial \zeta^2} \quad . \tag{3.28}$$

In this 1D form, the above equations provide a model describing the excitation of purely longitudinal plasma waves. It is thus strictly valid only when transverse components can be neglected, that is, if the contribution of the drive laser's transverse ponderomotive force, or, in case of electron drivers, of its transverse self-fields, are small. This constraint holds approximately true for mildly intense drivers with $a_0 \ll 1$ or $n_{b,0}/n_0 \ll 1$, or wide drivers with radius $\sigma_r \gg k_p^{-1}$. Nevertheless, the 1D cold fluid model is insightful to illustrate the general effects of varying driver parameters on the shape of the resulting plasma wave.

3.3 LINEAR PLASMA WAVES

Drivers of strength $a_0 \sim \tilde{Q} \ll 1$ impose only a small perturbation on the nominal plasma density. This, in turn, implies that $\varphi \ll 1$. In this case, the wake potential term in equation 3.26 is well approximated by its linear Taylor expansion $(1+\varphi)^2 \simeq 1 - 2\varphi$. The linearised version of equation 3.26 then takes the form[4]

$$\frac{\partial^2 \varphi(\zeta)}{\partial \zeta^2} = -k_p^2 \varphi(\zeta) + k_p^2 \left(\frac{a^2(\zeta)}{2} + \frac{n_b(\zeta)}{n_0} \right) \quad . \tag{3.29}$$

This corresponds to a driven harmonic oscillator with an oscillation period $2\pi/k_p = \lambda_p$. Under the constraint that the generated plasma waves remain purely longitudinal, solutions to this equation can further be straightforwardly expanded for 3D driver distributions. Analytic solutions to equation 3.29 can be derived, for example, for cylindrically symmetric bi-Gaussian drivers. The density distribution of such an electron driver in the co-moving frame is

$$n_b(\zeta, r) = n_{b,0} \exp\left(-\frac{\zeta^2}{2\sigma_z^2}\right) \exp\left(-\frac{r^2}{2\sigma_r^2}\right) \quad . \tag{3.30}$$

4 Here, the additional term $a^2\varphi$ has been neglected, since $\varphi \ll 1$ implies that $a^2\varphi \ll a^2$.

In an equivalent expression for a linearly polarised laser driver at focus, the cycle-averaged normalised vector potential corresponds to

$$\left\langle a^2(\zeta, r)\right\rangle = \frac{a_0^2}{2}\,\exp\left(-\frac{\zeta^2}{2\sigma_z^2}\right)\,\exp\left(-\frac{r^2}{2\sigma_r^2}\right) \propto I(\zeta, r) \quad , \tag{3.31}$$

with $\sigma_z = \sigma_t c$ and $\sigma_r = w_0/2$.

The electrostatic wake potential for Gaussian drivers in the linear regime then evaluates to [100, 112–114]

$$\varphi(\zeta, r) = -\varphi_0\,\sqrt{2\pi}\,k_p\sigma_z\,\exp\left(-\frac{k_p^2\sigma_z^2}{2}\right)\,\sin\left(k_p\,\zeta\right) \times \exp\left(-\frac{r^2}{2\sigma_r^2}\right) \quad , \tag{3.32}$$

with $\varphi_0 = a_0^2/4$ for laser drivers and $\varphi_0 = n_{b,0}/n_0$ for electron drivers. As this expression is a steady-state solution, it describes the shape of the plasma wake after its initial response to the driver, that is, for co-moving positions sufficiently far behind the driver. The corresponding longitudinal wakefield is derived, according to equation 3.27, from the co-moving derivative of the wake potential as

$$\begin{aligned}\frac{E_z(\zeta, r)}{E_{wb}} &= -k_p^{-1}\,\frac{\partial\varphi(\zeta, r)}{\partial\zeta} \\ &= \varphi_0\,\sqrt{2\pi}\,k_p\sigma_z\,\exp\left(-\frac{k_p^2\sigma_z^2}{2}\right)\,\cos\left(k_p\,\zeta\right) \times \exp\left(-\frac{r^2}{2\sigma_r^2}\right) \quad .\end{aligned} \tag{3.33}$$

Due to the transverse shape of the driver, the wake potential further inherits a non-vanishing radial derivative. This gives rise to a transverse electromagnetic wakefield component

$$\begin{aligned}\frac{(E_r - cB_\theta)(\zeta, r)}{E_{wb}} &= -k_p^{-1}\,\frac{\partial\varphi(\zeta, r)}{\partial r} \\ &= -\varphi_0\,\sqrt{2\pi}\,k_p\sigma_z\,\exp\left(-\frac{k_p^2\sigma_z^2}{2}\right)\,\sin\left(k_p\,\zeta\right) \times \frac{k_p r}{(k_p\sigma_r)^2}\,\exp\left(-\frac{r^2}{2\sigma_r^2}\right) \quad ,\end{aligned} \tag{3.34}$$

where B_θ denotes the azimuthal magnetic field. The longitudinal and transverse wakefields further obey the fundamental relation

$$\frac{\partial}{\partial r}E_z = \frac{\partial}{\partial\zeta}\left(E_r - cB_\theta\right) \quad , \tag{3.35}$$

which is known as the Panofsky-Wenzel theorem [87, 115]. The normalised plasma electron density variation in the linear regime is simply the inverse of the electrostatic wake potential, as

$$\begin{aligned}\frac{\Delta n(\zeta, r)}{n_0} &= k_p^{-2} \frac{\partial \varphi^2(\zeta, r)}{\partial \zeta^2} \\ &= -\varphi(\zeta, r) \quad .\end{aligned} \tag{3.36}$$

Evidently, the longitudinal shape of a plasma wave in the linear regime is characterised by sinusoidal oscillations with period λ_p. The electric field is thereby zero in the centre of the wake period, with positive values at the front and negative values towards the rear. Electrons can thus be accelerated only in the second half of a plasma wake period. The peak amplitude of the wake scales linearly with the driver strength parameter, but also depends on the driver length, according to the scaling $\varphi, E_z \propto k_p \sigma_z \exp\left(-k_p^2 \sigma_z^2/2\right)$. For a fixed a_0 or $n_{b,0}$, the maximum wake amplitude is thus attained when $k_p \sigma_z = 1$. This constitutes the resonance condition in the 1D cold fluid picture.

In the transverse dimension, the density variation, accelerating field and wake potential scale according to the radial shape of the driver. Therefore, the wake amplitude is largest on axis. The radial wakefield, in contrast, is zero on axis with increasing magnitude for $|r| < \sigma_r$. This is convenient for particle acceleration, as the plasma wave can not only provide accelerating, but also focusing fields. However, examining equations 3.33 and 3.34 reveals that the accelerating and focusing fields are longitudinally out of phase by $\pi/2$, which means that only the rear quarter of a linear plasma wave provides suitable conditions for electron acceleration.

3.4 NON-LINEAR PLASMA WAVES

As the driver strength increases, such that $a_0 \sim \tilde{Q} \sim 1$, the condition for the linear approximation $\varphi \ll 1$ no longer holds, and thus the full form of equation 3.26 must be considered. Furthermore, the transverse components of the driving force become increasingly significant for drivers of finite transverse extent [114]. Nevertheless, the 1D model is useful to illustrate the qualitative implications on the longitudinal plasma wave structure upon increasing the driver strength. The transition from the linear to the non-linear regime is illustrated in Figure 3.1 for laser drivers and, correspondingly, in Figure 3.2 for electron-beam drivers.

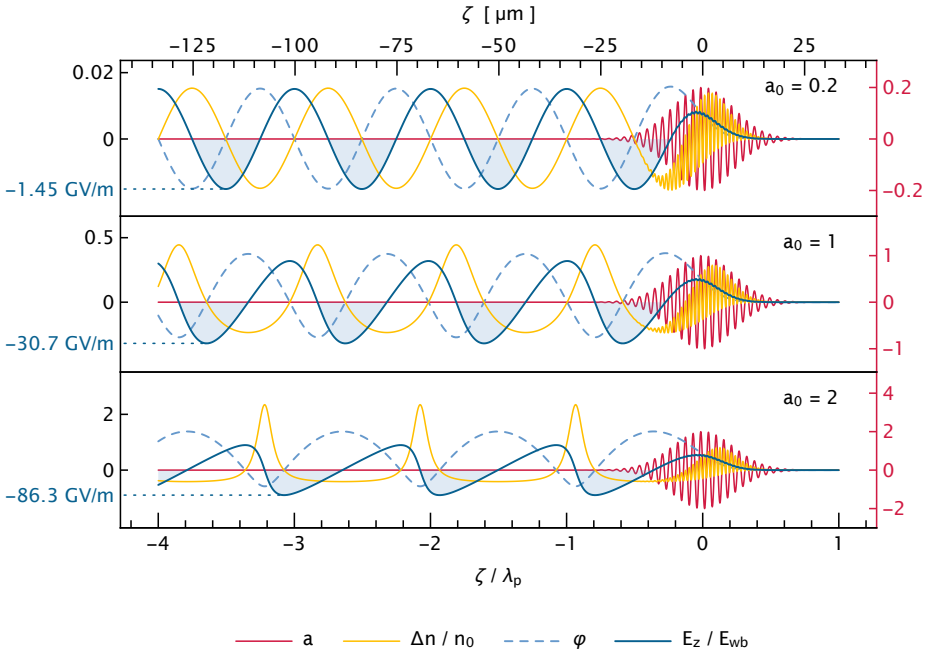

Figure 3.1: **Laser-driven plasma waves.** The transition from linear to non-linear plasma waves is illustrated for a linearly polarised Gaussian laser pulse driver with $k_p \sigma_z = 1$ and, from top to bottom, increasing a_0. In addition to normalised parameters, absolute values of the accelerating field amplitude are indicated for $n_0 = 10^{18}\,\mathrm{cm}^{-3}$.

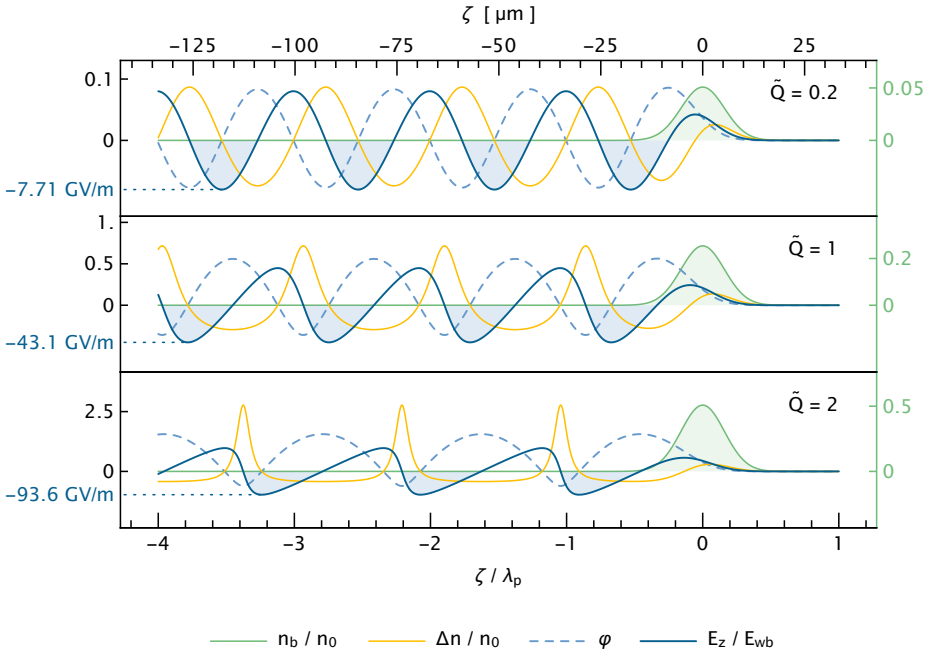

Figure 3.2: **Electron beam-driven plasma waves.** From top to bottom, the driver strength $\tilde{Q}$ increases, corresponding to a Gaussian electron beam with $k_p \sigma_z = 1$ and $k_p \sigma_r = 0.5$. Once again, absolute values of the accelerating field amplitude are indicated for $n_0 = 10^{18}\,\mathrm{cm}^{-3}$.

Both figures display numerical solutions to equation 3.26 for Gaussian drivers of varying strength. For small wake amplitudes, the electrostatic potential, electric field and electron density variations correspond to the analytic expressions found for the linear regime, recovering the characteristic harmonic oscillations. As the driver strength parameter approaches unity, the plasma electrons become increasingly relativistic and the shape of the resulting plasma wave deviates substantially from this sinusoidal form [111, 116–118]. The electron density then shows distinct peaks at the rear of the plasma wave period, and the wake potential becomes increasingly distorted. In turn, the amplitude of the electric field increases, and the position of the peak accelerating field shifts towards the rear of the wake. For even higher driver strength, the electron density evolves into strong spikes, while the electrostatic potential takes on a parabolic shape around the wake centre. The electric field, accordingly, exhibits a linear slope around the wake centre, with a sharp transition between accelerating and decelerating phase at the edges of each plasma period. Another observation is that the plasma wavelength increases, which can be attributed to relativistic mass increase of the plasma electrons [116].

3.5 BLOWOUT REGIME

A general characteristic of plasma waves in the 1D approximation is that the transverse wakefield is determined by the radial shape of the driver. This further implies that the accelerating field is non-uniform in the transverse dimension and the focusing field is non-uniform in the longitudinal dimension. However, a purely 1D model cannot be used to infer an accurate description for plasma waves driven by short, highly intense and tightly focused drivers, that is, for $a_0 \sim \tilde{Q} \gg 1$, $\sigma_z \lesssim \lambda_p/2$ and $k_p \sigma_r \lesssim 1$. For electron beam drivers, this implies $n_b > n_0$, such that the plasma is underdense with respect to the drive beam. The plasma response then becomes highly non-linear and is dominated by the transverse ponderomotive force or the space-charge field of the driver, respectively. Such conditions lead to the so-called blowout regime [108, 119], in which all plasma electrons are rapidly expelled radially off-axis, resulting in a region behind the driver that is completely void of electrons. The plasma ions, in contrast, still remain nearly stationary. Subsequent to the initial impulse of the driver, the plasma electrons therefore experience a radial restoring force emerging from the Coulomb attraction of the homogeneous background of positively charged ions. They thus ultimately return to the central axis at a distance of approximately one plasma wavelength behind the driver. This results in a closed structure trailing the driver, referred to as blowout. The formation of such a pure ion cavity surrounded by a thin sheath of plasma electrons is the defining characteristic of the blowout regime[5].

The necessary condition of expelling all plasma electrons from the central wake region inevitably implies that individual electron trajectories cross each other in the vicinity of the driver, which leads to the breakdown of the laminar flow assumption essential for fluid models [120]. Instead, a fully kinetic treatment of individual particle dynamics is generally required to accurately obtain the resulting wakefield over the entire blowout structure. The established method for studying specific blowout scenarios is therefore to resort to particle-in-cell (PIC) simulations, however, several phenomenological and semi-analytical models have been developed for both LWFA and PWFA scenarios [109, 121–127]. An example 3D PIC simulation[6] of an electron beam-driven plasma wave is presented in Figure 3.3, visualising the blowout structure in terms of the electron density, the longitudinal electric field and the transverse wakefield.

5 In reference to the resulting shape, the term bubble regime is often used synonymously in the literature when referring to the blowout regime.

6 Numerical simulations presented in this thesis are performed with the particle-in-cell code VSim [128], unless otherwise stated.

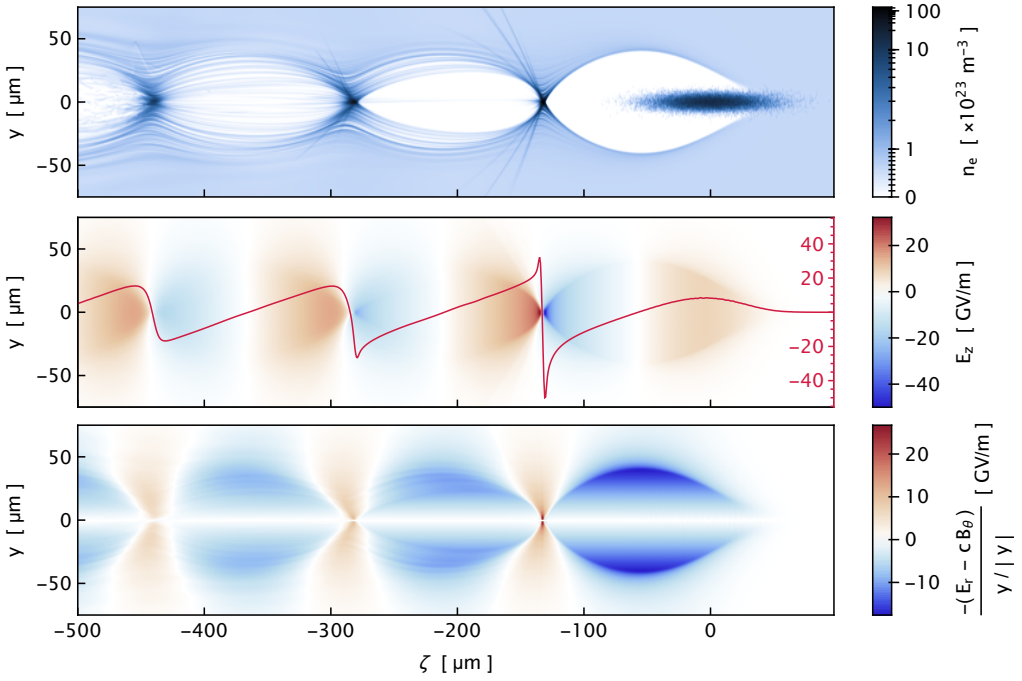

Figure 3.3: **Blowout regime.** Visualisation of a 3D PIC simulation of a plasma wave with nominal plasma wavelength of 150 µm, driven by a 10 GeV Gaussian electron beam with $Q \approx 1\,\mathrm{nC}$, $k_p\sigma_z = 1$ and $k_p\sigma_r \approx 0.15$, corresponding to $\tilde{Q} \approx 10$ and $n_b/n_0 \approx 30$. Shown are the central slices in the y,z-plane of the electron density (top), the longitudinal electric field (middle) and the transverse focusing field (bottom). The colour-coding in the longitudinal (transverse) field indicate accelerating (focusing) regions in blue, and decelerating (defocusing) regions in red. The solid red line indicates the on-axis longitudinal electric field.

The formation of an electron-free cavity around the driver is clearly apparent in the first wake period. The colour-scale used to illustrate the wakefield structure indicates where electrons would experience an accelerating and focusing phase in blue, whereas a red colour marks decelerating and defocusing regions, respectively. A discussion of the general blowout characteristic and the wake structure observed in Figure 3.3 can be formulated as follows:

At the rear of the blowout cavity, where the plasma electrons return on-axis, the electron sheath collapses into a vertex of tremendous electron density. The initial transverse charge separation induced by the driver thus translates into a longitudinal charge separation with a sharp density excursion at the rear of the blowout. The general structure of the associated on-axis wakefield in the blowout regime therefore closely resembles the non-linear 1D approximation, particularly in recovering the

linear slope of the on-axis longitudinal electric field around the wake centre (solid red line in Figure 3.3). The transverse wake structure, however, differs substantially from the 1D picture, due to the fundamentally different particle dynamics that lead to the formation of the wake. More specifically, the radial wakefield inside the blowout is not dictated by the driver shape, but the ion background instead. As the plasma ions form a static column of homogeneous positive charge density, the transverse wake component takes the form [108, 120, 121]

$$\begin{aligned} E_r - cB_\theta = E_r^{ion} &= \frac{k_p E_{wb}}{2} r \\ &= \frac{e n_0}{2\epsilon_0} r \ , \end{aligned} \tag{3.37}$$

such that its magnitude is zero on axis and linearly increases with r. Moreover, the homogeneity of the ion background implies that the transverse wakefield is uniform along ζ, such that $\partial_\zeta (E_r - c B_\theta) = 0$. It follows directly from the Panofsky-Wenzel theorem (see equation 3.35) that, in turn, the longitudinal wakefield is radially uniform across the entire blowout. This constitutes advantageous conditions for the acceleration of electrons, as the blowout provides longitudinally independent linear focusing fields along the entire wake structure[7], while at the same time providing radially independent accelerating fields.

Such a field configuration is a prerequisite for preserving the emittance of an electron distribution during acceleration (see chapter 4.1.1). Accessing the blowout regime is therefore the preferential mode of operation for a plasma wakefield accelerator. This typically requires laser pulses with a peak power of $\sim 100\,\mathrm{TW}$, or electron driver bunches with a peak current of several kiloampere. To efficiently generate a blowout, laser drivers thereby have to be focused to dimensions on the order of the nominal plasma wavelength, with even smaller transverse size required for electron drivers [120].

Most modern LWFAs rely on Ti:sapphire laser systems with a central wavelength of 800 nm to generate driver pulses with a few tens of femtoseconds duration and up to several hundreds of terawatt. At this wavelength, peak intensities beyond $\gtrsim 10^{18}\,\mathrm{W/cm^2}$ are required to reach the relativistic non-linear regime, which implies focal spot sizes of a few tens of micrometres. Modern LWFAs are hence typically operated at plasma densities on the order of $10^{18}\,\mathrm{cm^{-3}}$.

7 Conversely, this poses a fundamental challenge for positron acceleration.

PWFAs thus far rely on large-scale conventional linear accelerators to provide the electron drivers. Generating sufficiently short, high-current electron beams, however, imposes challenging operating conditions upon compressing, transporting and focusing the designated drivers. Such linac-driven PWFAs are thus typically restricted to operate at significantly lower plasma densities in the range of $10^{16} - 10^{17}\,\mathrm{cm}^{-3}$ [129]. An emerging promising alternative is to utilise electron beams generated in comparatively compact, high-density LWFAs as PWFA drivers, a concept further discussed in chapter 10.

4

ELECTRON BEAM DYNAMICS IN PLASMA WAKEFIELDS

Electrons placed inside a plasma wave can continuously gain forward momentum, provided that the wake structure persists and the electrons remain in the accelerating phase of the wake. A population of electrons accelerated in a plasma wakefield is commonly referred to as witness beam. As plasma wakefields are electromagnetic in nature, the predominant force acting on witness beam electrons is the Lorentz force

$$\vec{F}_L = \frac{d\vec{p}}{dt} = -e\left(\vec{E} + \vec{v} \times \vec{B}\right) \quad , \tag{4.1}$$

with relativistic momentum $\vec{p} = \gamma\, m_e \vec{v}$ and Lorentz factor

$$\gamma = \frac{E_{kin}}{m_e\, c^2} + 1 = \frac{1}{\sqrt{1 - \left|\vec{\beta}\right|^2}} \quad \text{, with} \quad \vec{\beta} = \frac{\vec{v}}{c} \ . \tag{4.2}$$

Because the wakefield phase propagates at relativistic velocities, witness electrons need to be initially injected into the accelerating structure. This can be an intricate process, and several methods of injection are discussed in chapter 6 . Under the approximation that the wake structure remains static and injected electrons match the phase velocity of the wake, some basic aspects of the longitudinal and transverse dynamics of the witness beam are discussed in the following.

4.1 BEAM QUALITY PARAMETERS

The tremendous accelerating fields inside a plasma cavity result in a huge energy gain over short distances, and therefore provide a pathway for building much more compact particle accelerators. However, the final witness energy is just one performance indicator. The output from an ideal particle accelerator would be a collimated electron bunch with small spatial dimensions, consisting of a large number of particles with equal kinetic energy. This goal is generally unattainable; a realistic particle ensemble of finite size will always inherit a finite energy distribution and a finite transverse momentum spread. Key quality parameters are therefore based on an analysis of the statistical moments of the particle beam distribution along several degrees of freedom.

4.1.1 *Beam emittance*

A single particle is fully characterised by its 6D phase space vector in the laboratory frame $\vec{u} = [x, p_x, y, p_y, z, p_z]^T$ and its evolution during acceleration. An ensemble of many particles, in turn, spans a phase space volume consisting of all individual particle phase vectors. The emittance is, in its broadest definition, a measure of this phase space volume. A high density in phase space is usually desired, therefore a small emittance is an indicator of high beam quality.

However, the entire 6D phase space distribution is inaccessible to a single simultaneous measurement [130]. Moreover, the typical experimental observable consists of a geometric projection of the particle beam onto a two-dimensional detection plane, determined by the slopes of the individual particle trajectories. Such geometric projections onto a (virtual) 2D plane depend on the choice of coordinate system. Therefore, the phase space is typically parametrised with respect to a reference trajectory, whereby the spatial coordinates are transformed onto an orthonormal basis centred around a reference vector and the transverse momentum variables are replaced by the angular deviation from the reference direction [131]. This forms the so-called trace space. Inside a plasma wakefield, the reference trajectory follows a straight line along the central wake axis and is thus determined by the driver trajectory. Following previous conventions, the acceleration direction is chosen along the z-dimension. The trace space vector is then $\vec{u}_{tr} = [x, x', y, y', \zeta, \delta]^T$, with the single-particle divergences $x' = dx/dz \approx p_x/p_z$ and $y' = dy/dz \approx p_y/p_z$, since $p_z \gg p_x, p_y$. The longitudinal trace space component is thereby expressed in terms of the co-moving beam coordinate $\zeta = z - \langle z \rangle$ and the particle's relative momentum deviation $\delta = (p_z - \langle p_z \rangle) / \langle p_z \rangle$, defined here with respect to the mean forward momentum $\langle p_z \rangle$. The 6D trace space distribution spanned by all particles may then be separated into three individual projections onto its principal planes, $\mathbf{X} = [x, x']^T$, $\mathbf{Y} = [y, y']^T$ and $\mathbf{Z} = [\zeta, \delta]^T$, such that each can be associated with its own emittance value. A robust definition of these emittances is based on statistical measures of the resulting 2D distributions, exemplified for $\mathbf{X}$ in the following.

In this transverse plane, the extent of the beam in x and x' dimensions can be expressed by the rms values σ_x and $\sigma_{x'}$ along the individual axes, respectively. The joint distribution, in turn, is characterised by the covariance matrix

$$\mathbf{\Sigma_{XX}} = \mathrm{Cov}(\mathbf{X}, \mathbf{X}) = \begin{bmatrix} \mathrm{Cov}(x, x) & \mathrm{Cov}(x, x') \\ \mathrm{Cov}(x', x) & \mathrm{Cov}(x', x') \end{bmatrix} = \begin{bmatrix} \mathrm{Var}(x) & \mathrm{Cov}(x, x') \\ \mathrm{Cov}(x, x') & \mathrm{Var}(x') \end{bmatrix} , \quad (4.3)$$

whereby diagonal elements correspond to the second central moments of the individual x and x' distributions and off-diagonal elements denote their linear correlation. The covariance matrix is symmetric and positive semi-definite, which implies that its eigenvectors are orthogonal with associated non-negative eigenvalues. More importantly, its determinant represents the generalised variance of the underlying two-dimensional distribution, quantifying the spread of points in the x-x' plane around their barycentre. The square root of the determinant, consequently, corresponds to the joint standard deviation from the mean, which defines the transverse trace space emittance

$$\epsilon_x = \sqrt{\det(\boldsymbol{\Sigma}_{\mathbf{xx}})} = \sqrt{\mathrm{Var}(x)\ \mathrm{Var}(x') - \mathrm{Cov}(x,x')^2}\ . \tag{4.4}$$

For a beam distribution centred around the reference trajectory, that is, for vanishing first central moments $\langle x\rangle = \langle x'\rangle = 0$, expression 4.4 corresponds to the rms emittance [132]

$$\epsilon_{x,\mathrm{rms}} = \sqrt{\langle x^2\rangle\,\langle x'^2\rangle - \langle x\,x'\rangle^2}\ . \tag{4.5}$$

The transverse trace space emittance is thus a key quality parameter of particle beams, providing a measure of the joint spread in transverse particle positions and divergences in units of metre times radian.

The geometric representation of this emittance is an ellipse in the trace space projection, encompassing all particles within the rms region of the joint particle distribution. An example of such rms trace space ellipse is shown in Figure 4.1. Its orientation is defined by the unit eigenvectors of the covariance matrix, with major and minor axes scaled with the square root of their corresponding eigenvalues. If the emittance is preserved, the area enclosed by the ellipse $A = \pi\,\epsilon_x$ is a constant of motion. The shape and orientation of the ellipse, however, is continuously altered along the particle beam's trajectory. The evolution of the projected beam distribution can thus be reduced to a parametric description of the trace space ellipse. This is achieved by normalising the covariance matrix by the emittance, such that it represents a unit area:

$$\frac{\boldsymbol{\Sigma}_{\mathbf{xx}}}{\epsilon_x} = \begin{bmatrix} \hat{\beta} & -\hat{\alpha} \\ -\hat{\alpha} & \hat{\gamma} \end{bmatrix}\ \text{, with}\quad \hat{\alpha} = -\frac{\langle x\,x'\rangle}{\epsilon_x}\ ,\quad \hat{\beta} = \frac{\langle x^2\rangle}{\epsilon_x}\ ,\quad \hat{\gamma} = \frac{\langle x'^2\rangle}{\epsilon_x}\ . \tag{4.6}$$

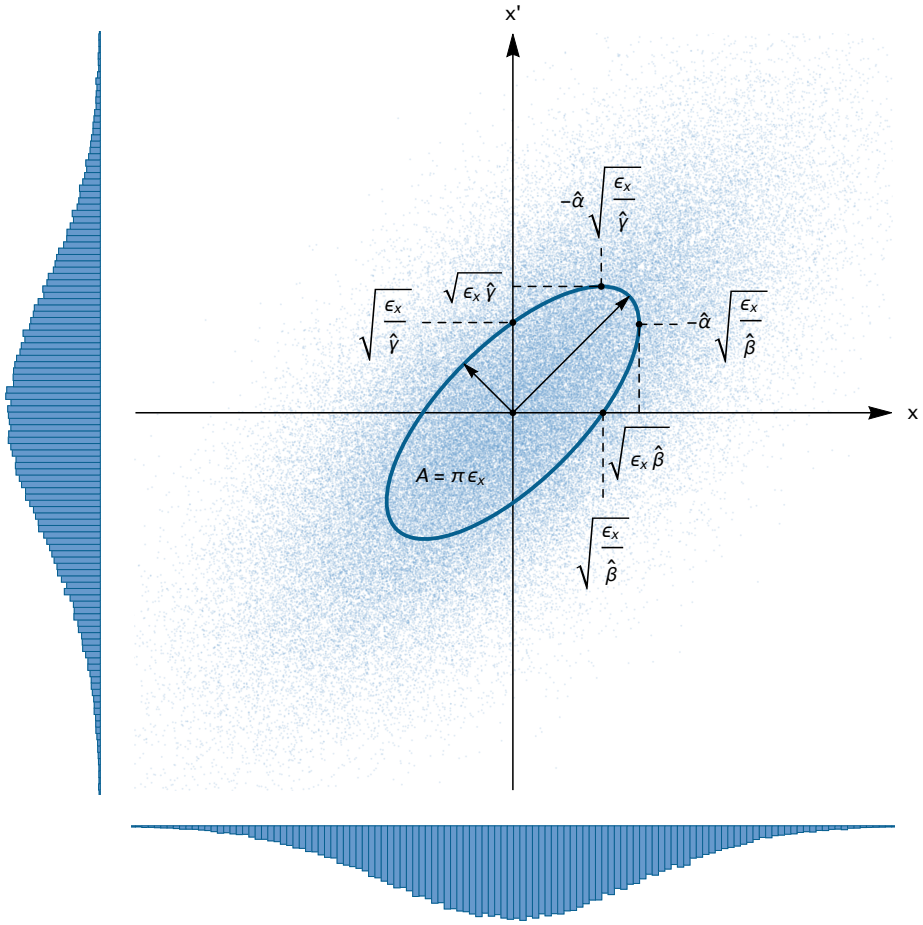

Figure 4.1: **Trace space rms emittance.** Individual distributions in x and x' are shown as histograms to the left and bottom, respectively. The rms region of the joint particle distribution is enclosed by an ellipse characterised by the Courant-Snyder parameters $\hat{\alpha}$, $\hat{\beta}$ and $\hat{\gamma}$. The area of the ellipse is defined by the emittance ϵ_x.

The determinant of the normalised covariance matrix then evaluates to $\hat{\beta}\,\hat{\gamma} - \hat{\alpha}^2 = 1$, with $\hat{\alpha}$, $\hat{\beta}$ and $\hat{\gamma}$ being the Courant-Snyder parameters [133]. An illustration of this parametrisation of the trace space ellipse is included in Figure 4.1.

The rms values of the particle distribution and the Courant-Snyder parameters are thus related according to

$$\sigma_x = \sqrt{\epsilon_x\,\hat{\beta}} \tag{4.7a}$$

$$\sigma_{x'} = \sqrt{\epsilon_x\,\hat{\gamma}} \tag{4.7b}$$

$$\rho_{x,x'} = -\frac{\epsilon_x\,\hat{\alpha}}{\sigma_x\,\sigma_{x'}} = -\frac{\epsilon_x\,\sqrt{\hat{\beta}\,\hat{\gamma} - 1}}{\sigma_x\,\sigma_{x'}}\ , \tag{4.7c}$$

where $\rho_{x,x'}$ is the linear correlation coefficient between x and x'. The correlation term vanishes for $\hat{\alpha} = 0$, corresponding to a collimated beam, whereas the beam is converging for $\hat{\alpha} > 0$ and diverging for $\hat{\alpha} < 0$.

Such a projected emittance and parametrisation of the corresponding trace space rms ellipse can be equivalently defined for all three principal projection planes **X**, **Y** and **Z** individually. In the longitudinal plane, $\sigma_\zeta = \sqrt{\langle\zeta^2\rangle}$ thereby corresponds to the rms beam length and $\sigma_\delta = \sqrt{\langle\delta^2\rangle}$ to the rms relative energy spread. The emittance of the full 6D trace space is generally obtained from the whole beam matrix

$$\epsilon_{x,y,z} = \sqrt{\det(\boldsymbol{\Sigma}_{\mathbf{X},\mathbf{Y},\mathbf{Z}})} = \sqrt{\det\left(\begin{bmatrix} \boldsymbol{\Sigma}_{\mathbf{XX}} & \boldsymbol{\Sigma}_{\mathbf{XY}} & \boldsymbol{\Sigma}_{\mathbf{XZ}} \\ \boldsymbol{\Sigma}_{\mathbf{YX}} & \boldsymbol{\Sigma}_{\mathbf{YY}} & \boldsymbol{\Sigma}_{\mathbf{YZ}} \\ \boldsymbol{\Sigma}_{\mathbf{ZX}} & \boldsymbol{\Sigma}_{\mathbf{ZY}} & \boldsymbol{\Sigma}_{\mathbf{ZZ}} \end{bmatrix}\right)}\ . \tag{4.8}$$

If, however, the individual projected distributions are linearly independent, that is, if the diagonal coupling elements of the beam matrix vanish[1], the generalised emittance reduces to the product of the principal emittances

$$\epsilon_{x,y,z} \approx \epsilon_x\,\epsilon_y\,\epsilon_z\ . \tag{4.9}$$

1 This is usually a desired condition, although deliberate coupling and emittance exchange between principal planes can be exploited for manipulating the shape of the 6D beam distribution (see, for example, Ha et al. [134]).

The full beam distribution is thus characterised by a six-dimensional rms hyperellipsoid of volume

$$V_{6D,\mathrm{rms}} = \frac{\pi^3}{6}\sqrt{\det(\boldsymbol{\Sigma}_{\mathbf{X},\mathbf{Y},\mathbf{Z}})} \approx \frac{\pi^3}{6}\,\epsilon_x\,\epsilon_y\,\epsilon_z \quad . \tag{4.10}$$

The average trace space density can then be formally defined as the charge contained in this volume, such that

$$\bar{\rho}_{6D} = \frac{Q_{V_{6D,\mathrm{rms}}}}{V_{6D,\mathrm{rms}}} \quad . \tag{4.11}$$

Liouville's theorem states that the trace space volume and, by extension, the trace space density is preserved under linear transformations and as long as energy is conserved [80, 131]. The latter is, of course, not the case in plasma wakefields, where the particles are supposed to continuously gain energy; the transverse divergences x' and y' and the relative energy spread δ reduce adiabatically with increased forward momentum. This energy gain can be accounted for by defining the normalised trace space emittances[2] [80, 132],

$$\epsilon_{n,x} = \langle\beta\,\gamma\rangle\;\epsilon_x \quad , \quad \epsilon_{n,y} = \langle\beta\,\gamma\rangle\;\epsilon_y \quad \text{and} \quad \epsilon_{n,z} = \langle\beta\,\gamma\rangle\;\epsilon_z \quad , \tag{4.12}$$

with $\beta\,\gamma = \sqrt{\gamma^2 - 1} = p_z/(m_e\,c)$. For highly relativistic beams, $\beta \to 1$ and is thus often dropped. Under the condition that the coupling terms between the principal trace space planes remain zero and the beam is subject only to linear focusing forces, such as offered by the blowout regime, the normalised transverse emittances are thus preserved under acceleration. Likewise, the normalised longitudinal emittance does not decrease during acceleration and is preserved under accelerating fields that only introduce a correlated energy spread. An accumulated correlated energy spread can thus be reversed, in principle (further discussed in chapter 4.3). However, this also implies that the uncorrelated fraction of the normalised energy spread, that is, an absolute residual energy spread, cannot be reduced without increasing the bunch length.

2 Note that an often implicitly used assumption is that the normalised trace space emittance obeys $\epsilon_{n,x} \approx (m_e\,c)^{-1}\sqrt{\langle x^2\rangle\,\langle p_x^2\rangle - \langle x\,p_x\rangle^2}$, and equivalently for the other principal planes. However, this approximation is only accurate for a sufficiently small energy spread, such that $\langle\beta\,\gamma\rangle^2 \approx \langle\beta^2\,\gamma^2\rangle$ [132, 135, 136].

4.1.2 *Beam brightness*

An important quality figure for many applications is the particle flux per area per solid angle, also known as Richtstrahlwert or, more commonly, the beam brightness [137, 138], defined as

$$\mathrm{dB} = \frac{\mathrm{dJ}}{\mathrm{dS}\,\mathrm{d}\Omega} \quad , \tag{4.13}$$

with beam current J, solid angle around a reference direction Ω and the corresponding normal surface area S. The brightness is thus generally a function of the longitudinal current profile and varies along the transverse trace space coordinates, though an average brightness may be measured (and defined) by the beam's projection through (virtual) apertures [137]. Associating a single brightness value for an entire particle beam is therefore often ambiguous and several conventions exist throughout the literature. A common method to quantify the beam brightness is based on the transverse rms trace space volume

$$V_{4D,\mathrm{rms}} = \frac{\pi^2}{2}\sqrt{\det(\boldsymbol{\Sigma}_{x,y})} \approx \frac{\pi^2}{2}\,\epsilon_x\,\epsilon_y \quad . \tag{4.14}$$

and the peak current J_p, thereby combining the transverse emittance implicitly with the beam charge and duration. The resulting 5D beam brightness may then be defined[3] as

$$B_{5D} = \frac{J_p}{V_{4D,\mathrm{rms}}} \approx \frac{2J_p}{\pi^2\,\epsilon_x\,\epsilon_y} \tag{4.15}$$

and its normalised equivalent, accordingly, as

$$B_{n,5D} = \frac{B_{5D}}{\langle\beta\,\gamma\rangle^2} \approx \frac{2J_p}{\pi^2\,\epsilon_{n,x}\,\epsilon_{n,y}} \quad . \tag{4.16}$$

Light source applications, particularly free electron lasers, not only benefit from high 5D brightness, but further have stringent requirements on small energy spread [139].

3 Similar common definitions drop the geometric factor $2/\pi^2$ or rely on a percentile of the trace space distribution instead of rms emittances.

A crucial quality parameter is then the 5D brightness per energy bandwidth, typically expressed in units of 0.1 % [80, 140], which defines the 6D brightness

$$B_{n,6D} = \frac{B_{n,5D}}{0.1\%\,\mathrm{bw}} \approx \frac{B_{n,5D}}{10^3\,\sigma_\delta} \quad . \tag{4.17}$$

The 6D brightness is therefore closely related to the trace space density[4]. It can thus be regarded as a compound measure of overall beam quality, as it is highest for a combination of high beam current, low transverse emittances and low energy spread.

Modern state-of-the-art X-ray FEL machines deliver electron beams with projected 6D brightness on the order of $\sim 10^{16}\,\mathrm{A/(m^2\,rad^2\,0.1\%)}$ [140], albeit relying on kilometre-scale linacs. Plasma-based accelerators could drastically reduce the spatial and economic footprint of such facilities, which is crucial to make them more accessible to a wider group of researchers. Moreover, both 5D and 6D brightness benefit from the comparatively small dimensions of plasma wakes, as they generate intrinsically short, and thus high peak-current electron beams. Recent experimental breakthroughs towards plasma-based FELs were attained with projected 6D brightness values on the order of $\sim 10^{13} - 10^{14}\,\mathrm{A/(m^2\,rad^2\,0.1\%)}$ (estimated from data in [31] using equations 4.16 and 4.17). Alongside enhancements of final energy, reproducibility and repetition rates, a substantial improvement in beam brightness through a reduction of energy spread and emittance is thus a primary objective of current plasma-based accelerator research [31, 33]. The inverse quadratic scaling of brightness with transverse emittance thereby emphasises not only the necessity for low-emittance injection methods, but also the importance of emittance preservation during acceleration and beam extraction from the plasma.

While the focusing fields inside a blowout provide a linear system, the transverse emittance may nevertheless deteriorate, due to non-linearities arising from space charge forces [141] or non-negligible ion motion [142], due to chromatic effects combined with misalignment or mismatching, Coulomb scattering and collisions, or higher-order mode couplings [143]. Not all of these processes necessarily increase the total phase space volume, specifically if they only introduce linear correlations between the transverse and longitudinal planes. Those processes are thus reversible, in principle [144]. The severity of each effect further differs for specific scenarios, with chromatic effects usually being the most common source of projected emittance growth, as discussed in the following chapter.

4 Similar to the 5D brightness, definitions differ, and some works equate the 6D brightness directly with the 6D trace- or phase space density.

4.2 BETATRON OSCILLATIONS AND TRANSVERSE MATCHING

An electron beam inside a blowout experiences two competing transverse fields, the focusing field of the wake and its own repulsive space-charge field. The effective radial Lorentz force on an electron propagating in z-direction is thus

$$\begin{aligned} F_r &= F_{w,r} + F_{b,r} \\ &= -e\left[(E_{w,r} - \beta c\, B_{w,\theta}) + (E_{b,r} - \beta c\, B_{b,\theta})\right] \quad , \end{aligned} \tag{4.18}$$

where the index w indicates the contribution from the wake and b denotes the space charge components from the beam itself. Recalling equations 3.20 and 4.2 , the transverse space charge force can be expressed as

$$\begin{aligned} F_{b,r} &= -e\left(E_{b,r} - \beta^2 E_{b,r}\right) \\ &= -e\, E_{b,r}\left(1 - \beta^2\right) \\ &= -e\,\frac{E_{b,r}}{\gamma^2} \quad . \end{aligned} \tag{4.19}$$

Space charge effects are therefore quickly suppressed upon acceleration and effectively "frozen" for ultra-relativistic electron beams. This has two significant consequences.

First, an electron beam with $\beta \to 1$ propagates ballistically in the absence of external fields, whereby the evolution of its transverse extent is governed by the transverse emittance [131],

$$\sigma_r(z) = \sigma_{r,0}\sqrt{1 + \left(\frac{z - z_0}{\hat{\beta}_0}\right)^2} \quad , \quad \text{with} \quad \hat{\beta}_0 = \sigma_{r,0}^2\,\frac{\gamma}{\epsilon_n} \quad . \tag{4.20}$$

Second, the transverse evolution of the beam inside a blowout is dominated by the linear focusing wakefield[5]. Making again use of the ultra-relativistic approximation

5 In plasma-based accelerators, space charge effects may nevertheless play a significant role, especially in the early stages of acceleration [106, 141].

and recalling equation 3.37, the transverse restoring force acting on an electron beam inside a blowout reduces to

$$\begin{aligned} F_r &\approx F_{w,r} + 0 \\ &\approx -e\,(E_{w,r} - c\,B_{w,\theta}) = -\frac{e^2\,n_0}{2\epsilon_0}\,r \\ &= -K\,r \quad . \end{aligned} \tag{4.21}$$

This corresponds to a harmonic oscillator with frequency

$$\omega_\beta = \sqrt{\frac{K}{\gamma\,m_e}} = \frac{\omega_p}{\sqrt{2\gamma}} \propto \sqrt{\frac{n_0}{\gamma}} \quad . \tag{4.22}$$

Each electron thus perform transverse oscillations around the central propagation axis, known as betatron oscillations. The betatron frequency ω_β thereby increases with plasma density and decreases with the kinetic energy of the electrons, and is thus damped during acceleration.

Following equation 4.21 and assuming $\beta_r \ll 1$, the transverse equation of motion of a single electron [145, 146] is

$$\frac{d^2x}{dz^2} + \frac{1}{\gamma}\frac{d\gamma}{dz}\frac{dx}{dz} + k_\beta^2(z)\,x = 0 \quad , \tag{4.23}$$

where $k_\beta(z) = \sqrt{K(z)\,/\,(\gamma(z)\;m_e c^2)} = k_p(z)\,/\sqrt{2\gamma(z)}$ is the betatron wavenumber. This corresponds to a continuous spiralling motion of each individual particle in the transverse trace space. However, not all electrons of the beam ensemble are simultaneously at the same oscillation phase, which is a direct reflection of a finite transverse emittance. Nevertheless, if all particles have the same kinetic energy, they all rotate in trace space coherently at an equal rate. In this case, the normalised transverse emittance is preserved and the rms trace space ellipse rotates as a whole at twice the betatron frequency.

Any energy spread, in turn, means that the phase relation between individual particles is no longer constant. This betatron decoherence, consequently, increases the phase mixing and thus the projected transverse emittance upon every turn of the trace space ellipse, until full decoherence is reached and the emittance saturates [112, 147–149]. At this point, the rms trace space ellipse aligns with the individual particle trace space trajectories, and the rms beam envelope will cease to oscillate. The beam is then said to be matched to the focusing field.

An initially mismatched beam with a finite energy spread will thus asymptotically develop into a matched beam due to phase mixing, albeit with increased final transverse emittance[6]. It is therefore prudent to achieve matching of a witness beam already during injection to mitigate transverse emittance growth during acceleration. The matching condition can be expressed in terms of the Courant-Snyder parameters as [148, 152]

$$\hat{\beta}_m = \frac{1}{k_\beta(z)} \quad , \qquad \hat{\alpha}_m = -\frac{1}{2}\frac{d\hat{\beta}_m}{dz} \qquad \text{and} \qquad \hat{\gamma}_m = \frac{(1+\hat{\alpha}_m^2)}{\hat{\beta}_m} \quad . \tag{4.24}$$

In a plasma channel with uniform density and no acceleration, this corresponds to $\hat{\beta}_m = \sqrt{2\langle\gamma\rangle}/k_p$, $\hat{\alpha}_m = 0$ and $\hat{\gamma}_m = 1/\hat{\beta}_m$. The matched spot size of the electron beam can then be retrieved from equation 4.7a

$$\sigma_{x,m} = \sqrt{\frac{\epsilon_{n,x}\,\hat{\beta}_{m,x}}{\langle\gamma\rangle}} = \left(\sqrt{\frac{2}{\langle\gamma\rangle}}\frac{\epsilon_{n,x}}{k_p}\right)^{1/2} \quad . \tag{4.25}$$

The emittance growth due to an initial mismatch of the whole beam distribution can be quantified by means of the mismatch parameter [153]

$$\mathcal{M} = \frac{1}{2}\left(\tilde{\beta}+\tilde{\gamma}+\sqrt{(\tilde{\beta}+\tilde{\gamma})^2-4}\right) \quad , \tag{4.26}$$

where $\tilde{\beta} = \hat{\beta}/\hat{\beta}_m$, $\tilde{\alpha} = \hat{\alpha} - \hat{\alpha}_m\tilde{\beta}$ and $\tilde{\gamma} = (1+\tilde{\alpha}^2)/\tilde{\beta}$ denote the relative deviations from the matched parameters. Full betatron decoherence then occurs over a distance of $L_{dc} \approx 2\pi\hat{\beta}_m/\sigma_\delta$ [147, 150] and the final transverse emittance increases to [143, 151]

$$\epsilon_{sat.} = \epsilon_{init.}\,\frac{1}{2}\left(\mathcal{M}+\frac{1}{\mathcal{M}}\right) \quad . \tag{4.27}$$

The emittance increase therefore only depends on the initial mismatch, whereas the relative energy spread determines the emittance growth rate. For large betatron oscillation amplitudes, radiation effects additionally affect the emittance and energy spread evolution [150].

While emittance growth due to chromatic decoherence is thus minimised if the whole beam is initially matched to its central kinetic energy according to expressions 4.24 , energy components that deviate from the central energy may still be

6 Very similar arguments apply for emittance growth due to transverse misalignment [143, 150, 151].

mismatched. Such a partial mismatch per energy deviation can be expressed in terms of the chromatic amplitude [154, 155]

$$\mathcal{W} = \sqrt{\left(\frac{\partial\hat{\alpha}}{\partial\delta} - \frac{\hat{\alpha}}{\hat{\beta}}\frac{\partial\hat{\beta}}{\partial\delta}\right)^2 + \left(\frac{1}{\hat{\beta}}\frac{\partial\hat{\beta}}{\partial\delta}\right)^2} \quad , \tag{4.28}$$

which results in an estimated relative growth in transverse rms emittance of [155]

$$\frac{\Delta\epsilon}{\epsilon_{\text{init.}}} \approx \frac{1}{2}\mathcal{W}^2\,\sigma_\delta^2 \quad . \tag{4.29}$$

Once a beam becomes fully matched, however, it will maintain to be matched and its normalised emittance is preserved – as long as changes in k_β occur adiabatically, that is, for $\left|dk_\beta/dz\right| \ll k_\beta$. In an accelerating structure with constant focusing forces, this translates to $|d\gamma/dz|\,/\,(2\gamma) \ll 1$, hence pure acceleration is adiabatic once the electron beam is sufficiently relativistic. If the accelerating gradient is also constant, the matched beta function then scales with $\hat{\beta}_m \propto z^{1/2}$ and the matched spot size with $\sigma_{x,m} \propto z^{-1/4}$. Variations in plasma density further alter the matching conditions, whereby $\hat{\beta}_m \propto n_0^{-1/2}$ and $\sigma_{x,m} \propto n_0^{-1/4}$. Adiabatic matching via tailored plasma density ramps can thus be used to mitigate emittance deterioration during plasma-vacuum transitions and to facilitate coupling the electron beam between plasma and conventional beam transport components [148, 149, 156–160].

4.3 BEAM LOADING

The accelerating field in a plasma wake is generally not longitudinally uniform and exhibits a slope $dE_z/d\zeta$. A witness beam of finite length will thus experience a differential energy gain and accumulate an energy correlation in ζ, also termed chirp. Transverse emittance growth due to betatron phase mixing can then be understood as differential decoherence [112, 144] of longitudinal slices along ζ, whereby the trace space ellipses of each individual (unmatched) slice rotate at different rates. It is therefore important to differentiate between a correlated energy spread emerging from a chirp, and the uncorrelated, or residual energy spread component within each longitudinal slice. Betatron decoherence due to residual energy spread develops into transverse emittance growth within each slice, whereas a purely correlated energy spread does not deteriorate the slice emittance, provided that no particle exchange between slices occurs [161]. Moreover, a linear chirp does not affect the normalised

longitudinal emittance, which implies that the correlated fraction of the energy spread is also reversible without deteriorating the (slice) transverse emittance.

An important phenomenon affecting the magnitude and shape of the chirp is the effect of beam loading [92, 162, 163]. Any charge placed inside the accelerating phase of a plasma wake will experience the wakefield generated by the driver, as well as its own wakefield [92]. A witness beam with sufficient current can therefore significantly alter the effective wakefield. Figure 4.2 illustrates the effect of beam loading in the 1D cold fluid model, corresponding to the scenario shown in Figure 3.2 for $\tilde{Q} = 2$ in the presence of a witness beam with varying peak density. It shows that

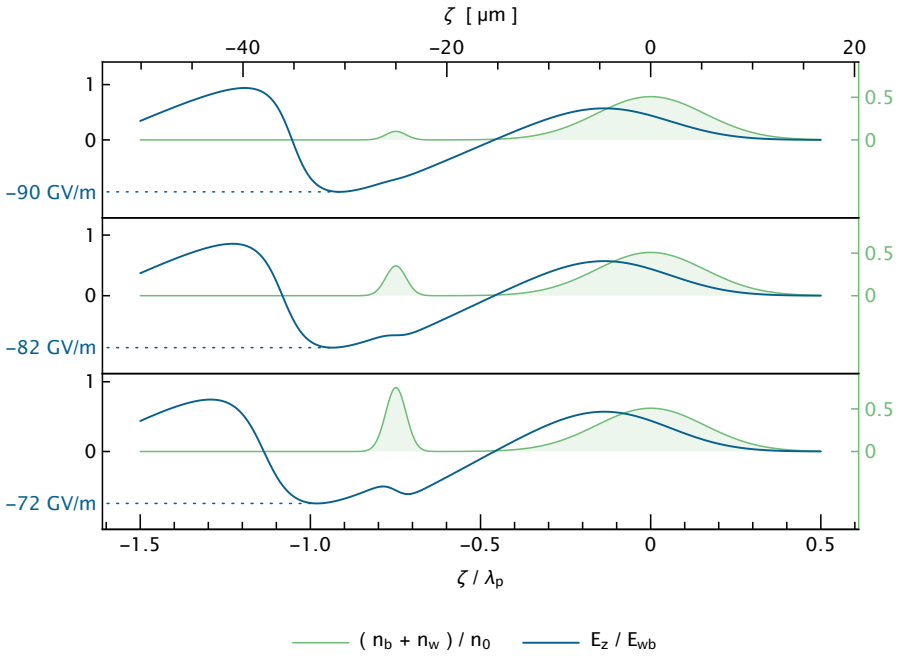

Figure 4.2: **Illustration of beam loading.** Shown is the first wake period corresponding to $\tilde{Q} = 2$ in Figure 3.2 in the presence of a witness beam with $\sigma_{z,w} = 1\,\mu m$ located at $\zeta = -25\,\mu m$. From top to bottom, the witness peak density $n_{w,0}$ increases, resulting in negligible beam loading (top), a nearly flattened wake at the centre of the witness (middle), and an overloaded wake (bottom).

the wakefield is increasingly deformed upon higher witness densities, resulting in a reduced peak accelerating field and an elongated wake period. The wakefield is also locally modulated along the witness, which can result in a local flattening of the accelerating field or even a reversal of the longitudinal wake slope. This further implies that only a limited amount of charge can be efficiently accelerated in a given plasma wakefield [92, 162–167]. The influence of the witness current profile on the

local wake slope has been theoretically investigated for the linear [162, 163] and 3D non-linear regime [168, 169], suggesting that wake flattening over the entire witness beam length can be achieved, in principle, for trapezoidal current profiles.

In terms of witness beam quality, beam loading may or may not be a desired effect. On the one hand, deliberate beam loading can be exploited to reduce the correlated energy spread of a witness, either by suppressing the accumulation of a chirp in the first place [41, 170–173], or by reverting a previously accumulated chirp via overloading the wake with another beam [174, 175]. Precisely tuned beam loading can even be used to transiently restore partial betatron coherence in scenarios where initial phase mixing occurs during injection [176].

On the other hand, the high witness charge density required for beam loading implies that its transverse emittance may be significantly deteriorated due to space charge effects in the early stage of acceleration. Moreover, a correlated energy spread and the resulting betatron decoherence is a well-known mechanism that mitigates the growth of resonant instabilities arising from transverse beam loading that could otherwise lead to complete beam loss [177–180].

5

DIFFERENCES IN LWFAS AND PWFAS

Laser- and electron beam-driven plasma accelerators share the same working principle, however, the distinct nature of the drivers implies also profound differences [181]. Perhaps the most striking distinctness is found in the driver field configuration: the oscillating field of laser drivers is in direct contrast to the unipolar space-charge field of electron beam drivers. An illustration of the electric field of an exemplar Gaussian laser pulse and electron beam is juxtaposed in Figure 5.1. Both drivers are considered to be at focus and are capable of driving a blowout at plasma densities of $\sim 10^{18}\,\mathrm{cm}^{-3}$.

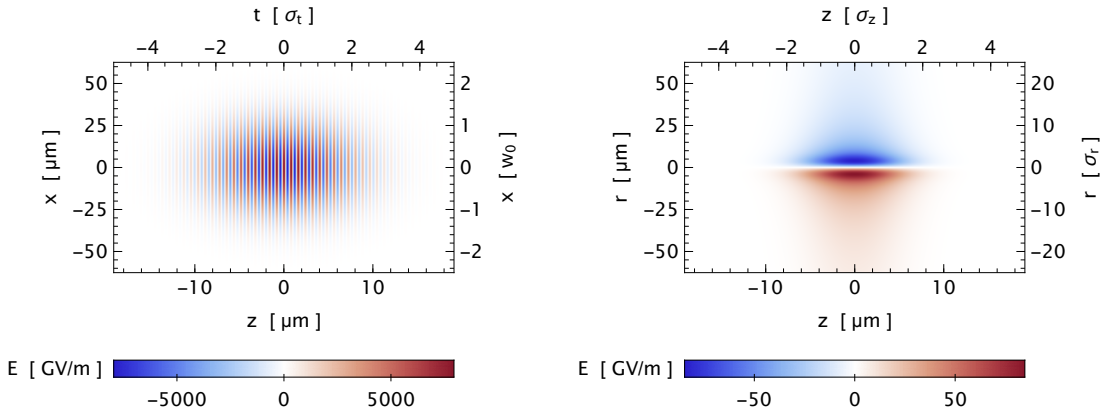

(a) laser pulse

(b) electron beam

Figure 5.1: **Driver electric field.** (a) shows the oscillating field of a laser driver with wavelength $\lambda_l = 800\,\mathrm{nm}$, $\tau_{FWHM} = 30\,\mathrm{fs}$, $w_0 = 25\,\mu\mathrm{m}$ and $a_0 = 2$. (b) shows the unipolar field of an electron driver with equivalent length, $Q = 250\,\mathrm{pC}$, $\sigma_r = 2.5\,\mu\mathrm{m}$, which results in a peak current of $\approx 7.8\,\mathrm{kA}$. Its normalised charge amounts to $\tilde{Q} \approx 10.4$ for a plasma density of $n_0 = 10^{18}\,\mathrm{cm}^{-3}$.

A few further general observations can be made directly. As noted in chapter 3.1, the electric field strength of a Gaussian laser driver peaks at its centre and reduces exponentially in transverse dimension. The reach of its ponderomotive force is thus effectively confined to the transverse extent of the laser. Conversely, the transverse field of an electron beam is zero on axis with a maximum at $r \approx 1.585\,\sigma_r$. It extends much farther than the laser field, due to the $1/r$ scaling for $r \gg \sigma_r$. This distinction, along with guiding considerations discussed later in chapter 5.2, motivates the substantially

different spot sizes of the example laser- and electron drivers. Another key observation is that LWFA drivers require much higher field strength than PWFA drivers for similar operating conditions. In the example presented in Figure 5.1, the laser pulse field amplitude exceeds the electron beam peak field by two orders of magnitude. This is a direct consequence of the ponderomotive force being a cycle-averaged gradient force, as opposed to the Coulomb force exerted by an electron beam. Such discrepancy in field strength also implies that LWFA drivers are, in virtually all practical scenarios, able to ionise a gaseous target already at the front edge of the laser pulse, whereas PWFAs often employ auxiliary setup components to create a pre-formed plasma environment.

LWFAs and PWFAs further differ not only in the mechanism of generating the wake, but also in the evolution of the driver during its passage through a plasma. Therefore, different scalings and limitations on the effectively attainable accelerating distance apply.

5.1 DRIVER AND WAKEFIELD VELOCITIES

A more subtle difference between laser- and electron-driven plasma waves lies in their respective phase velocity. As such, the wake velocity is predominantly determined by the driver velocity, which generally approaches the vacuum speed of light to a reasonable approximation. For the sake of introducing the general wake properties in chapter 3, the plasma wave was hence considered in the limit of propagating with a phase velocity of $v_\varphi \to c$. On a closer examination, however, the velocities of electrons and laser pulses in plasma follow fundamentally different scalings.

The velocity of electrons, be it driver or witness electrons, is determined solely by their kinetic energy, regardless of whether they traverse a vacuum or plasma environment. It can be expressed in terms of their Lorentz factor (see equation 4.2),

$$v_e = c\sqrt{1 - \frac{1}{\gamma_e^2}}\ , \tag{5.1}$$

and asymptotically approaches the speed of light for $\gamma_e \gg 1$. The transverse momentum component of a highly relativistic electron driver is thereby usually considered to be small compared to its forward momentum, such that the phase velocity

of a PWFA wake can be associated with a Lorentz factor approximately equal to that of the driver[1],

$$\gamma_\varphi^{\mathrm{PWFA}} \simeq \gamma_e \quad . \tag{5.2}$$

In contrast to electron beams, however, laser drivers in plasma are subject to dispersion, according to equation 1.7. The plasma wave phase velocity is then determined by the group velocity $v_l \equiv \partial\omega_l/\partial k$ of the laser pulse [49], which, following equations 1.8 and 1.10, can be expressed as

$$v_l \equiv \frac{\partial\omega_l}{\partial k} = c\,\eta = c\sqrt{1-\frac{\omega_p^2}{\omega_l^2}} = c\sqrt{1-\frac{n_0}{n_{\mathrm{crit.}}}} < c \quad . \tag{5.3}$$

Comparing above equation 5.3 to the relations for beam-driven plasma waves, stated in equations 5.1 and 5.2, yields the Lorentz factor associated with an LWFA wake,

$$\gamma_\varphi^{\mathrm{LWFA}} \simeq \gamma_l = \frac{\omega_l}{\omega_p} = \sqrt{\frac{n_{\mathrm{crit.}}}{n_0}} \quad . \tag{5.4}$$

The group velocity of a laser pulse, and accordingly the phase velocity of a laser-driven plasma wave, is thus always lower than c and constant for a given laser frequency and plasma density[2]. Witness electrons injected into a plasma wake, however, asymptotically approach the vacuum speed of light upon gaining kinetic energy. That means that electrons accelerated in a laser-driven plasma wave will eventually outrun the wake, until they enter the decelerating phase of the wakefield. This effect, termed dephasing, limits the attainable energy gain in LWFA scenarios.

The relation between electron and laser velocities is further visualised in Figure 5.2, exemplified for a laser wavelength of 800 nm. It shows the ratio γ_e/γ_l, depending on the plasma density and electron energy. Regions coloured in shades of red indicate the parameter range over which an electron beam propagates faster than a laser pulse in plasma, and vice versa for regions coloured in shades of blue. Solid lines, respectively, indicate contours of constant velocity ratio v_e/v_l. The black solid line marking equal velocities illustrates that the laser group velocity approaches zero at the critical density of $\approx 1.74 \times 10^{21}\,\mathrm{cm}^{-3}$. It also shows that an electron energy of a few tens of MeV is sufficient to outrun a laser-driven plasma wave for plasma densities $\sim 10^{18}\,\mathrm{cm}^{-3}$. The

1 It is further implicitly assumed that driver head erosion, discussed in chapter 5.2, is negligible.

2 In fact, the wake phase velocity in LWFAs can be even lower than suggested by equation 5.4, due to non-linear and 3D effects [87, 182] such as laser etching discussed in chapter 5.3.

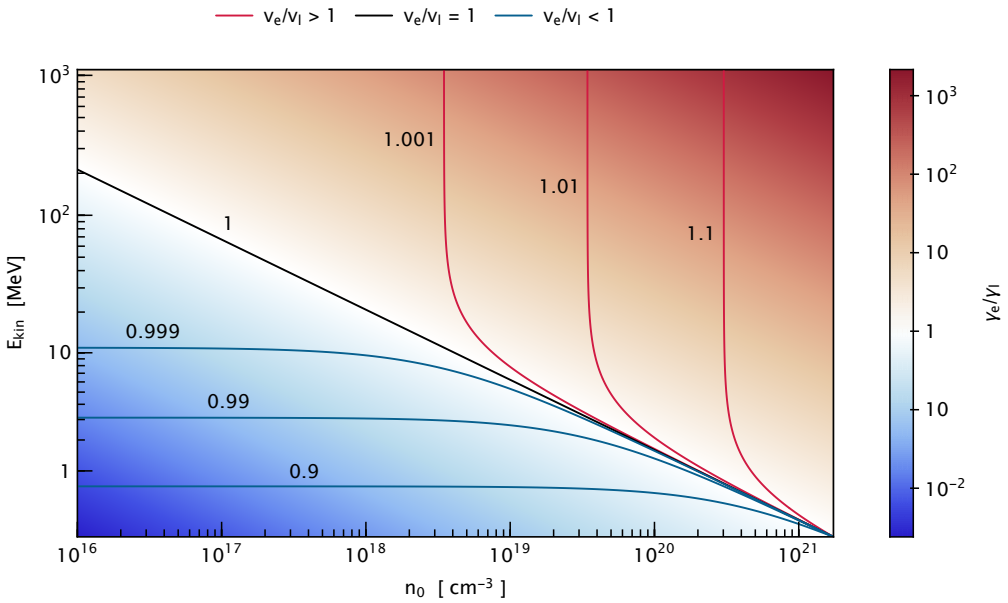

Figure 5.2: **Laser- and electron velocities in plasma.** The colour-coding represents γ_e/γ_l, indicating the minimum electron kinetic energy required to outrun a laser pulse in plasma, exemplified for a laser wavelength of 800 nm. Solid lines correspond to contours of constant ratio v_e/v_l.

almost vertical slope of the red lines towards higher energies corresponds to electron velocities approaching c and illustrates that v_e is virtually constant over a wide range of energies, even though γ_e differs by orders of magnitude. For this reason, dephasing is negligible in PWFA scenarios, provided both driver and witness beam are highly relativistic.

The iso-contours of constant velocity ratios also reveal that the relative difference in electron and laser velocities remains in the sub-permille range for typical plasma densities, even for high electron energies. While this seems miniscule, the absolute velocity difference is indeed significant in limiting the effective acceleration distance in LWFAs [183]. This limit, referred to as dephasing length, is reached when the witness electrons approach the decelerating phase of the wake, that is, once their forward phase slippage amounts to approximately half the plasma wavelength. Following the considerations above, the dephasing length can be approximated as $L_{deph.} \simeq \gamma_l^2 \lambda_p$ [87], which amounts to $\approx$5.8 cm for a plasma wave driven at $n_0 = 10^{18}\,cm^{-3}$ by an 800 nm laser. This overly simplified estimation, however, is based on assumptions that restrict its validity to the 1D linear regime. It specifically assumes that the plasma density remains largely unperturbed and further neglects any evolution of the driving laser

pulse, as well as additional non-linear dispersive effects originating from high laser intensities and a finite frequency spectrum [184]. More elaborate expressions for the dephasing length have been derived in the 1D [87] and 3D non-linear regime [166]. The latter suggests that the dephasing length for $a_0 \geqslant 2$ scales according to

$$L_{\text{deph.}} \simeq \frac{4}{3} \frac{\omega_l^2}{\omega_p^2} \frac{\sqrt{a_0}}{k_p} \quad . \tag{5.5}$$

This results in $L_{\text{deph.}} \approx 1.8$ cm for the example above, which is substantially lower than the estimate from linear theory. The apparent discrepancy can be attributed mostly to local driver depletion, discussed in section 5.3 .

Several mitigation strategies have been proposed to overcome the dephasing limit in LWFAs, for example by gradually or rapidly increasing the plasma density along the acceleration distance [185–188], or employing multiple [189] or structured laser pulses [190]. In turn, dephasing can also be deliberately exploited to manipulate or narrow the energy distribution of the accelerated witness beam, as was partially utilised in the seminal LWFA publications of 2004 [35–37].

5.2 DRIVER GUIDING AND WAKEFIELD STABILITY

Accessing the blowout regime necessitates drivers that are sufficiently short, but also sufficiently narrow. Laser and electron drivers alike thus need to be focused to small, albeit different, transverse sizes when entering the plasma [120]. In the absence of further focusing effects, the driver will naturally diverge once it passes its focus, associated with an attenuating driver strength parameter. Such driver expansion, if not compensated, thus eventually leads to the collapse of the wake and poses a further limitation on the attainable acceleration distance.

The characteristic diffraction scale of a Gaussian laser pulse is defined by its Rayleigh length z_R , and for electron drivers by its beta function at focus $\hat{\beta}_0$ (compare equations 3.12 and 4.20). These two expressions are equivalent in the sense that the Rayleigh length denotes the distance from the focus where the laser intensity halves, whereas $\hat{\beta}_0$ corresponds to the distance at which $n_b = n_{b,0}/2$. While both z_R and $\hat{\beta}_0$ scale with the driver size at focus, the laser diffraction length depends on its wavelength, whereas the electron beam divergence is determined by its normalised emittance and

energy[3]. Figure 5.3 illustrates the natural transverse size evolution of the two drivers previously considered in Figure 5.1, whereby the electron driver is depicted for a conservative emittance value of $\epsilon_n = 5\,\mu\text{m rad}$ and moderate kinetic energies. It shows that the electron driver diverges considerably less than the laser driver, even though it is focused to a substantially smaller spot size.

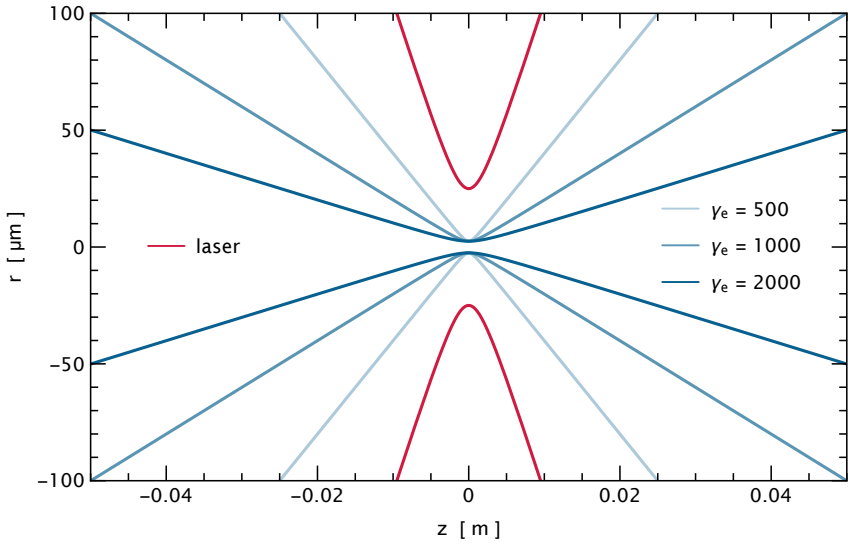

Figure 5.3: **Driver size evolution in vacuum.** LWFA and PWFA drivers require different focus sizes to drive a blowout at the same plasma density. While the characteristic diffraction scale for laser drivers is fixed for a specific focus size and laser wavelength, the divergence of electron drivers is determined by their emittance and energy. Shown is the transverse envelope evolution of the example drivers in Figure 5.1, with red lines corresponding the laser driver and blue lines to the electron driver with $\epsilon_n = 5\,\mu\text{m rad}$ and different kinetic energies.

To maintain a wakefield over extended distances much longer than the natural diffraction scale, however, any driver needs to be guided through the plasma. In case of electron drivers, the blowout regime offers the same advantageous focusing field configuration as for the witness beam, in principle. The considerations for betatron oscillations and transverse matching discussed in chapter 4.2 thus also apply to the driver, as long as it remains sufficiently narrow with respect to the local blowout radius. This prerequisite, however, is not fulfilled at the very front of the driver where the

3 Energy here refers to the kinetic energy of the individual driver electrons, in analogy to the energy associated with the laser frequency $\hbar\omega_l$. The laser frequency is, however, typically fixed in LWFA scenarios. It is further assumed that both laser and electron drivers are mono-energetic for the sake of simplicity.

focusing ion cavity is not yet fully established (see Figure 3.3). A fraction of the driver front will thus always continue to expand, an effect termed head erosion [191]. As a result, the local driver density at the front will gradually decrease and the leading edge of the ion cavity will slowly shift backwards with respect to the driver. Considerable head erosion can thus lead to a decrease in PWFA wake phase velocity reminiscent of dephasing, albeit due to a fundamentally different process. Along the core of the driver, however, the sheath electrons forming the blowout are rapidly expelled outwards and follow trajectories beyond the driver charge distribution, where they are then dominated by the driver's long-ranging transverse electric field component. This also means that the blowout structure is remarkably resilient against small betatron oscillation amplitudes of the driver [192], as the electric field sufficiently far from the driver core is independent from the exact shape of its local charge distribution, according to Gauss's law [49].

In contrast, the ponderomotive force of a laser driver is directly tied to its transverse intensity distribution. The blowout structure in LWFAs is thus much more susceptible to the transverse evolution of the driver. Combined with the typically shorter diffraction scale compared to electron drivers, guiding the laser driver in LWFAs is crucial to attain acceleration distances beyond a few millimetres. One method to achieve this is to generate a preformed plasma channel with a transverse density gradient, such that the thereby altered index of refraction provides a tailored guiding structure [29, 60, 193–201]. However, the non-linear response of plasma to a highly intense laser pulse also affects the index of refraction. As the quiver velocity of plasma electrons in the oscillating laser field approach the speed of light, their relativistic mass increase effectively lowers the local plasma frequency. This leads to a gradient in the refractive index with largest values on axis where the intensity is highest, thus providing a focussing effect. Such relativistic self-focusing [202, 203] can be sufficient to balance the diffraction of the laser, which is achieved at a critical laser power of

$$P_{\text{crit.}} = 2c \cdot 4\pi\epsilon_0 \left(\frac{m_e c^2}{e}\right)^2 \frac{\omega_l^2}{\omega_p^2} \approx 17.42\,\text{GW}\, \frac{\omega_l^2}{\omega_p^2} \quad . \tag{5.6}$$

Further, the local plasma density rarefication imposed by the driver in itself forms a focusing transverse density gradient, known as ponderomotive guiding [204]. Additional non-linear effects render predicting the precise evolution of a laser pulse in plasma challenging, and is typically assisted by numerical simulations. A phenomenological model obtained this way suggests that guiding the driver in LWFAs under blowout conditions can be achieved when the laser spot size follows the relation

$k_p\, w_0 \simeq 2\sqrt{a_0}$ [166]. Experimental findings corroborate that thereby even short pulses can be self-guided over multiple Rayleigh lengths [205].

5.3 DRIVER ENERGY TRANSFER AND ACCELERATION LENGTH

In LWFAs and PWFAs alike, the plasma acts as a medium to transfer energy from the driver to the witness beam via the wakefield. The driver energy is thus gradually depleted upon establishing and maintaining the wake. After dephasing and diffraction, driver depletion constitutes an ultimate limit to the attainable acceleration distance in a single plasma wakefield accelerator stage.

In PWFAs, the kinetic energy of the driver is transferred into the plasma wave. The rate of energy transfer is therefore directly correlated with the electric field strength in the decelerating phase towards the front of the wake. The exact shape of the decelerating field along the driver is thereby largely determined by its axial current profile and is generally non-uniform. Longitudinally separated slices of the driver thus experience varying depletion rates, with the most anterior electrons remaining virtually unimpaired [92]. The propagation distance over which the earliest slice is decelerated to non-relativistic energies defines the depletion length [116, 185]

$$L_{\text{depl.}}^{\text{PWFA}} \simeq \frac{m_e c^2}{e} \frac{\gamma_d}{\left|E_{z,\max}^{+}\right|} \quad , \tag{5.7}$$

where $E_{z,\max}^{+}$ denotes the peak decelerating field. Beyond the depletion length, an increasing number of electrons will slip back with respect to the remaining part of the driver. The driver current profile is thus no longer maintained and the wake will gradually degrade. During this process, a fraction of initially depleted driver electrons may even enter the accelerating phase of the altered wake and get partially re-accelerated [56, 206, 207]. However, continuous depletion of further portions of the driver will ultimately result in the collapse of the wake. The depletion length therefore constitutes an estimate of the maximum acceleration distance over which an electron driver with a certain kinetic energy can sustain a stable wakefield with consistent accelerating conditions. A considerable energy spread of the driver can result in an effective depletion length significantly lower than its nominal value.

While the peak decelerating field $E_{z,\max}^{+}$ defines the maximum rate of energy transfer from the driver to the wake, the peak accelerating field $E_{z,\min}^{-}$ determines the maximum rate at which the witness beam can extract energy from the wake. A key

performance figure in PWFAs is thus the so-called transformer ratio [92, 208–210], defined as

$$R_T \equiv \frac{\left|E^-_{z,\min}\right|}{\left|E^+_{z,\max}\right|} \quad . \tag{5.8}$$

In this form, the transformer ratio indicates the maximum attainable rate of energy transfer from the driver to the witness. In a practical scenario, however, the witness beam may not be situated at precisely the peak accelerating phase of the wake, which has to be considered when deriving the effectively realised transformer ratio. In both cases, the maximum energy gain of a witness electron is

$$\Delta\gamma_w^{\mathrm{PWFA}} \simeq R_T\,\gamma_d \quad . \tag{5.9}$$

A transformer ratio $R_T > 1$ thus suggests that the witness energy gain can exceed the mean kinetic energy of the driver. Energy conservation dictates that this is only possible if the witness beam carries substantially less charge than the driver. This may also be understood from an alternative point of view: a witness beam with considerable charge will attenuate the accelerating gradient via beamloading, and thereby diminish the effective transformer ratio. While a high transformer ratio is thus generally desirable for maximising the mean kinetic energy of the witness electrons, it is distinct from the overall energy-transfer efficiency, that is, the fraction of total energy transferred from the driver to the witness [170, 173, 211].

The transformer ratio is theoretically maximised if all driver slices (except the very front) are depleted at an equal rate, which requires a flat decelerating field along the majority of the driver. The fundamental theorem of beamloading [212] implies that this is not possible for longitudinally symmetric drivers. Linear theory predicts that the nominal transformer ratio is restricted to $R_T \leqslant 2$ in this case [92, 93, 209], although this limit can be exceeded in the blowout regime [213]. Various asymmetric bunch profiles that aim to optimise the transformer ratio have been conceptualised theoretically [116, 185, 208–210, 214, 215] and, recently, explored experimentally [216, 217].

Driver depletion in LWFAs manifests itself in a redshift of the laser frequency spectrum [218–222]. Conversely to electron drivers, the front of the laser pulse gets depleted fastest in the highly non-linear regime [218, 223]. Since the group velocity of a wave packet is reduced for lower frequencies (see equation 5.3), the depleted front will start to slip back, similarly to depleted PWFA driver electrons. In contrast to PWFAs,

however, the slippage of the laser front commences immediately upon interacting with the plasma. The LWFA wake will thus continuously recede approximately with an etching velocity [166, 223] of

$$v_{\text{etch}} \approx c \, \frac{\omega_p^2}{\omega_l^2} \quad . \tag{5.10}$$

This, in effect, further decreases the wakefield phase velocity and thus exacerbates the dephasing issue in LWFAs. Laser etching due to local driver depletion is considered in the dephasing length estimate provided by the scaling in equation 5.5 .

The etching rate also provides an estimate for the overall depletion length, that is, once the laser front has receded by a distance on the order of the initial driver length. The LWFA depletion length in the 3D non-linear regime [166] can thus be expressed as

$$L_{\text{depl.}}^{\text{LWFA}} \simeq c \, \frac{c \, \tau_{\text{FWHM}}}{v_{\text{etch}}} = c \, \tau_{\text{FWHM}} \, \frac{\omega_l^2}{\omega_p^2} \quad . \tag{5.11}$$

Referring once more to the example laser in Figure 5.1 , driving a blowout at a nominal plasma density of $n_0 = 10^{18}\,\text{cm}^{-3}$ yields a depletion length of $\approx 1.6\,\text{cm}$, implying that depletion occurs before dephasing in this scenario. This is not ideal, as depletion commences immediately, but dephasing only after witness electrons have been injected into the wake. According to these scalings, the laser pulse duration should therefore be $\tau_{\text{FWHM}} \geqslant 4/3 \, \sqrt{a_0}/\omega_p$ to ensure that the depletion length is slightly larger than the dephasing length. It is noteworthy that this relation is independent of the plasma density, since $L_{\text{depl.}}^{\text{LWFA}} \propto L_{\text{deph.}} \propto n_0^{-3/2}$ as long as the laser pulse duration is scaled accordingly.

Due to dephasing, an LWFA witness electron will experience a diminishing accelerating field $E_{\text{acc.}}$ along its acceleration distance $L_{\text{acc.}}$. The attainable witness energy gain is thus $\Delta\gamma_w^{\text{LWFA}} = e/\left(m_e \, c^2\right) \, L_{\text{acc.}} \, \langle E_{\text{acc.}} \rangle$. In the blowout regime, the average accelerating field over a dephasing length can be estimated as $\langle E_{\text{acc.}} \rangle \simeq E_{\text{wb}} \, \sqrt{a_0}/2$ [166]. The maximum energy gain in a dephasing-limited LWFA thus evaluates to

$$\Delta\gamma_w^{\text{LWFA}} \simeq \frac{2}{3} \, \frac{\omega_l^2}{\omega_p^2} \, a_0 \propto \frac{1}{n_0} \quad . \tag{5.12}$$

This suggests that higher witness energies can be achieved for lower plasma densities, despite a reduced peak accelerating field.

The reason is that $\langle E_{acc.} \rangle \propto E_{wb} \propto n_0^{1/2}$, while the attainable acceleration distance scales as $L_{acc.} \propto n_0^{-3/2}$. However, to maintain self-guiding conditions, $k_p w_0$ has to be kept constant, which means that the laser spot size has to be increased when operating an LWFA at lower plasma densities. In turn, the laser power and energy have to be increased to maintain the same a_0. Moreover, scaling the depletion length alongside the dephasing length requires to keep $\omega_p \tau$ constant, which results in a longer pulse duration and further increases the demand in laser energy. Under these considerations, the attainable witness energy gain thus scales according to

$$\Delta\gamma_w^{LWFA} \propto P_0 \propto W_{laser}^{2/3} \ , \tag{5.13}$$

with peak power P_0 and total energy W_{laser} of the driver (see chapter 3.1.1). In other words, to increase the attainable witness energy gain tenfold, one requires ten times higher laser power, but already $\approx$32 times more energy contained in the laser pulse.

6

CONTROLLED WITNESS BEAM INJECTION

One of the key objectives for progressing plasma-based accelerators into application-ready platforms is ensuring reliable and stable operation, while at the same time providing high-quality electron beams. As outlined in the previous chapters, this necessitates identifying intrinsic processes that enable a stable wakefield configuration and beam quality preservation along the acceleration distance, but also the development of technical solutions for supporting infrastructure and diagnostics [224].

Another equally important prerequisite is a mechanism to precisely control how electrons are situated into the wake structure. The process of injecting electrons into the plasma wake defines the initial phase space of the witness beam distribution and its phase relation to the accelerating gradient, and thus predetermines the attainable beam quality. The desired beam parameters ultimately depend on the anticipated application, however, low energy spread, low transverse emittance and high peak-current are generally required to achieve high beam brightness. An ideal injector thereby offers not only a tunable balance between these parameters, but simultaneously high robustness and reasonable experimental complexity.

Over the past decades, numerous injection techniques have been proposed and realised experimentally. One may categorise them according to the source of injected particles. In principle, there are three main approaches of injecting electrons into the plasma wake: witness electrons can be provided externally from a separate pre-accelerator, captured from the plasma forming the wakefield, or additional electrons can be released directly inside the wake via ionisation of an ambient atom or ion species.

6.1 EXTERNAL INJECTION

In contrast to conventional accelerators, the accelerating structure formed by plasma waves is not static, but trails the driver at highly relativistic speed. As a consequence, charged particles must match the phase velocity of the wake to continuously gain energy. One of the earliest approaches for demonstrating a functional plasma wakefield accelerator was thus to augment conventional accelerators with a plasma booster stage [225–227]. Thereby, multiple electron bunches were brought to relativistic en-

ergies prior to entering a plasma, where subsequent energy transfer between the preceding and trailing electron populations could be observed.

Similarly, energy transfer from the head to the tail of a single electron bunch with length on the order of a plasma wavelength has been shown, resulting in a continuous energy distribution up to twice of its initial central value of 42 GeV in less than a metre of plasma [28]. Aiming for a narrow-band energy spectrum, however, generally requires a defined spatial separation between the driving and trailing electron populations, owing the continuous gradient of the longitudinal electric field inside a plasma wave. Systematically generating such discrete pairs of sufficiently short driver and witness bunches can be achieved by dividing one individual bunch [228], for example via employing masks in a dispersive section [170, 211, 229]. The advent of photocathode electron sources, combined with sophisticated bunch compression modules, enabled further means of generating two bunches in quick succession while controlling their individual charge and shape, with notable achievements such as the demonstration of high transformer ratio wakefields [216], witness energy spread compensation [230] and first lasing of a PWFA-driven free electron laser [231].

Ultimately, the need for a conventional RF-accelerator can be overcome entirely when utilising a compact laser-driven plasma wakefield accelerator as the source for both driver and witness bunches. This approach is based on the idea of generating two individual electron populations in consecutive cavities of a laser-driven plasma wave [232]. The spatial extents of these discrete bunches, as well as their inter-bunch separation, naturally scales with the LWFA plasma density. Consequently, such dual-bunches can, in principle, provide excellent driver-witness pairs for a subsequent PWFA stage operated at slightly lower density. A first experimental demonstration of this dual-bunch LWFA-PWFA conversion scheme has ben recently achieved [233][45].

In addition to electron-electron driver-witness configurations, external injection of a pre-formed witness bunch has been shown also for electron-positron [88], positron-positron [234], as well as proton-electron [95] variants. Besides these PWFA concepts, pre-accelerated bunches were also utilised for some of the earliest demonstrations of electron acceleration in laser-driven wakefields [235–238]. Today, external injection into LWFAs remains the subject of extensive research and development, for example as one of the projects within the EuPRAXIA Conceptual Design Report [32]. The main prospect of this approach is the potential to define the initial bunch characteristics before injection via well-understood mechanisms in conventional accelerator structures, aiming for precise control and enhanced stability. Yet, the vastly different spatial scales and field strengths between RF technology and typical plasma wakes

render the technical aspects of external injection multi-faceted. Providing pre-formed electron bunches with femtosecond-scale duration and transverse extents matched to high-density plasma wakefields [147][239, 240], while simultaneously maintaining attractive emittance and charge levels, requires elaborate machines with sophisticated bunch compression and focusing methods [241–243]. Precise synchronisation and pointing between the laser-driven wake and the injected electron bunch pose further challenges for successful injection and bunch quality preservation. Despite these intrinsic complexities, external injection with a charge capture efficiency of nearly 100 % has been reported recently [244]. Further novel approaches are actively being explored, for example to compensate synchronisation jitter [245] and to reverse an accumulated energy spread in a staged LWFA concept [246].

6.2 CAPTURE OF AMBIENT PLASMA ELECTRONS

A fundamentally different approach to external injection is to modify the plasma wave to capture its own electrons. Since the entire accelerating structure is formed in plasma, there is already a vast reservoir of ambient electrons that can, in principle, be injected into the wake to be accelerated. This is achieved when a fraction of electrons participating in the wake formation, at least temporarily, exceeds the plasma wave phase velocity and ultimately remains located in the accelerating phase of the wakefield.

6.2.1 *Wave breaking*

Following early theoretical works on non-linear plasma waves [247], it soon became apparent that the 1D cold fluid model predicts a finite upper limit for the attainable wakefield amplitude [86]. Beyond this field strength, some plasma electrons nominally gain sufficient forward momentum to exceed the phase velocity of the wake, which substantially alters the wake structure. This process is referred to as wave breaking. Under wave breaking, the coherence of the plasma wave oscillations collapses and individual particle trajectories intersect. As a consequence, a fraction of the plasma wave electrons may be captured in the accelerating phase at the rear of the broken wave. The range of complex dynamics involved in this process is often gathered under the rather loosely defined collective term of self-injection.

Wave breaking manifests itself in fluid models as singularities in the associated plasma density [86]. While fluid approaches are thus incapable of providing an accurate description of the ensuing plasma wave breakdown, they can indicate the field strength at which self-injection can occur. In its simplest form, that is, neglecting relativistic and thermal effects, the 1D fluid model predicts wave breaking at field strengths beyond [86]

$$E_{wb} = \omega_p \frac{m_e c}{e} \quad . \tag{6.1}$$

A full relativistic treatment reveals that highly non-linear plasma waves can sustain substantially larger wake amplitudes before breaking [107, 247–249],

$$E_{wb}^{rel.} = E_{wb} \sqrt{2 (\gamma_\varphi - 1)} \quad , \tag{6.2}$$

where γ_φ corresponds to the Lorentz factor associated with the plasma wave phase velocity. A finite plasma temperature, in turn, lowers the effective wave breaking threshold [107, 248, 250–254]. Self-injection that follows this purely longitudinal wave breaking picture is characterised by the capture of plasma electrons originating from positions initially close to the central axis defined by the driver. When further considering the entire 3D structure of a highly non-linear plasma wave and the transverse momentum distribution imposed on the plasma electrons by the driver, self-injected particles may also originate from positions further off-axis. Such transverse wave breaking [121, 255–257] is the leading mechanism for self-injection in the blowout or bubble regime and can occur at wake amplitudes significantly below the 1D limit [120, 258, 259]. Moreover, operating a plasma wakefield accelerator close to the wave breaking threshold means that the conditions to initiate and terminate self-injection become sensitive to variations of the wake structure induced by the driver evolution [260–266].

While the majority of theoretical and numerical studies on wave breaking have been carried out in the context of LWFAs, the general mechanism also applies for PWFAs. However, self injection in LWFAs is strongly facilitated in comparison to PWFAs, due to the combination of lower phase velocities of laser-driven plasma waves, the considerable heating of plasma electrons during their interaction with the laser driver, and the typically higher plasma densities at which LWFAs can be operated. In addition, the short diffraction scales and oscillating electromagnetic field of laser drivers enable self-injection schemes based on driver self-focusing and -compression [267–269]. In PWFA scenarios, driver focusing does not significantly

alter the wake structure once the blowout regime has been reached and the driver becomes substantially narrower than the blowout radius [270]. A transition from the linear to the blowout regime through (self-)focusing of an electron-beam driver can nevertheless lead to self-injection, albeit this is predicted to require exceptionally high driver peak-currents and particularly high plasma densities [270].

The accessibility of self-injection due to wave breaking in laser-driven wakefield accelerators has contributed to early experiments on LWFA electron-bunch generation [35–37, 271, 272], and has since remained prevalent in numerous LWFA scenarios [29, 195, 196, 273–277]. However, the complexity of the self-injection process and its inherent non-linear dependence on driver parameter evolution renders self-injection susceptible to shot-to-shot instabilities. This is particularly applicable for transverse wave breaking, as emphasised by a direct experimental comparison of longitudinal and transverse self-injection [278].

6.2.2 *Plasma density gradients*

Instead of modifying the wake structure by means of driver evolution, a similar mechanism of initiating and terminating wave breaking injection can be achieved through longitudinal plasma density transitions [256, 279]. A longitudinally varying plasma density $n_0(z)$ locally alters the nominal plasma wave number $k_p(z)$ (recall equations 1.6 and 3.1), and thus the plasma wave phase $\hat{\varphi} = k_p(z)\,\zeta = k_p(z)\,(z - v_d t)$. The instantaneous plasma wave frequency $\hat{\omega} = -\partial\hat{\varphi}/\partial t$ and plasma wave number $\hat{k} = \partial\hat{\varphi}/\partial z$ then define the nominal plasma wave phase velocity in the co-moving frame (also recall equations 3.23), according to [87, 279–281][1]:

$$\begin{aligned} v_\varphi(\zeta, z) \equiv \frac{\hat{\omega}}{\hat{k}} &= v_d \left(1 + \frac{\zeta}{k_p(z)} \frac{\partial k_p(z)}{\partial z}\right)^{-1} \\ &= v_d \left(1 + \frac{\zeta}{2n_0(z)} \frac{\partial n_0(z)}{\partial z}\right)^{-1} . \end{aligned} \tag{6.3}$$

A negative plasma density gradient thus leads to a gradual reduction of the phase velocity at increasing distances $\zeta < 0$ behind the driver. This is equivalent with an increase in nominal plasma wavelength and, therefore, blowout expansion. Naturally, a reduced plasma wave phase velocity at the rear of the wake facilitates wave breaking. It follows that a localised, sufficiently steep transition from higher to lower plasma

1 Here, the influence of the plasma density variation on the group velocity of a laser driver is neglected.

density can be utilised to elicit transient injection largely decoupled from the driver evolution. Employing a tailored density down-ramp, therefore, enables enhanced control and stability of the injection rate and duration.

Optimising the down-ramp shape, gradient and dimensions has been extensively explored theoretically for both LWFA [282–286] and PWFA scenarios [281, 287–292]. A general distinction can be made between the limiting cases of gradual down-ramps with an extent $L_{ramp} \gg \lambda_p$ and sharp ramps on the order of a single plasma wavelength, for similar initial and final densities. The former is governed by adiabatic expansion of the blowout and steady injection at the rear of the wake [262, 286], whereas the latter is characterised by a rapid transverse collapse of the wake structure and re-phasing of electrons enclosed by the newly forming blowout sheath at the lower density plateau [286–288]. Detailed numerical studies predict a clear scaling of injected charge with increasing ramp steepness, however, also suggest that the resulting beam quality parameters show a rather complex dependence on the specific driver and density down-ramp scenario [281, 285, 286].

Moreover, practical differences between electron- and laser-driven plasma waves arise, due to similar considerations as for self-injection [293]. The driver velocity in LWFAs, by its nature, generally depends on the plasma density, hence $v_{\varphi,0}$ in equation 6.3 becomes a function of z and slightly increases during a density down-ramp. Conversely, the constant, but higher, driver velocity in PWFAs, combined with the prerequisite of high driver peak-current to achieve sufficient forward momentum of the sheath electrons [281], typically necessitates particularly steep gradients to access density down-ramp injection in beam-driven scenarios. Experimental realisations of down-ramp injection, therefore, have proven remarkably elusive for PWFAs, whereas they have become part of the standard repertoire of LWFA operations.

Such LWFA density down-ramp injectors can be further distinguished by the method of generating the plasma density transitions. Gradual ramps have been successfully employed for injection by tailoring the hydrodynamic flow in gas targets [294–297]. Partially obstructing the flow in supersonic gas jets can further be utilised to generate localised density shocks with steep gradients [183, 187, 298–304]. This commonly applied technique, for example, has been a key element in the first proof-of-principle experiment demonstrating exponential amplification in an LWFA-based free electron laser [305]. Another variant deploys an additional transverse laser to form density structures in the plasma directly, instead of modifying the underlying gas target. Thereby, an intense laser forms a hot plasma column prior to the main laser driving the wake, which subsequently expands rapidly into the surrounding neutral gas [60,

306–308]. On a time scale of a few nanoseconds, the transient plasma profile exhibits a region of lowered density in the centre of the expanding pre-ionised channel and correspondingly increased density at its edges. Adjusting the transverse pre-ionising laser parameters and the expansion time delay then provides means of tuning the injection along the emerging longitudinal density ramps [309–315].

Introducing a transverse laser pulse was also the key element in demonstrating the very first density down-ramp injection in a PWFA setup [40]. Although similar in its components, the corresponding technique, termed plasma torch injection [316, 317], follows a distinctly different concept, which is further discussed in chapter 8.

6.2.3 *Colliding laser pulses*

An intense transverse laser directly intersecting the wake structure has also been proposed as injection method [318]. This concept is based on exploiting the ponderomotive push of an orthogonal laser pulse to transfer additional forward momentum directly to the plasma electrons sustaining the wake. A fraction of these electrons may thus be injected into the accelerating phase of the wake, provided a sufficiently high injector laser intensity and proper delay with respect to the driver [319].

A refined variation of this initial idea was formulated shortly after, suggesting to use two longitudinally counter-propagating injector lasers instead [320]. This colliding-pulse injection (CPI) scheme relies on the ensuing beat wave pattern when the two injector pulses interfere inside the wake, which locally and rapidly alters the momentum of wake electrons to facilitate injection [320–323]. In the simplest case of two counter-propagating lasers with identical wavelength and polarisation, a standing wave is formed during the time of their overlap, providing a transient longitudinal ponderomotive force component in addition to the wakefield. However, numerical studies reveal more complex dynamics to be involved in colliding-pulse injection, including a contribution of stochastic electron motion [324, 325] as well as transient wake deformation [326]. The prerequisite of multiple high-intensity laser pulses renders CPI de facto exclusive to LWFA scenarios, where the drive laser can simultaneously act as one of the two injector pulses [322, 323]. Such a configuration led to the first experimental demonstration of colliding-pulse injection [327, 328], where a drive laser with $a_0 = 1.3$ was applied in conjunction with an injector laser with $a_0 = 0.4$.

Despite its conceptual simplicity, the collision of two high-intensity laser pulses imposes considerable complexity on the experimental setup, with stringent requirements

on alignment and synchronisation as well as necessitating safety guards to prevent damaging critical laser components. Further experimental realisations [329–334] alleviate the latter issue by introducing a small angle between the two pulses. The principal capabilities of CPI for tuning the resulting beam parameters were shown by adjusting the collision delay, the laser intensities and their respective polarisations [335–338]. Nevertheless, the intricacies of colliding-pulse injection experiments has restricted their exploration to only a handful of groups over the past two decades, and thus remains rather exotic in the realm of injection concepts.

6.3 IONISATION INJECTION

A more direct approach for injection is to release electrons directly inside the wakefield structure via additional ionisation. The defining characteristic of such ionisation injection is that the electron source for injection is distinct from the electrons forming the plasma wave. This necessitates the abundance of an ambient medium within the plasma wake with at least one remaining ionisation level. Typical experimental realisations employ a mixture of gas species consisting of a low ionisation threshold (LIT) component and high ionisation threshold (HIT) dopant. The wakefield is thereby driven in the LIT medium, either pre-ionised by a dedicated ionisation technique or by the electric field of the driver itself. Importantly, the mechanism generating the plasma in the LIT component leaves the target HIT level at least partially unionised, providing a reservoir for deliberately releasing additional electrons within the wakefield structure via further ionisation.

In contrast to external injection or density manipulation techniques, ionisation injection usually feeds electrons into the plasma wave with negligible initial forward momentum. Such electrons will slip back with respect to the wakefield, and thus have to be accelerated to match the phase velocity of the wake within one period of the plasma wave in order to get carried along with the wakefield. This capturing process, referred to as trapping, therefore requires a sufficiently strong accelerating field. The condition for successful trapping can be expressed in terms of the electrostatic trapping potential [259, 339, 340]

$$\psi(r,\zeta) = -\frac{e}{m_e c^2}\int_{\infty}^{\zeta} E_z\left(r,\zeta'\right)\,\mathrm{d}\zeta' \quad , \tag{6.4}$$

where $\zeta = z - v_\varphi t$, and a quasi-static wakefield in the blowout regime is implied.

Electrons injected with initial longitudinal velocity v_i and corresponding Lorentz factor γ_i will reach the wake velocity once they experience a potential difference [259, 341]

$$\Delta\psi = \psi_i - \psi_f = \frac{\gamma_f}{\gamma_\varphi^2} - \gamma_i \left(1 - \frac{v_\varphi v_i}{c^2}\right) \quad , \tag{6.5}$$

provided their trajectories lie within the blowout region. Here, ψ_i and ψ_f refer to the potential values at the injection and final trapping location, γ_f and γ_φ refer to the Lorentz factors of the electron at the instant of trapping and the wake, respectively. For electrons released at rest close to the central axis, $v_i = 0$, $\gamma_i = 1$ and $\gamma_f = \gamma_\varphi$, the trapping condition reduces to its 1D form

$$\Delta\psi = \psi_i - \psi_f = \frac{1}{\gamma_\varphi} - 1 \quad . \tag{6.6}$$

When the phase velocity of the wake furthermore approaches the speed of light, as is the case for plasma waves driven by ultra-relativistic electron beams, the on-axis injection region that leads to trapping is confined according to

$$\Delta\psi = \psi_i - \psi_{max} \leqslant -1 \quad , \tag{6.7}$$

where ψ_{max} denotes the maximum of the trapping potential located at the rear of the wake. Such a scenario is illustrated in Figure 6.1, showing the longitudinal electric field and the corresponding on-axis trapping potential for the first plasma cavity of a beam-driven plasma wakefield obtained from a PIC simulation with equivalent parameters as presented in Figure 3.3. The electric field exhibits its characteristic linear gradient around the blowout centre, from which follows that the trapping potential inherits an approximately parabolic shape. Naturally, the extrema of the trapping potential correspond to the zero crossings of the longitudinal electric field, with its minimum located at the transition from decelerating to accelerating phase at the blowout centre, and vice versa, its maximum located at the transition from accelerating to decelerating phase at the blowout vertex. The trapping region, that is, the set of injection positions where $\Delta\psi \leqslant -1$, is indicated by the dark blue shaded area. It extends into the vicinity of the drive beam, showing that electrons do not necessarily need to be released in the accelerating phase of the wake in order to get trapped.

The initial injection position $\zeta_{inj.}$, however, defines the final trapping location ζ_{trap}, and therefore the accelerating phase experienced by the trapped electron. This is illustrated by the inset bars in Figure 6.1. Their extents indicate the on-axis injection

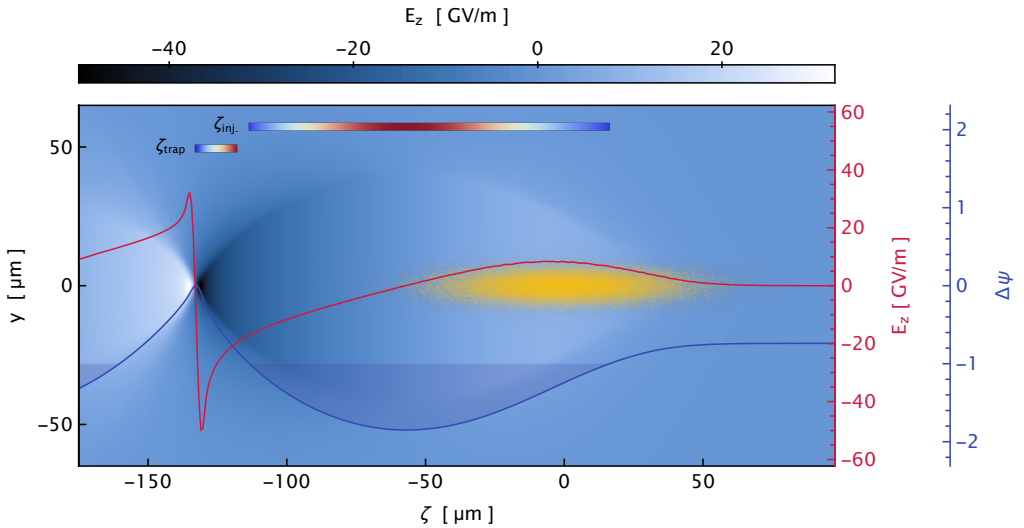

Figure 6.1: **PWFA trapping region.** Central slice of a wakefield structure driven by an electron-beam (yellow), obtained from a PIC simulation equivalent to Figure 3.3 . The on-axis electric field (red line) exhibits a linear slope around the blowout centre, resulting in a nearly parabolic shape of the corresponding trapping potential $\Delta\psi$ (blue line). Electrons injected at rest at positions fulfilling $\Delta\psi \leqslant -1$ (dark blue shaded area) can get trapped at the rear of the wake. The inset bars visualise the relation between injection positions $\zeta_{\text{inj.}}$ and trapping positions $\zeta_{\text{trap.}}$.

range and the corresponding range of trapping positions, respectively, while their colour-coding visualises the trapping function relating $\zeta_{\text{inj.}}$ to ζ_{trap} . One immediate observation is that the range of final trapping positions is substantially shorter than the initial release range. This implies that an electron population injected with an initial spread in release positions can experience significant longitudinal compression during trapping. The compression effect is attributed to rapid velocity bunching [341–343], which is particularly efficient when the electrons are not yet fully relativistic. The possibility for intrinsic bunch compression therefore constitutes an important characteristic of ionisation injection. The colour-coding furthermore reveals that electrons released closest to the trapping potential minimum are trapped at the most anterior position in the wake, whereas electrons injected towards the edges of the trapping region will accumulate towards the rear of the blowout. It also shows that the trapping function is a nearly symmetric surjective map, indicating that electrons released with a similar absolute offset from the trapping potential minimum will share the same final trapping location. Releasing electrons closely around the trapping potential minimum thereby results in highest attainable bunch compression during injection. This is a

direct consequence of the approximately parabolic shape of the trapping potential around the blowout centre.

It follows from these considerations that precise tuning of the release positions can be utilised to manipulate and optimise the resulting trapped bunch distribution, in principle. The actual accessible injection region and the degree of control over electron release positions, injection duration and injected charge, however, varies for different realisations of ionisation injection schemes, depending on their specific method for achieving excess ionisation of the HIT component. In general, ionisation injection mechanisms rely on strong field ionisation induced via a localised maximum in absolute electric field strength. Such confined regions of strong electric fields can be readily provided by the driver, by the wakefield itself or by introducing auxiliary laser pulses.

6.3.1 *Driver ionisation*

The laser pulse or electron beam driving a plasma wakefield suitable for ionisation injection is typically substantially shorter than the trapping region and naturally carries a considerable electric field. The peak field of the driver can thus be utilised for injection, provided the driver field magnitude and duration is adequate for ionising the HIT medium, and the trapping region extends sufficiently towards the front of the wake into the vicinity of the driver.

This is particularly applicable for laser-driven plasma wakefield accelerators. A laser pulse with $a_0 = 1$ and $\lambda_l = 800\,\mathrm{nm}$ yields a peak electric field of $E_0 \approx 4 \times 10^{12}\,\mathrm{V/m}$, providing ample field strength to ionise even the innermost shell electrons of various gaseous elements. Consequently, already the rising edge of the laser pulse is capable of fully ionising the LIT component and several levels of the HIT dopant. The thereby released electrons are then subsequently expelled off axis by the ponderomotive force of the driver and establish the wakefield. A careful choice of a HIT species with higher ionisation levels that are only accessible by the very peak of the laser pulse then enables the release of additional electrons directly inside the fully formed wakefield. These peak-ionised electrons are therefore available for trapping, provided that their ionisation front sufficiently overlaps with the trapping region.

Various HIT gas types have been explored experimentally [344–346] for ionisation injection in LWFAs. Combining helium ($\xi_{He^+} \approx 24.6\,\mathrm{eV}$) with traces of nitrogen has since been established as a practical mixture of LIT and HIT media, due to the large gap in ionisation potentials between the 5^{th} L-shell electron ($\xi_{N^{5+}} \approx 98\,\mathrm{eV}$) and the

two innermost K-shell electrons ($\xi_{N^{6+}} \approx 552\,\text{eV}$ and $\xi_{N^{7+}} \approx 667\,\text{eV}$) of nitrogen atoms. A representative example of the resulting on-axis ionisation fronts in such a helium-nitrogen mix is depicted in Figure 6.2, showing the spatial separation of ionisation positions with respect to the drive laser pulse. In this scenario, helium and the first five levels of nitrogen are fully ionised already by the rising edge of the laser pulse, whereas the 6^{th} and 7^{th} levels of nitrogen are partially ionised only close to the laser peak amplitude.

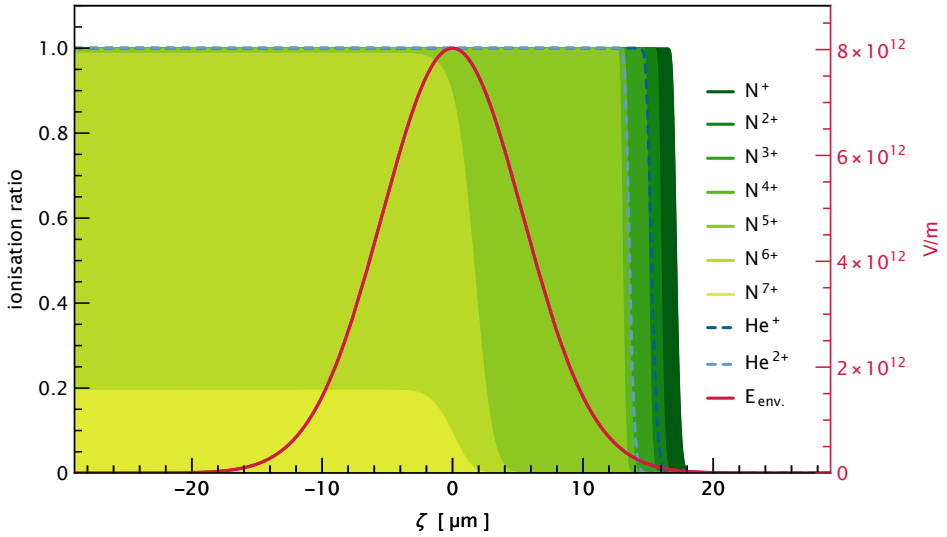

Figure 6.2: **LWFA driver ionisation.** Ionisation fronts for a typical ionisation injection scenario in LWFA, with helium as LIT medium and nitrogen as dopant HIT species. The red line represents the electric field envelope of the laser driver (here, $a_0 = 2$, $\lambda_l = 800\,\text{nm}$, $\tau_{\text{FWHM}} = 30\,\text{fs}$) on axis. The rising edge of the driver is capable of fully ionising helium, as well as the outer five electrons of the nitrogen dopant. These electrons thus contribute to the wakefield formation. The two electrons from the innermost nitrogen shell, in contrast, are accessed only near the peak laser amplitude located inside the wake.

A finite ionisation volume around the peak of the laser driver, however, also implies that released electrons are immediately subject to a considerable transverse ponderomotive push, which poses a conceptual limit on the attainable emittance [347]. The usual linear polarisation of the drive laser further leads to an asymmetry in emittance and divergence between the plane parallel and orthogonal to the laser polarisation [301, 344, 345, 347, 348].

Moreover, continuous ionisation injection tends to generate correspondingly continuous, broadband energy spectra, as electrons injected at later times experience

shorter accelerating distances [347, 349, 350]. When aiming for electron bunches with a defined central energy, the injection process is thus ideally confined not only to a localised region within the wakefield, but also to a brief period of time. As for any injection scheme, continuous accumulation of charge in the wake is eventually terminated by overloading the wake (see chapter 4.3). More control over the injection duration can be achieved by confining the volume of HIT gas to a specific section along the accelerator. Such cascaded LWFAs utilising sophisticated gas target designs with dedicated injection and acceleration sections have been demonstrated experimentally [351–356]. The length of the injection section was thereby reduced to a few millimetres, resulting in peaked electron energy spectra with several percent energy spread, albeit with comparatively low charge.

Another approach for manipulating the injection duration is to exploit the intrinsic laser evolution during its passage through the plasma. It has been shown that ionisation injection in LWFAs can occur even for laser intensities initially below the threshold of ionising the higher HIT levels, as the peak field strength of the driver is increased through self-focusing [357, 358]. This concept can be extended to not only initiate, but also deliberately terminate the injection process for highly intense laser drivers. Such self-truncated ionisation injection (STII) schemes specifically exploit the rapid self-focusing of an intentionally unmatched laser pulse to either substantially modify the wake until the trapping condition is no longer fulfilled [359], or to subsequently prompt laser diffraction until the laser intensity becomes insufficient to ionise the target HIT level [360]. The injection distance can thereby be confined to a region as short as a few tens of micrometres, promising low-energy spread electron bunches. After injection, the laser driver ideally enters an approximately guided mode for the remaining acceleration distance.

Experimental realisations of self-truncated ionisation injection have demonstrated the generation of electron beams with several hundred MeV energy and few percent energy spread [361], with remarkable reproducibility [43]. The amount of trapped charge can thereby be controlled by varying the HIT dopant concentration, which enables energy spread optimisation via beamloading [41, 171]. Nowadays, such LWFA systems utilising $\sim$100 TW class laser drivers and employing STII excel in routinely delivering electron bunches approaching nanocoulomb charge levels, with associated peak currents of several tens of kiloampere.

In comparison, realising driver-induced ionisation injection in PWFAs is generally more challenging than in LWFAs, owing the substantially lower peak electric field of the driver in typical scenarios. Moreover, the maximum electric field for radially

symmetric particle drivers is located off-axis (see chapter 3.1.2). Successful driver-induced ionisation injection in PWFAs therefore requires particularly narrow drivers that carry sufficient peak current to achieve ionisation of the HIT component within the trapping region. Experimental results are thus comparatively scarce, yet have been reported for the first time [340] utilising lithium vapour ($\xi_{Li^+} \approx 5.4\,\mathrm{eV}$) generated in a heat-pipe oven [362] as LIT medium, with helium as HIT dopant for injection. These initial results were subsequently refined and discussed in more detail [363, 364], indicating a final witness beam emittance roughly ten-fold lower than the original drive beam. However, inherent off-axis injection paired with transverse momenta imprinted by the driver fields during injection again ultimately limits the minimum attainable emittance. Ionisation injection in a PWFA was further observed in a series of similar experiments using rubidium vapour [365, 366], serving simultaneously as LIT and HIT medium ($\xi_{Rb^+} \approx 4.2\,\mathrm{eV}$, $\xi_{Rb^{2+}} \approx 27.3\,\mathrm{eV}$). Similar to LWFAs, a deliberate mechanism for self-truncation of driver-induced ionisaton injection in PWFAs has been conceptualised, based on betatron oscillations and periodic focusing of the drive beam inside the plasma wake [367], with the potential for producing several energy-separated witness beams over extended acceleration distances. Finally, the use of HIT media with generally substantially lower ionisation thresholds than in LWFAs also implies that additional ionisation injection may be induced by the space-charge field of the trapped witness beam [368], which is usually regarded as an undesired source of dark current.

6.3.2 *Wakefield ionisation*

At the opposite end of the plasma cavity, the accelerating field of the wake reaches its peak, providing a second localised electric field maximum. An appropriate combination of driver parameters, plasma density and ambient gas media may thus yield wakefield amplitudes sufficiently high to enable selective ionisation of a chosen HIT species. As an example, the electric field close to the rear of a plasma wake operated in the blowout regime is capable of ionising a significant fraction of helium already at moderate plasma densities of $\sim 10^{17}\,\mathrm{cm}^{-3}$ [363].

The intrinsic wakefield itself can therefore, in principle, also be utilised for ionisation injection [369]. A prerequisite for such wakefield-induced ionisation injection (WII) is that the targeted HIT medium is not depleted at the front of the wake. More specifically, when aiming for isolated WII, the absence of driver-ionised electrons is desired, which implies that the peak wakefield exceeds the field strength of the driver.

In direct contrast to driver-induced ionisation injection, WII is hence most relevant for PWFA scenarios.

Nonetheless, similar considerations as for driver-induced ionisation injection apply. Another prerequisite for successful wakefield-induced ionisation injection is thus sufficient overlap between the ionisation volume and the trapping region. This necessitates particularly strong wakefields, which in turn is associated with the requirement for electron beam drivers with high peak-current $\geqslant 8.5\,\mathrm{kA}$ [370]. In comparison to driver-induced ionisation injection, however, the strength of the wakefield – and consequently the ionisation yield – is less susceptible to microstructures in the driver, promising improved shot-to-shot stability. A comparatively small intersection between ionisation volume and trapping region in WII results in intrinsically short electron bunches trapped at the rear of the blowout close to the strongest accelerating phase. Moreover, wakefield-ionised electrons released towards the rear of the plasma cavity do not experience transverse emittance degradation from the driver field and are immediately subject to the focusing wakefield. As a consequence, WII promises to deliver high-quality electron bunches with sub-µm bunch lengths and sub-µm rad emittances for plasma densities on the order of $10^{18}\,\mathrm{cm}^{-3}$ [370].

While the release of electrons in WII is inherently localised in the co-moving frame of the wakefield, the injection duration can be limited by confining the spatial extent of the HIT gas distribution [369, 370]. This measure also prevents further, in this case, undesired, ionisation injection due to driver focusing for the remainder of the acceleration distance. With a confined injection section, the trapped charge in WII is then tunable via controlling the dopant density, facilitating the optimisation of beamloading conditions to attain low energy spread.

Wakefield-induced ionisation injection therefore offers a promising approach for generating high-quality electron beams in PWFAs, with its primary attraction being its conceptual simplicity. However, successful WII has thus far not been directly demonstrated experimentally, although it may have played a role in studies exploring the viability of rubidium vapour as plasma source [365, 366]. One of the reasons may be found in the experimental challenge of accessing the blowout regime at comparatively high plasma densities, which necessitates particularly short, high peak-current drive beams. Such drive beams enabling WII could, however, be provided by laser-wakefield accelerators [41, 277][371].

6.3.3 *Auxiliary laser pulses*

Ionisation injection by either driver or wakefield inherently confines the release volume to the front or the rear of the wake, respectively. Albeit, it can be argued that the ideal release position is located at the centre of the blowout:

Similar to WII, particles released in the wake centre are not subject to inheriting transverse momentum from the driver, provided the driver is sufficiently short. Releasing particles at the trough of the trapping potential, however, relaxes the requirement on wakefield strength for successful injection. Further, the bunch compression effect is maximised, yielding high-current witness beams even for moderate levels of injected charge, while simultaneously minimising the accumulation of correlated energy spread. Targeting the wakefield centre for ionisation injection thus promises intrinsically enhanced witness brightness.

The injection scheme offering arbitrary choice of release positions inside the wake is the ultracold underdense plasma photocathode [38, 39]. Its eponymous key element is an additional laser pulse tightly focused directly into the plasma cavity to locally ionise the HIT medium. In a collinear geometry, that is, the injector laser co-propagating with the blowout, its focusing, alignment and delay with respect to the driver can be utilised to precisely tune the electron release positions, the overall release volume and injection duration. Also known under the colloquial term Trojan Horse Injection, this injection scheme was originally proposed in the context of PWFA, where selective ionisation of the designated HIT species can be achieved with comparatively low injection laser intensities. The released electrons thus inherit marginal transverse momentum from the injector laser, opening a pathway for generating witness beams with unprecedentedly low emittance and, accordingly, extreme brightness values. Further details of the plasma photocathode are discussed in chapter 7, and a first proof-of-principle experimental realisation in a perpendicular injector geometry [40] is presented in chapter 9.

Further variants of this scheme have been proposed, including a counter-propagating injector geometry [372], as well as utilising two colliding injector lasers to further restrict the ionisation volume in a transverse injector geometry [373]. It has also been theorised that trapping of electrons released via a dedicated injector laser pulse can be facilitated even for wakefields below the nominal trapping threshold, by either applying a plasma photocathode on a plasma density down-ramp [341] or exploiting the additional ponderomotive push of a mildly relativistic injector laser traversing the plasma cavity under an oblique angle [374].

Employing an injector laser for selective ionisation in a laser-driven wake, however, faces additional conceptual challenges. Since the peak electric field of laser drivers is typically orders of magnitude larger than the electric self-field of electron drive beams, highly relativistic injector laser intensities are required to access remaining elevated ionisation levels of an ambient HIT medium [375]. This effectively means that the injector laser itself is usually capable of driving a substantial plasma wave, at least transiently when it is close to its focus. The trapping dynamics are thus more complex and increasingly governed by emittance-degrading ponderomotive effects for higher injector laser intensities. A numerical study exploring the LWFA equivalent of a transverse colliding injector geometry reveals that ionisation can then become only a secondary contribution to injection [376].

To circumvent this issue, ionisation injection facilitated by a co-propagating injector laser pulse has also been conceptualised for LWFA scenarios employing laser drivers with only mildly relativistic intensities $a_0 \lesssim 1$ [377]. A first experimental realisation of such a configuration has been recently reported [378], however, the laser-driven wakefield in this scheme is operated in a quasi-linear regime and the prospects for attaining sub-µm rad emittances are likewise inherently limited [377, 378].

Further proposed LWFA adaptions suggest the utilisation of an injector laser with substantially higher frequency than the driving pulse to mitigate the ponderomotive emittance contribution during injection. This approach explicitly makes use of the scaling $a_0 \propto E_0/\omega_l$, which means that the ponderomotive force of a high-frequency injector laser can be attenuated despite its electric field strength exceeding the peak field of the driver. In turn, longer driver wavelengths combined with circular polarisation maintain a strong ponderomotive force even for considerably reduced driver field amplitudes. Such two-colour LWFA driver and injector laser schemes have been explored theoretically in both longitudinal and transverse injection geometries [379–381].

Yet another proposed LWFA concept similarly employs a higher-harmonic injector laser in collinear geometry, albeit with the injector pulse initially superimposed on the drive laser [382, 383]. The frequency difference between driver and injector lasers then leads to a relative phase shift between the two pulses due to their different dispersion within the plasma. This leads to a transient increase of their combined electric field strength which can be utilised to induce and tune ionisation injection. In essence, this scheme thus resembles laser-assisted driver ionisation injection in LWFA.

6.4 OTHER METHODS & INJECTION SCHEME COMBINATIONS

Besides the above non-exhaustive overview of distinct injection modes, a plethora of alternative methods and injection scheme combinations have been conceptualised. For example, applying external magnetic fields has been investigated as means for enhancing and controlling self-injection [384, 385], ionisation injection [386] and density down-ramp injection [387]. Suppressing self-injection on a plasma up-ramp, followed by rapid injection at the transition to a subsequent density plateau has been theorised as a method of generating sub-femtosecond electron bunches [388, 389]. Another approach for assisting and controlling self-injection in LWFAs introducing nanowires [390] or nanoparticles [391] was conceptualised, with encouraging initial experimental results [392, 393] and recently reporting the injection and acceleration of a $\sim$340 pC electron beam up to 10 GeV [30].

Further noteworthy experimental achievements include a combination of shock-front and colliding-pulse injection in a single LWFA stage, by which a dual-bunch configuration with tunable energy separation and delay was demonstrated [394]. Density down-ramps have been successfully employed to initiate and localise driver-induced ionisation injection in LWFAs [395, 396]. A carefully tuned combination of tailored density ramps and ionisation injection in composite gas targets has since been shown to provide remarkable reproducibility and further means of controlling the final beam parameters [172, 354].

LASER-INDUCED INJECTION IN PWFA

7

PLASMA PHOTOCATHODE

As outlined in the previous chapter, one of the virtues of plasma-based accelerators is that they can be simultaneously operated as injector, with a rich variety of methods resulting in different witness beam characteristics. The majority of such internal injection schemes, however, relies on either exploiting the driver evolution, deliberate modifications of the wake structure, or combinations thereof to initiate and terminate the injection process. In contrast, the plasma photocathode employs a dedicated injector laser pulse to release electrons directly inside the wake via selective tunnel ionisation. The plasma photocathode therefore uniquely decouples injection control from the driver and the accelerating structure. This offers a distinctive versatility in tuning the witness beam parameters, including the generation of ultra-short, ultra-low emittance beams with correspondingly ultra-high brightness [38, 39, 397, 398].

As other ionisation injection methods, the plasma photocathode relies on the availability of an ambient HIT medium combined with a strong blowout with sufficiently deep trapping potential to capture the HIT electrons released by the injector laser. The decisive capability of the plasma photocathode method is to prompt localised and swift injection around the transverse and longitudinal centre of the wake. This principal injection mode is illustrated in Figure 7.1 for a collinear injection geometry in a PWFA scenario. A high peak-current electron beam drives a blowout associated with a sufficiently deep trapping potential in an ambient, pre-ionised LIT medium. The driver is thereby sufficiently short as to not affect the wake centre. An independent, co-propagating laser pulse trails the driver on-axis at a distance corresponding to the minimum of the trapping well. Upon traversing its focus, the injector laser thus transiently releases HIT electrons in a confined volume around the wake centre. These electrons slip back with respect to the wakefield until they are trapped at an accelerating phase towards to the rear of the wake. Targeting the longitudinal wakefield centre for injection thereby specifically exploits the intrinsic bunch compression effect (recall Figure 6.1).

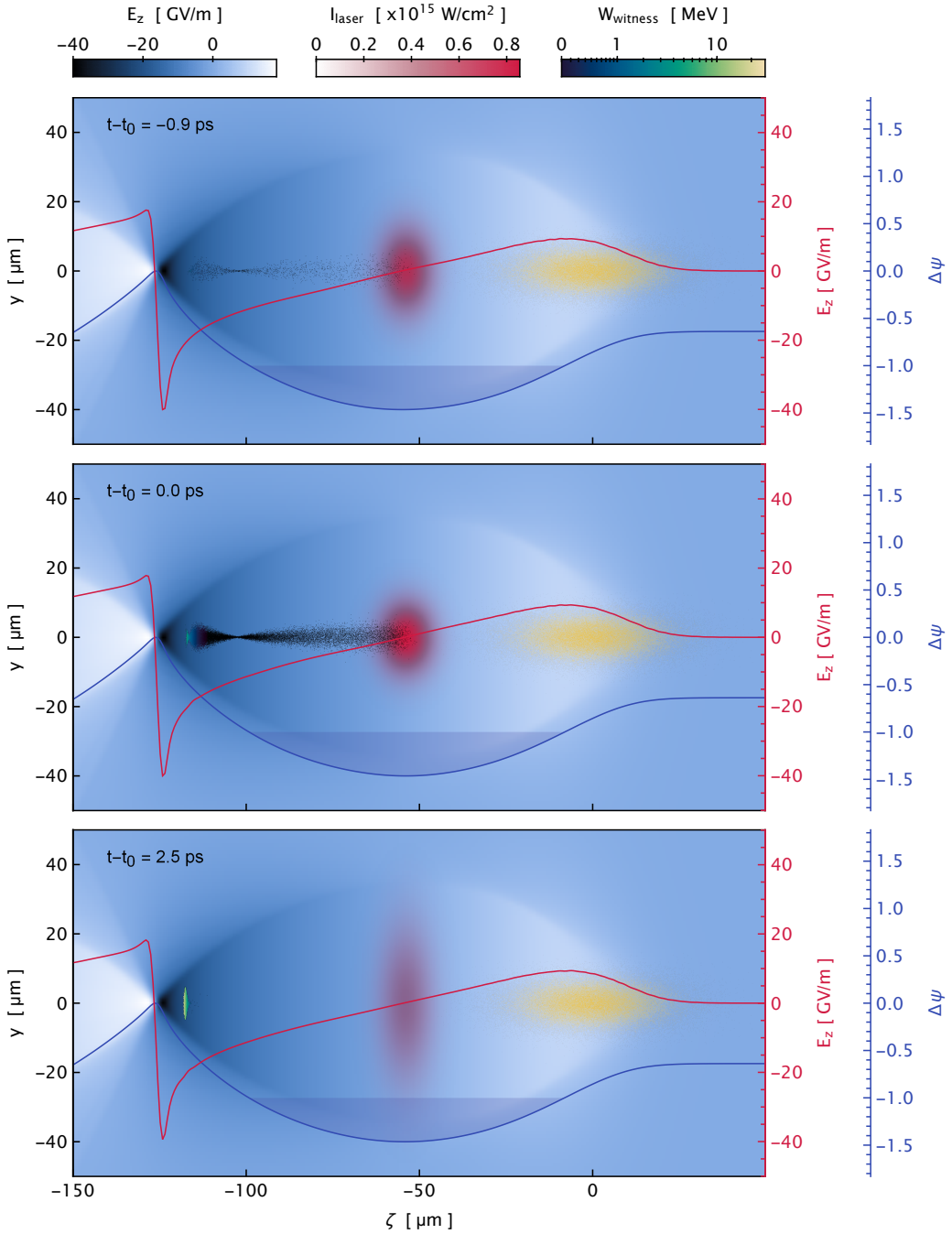

Figure 7.1: **Plasma photocathode injection.** Visualisations of a PIC simulation at successive time frames illustrate the plasma photocathode injection process, exemplified here for a 1:1 mixture of hydrogen and helium. The electron beam (yellow) with $\tilde{Q} = 5$ and $k_p \sigma_z = 0.5$ and a peak current of $I_p \approx 5.4\,\mathrm{kA}$ drives a blowout in the pre-ionised hydrogen plasma with density corresponding to $\lambda_p = 150\,\mu\mathrm{m}$. An independently tunable injector laser (red colour-scale), here shown in collinear geometry with $\lambda_l = 800\,\mathrm{nm}$, $\tau_{\mathrm{FWHM}} = 30\,\mathrm{fs}$, $w_0 = 10\,\mu\mathrm{m}$ and $a_0 = 0.02$, transiently releases cold helium electrons around the wake centre upon traversing its focus at t_0. The released electron population (colour-coded energy) is trapped and accelerated at the rear of the wake to form a witness beam, in this example with length $\sigma_{z,w} \approx 0.1\,\mu\mathrm{m}$, charge $Q_w \approx 5.3\,\mathrm{pC}$ and emittance of $\epsilon_{n,x} \approx \epsilon_{n,y} \approx 150\,\mathrm{nm\,rad}$.

As such, the injection phase, effective release volume and release duration are determined by the injector laser parameters[1]. More specifically, the injector laser intensity, focal spot size and pulse duration jointly define the central co-moving position, length, width and curvature of the ionisation front, as well as the relative velocity[2] and maximum longitudinal variation with which the ionisation front sweeps back and forth with respect to the pulse centre [341]. Provided a sufficiently strong wakefield, all electrons thereby released within the trapping volume are ultimately captured and form the witness beam. For fixed laser parameters, the resulting witness charge can hence be independently controlled by adjusting the HIT dopant density.

The potential of the plasma photocathode is indeed most advantageously exploited in PWFA scenarios. Electron-driven plasma wakefields can provide tens to hundreds of gigavolt-per-metre accelerating fields while being largely immune to self-injection, due to their ultra-relativistic phase velocities. Comparatively low PWFA driver electric fields further facilitate the retention of an adequate HIT medium that can in turn be accessed via tunnel ionisation with non-relativistic laser intensities $a_0 \ll 1$. For example, intensities on the order of $\sim 10^{15}\,\mathrm{W/cm^{-2}}$ are sufficient to tunnel-ionise a significant fraction of helium, corresponding to $E_0 \sim 80\,\mathrm{GV/m}$ or $a_0 \sim 0.02$ for typical linearly polarised Ti:sapphire laser pulses with 800 nm central wavelength (see also Figure 2.3 and equation 3.14). Such injector laser intensities just above the tunnel ionisation threshold release electrons with negligible inherited temperature corresponding to $< 10\,\mathrm{eV}$ [381, 397][399]. In this configuration, the initial witness beam emittance is therefore governed by the transverse spread in release positions and the linear focusing force of the blowout. Assuming a Gaussian laser in collinear injector geometry, the resulting transverse residual emittance can then be estimated as [381]

$$\begin{aligned}\epsilon_{n,x} \simeq \epsilon_{n,y} &= k_p\, a_0\, \frac{w_0^2}{\lambda_l}\, \frac{3\pi\, r_e}{4\sqrt{2}\,\alpha} \left(\frac{\xi_H}{\xi_{HIT}}\right)^{\frac{3}{2}} \\ &\approx 1.56 \times 10^{-11} \sqrt{n_0\ [\mathrm{cm^{-3}}]}\, a_0\, \frac{(w_0\ [\mu\mathrm{m}])^2}{\lambda_l\ [\mathrm{nm}]}\, (\xi_{HIT}\ [\mathrm{eV}])^{-\frac{3}{2}}\ ,\end{aligned} \tag{7.1}$$

where $r_e = e^2/\left(4\pi\epsilon_0 m_e c^2\right)$ is the classical electron radius, $\alpha = e^2/(4\pi\epsilon_0\hbar c)$ is the fine structure constant and $\xi_H \approx 13.6\,\mathrm{eV}$ is the ionisation potential of atomic hydrogen.

1 It is assumed that the absolute wakefield magnitude close to the blowout centre is small compared to the injector laser field strength. In this case, the contribution of the wakefield to the net ionisation rate can be neglected. The influence of superimposed laser- and wakefields, however, may be significant for exceptionally strong wakes or different injector geometries.

2 For Gaussian injector laser pulses, the ionisation front moves superluminal before traversing the focus, and subluminal afterwards.

Therefore, ultra-low residual emittances on the order of 10^{-9} m rad to 10^{-8} m rad are attainable from a PWFA plasma photocathode operated at typical plasma densities $n_0 \sim 10^{17}\,\mathrm{cm}^{-3}$, utilising injector lasers with wavelength of $\lambda_l \sim 800\,\mathrm{nm}$, focal spot size $w_0 \lesssim 10\,\mu\mathrm{m}$ and $a_0 \ll 1$ to ionise a suitable HIT medium. Witness electrons released in such an environment are rapidly accelerated to relativistic velocities, minimising subsequent emittance growth due to non-linear space-charge forces [400, 401] (also recall equation 4.18). Strong accelerating gradients, in conjunction with ultra-relativistic PWFA wakefield phase velocities furthermore maximise the intrinsic bunch compression during injection [341–343]. The plasma photocathode is thus capable of generating ultra-short witness beams with sub-femtosecond duration and correspondingly multi-kiloampere peak currents already for picocoulomb-scale injected charge [398]. At the same time, such short witness beam durations minimise the accumulation of correlated energy spread. The residual energy spread, in turn, is determined by the longitudinal variation of release phases and the injection duration. The latter is proportional to the Rayleigh length z_R of the laser pulse and usually constitutes the dominant contribution to the residual energy spread in collinear injection geometry [402], which can thus be approximated as [403][174]

$$\Delta W_{\mathrm{rms}} \simeq \frac{2\pi}{5}\,\frac{w_0^2}{\lambda_l}\,E_{z,\mathrm{trap.}} \quad . \tag{7.2}$$

Here, $E_{z,\mathrm{trap.}}$ denotes the accelerating field at the mean trapping location. The estimated residual energy spread obtained from plasma photocathodes is thus typically on the order of a few MeV or below, which translates to relative values of $\ll 1\,\%$ upon reaching GeV energies. Both residual emittance and energy spread scale, for fixed wake conditions, with the effective ionisation volume $\propto w_0^2/\lambda_l$. A confined release volume around the wake centre, combined with comparatively low witness charge thereby also minimises longitudinal and transverse phase mixing during and after injection [397, 402, 404]. In conjunction with practically phase-constant acceleration in a quasi-static blowout up to driver depletion offered by PWFAs, the plasma photocathode thus provides a pathway towards generating multi-GeV electron beams with unprecedented (5D) brightness values beyond $\sim 10^{19} - 10^{20}\,\mathrm{A}/(\mathrm{m}^2\,\mathrm{rad}^2)$ [398][399, 405], surpassing the capabilities of conventional accelerators by several orders of magnitude.

Importantly, the quality demands on the electron driver are very moderate in comparison. While realising the plasma photocathode necessitates drivers with a substantial peak current $\gtrsim 5\,\mathrm{kA}$ to establish adequate trapping conditions, the formation of a stable blowout is largely impervious to the initial emittance and energy spread

of the driver. In fact, a reasonably large matched spot size and considerable betatron phase mixing of the driver is prudent to efficiently inhibit dark current originating from, in this case, undesired driver ionisation [406]. Consequently, witness beams generated by a plasma photocathode may exceed the brightness of the initial driver by several orders of magnitude in exchange for reduced charge, albeit maintaining similar or even higher peak-currents. The plasma photocathode can therefore operate as a highly efficient brightness transformer of the original electron driver source.

The intrinsic versatility of the plasma photocathode concept thereby offers a broad variety of scenarios and adaptions, including multiple laser pulses and different injector geometries [372, 373][407]. Multiple injector lasers may also be successively deployed to generate witness beams with defined energy separation in a single or consecutive wake cavities [408, 409][399]. Sequential plasma photocathode injection can furthermore be exploited to subsequently adjust the longitudinal phase space of a previously injected witness beam. While comparatively low injected charge is beneficial for achieving lowest emittances, such a witness beam typically does not significantly load the wake and hence accumulates a correlated energy spread during acceleration. However, once this low-emittance electron beam becomes relativistically stable and largely resilient against space-charge forces, a second plasma photocathode injector laser may be utilised to inject a high-charge, lower quality electron distribution superimposed on the original witness beam. The secondary electron beam thereupon overloads the wake locally and effectively reverts the correlated energy spread of the previous witness beam without compromising its emittance [403][174, 175]. This technique thus not only further enhances the 6D brightness, but also largely facilitates emittance-preserving extraction from the plasma and subsequent transport of the primary witness beam. A recent simulation study showcases that thereby electron beams with 6D slice brightness on the order of $\sim 10^{19}$ A/(m^2 rad^2 0.1%) can be generated, isolated and delivered to drive a hard X-ray free electron laser with substantially reduced gain length [403][407]. Further optimisations of the witness beam parameters may be achieved through enhanced control over the size and shape of the effective ionisation volume upon utilising advanced injector laser optics [410–413][175, 399].

Generally, the plasma photocathode offers a wide variety of witness phase space control mechanisms beyond tuning the laser focus size and intensity, for example by deliberately detuning the injector laser delay, adjusting the pulse duration, frequency and polarisation, as well as introducing transverse offsets and oblique angles [399, 405]. Even exotic witness beam phase space distributions may be generated with structured laser pulses [414].

The principle injection mechanism, meanwhile, is independent of the injection geometry. However, when utilising injector lasers with Rayleigh lengths larger than the blowout dimensions at arbitrary angles, the electron release region may extent beyond the nominal wakefield. The spread of witness beam origin locations is then determined by the geometric overlap of the ionisation volume and the trapping region. Experimental realisations may be nevertheless largely facilitated specifically in perpendicular laser geometry. Such a 90° injection mode has been exploited in the E-210 experiment presented in chapter 9, resulting in the first demonstration of a plasma photocathode [40].

8

PLASMA TORCH INJECTION

The conceptual setup components of a 90° plasma photocathode can alternatively be utilised to generate steep density gradients ahead of an electron-driven wake. In this scenario, the injector laser traverses the central axis several picoseconds before the arrival of the driver and ionises a substantial fraction of the ambient HIT medium along its path. This results in a confined column of elevated plasma density perpendicular to the driver trajectory, colloquially termed plasma torch [316, 317, 415]. Upon traversing the resulting longitudinal density variation, the wake can thus be significantly distorted to prompt injection via a density transition mechanism (see chapter 6.2.2).

In contrast to density down-ramp injection schemes relying on hydrodynamically shaped gas profiles or hot plasma expansion, the plasma torch gradients result purely from localised, selective ionisation. Generating a sufficiently dense plasma torch for injection therefore requires an adequate two-component mixture of a LIT and HIT medium, whereby the HIT component must remain largely unaffected by the driver. Plasma torch injection is thus mostly applicable in PWFA scenarios. In a typical PWFA environment, however, a comparatively low-intensity laser pulse is sufficient to access the designated HIT component, resulting in a cold plasma filament superimposed on the plasma originating from the LIT medium. The shape of the resulting plasma torch is therefore determined by the laser intensity profile and remains nearly static on a nanosecond time scale [40, 416]. Combined with the non-linear sensitivity of tunnel ionisation rates on electric field strength, the laser-generated plasma torch can hence exhibit exceptionally sharp density gradients suitable for PWFA down-ramp injection [316, 317, 415, 417][40, 416].

The maximum attainable density enhancement within the plasma torch is defined by the underlying HIT density and the targeted ionisation levels. Upon full ionisation, the plasma torch density thus becomes invariant to the local laser intensity, such that flat-top density profiles with tunable plateau and ramp lengths can be generated. A HIT species with multiple available ionisation levels may also produce several density steps. Employing a laser pulse with a Rayleigh length and diameter considerably larger than the nominal plasma wavelength thereby generates nearly uniform longitudinal density gradients over the entire width of the blowout.

However, laser spot sizes significantly smaller than the blowout dimensions can also be utilised to intentionally generate confined plasma filaments with strongly localised density gradients. The plasma torch therefore offers unique capabilities of perturbing the wake uniformly, but also partially at defined locations. The ensuing injection dynamics then depend on the volumetric overlap of the 3D plasma torch density profile with the wakefield [417][416]. In effect, the plasma torch approach allows density down-ramp injection to be extended to multiple dimensions. This provides advanced techniques for manipulating the resulting witness beam distribution, arising from adjusting the laser intensity, focal spot size, as well as varying the incident angle and spatio-temporal offsets with respect to the driver. Various injection scenarios can thus be realised, including the generation of asymmetric witness beams and twin beamlets with defined separation in transverse phase space. Further aspects of these multi-faceted injection dynamics and their specific dependencies are discussed in detail in [417][416].

Evidently, plasma torch injectors are similar to plasma photocathodes in their essential setup components and tunability methods. However, both schemes are based on fundamentally distinct injection processes. The defining difference is that the plasma torch releases additional HIT electrons sufficiently ahead of the wake to elicit density down-ramp injection, whereas the plasma photocathode releases electrons directly inside the wakefield. Nevertheless, plasma torch and plasma photocathode injection can, in principle, be realised in the same experimental configuration [40]. Plasma torch and plasma photocathode modes then differ in injector laser delay and minimum required laser intensity. The plasma photocathode further necessitates accurate timing of the injector laser to coincide with the wake. In contrast, plasma torch injection is feasible within a vastly larger timing window, due to the relative longevity of the cold, laser-generated plasma density profile. Plasma torch injection can thus be exploited as a robust intermediate operating mode to facilitate accessing and isolating the plasma photocathode regime. This strategy was successfully applied in the E-210 experiment discussed in the following chapter.

The nature of plasma torch injection further does not strictly demand wakefields capable of trapping electrons from rest, and can thus be also realised in PWFA configurations insufficient to support plasma photocathode injection. Following its first implementation in the E-210 experiment, such a stand-alone plasma torch injector has been demonstrated at the FLASH-Forward facility [418].

9

THE E-210 EXPERIMENT

Corresponding publication [40]:

A. Deng, O. S. Karger, T. Heinemann, A. Knetsch, P. Scherkl, G. G. Manahan, A. Beaton, D. Ullmann, G. Wittig, A. F. Habib, Y. Xi, M. D. Litos, B. D. O'Shea, S. Gessner, C. I. Clarke, S. Z. Green, C. A. Lindstrøm, E. Adli, R. Zgadzaj, M. C. Downer, G. Andonian, A. Murokh, D. L. Bruhwiler, J. R. Cary, M. J. Hogan, V. Yakimenko, J. B. Rosenzweig and B. Hidding. 'Generation and acceleration of electron bunches from a plasma photocathode'. In: *Nature Physics* 15.11 (Aug. 2019), pp. 1156–1160. DOI: 10.1038/s41567-019-0610-9. A. Deng and O. S. Karger contributed equally to this work

Realising the plasma photocathode imposes several principal prerequisites. The imperative condition is a plasma blowout with sufficiently deep trapping potential, which implies electron drivers with a high peak-current on the order of 5 kA to 10 kA . The second requirement is an adequate plasma source to accommodate the electron-driven wake while maintaining a HIT medium with sufficiently separated ionisation energy. The third fundamental component is a corresponding laser pulse, focused into the wake with appropriate synchronisation to access such a HIT medium for injection.

Linac-driven PWFA facilities able to provide these conditions simultaneously are extremely scarce, and could thus far only be offered by the Facility for Advanced Accelerator Experimental Tests (FACET) [129] at the SLAC National Accelerator Laboratory. Prior to the commissioning of FACET, major milestones in PWFA research and development have been achieved at the Final Focus Test Beam (FFTB) facility [28, 340, 363, 419, 420], utilising electron and positron beams from the ~3 km SLAC linac which previously powered the Stanford Linear Collider. As successor to the FFTB facility, FACET comprised the first 2/3 of the SLAC linac and was operated as user facility from 2011 to 2016.

An international collaboration between several research teams and industry partners from Europe and the USA was thus formed to explore plasma photocathode injection at FACET in a dedicated experimental programme titled "E210: Trojan Horse PWFA". While FACET could deliver electron drivers with sufficient peak current of ~10 kA , several technical aspects of the experimental target design had to be developed and

refined during the E-210 programme, specifically for generating a metre-scale plasma compatible with dark current free PWFA operation [406], as well as achieving accurate spatial superposition and synchronisation of the injector laser and plasma wake [421]. To facilitate addressing these challenges, the experiment was designed and realised in a 90° injector geometry. This configuration further enabled the implementation of the plasma torch injection method in the same setup to assist accessing the plasma photocathode regime.

The author has been involved in the process of designing the experiment throughout its various iterations, and joined the experimental team on-site during the last three months of the E-210 campaign. With joint effort and valuable support by other FACET experiments and SLAC personnel, this campaign resulted in the first demonstration of a plasma photocathode, utilising the plasma torch method as an intermediate stepping stone. The author thereafter assisted in analysing the recorded measurements and contributed extensively to subsequent numerical simulations that provided further insights on the injection and acceleration dynamics under the specific conditions realised in the experiment.

The following summarises key design aspects, methods and the main results of the E-210 campaign. These results are also reported in [40, 422], and additional insights, experimental strategies and arising perspectives are discussed in accompanying publications [399, 416, 421], as well as various related theses [341, 403, 409, 417, 423, 424].

9.1 EXPERIMENTAL CONCEPT

Experiments at FACET are located 10 m underground in sector 20 of the SLAC linac tunnel. For the E-210 experiment, FACET delivers electron beams with a charge of $Q \approx 3.2\,\mathrm{nC}$, energy of $W \approx 20.35\,\mathrm{GeV} \pm 2\,\%$ FWHM and transverse emittances of $\epsilon_{n,x} \approx 100\,\mu\mathrm{m\,rad}$ and $\epsilon_{n,y} \approx 10\,\mu\mathrm{m\,rad}$ to the experimental area. They originate from a thermionic electron gun and are cooled in an emittance damping ring before being subsequently accelerated in a series of S-band radio-frequency cavities to $\approx 9\,\mathrm{GeV}$, compressed in a magnetic chicane, and further accelerated to their final energy along the remainder of the $\sim 2\,\mathrm{km}$ beam line [425]. Upstream of the interaction point (IP), the E-210 driver is ultimately compressed to a bunch length of $\sigma_z \approx 20 - 40\,\mu\mathrm{m}$ and focused to transverse sizes of $\sigma_x \approx 25\,\mu\mathrm{m}$ and $\sigma_y \approx 30\,\mu\mathrm{m}$, respectively.

The second essential infrastructure utilised in the E-210 experiment is a $\sim 10\,\mathrm{TW}$-class Ti:sapphire laser system located on the surface level near sector 20, providing

~ 500 mJ pulses at a central wavelength of 800 nm. The laser pulses are locked to the RF phase of the linac and delivered into the tunnel via a 28 m vacuum transport beam line [426]. The main laser energy is allocated to several laser paths inside the experimental area, providing individual pulses for diagnostics, plasma generation and injection.

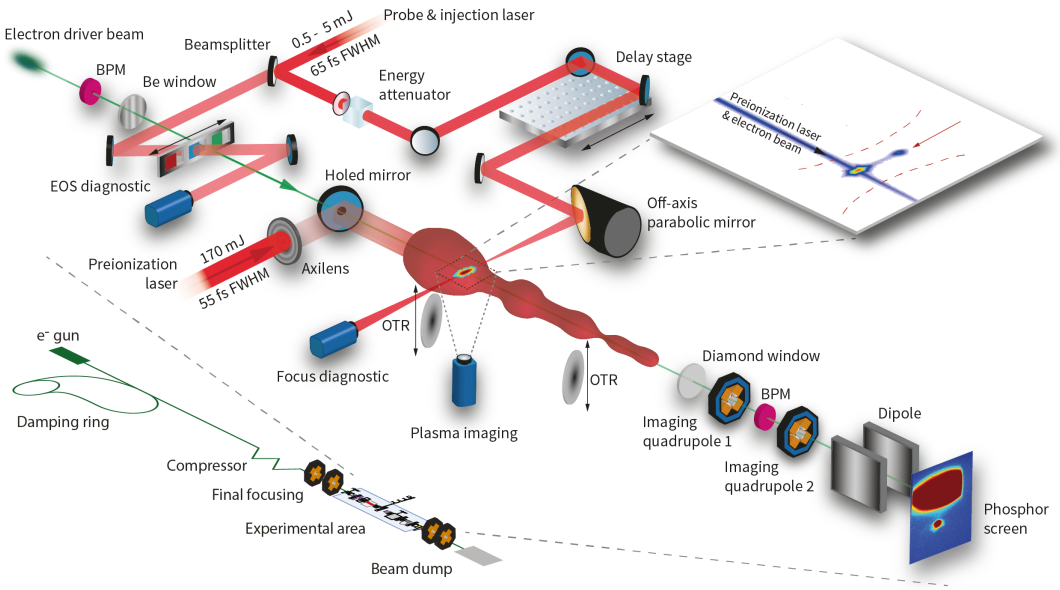

Figure 9.1: **E-210 experimental setup.** The electron drive beam is generated in the ~2 km SLAC linac and delivered into the experimental area after final compression and focusing. The interaction section is homogeneously filled with a gas mixture of hydrogen and helium, confined by an upstream and downstream window. The high-power fraction of the FACET laser ionises the hydrogen component and generates a plasma channel along the driver axis. The electron beam then drives a highly non-linear plasma wave in the pre-formed plasma. A comparatively low-power injector laser pulse with adjustable energy and delay is focused perpendicularly onto the driver axis to ionise the remaining neutral helium. Several cameras observe the injection region. The inset on the top right shows a snapshot obtained from the camera positioned below the injection point. An additional EOS diagnostic provides information about the relative delay between the injector laser and electron drive beam. BPMs and OTR screens assist in alignment of the electron beam and plasma channel. An imaging spectrometer downstream of the interaction section is used to characterise the resulting witness beams. Illustration composed by P. Scherkl with assistance from the author, published in [40].

A conceptual layout of the main experimental components comprising the E-210 setup is illustrated in Figure 9.1. The interaction section of the experiment is isolated from the vacuum accelerator beam line, enclosed upstream by a 50 µm thin beryllium

foil and downstream by a 100 µm diamond window. This entire ~ 5.4 metre long region is filled with a 1:1 gas mixture of hydrogen and helium with $n_{H_2} \approx n_{He} \approx 0.65 \times 10^{17}\,\mathrm{cm}^{-3}$ to provide the LIT and HIT medium, respectively. The main fraction of the FACET laser is used to generate a metre-scale plasma channel along the driver axis by selectively ionising the hydrogen component. The FACET electron beam then drives a highly non-linear plasma wave in the pre-formed hydrogen plasma. An independently tunable injector laser pulse is focused perpendicularly into the pre-formed plasma channel to release additional electrons from the remaining neutral helium.

A third laser pulse, derived from the same beam line that powers the injector laser, supplies an electro-optical sampling (EOS) diagnostic. This EOS diagnostic is used to infer the relative delay between the injector laser and the electron driver [341]. The trajectory of the electron driver is monitored online by two beam position monitors (BPMs) located upstream and downstream of the interaction section. These BPMs additionally function as intermediate charge monitors. Retractable optical transition radiation (OTR) screens within the experimental section assist in aligning the pre-ionisation laser to the driver axis.

After traversing the downstream diamond window, the driver and resulting witness beams are characterised by an imaging electron spectrometer, consisting of a tunable quadrupole doublet and an electromagnetic dipole. At the end of the ~22 m long spectrometer vacuum transport section, the dispersed electrons traverse a 5 mm aluminium plate and are subsequently observed on scintillating screens. The charge and energy read-out of the spectrometer is calibrated against the unperturbed driver prior to filling the interaction section with gas.

Precise coordination between the electron driver and laser pulses constitutes the major technical and operational challenge in the E-210 experiment. This includes generating an adequate plasma environment along the driver axis, as well as focusing the injector laser onto this central axis with a specified delay. A controlled interplay of all components thus requires robust spatial alignment procedures with high accuracy, in conjunction with determining and adjusting the temporal synchronisation of the injector laser to the electron-driven plasma wake. The 90° injector geometry thereby facilitates establishing such spatio-temporal alignment, but also enables exploiting plasma torch injection as intermediate step towards the first demonstration of a plasma photocathode. Further aspects of the E-210 plasma source, injector laser and alignment procedures are discussed in the following.

9.1.1 *Plasma source*

During its operation, FACET was the only facility capable of delivering sufficiently dense, high-current electron beams for driving a blowout suitable for plasma photocathode injection. A closely related prerequisite is an adequate plasma source sustaining the electron-driven plasma wake, while at the same time conserving a higher ionisation level for controlled injection. This can be realised through a suitable combination of LIT and HIT media and selective tunnel ionisation of each component via individual laser pulses with appropriate intensities. Such laser pulses are offered by the FACET laser system.

The E-210 experiment employs hydrogen and helium as LIT and HIT species, respectively. This choice provides several conceptual and operational advantages. Both media exist in a gaseous state at room temperature, which facilitates maintaining a homogeneous target species density with controlled mixing ratio over the entire interaction section. This configuration further enables the addition of essential access ports and windows to the enclosure for diagnostics, monitoring the generated plasma, and, crucially, in-coupling of the injector laser. Molecular hydrogen thereby provides up to two electrons with a comparatively low threshold for full ionisation. Beyond this threshold, the resulting hydrogen plasma density is thus insensitive to higher laser intensities. Gaseous helium, in turn, is an adequate complementary HIT medium, as its first ionisation level exhibits the highest binding energy of any element. The space-charge field of the FACET electron beam, with parameters used in the E-210 experiment, is not sufficient to ionise the hydrogen component. Instead, a pre-formed plasma is provided by means of a dedicated pre-ionisation laser pulse.

An ideal plasma source for the E-210 experiment fulfils further necessary and desired conditions simultaneously. The hydrogen plasma density needs to be sufficiently low to allow the FACET electron beam to drive a blowout, but at the same time sufficiently high to generate accelerating fields capable of trapping helium electrons released directly inside the wake. Further, a reasonable level of complementary matching between the plasma density and driver is necessary to avoid a strong pinch of the electron beam, as to prevent premature depletion of the helium component by driver ionisation and potential dark current injection [406]. Moreover, transferring a decent amount of driver kinetic energy to the injected witness demands tens of centimetres acceleration distance, and thus a correspondingly long plasma environment. At the same time, maintaining a stable wakefield requires a radial plasma extent that encompasses the blowout transversely over the entire accelerating distance. Generating

such adequately long and sufficiently wide plasma channel constitutes one of major technical challenges of the E-210 experiment.

The ultimately realised plasma source implementation is a result of a reasonable balance between the electron driver parameters, attainable laser power and spatial constraints in the experimental area. In this configuration, the pre-ionisation laser utilises 90 % of the FACET laser energy delivered into the tunnel, where it is subsequently compressed in a dedicated vacuum chamber to a FWHM pulse duration of about 55 fs. After compression, a total energy of ≈170 mJ is focused by a holographic axilens [341, 425, 427] with a focal length of 3 m and depth of focus of 1 m. Such axilens, in principle, generates a Bessel-shaped beam profile with the sought-after balance of distributing the laser intensity over a longitudinally elongated and wide focus, while maintaining peak intensities below the ionisation threshold of helium. The estimated intensity distribution of the axilens focus realised in the experiment is shown in Figure 9.2, calculated from the measured input beam profile.

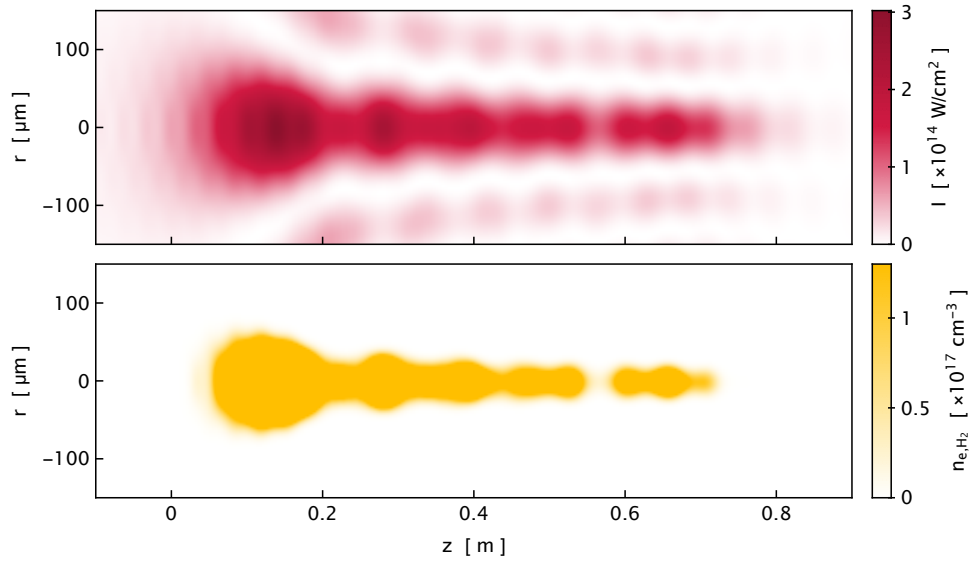

Figure 9.2: **E-210 plasma channel.** The top panel visualises the calculated intensity profile of the pre-ionisation laser after being focused by the axilens, derived from the measured input beam profile. The bottom panel shows the corresponding plasma electron density distribution along the electron driver axis, calculated for a hydrogen gas density of $n_{H_2} \approx 0.65 \times 10^{17}\,\mathrm{cm}^{-3}$. The pre-ionisation laser is thus capable of generating a fully ionised hydrogen plasma channel over several tens of centimetres, albeit with varying width. Data generated by M. Litos for [40]. Figure adapted from [399] under license CC BY 4.0.

The pre-ionisation laser is folded onto the electron beam axis via a holed mirror (see Figure 9.1) before it reaches its focus. There, it ionises the hydrogen component about 20 ps prior to the electron beam arrival. The resulting electron density distribution along the driver axis is further shown below the intensity profile in Figure 9.2, illustrating that a fully ionised hydrogen plasma channel is indeed generated over several tens of centimetres, albeit inheriting a complex transverse shape. While the plasma channel diameter initially extents up to 130 µm, it subsequently narrows along the driver propagation axis.

This entails a lower limit on the applicable plasma density at which a stable blowout can be maintained over the entire plasma length, as otherwise the nominal blowout radius exceeds the transverse channel boundary. In turn, an upper limit is imposed by the imperative to avoid excessive driver focusing and concomitant premature depletion of the helium species [406]. These considerations are not conceptual limitations of the plasma photocathode per se, but rather inherited from the technical realisation specific to the E-210 experiment. As a trade-off between these boundary conditions, the hydrogen gas density is set to $n_{H_2} \approx 0.65 \times 10^{17}\,\mathrm{cm}^{-3}$, resulting in a fully ionised plasma density of about $1.3 \times 10^{17}\,\mathrm{cm}^{-3}$ and a corresponding nominal plasma wavelength of $\sim 90\,\mu\mathrm{m}$.

The experiment is thus operated at a slightly higher plasma density than desired for optimal plasma photocathode injection conditions [397], in exchange for reduced blowout dimensions. This also implies that the driver longitudinally extends deeper into the wake and may thus detrimentally affect the attainable emittance of electrons released in its direct vicinity. A further consequence is an increased sensitivity of the injection process on the spatio-temporal alignment accuracy and precision of the injector laser.

9.1.2 *Injector laser*

Another central element of the E-210 experiment is an independently tunable laser pulse to ionise the HIT medium. This injector laser is derived from the remaining low-energy contingent of the FACET laser, which is individually compressed in air to a pulse duration of $\tau_{FWHM} \approx 65\,\mathrm{fs}$. A 10 % portion of this auxiliary beam line is also used to supply the EOS diagnostic.

The subsequent injector laser arm is further equipped with an energy attenuator, consisting of a $\lambda/2$ wave plate and a polarising beam splitter. The energy of the injector laser can thus be remotely adjusted in a range of $0.5 - 5\,\mathrm{mJ}$. An additional motorised

delay stage is used to individually control the temporal offset of the injector relative to the other laser pulses. A joint delay of all laser arms with respect to the electron driver is tuned by varying the synchronisation between the FACET laser and the linac RF phase. The collimated injector laser is then transported through a CaF_2 window into a vacuum chamber attached to one of the available access ports of the interaction section, where it is focused onto the driver axis by an $f/22.9$ off-axis parabolic mirror (OAP) to a vacuum spot size of $w_0 \sim 20\,\mu m$. As a result of this fixed geometry, the injector laser intersects the pre-formed plasma channel at a longitudinal position corresponding to $0.2\,m$ in Figure 9.2. The pitch, yaw and roll of the OAP can be remotely adjusted, whereby the latter is used to align the injector laser focus vertically onto the driver axis. The focus spot is further monitored on a dedicated diagnostics camera.

With maximum energy supplied to the injector laser, its peak intensity is estimated to $I_0 \approx 1.17 \times 10^{15}\,W/cm^{-2}$, sufficient to fully ionise the helium HIT medium. The nominal Rayleigh length thereby corresponds to $z_R \approx 1.6\,mm$, which implies that the injector laser generates a helium filament substantially longer than the nominal plasma wavelength $\lambda_p \approx 90\,\mu m$ associated with the hydrogen LIT medium density. On the one hand, such configuration compromises the minimum attainable emittance in a 90° plasma photocathode, as it implies that the injector laser releases electrons across the entire width of the electron-driven blowout, thus introducing additional transverse momentum spread to the resulting witness beams. On the other hand, a perpendicular plasma filament with steep longitudinal density gradients over the entire blowout width provides ideal conditions to realise plasma torch injection. The E-210 injector laser implementation thus enables the exploration of both plasma torch and plasma photocathode methods in the same setup.

Thereby, the capability of the injector laser to generate a millimetre-long helium plasma filament effectively alleviates the required spatial alignment accuracy in the horizontal dimension. Moreover, observing the interaction of the electron driver with only the injector laser filament proves to provide a critical tool for refining the alignment in the remaining vertical and temporal dimensions, as discussed in the following section.

9.1.3 *Spatio-temporal alignment*

Meticulous spatio-temporal alignment between the electron driver and laser pulses is one of the fundamental prerequisite in the E-210 experiment. However, conventional alignment and synchronisation diagnostics cannot be applied directly in a plasma

environment with coinciding high-intensity electron beams and ionising laser pulses. Interceptive methods, such as OTR screens, are susceptible to damage, whereas indirect methods, such as the EOS system, are impaired by the shielding properties of the plasma or overpowered by a strong plasma response to the electron driver. The application of such methods is therefore either restricted to locations afar from the plasma and injection point, or to operating modes with substantially attenuated laser pulses. In contrast, a spatially confined plasma is not only resilient to damage, but at the same time highly sensitive to the intersection with the electron beam. The plasma itself can therefore be exploited as detector medium to characterise spatio-temporal alignment. The E-210 experiment thus employs an incremental alignment procedure, utilising a combination of established methods refined by plasma-based diagnostics.

9.1.3.1 *Pre-ionisation laser alignment*

The pre-ionisation laser generates a plasma channel with a diameter on the same order of magnitude as the anticipated blowout width. This, in turn, demands a particularly stringent superposition of the pre-ionisation laser path and the electron beam axis.

To first determine the driver trajectory through the interaction section, two 500 µm thick titanium OTR foils are alternately inserted onto the central axis and monitored with dedicated cameras through viewing ports. The pre-ionisation laser is then released as well, albeit with substantially reduced energy. This way, the laser does neither generate a plasma nor damage the OTR screens and cameras. Instead, the electron beam OTR signal and the transverse Bessel-shaped profile of the pre-ionisation laser are observed together on the respective cameras with similar intensities. The laser profile is then centred around the electron beam signal in an iterative two-point alignment process.

After this initial procedure, the viewing screens are retracted and the pre-ionisation laser is enabled with full power, allowing the electron beam to interact with the pre-ionised plasma channel. This driver-plasma interaction is thereafter used to assess the accuracy of the preliminary alignment; a potentially remaining angular misalignment between the narrow plasma filament and electron beam alters the outgoing electron beam trajectory [428], which can be detected on the downstream BPM. The previous alignment can thus be refined by further steering the laser in minute steps until the output trajectory of the driver matches the original BPM readout observed without plasma. This plasma-based method is further used to ensure that accurate alignment is maintained during the measurements. Potential drifts of the driver input trajectory

are additionally monitored on the upstream BPM, variations in the laser pointing are detected online on various near- and far-field monitors along the laser beam line.

9.1.3.2 *Injector laser alignment*

To realise plasma photocathode injection, the injector laser must ultimately intersect with the electron-driven wake. This necessitates a high spatial alignment accuracy corresponding to a few micrometres, as well as a synchronisation accuracy on the scale of a few tens of femtoseconds. This is again achieved in an incremental procedure, whereby the pre-ionisation laser remains blocked.

A coarse vertical alignment of the injection laser is achieved by adjusting the roll of the OAP, such that its focal spot coincides with the previously determined electron beam axis. This is monitored, for example, on the injector laser focus diagnostic (see Figure 9.1). An additional plasma imaging camera observes the horizontal plane of the injection region from below and thereby detects the recombination and relaxation light emitted from the thin plasma filament generated by the injector laser (see again Figure 9.1). This plasma afterglow signal [61, 62] is collected over an exposure time of 25 ms . To confirm that the injector laser is capable of ionising the helium component of the gas mixture, the camera is equipped with a remotely inserted 10 nm bandpass filter centred around a particularly prominent helium emission wavelength at ≈ 587 nm . The integrated plasma imaging camera read-out thus provides an empirical relative measure of the amount of ionised helium.

The delay of the injector laser is then adjusted such that it crosses the central axis about 2 ps prior to the arrival of the driver. Once the electron beam interacts with the plasma filament, a substantial enhancement of the afterglow signal is observed. This effect is attributed to the transient energy transfer of the electron beam into the filament [429], resulting in subsequent plasma heating and expansion associated with secondary impact ionisation of the surrounding neutral gas [421]. The amount of transferred energy thereby depends on the geometric overlap of the electron beam with the plasma filament. Consequently, the magnitude of the integrated afterglow signal is highly sensitive to the vertical alignment of the injector laser with respect to the driver axis.

Such scaling of measured afterglow enhancement in relation to a vertical offset is illustrated in Figure 9.3 , together with the driver-to-plasma energy transfer derived from PIC simulations. The afterglow magnitude is thereby characterised over a series of 99 consecutive measurements, recorded while scanning the OAP rotation. Comparing

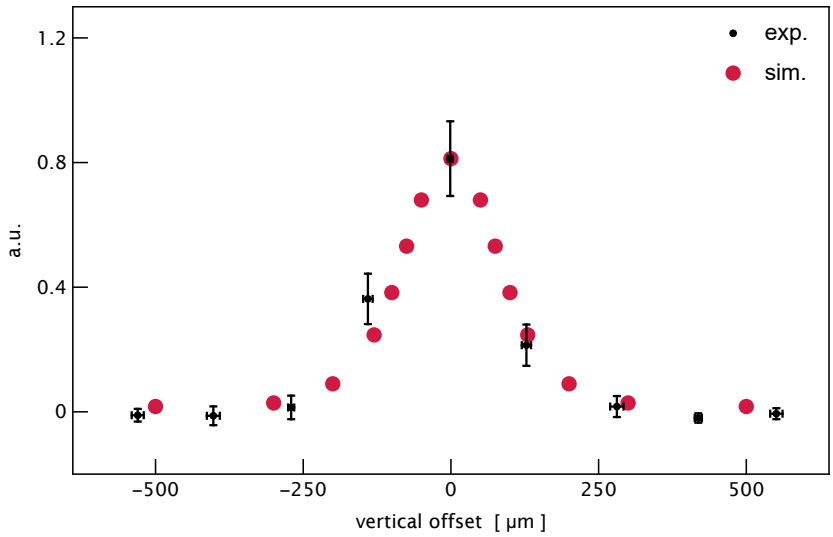

Figure 9.3: **Plasma afterglow vertical alignment.** The vertical offset the injector laser to the electron-beam axis is adjusted by rotating the OAP. The magnitude of the measured afterglow enhancement (black data points) is thereby proportional to the amount of energy transferred from the driver into the plasma filament (red data points, inferred from PIC simulations). A maximum observed afterglow signal thus indicates optimal vertical alignment. Figure adapted from [421] under license CC BY 4.0 .

experiment and simulations suggests that the magnitude of the afterglow enhancement is proportional to the energy deposited into the plasma, with both maximised upon overlapping the centres of the electron beam and plasma filament. Based on this measurement, the optimal vertical alignment of the injector laser is then determined with an accuracy of 4.1 µm , which is substantially smaller than the dimensions of the electron driver and its associated wake.

Further aspects of the complex electron dynamics induced by the driver upon traversing the plasma filament, subsequent energy dissipation and secondary plasma generation are discussed in [421], as well as in [341] and [409]. In effect, the plasma afterglow enhancement maps the initial femtosecond-micrometre scale interaction onto a millisecond-millimetre observable. The plasma afterglow diagnostic thus provides an efficient and robust tool to characterise and ascertain the superposition of injector laser and electron driver.

This technique is therefore similarly applied to also determine the temporal synchronisation between the injector laser and the electron driver, in conjunction with the EOS diagnostic. Such electro-optical sampling is an established method for inferring

temporal structures as well as the time of arrival (TOA) of highly relativistic electron beams [430–433]. The EOS system used in the E-210 experiment is located upstream of the plasma section, comprising a 100 µm thick electro-optic gallium phosphide (GaP) crystal positioned a few millimetres above the electron beam axis. A short laser pulse, derived from the same beam line that supplies the injector laser, traverses the GaP crystal under an angle of 45°. The laser thus illuminates different parts of the crystal at different times. The crystal surface is further imaged onto a camera, equipped with a polariser set to maximum extinction. Under the influence of the electric field of the driver passing below, however, the crystal exhibits a transient birefringence, such that the polarisation of the laser is partially rotated and a signal is detected on the camera. A change of the electron beam TOA then results in a lateral shift of the observed EOS signal. Further details of the EOS setup and analysis are discussed, for example, in [341].

The EOS system thus provides a non-intrusive online method to determine the relative delay between the driver and injector laser for each shot. The single-shot TOA can thereby be determined with an accuracy of $25 \pm 2.5\,\mathrm{fs}$, again substantially shorter than the duration of the driver and its wake. The EOS diagnostic is also used to quantify the rms synchronisation jitter between driver and injector laser, which corresponds to an rms value of $109 \pm 12\,\mathrm{fs}$. Individual measurements obtained in the E-210 experiment are therefore sorted according to their corresponding EOS delay.

However, the timing information inferred from the EOS diagnostic on its own does not provide knowledge of the absolute zero delay, that is, when the driver and injector laser overlap temporally at the injection point. Such absolute calibration of the EOS time stamps is attained by again utilising the afterglow diagnostic [421][341, 409]. In this procedure, the injector laser delay is varied over a range of several picoseconds, such that laser ultimately traverses the central axis at the injection point before and after the passage of the electron beam.

This transition is illustrated in Figure 9.4, showing the afterglow enhancement obtained from a dataset of 256 consecutive measurements while scanning the injector laser delay. Individual data points are thereby sorted according to their corresponding EOS time stamp. When the laser arrives too late, the electron beam has already passed the injection point and therefore does not interact with the plasma filament at all. Consequently, only the initial afterglow of the laser-generated plasma is observed. In the opposite scenario, when the laser arrives sufficiently early, the driver traverses a fully formed plasma environment yielding a maximum enhancement of the afterglow signal. During intermediate timings, however, the driver samples a varying amount of

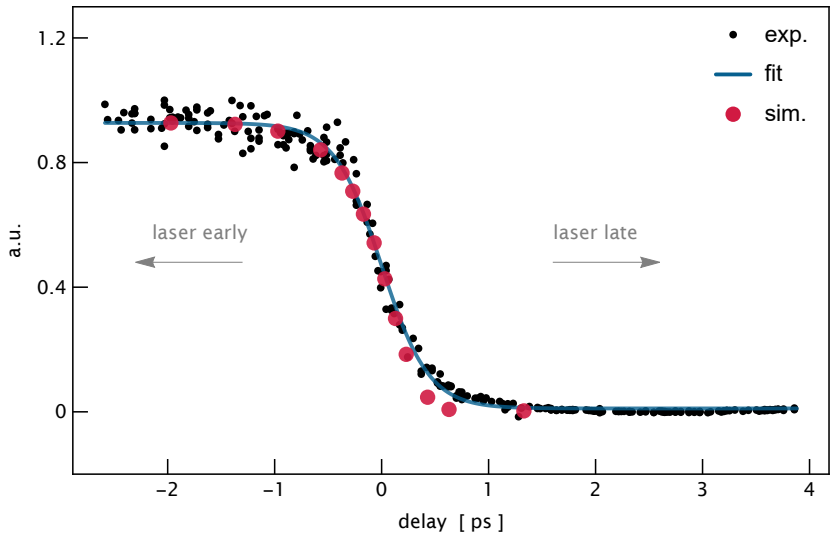

Figure 9.4: **Plasma afterglow temporal alignment.** Upon scanning the delay of the injector laser over a range of several picoseconds, the electron beam interacts with a varying amount of plasma. The magnitude of the observed afterglow enhancement (black data points) can thus be utilised to characterise the temporal overlap between the injector laser and electron beam. Individual experimental data points are sorted according to their EOS time stamp, revealing a steep slope for intermediate timings. A similar transition is apparent from analysing the energy transferred from the driver to the plasma in PIC simulations (red data points). The inflection point of a sigmoid fitting function (blue line) is used to define the absolute zero delay reference for subsequent measurements. Figure adapted from [421] under license CC BY 4.0 .

plasma and the afterglow magnitude exhibits a steep slope. Once more, the observed transition agrees well with the simulated energy transfer from the driver into the plasma. Such simulations further suggest that the width of the transition window and the associated slope of the observed afterglow enhancement inherently depend on the relative transverse dimensions of the plasma filament and electron beam, as well as the bunch length and adiabaticity of the interaction [421][409].

The nominal centre of the measured transition window can be determined by evaluating a sigmoid fitting function applied to the experimental data points. Subsequent measurements obtained in the E-210 experiment hereafter utilise the EOS time stamp associated with the inflection point of the fitting function to reference the zero time of arrival.

9.2 FROM PLASMA TORCH TO PLASMA PHOTOCATHODE

Equipped with reliable spatio-temporal alignment procedures, the main E-210 experiment is conducted following a stepwise strategy. To at first evaluate the synergistic interplay of all experimental setup components, exploring the plasma torch injection scheme provides a conveniently robust starting point; it is largely insensitive to timing, as long as a longitudinal plasma density profile with sufficiently steep gradients is fully formed prior to the arrival of the electron driver.

The injector laser is thus initially deployed with maximum energy and set to cross the injection point about a picosecond before the electron driver. It thereby generates a localised column of increased plasma density by ionising the helium HIT medium on top of the pre-ionised hydrogen plasma. Upon establishing spatial alignment, a first indicator for successful injection is observed in the form of excess charge detected on the beam position monitor located downstream of the interaction section. To ascertain that injection is evoked solely by means of the injector laser, the corresponding laser path is repeatedly blocked over a series of 360 consecutive shots.

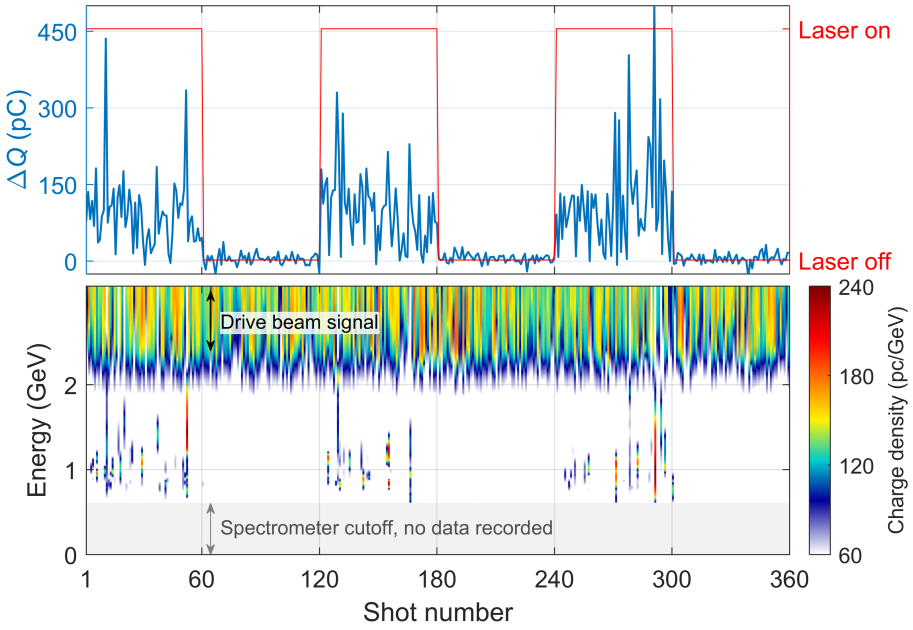

Figure 9.5: **Plasma torch injection.** The top panel illustrates the excess charge detected on the downstream BPM upon repeatedly engaging and disabling the injector laser over a series of 360 consecutive shots. Corresponding electron spectra are shown below, signifying injection and acceleration of witness electrons up to about 2 GeV . Figure adapted from [40].

The result of this measurement is illustrated in Figure 9.5 , showing the recorded charge difference between the downstream and upstream BPMs, alongside the corresponding electron spectra. A substantial amount of excess charge is observed in nearly every shot when the injector laser is engaged. In contrast, no significant charge is observed with the injector laser disabled. In addition, energetically distinct witness beam signatures are observed on the electron spectrometer up to 2 GeV , beyond which they start to merge with the signal associated with the non-imaged driver distribution[1]. These measurements provide compelling experimental evidence of plasma torch injection. To the author's knowledge, this finding further constitutes the first demonstration of density down-ramp injection in PWFAs.

Moreover, this initial result confirms the principal operating capabilities of the E-210 experiment; the FACET electron beam is able drive a dark-current free wake in the pre-ionised plasma, which at the same time is suitable to accelerate witness electrons to considerable energies. Spatial overlap of the injector laser with the driver axis can be achieved, upon which injection is reliably observed. The accelerated witness beams can also be transported through the electron spectrometer.

With these essential operating conditions established, the injection dynamics can be further controlled by adjusting the injector laser parameters. Specifically, a deliberate transition from plasma torch to plasma photocathode injection can be elicited by tuning the injector laser delay and energy. The conceptual difference between these two injection modes is illustrated in Figure 9.6 , showing visualisations of PIC simulations representative of the E-210 operating conditions.

Plasma torch injection is realised when the injector laser generates a sufficiently pronounced plasma filament ahead of the wake. Upon traversing this region of locally increased plasma density, the blowout sheath is transiently distorted and ambient plasma electrons are injected into the wake. The resulting witness beam thus comprises electrons originating from locations outside of the blowout. A pure plasma torch injection process is thereby restricted to timings when the injector laser crosses the driver axis sufficiently early, and ceases for later delays. Similarly, the plasma torch becomes increasingly ineffective for reduced laser energies. Once the laser ionises only a certain fraction of the available helium reservoir, the diminished plasma density perturbation is insufficient to significantly deform the blowout.

1 During this measurement, the nominal imaging energy of the electron spectrometer is adjusted to 0.5 GeV . As a result, the projection of the higher-energy driver electrons onto the spectrometer screen is dominated by their divergence and does not reflect the actual driver energy. The effective deceleration of the driver is characterised in an ancillary measurement and amounts to about $2-4$ GeV .

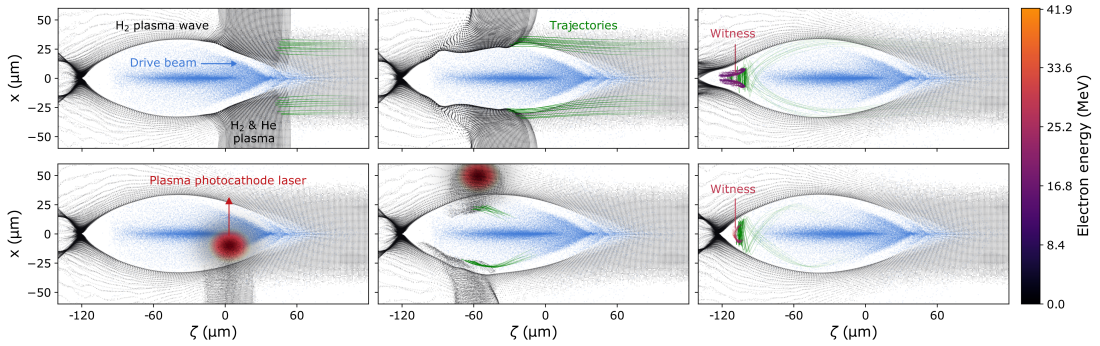

Figure 9.6: **E-210 injection simulations.** Distinct injection dynamics differentiate the plasma torch (top row) from the plasma photocathode regime (bottom row). Visualised is the horizontal plane of PIC simulations representing the conditions around the injection point in the E-210 experiment (corresponding to 0.2 m in Figure 9.2). From left to right, individual frames depict sequential simulation snapshots: when the driver (blue) arrives at the injection point, during injection, and after about 1 mm of propagation. Dots colour-coded with energy represent pre-ionised hydrogen plasma electrons, as well as hydrogen and helium electrons released by the injector laser. In both shown scenarios, the driver generates an equivalent blowout in the hydrogen plasma channel before injection. Plasma torch and plasma photocathode modes then differ in energy and delay of the injector laser. In the top row, a 5 mJ injector laser generates a fully ionised helium plasma filament ahead of the wake. Upon traversing this region of locally increased density, the blowout is substantially distorted and electrons are subsequently injected into the wake. Trajectories (green lines) indicate that these electrons originate from outside the blowout. In the bottom row, the injector laser energy is substantially reduced to 0.5 mJ and its delay adjusted to intersect the wake. The injector laser (red) thus releases helium electrons directly inside the wake, without altering the blowout structure significantly. Figure adapted from [40].

In contrast, the plasma photocathode regime is only accessible in a finite timing window during which the injector laser is able to traverse the blowout. The laser then releases helium electrons directly within the wake, which are subsequently trapped and accelerated. Plasma photocathode injection thus remains functional even if the injector laser ionises only a small fraction of the helium component.

These considerations inform a strategy to isolate the plasma photocathode in the E-210 experiment: Starting from the established plasma torch injection regime, a series of sequential timing scans is performed, whereupon the injector laser energy is successively reduced. The results of this procedure are presented in Figure 9.7 . The measurements depict the injected charge detected on the electron spectrometer in relation to the relative TOA between injector laser and electron driver as inferred from the EOS time stamps. Negative timings thereby indicate that the laser reaches the

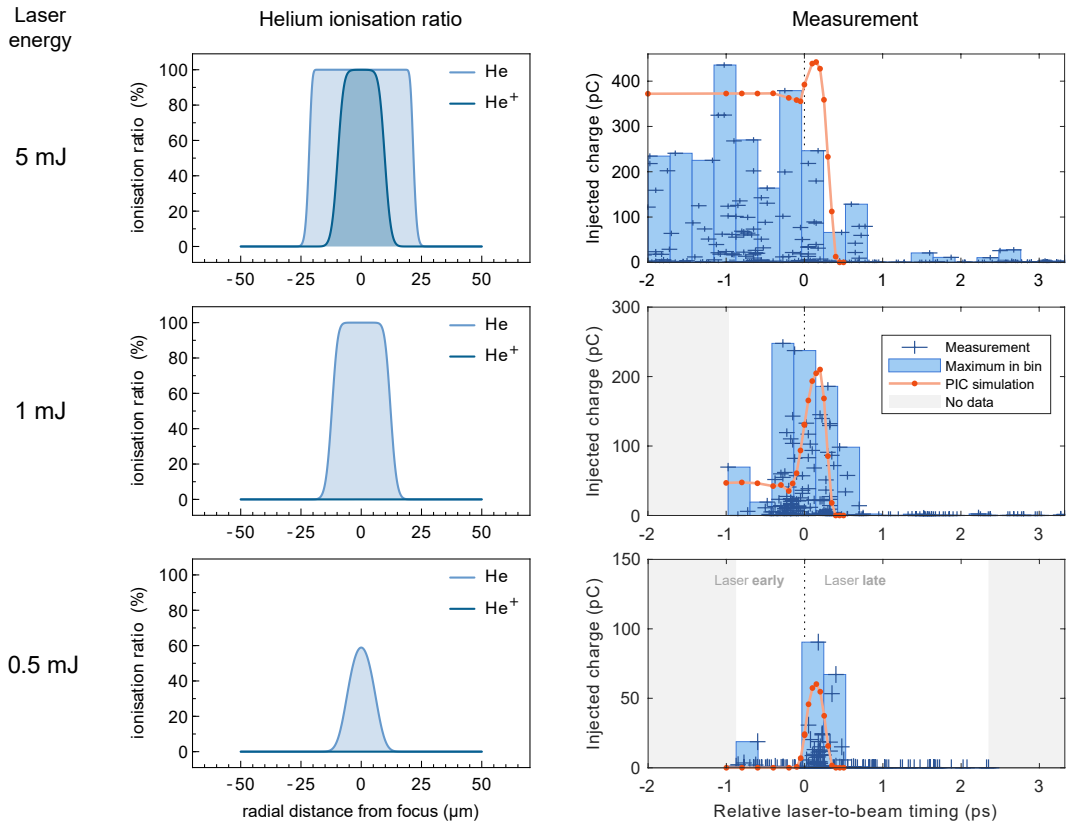

Figure 9.7: **Transition from plasma torch to plasma photocathode.** A series of timing scans with varying injector laser energy reveals and isolates the plasma photocathode regime (right column). Individual measurements (blue crosses) represent the injected charge determined from the electron spectrometer. The relative timing between the injector laser and drive beam is inferred from the EOS diagnostic. Blue bars visualise the maximum measured charge per timing bin. Plasma torch injection is accessed when the laser generates a sufficiently dense helium filament before the electron driver arrives at the injection point (negative timings). Successively reducing the injector laser energy lowers the nominal helium ionisation ratio (middle column, calculated assuming a Gaussian laser focus) and thus attenuates the plasma torch filament. For lowest laser energy, the plasma torch process is inhibited and pure plasma photocathode injection is realised. The observed scaling of injected charge with laser energy and timing agrees well with PIC simulations (red data points). The right panel of the figure is adapted from [40].

injection point earlier than the driver, and positive timings vice versa. The previously observed plasma torch injection is recovered when the laser arrives earlier than the driver and a high laser energy of 5 mJ is maintained. The injected charge thereby remains fairly consistent over all measured negative timings, as is characteristic for the

plasma torch regime. Once the delay is adjusted to positive timings, the detected charge quickly diminishes. Upon reducing the laser energy to 1 mJ , consistently less charge is injected for negative timings. This indicates a diminished effectiveness of the plasma torch injection mechanism, concordant with an attenuated helium filament. However, a pronounced increase in injected charge is then observed around the zero delay. This implies a gradual transition from the plasma torch to the plasma photocathode regime, associated with an intermediate mixed mode. In a final iteration, the laser energy is further reduced to 0.5 mJ . Significant injection is then exclusively observed within a short timing window when the laser arrives immediately after the driver. The width of this injection window is thereby consistent with the temporal range over which the injector laser overlaps with the first plasma wake period, which is further corroborated by accompanying simulations. Witness beams generated during this operating mode must therefore be attributed to a pure plasma photocathode injection process.

Exploiting the characteristic injection dynamics and distinct scalings differentiating the plasma torch from the plasma photocathode thus unambiguously reveals and isolates the plasma photocathode regime. This first experimental demonstration of a plasma photocathode constitutes the main achievement of the E-210 experiment.

9.3 DISCUSSION

In summary, the E-210 programme at FACET culminated in the implementation of controlled laser-induced injection in a PWFA via two complementary mechanisms, the plasma torch and the plasma photocathode scheme. Plasma torch injection is thereby utilised as a stepping stone to facilitate a deliberate transition into a pure plasma photocathode mode. These measurements further demonstrate that both mechanisms can be distinguished and accessed independently.

The E-210 experiment hence successfully accomplished its main objective of realising the very first plasma photocathode. Its technical configuration is, however not yet optimised to deliver highest witness beam quality. While instrumental to establish plasma torch injection, the perpendicular injector laser geometry combined with a long Rayleigh length implies that the plasma photocathode releases electrons across the whole width of the wake, suggesting an increased transverse momentum spread and thus a larger inherited source emittance. This effect is further exacerbated by the presence of the driver throughout a large fraction of the wake, which may additionally impart transverse momenta onto the witness electrons during injection (as illustrated, for example, by the trajectories in Figure 9.6). To a large extent, this condition is a result of the restrictions imposed by the narrow pre-ionised plasma channel.

Moreover, the varying width of the plasma channel continuously alters the wakefield phase experienced by the trapped witness beams during their propagation. This distortion of the wake along the channel is visualised in Figure 9.8 , obtained from simulating the driver interaction throughout the whole length of the plasma. While a comparatively stable wakefield is generated within the initial plasma section, where the channel radius is largest, the wakefield successively deteriorates after passing the injection point. The wake structure repeatedly expands and contracts upon traversing plasma regions of alternating width, until the accelerating phase vanishes eventually. Tracing the longitudinal electric field corresponding to the witness trapping position through the simulation further suggests that injected electrons may be initially accelerated to GeV energies, however, subsequently experience a decelerating wakefield over a substantial fraction of the remaining propagation distance.

The underlying dependence of the E-210 blowout dynamics on the plasma channel width has been discussed, for example, in [40, 399, 406] and is further illustrated in Figure 9.9 . Depicted is an idealised simulation scenario akin of the E-210 conditions, wherein a FACET-like driver interacts with a perfectly cylindrical plasma channel. Individual panels visualise the resulting plasma response associated with different

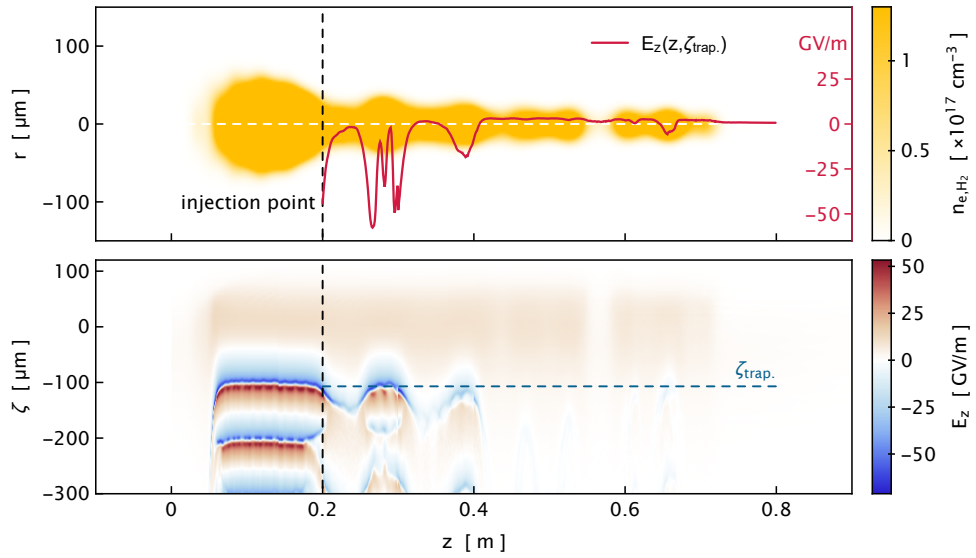

Figure 9.8: **Wakefield evolution along the E-210 plasma channel.** The longitudinal wakefield along the pre-ionised plasma channel is traced through a dedicated PIC simulation. The channel profile with varying width is again shown in the top panel, the bottom panel corresponds to the unloaded on-axis electric field. A co-moving coordinate of $\zeta = 0$ thereby corresponds to the driver centre. The vertical dashed line indicates the injection point in the E-210 experiment, the blue dashed line denotes the co-moving witness trapping position at $\zeta \approx -107\,\mu m$, inferred from injection simulations. Around the injection point, the channel diameter narrows below the nominal blowout width and the wake structure is altered. Downstream of the injection point, the wake repeatedly elongates and contracts according to the channel width. The electric field at the trapping position, indicated by the red solid line, therefore varies substantially throughout the channel. This suggests that witness beams experience an accelerating wakefield phase only over a fraction of the propagation distance, and may even be partially decelerated along the second half of the channel. The top panel of the figure is adapted from [40], the bottom panel is adapted from [399] under license CC BY 4.0.

channel radii. With an initial channel radius of 60 µm, the plasma is sufficiently wide to accommodate the blowout. A strong wake is formed over several plasma periods, with an on-axis electric field and trapping potential characteristic to the blowout regime. Once the channel narrows to 45 µm, approximately the same extent as the nominal blowout radius, the electron sheath partially extents beyond the region of isotropic ion density. This leads to a spread in effective plasma frequencies towards lower values. The associated sheath electron trajectories are thus altered and the first plasma

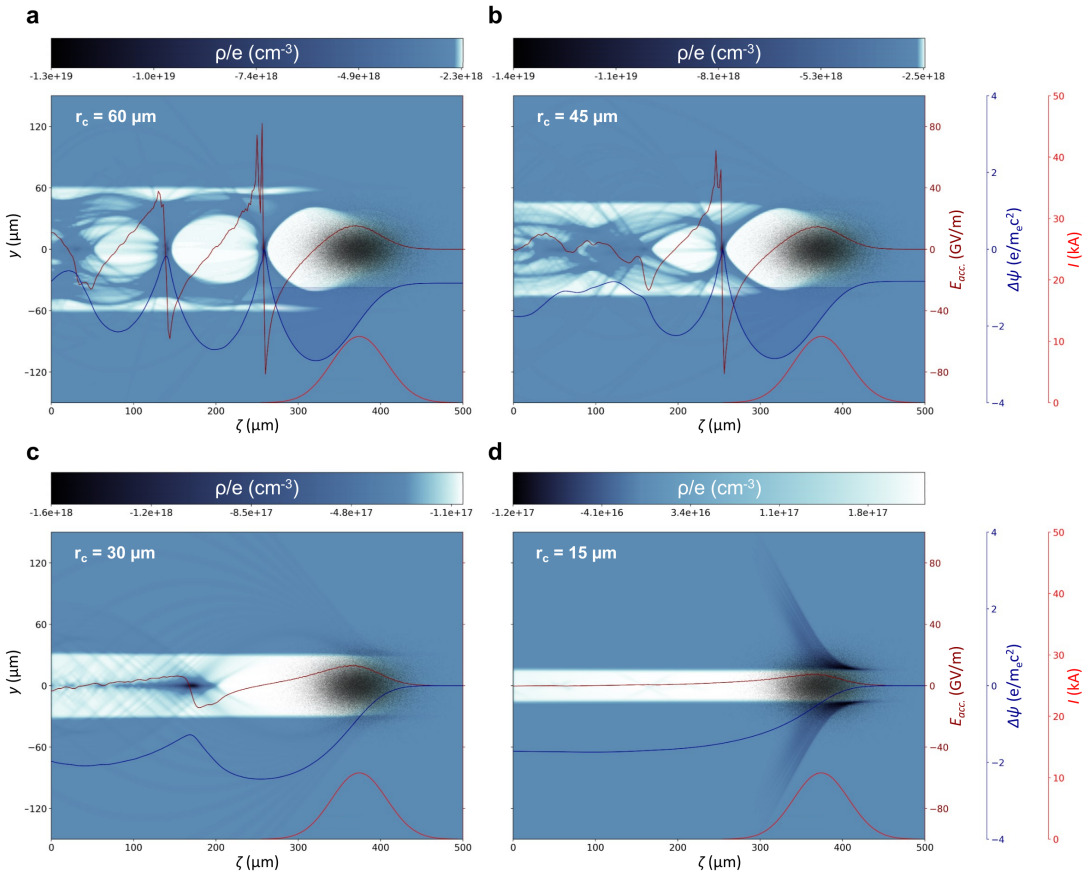

Figure 9.9: **Blowout dynamics in a confined plasma channel.** Idealised simulations of the E-210 conditions illustrate the plasma dynamics imposed by the driver (black) traversing a confined cylindrical pre-ionised plasma channel. (a) A characteristic blowout is generated for a sufficiently wide channel radius $r_c = 60\,\mu m$, with strong on-axis accelerating field (dark red line) and sufficiently deep trapping potential for injection (blue line). (b) A plasma channel of $r_c = 45\,\mu m$ leads to elongation of the first blowout cavity and deterioration of subsequent wake periods. (c) Narrowing the channel to $r_c = 30\,\mu m$ results in severe distortion of the wake structure, associated with further blowout lengthening and a substantially elongated wake vertex. Consequently, the accelerating field is largely diminished. (d) With $r_c = 15\,\mu m$, plasma electrons are ultimately expelled from the channel region entirely and a wakeless ion channel is generated behind the driver. Data generated by the author for [434]. Figure adapted from [399] under license CC BY 4.0.

cavity becomes effectively elongated[2]. While a similar accelerating field and trapping potential is maintained in this first cavity, the blowout is substantial deteriorated behind the first wake vertex. Such conditions are representative of the presumed blowout structure at the injection point in the experiment (as shown in Figure 9.6), and thus elucidate why no significant plasma photocathode injection is observed when the injector laser coincides with subsequent wake cavities (see Figure 9.7). Upon further reducing the channel radius to 30 µm , the blowout is severely distorted, resulting in increased cavity lengthening and substantial elongation of the wake vertex. The accelerating field is thus largely diminished and trapping conditions are no longer maintained. In addition, an increasing fraction of the plasma electrons does not return to the central axis within a time scale of $\sim 1/\omega_p$. The blowout structure ultimately collapses entirely when the plasma channel is further constricted. With a channel radius of 15 µm , practically all plasma electrons are rapidly expelled far beyond the focusing ion region. The electron beam therefore generates a pure ion channel with negligible wakefield at locations sufficiently behind the driver.

Certain aspects of the driver interaction with a confined plasma channel are interesting in their own right. For example, the intermediate regime characterised by an elongated wake vertex can provide beneficial conditions for positron acceleration [435, 436]. The generation of a purely electron-focusing ion channel in the wakeless regime is highly attractive for the realisation of an ion channel laser [437, 438][399, 405].

In the E-210 experiment, however, the profound impact of the plasma channel topology on the blowout structure is detrimental for emittance preservation and limits the attainable energy gain. Furthermore, the narrow plasma channel renders the injection and acceleration process highly susceptible to pointing deviations between the electron beam and the pre-ionisation laser. The spatial offset jitter of the pre-ionisation laser, determined at the injection point, amounts to ~20 µm rms, compared to a ~5 µm rms jitter of the driver and ~9 µm rms for the injector, respectively [40, 399]. The largest jitter contribution thus originates from the pre-ionisation laser pointing, exacerbating the adverse effects attributed to the radial constrictions of the plasma channel. It is therefore reasonable to argue that the plasma source setup represents the main technical limitation in the E-210 experiment, affecting the attainable witness beam quality and energy as well as injection stability. As a consequence, a large spread in witness charge is observed during the measurements presented in Figure 9.7 .

2 A slightly narrowing plasma channel hence has similar implications as a density down-ramp, albeit due to a fundamentally different process. Nevertheless, an injection method based on a rapid constriction of the plasma channel is conceivable.

Nevertheless, selected electron spectra obtained in the plasma photocathode regime, shown in Figure 9.10, showcase that witness beams in the range of $\sim 300 - 700\,\mathrm{MeV}$ are detected with an energy spread of $\sim 2\,\%$ and derived emittance on the order of $\sim 1.5\,\mu\mathrm{m\,rad}$.

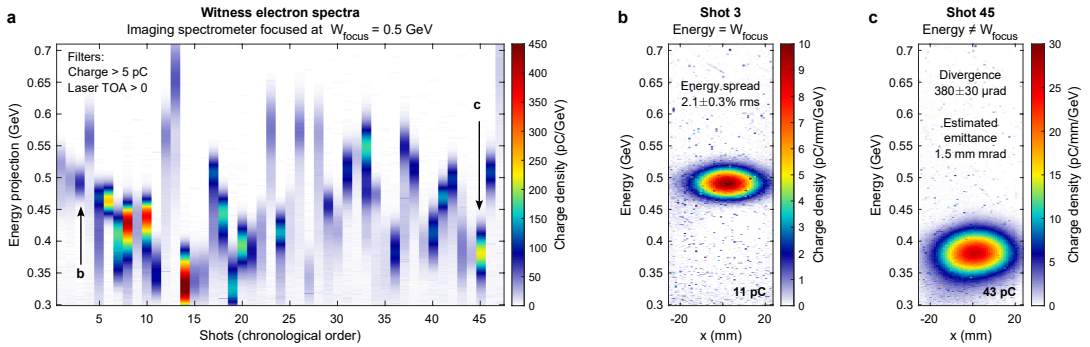

Figure 9.10: **E-210 plasma photocathode electron spectra.** (a) Witness beam energy projections, obtained from successive measurements in the pure plasma photocathode regime with injected charge $> 5\,\mathrm{pC}$ and TOA > 0. (b) Selected spectrum of a witness beam with central energy close to the spectrometer imaging energy of $500\,\mathrm{MeV}$, from which an rms energy spread of $2.1 \pm 0.3\,\%$ is determined. (c) Selected witness spectrum with central energy below the imaging energy, which enables to determine the horizontal divergence to $380 \pm 30\,\mu\mathrm{rad}$, corresponding to an estimated normalised emittance of $1.5\,\mu\mathrm{m\,rad}$. Figure adapted from [40].

On the one hand, such a result is encouraging as it serves to show that, even under suboptimal conditions, the plasma photocathode can be realised and is able to generate witness beams with substantially lower emittance than the original driver. This finding therefore substantiates the prospects of utilising plasma photocathodes as brightness transformers. On the other hand, the insights gained during the E-210 programme reveal ample potential for technical improvements of the setup and experimental concept. Major advancements are anticipated through its successor programme "E-310 Trojan Horse-II" and supporting ancillary experiments at FACET-II [439–441]. These include enhanced performance and stability of the electron beam and laser pulses, as well as optimised pre-ionisation laser optics for generating a substantially wider plasma channel. Such amendments would allow the plasma photocathode to be realised at lower plasma densities and correspondingly larger blowout dimensions. A sufficiently wide region of fully ionised LIT plasma would therefore not only effectively neutralise the influence of fluctuations attributed to the plasma source, but also substantially alleviate the impact of spatio-temporal jitters between the driver and injector laser [40, 399].

Such a scenario is particularly powerful when combined with a collinear injector geometry, as showcased in a dedicated simulation study investigating a potential E-310 plasma photocathode operated at a nominal plasma wavelength of 250 µm [403][399]. These simulations demonstrate prospects of generating witness beams with normalised emittance as low as $\sim 15\,\mathrm{nm\,rad}$ and corresponding 5D brightness up to $\sim 10^{19}\,\mathrm{A\,m^{-2}\,rad^{-2}}$, in conjunction with remarkable resilience against spatial jitters as encountered in the E-210 experiment as well as variations in the effective TOA and injector laser energy.

In a converse strategy, the plasma photocathode may also be explored at substantially higher plasma densities, albeit targeting a HIT medium with elevated ionisation energy. Considerably reducing the blowout dimensions would, in principle, greatly facilitate the provision of an adequate plasma source. The adverse impact of spatial alignment jitters between the driver and injector laser can, in turn, be mitigated when the blowout extent is similar to or smaller than the injector laser, since electrons are then invariably released over the entire wake. Nonetheless, witness beams with exceptionally high brightness may still be generated, as with sufficiently high plasma density the effective trapping region is also inherently confined to a tiny absolute volume. In this specific scenario, best results might, in fact, be obtained in perpendicular plasma photocathode geometry, because injection is then further temporally confined to the short time frame of spatial overlap between the injector laser and wakefield. Such miniaturised plasma photocathodes, however, require a unique new class of particularly compact, high peak-current drive beams. As shall be elaborated on in the remaining part of this thesis, such drivers can, indeed, be provided by current laser-driven wakefield accelerators.

HYBRID LWFA-PWFA STAGING

10

OVERVIEW

Today's landscape of plasma-based accelerators consists predominantly of LWFAs. This is a direct reflection of the prevalence of high-power laser facilities [442], largely enabled by the adaption of chirped pulse amplification (CPA) [443] to optical frequencies [34]. The significance of this development has since been recognised with a Nobel prize in physics for Donna Strickland and Gerard Morou in 2018 [444].

The majority of LWFAs today rely on CPA-based Ti:sapphire laser systems, capable of delivering pulses with a duration of a few tens of femtoseconds and peak power in the terawatt to petawatt range. Resting upon continuous development, LWFAs nowadays routinely deliver highly energetic electron beams in university-scale laboratories all over the world, with remarkable achievements such as generating multi-GeV electron beams [29, 30, 275, 445], advancements in output control and stability [172, 274, 348, 446] and demonstrations of LWFA-powered light sources based on betatron radiation [447–449], Compton scattering [450–456] and alternating magnetic structures [457–460], including first signatures of FEL lasing at infrared [461] and extreme ultraviolet [305] wavelengths. Nevertheless, the complexity of the laser-plasma interaction and the intrinsic sensitivity of the wakefield on the driver evolution, combined with continuous dephasing and driver depletion pose considerable challenges for achieving witness beam parameters compatible with the stringent quality requirements of X-ray FELs.

PWFAs operated in the blowout regime, in comparison, promise enhanced wakefield stability and phase-constant accelerating over extended distances (see chapter 5), thereby providing auspicious prospects for witness beam emittance preservation, energy spread control via persistent beam loading conditions, and, concomitantly, facilitate the generation of ultra-high brightness beams via advanced injection schemes such as the plasma photocathode or wakefield-induced ionisation injection. Yet, the necessity for adequate high peak-current PWFA drivers has hitherto restricted the exploration of such operating modes to a very limited number of dedicated large-scale conventional accelerator facilities.

This disparity of capacities is illustrated in Figure 10.1 , showing a non-exhaustive list of high-power laser facilities over the world together with sites of dedicated PWFA research and development (R&D) centres. Moreover, only the FACET facility could

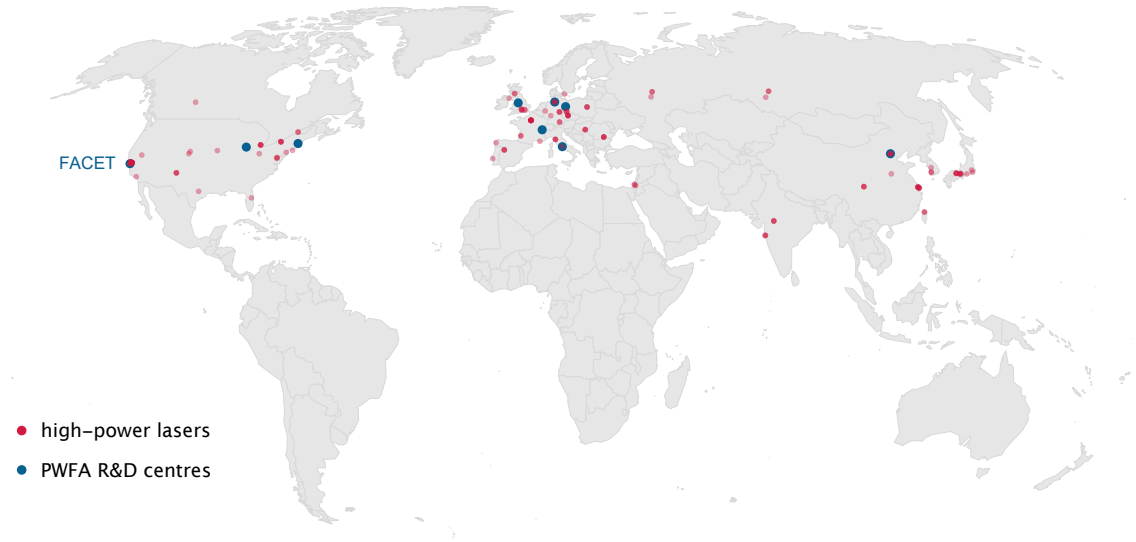

Figure 10.1: **Selection of high-power laser facilities and PWFA R&D centres over the world.** Red dots indicate laser systems with a peak power beyond 10 TW, known to the International Committee on Ultra-High Intensity Lasers (ICUIL) [462], blue dots correspond to dedicated PWFA R&D centres [463]. While not all of the shown laser facilities currently engage in LWFA studies, it serves to illustrate the discrepancy in elementary LWFA and PWFA research capacities. Even more so, only the FACET facility was thus far able to provide electron drive beams enabling the exploration of plasma photocathode injection in PWFAs.

thus far deliver electron drivers capable of establishing a blowout with sufficient trapping conditions to realise a plasma photocathode.

In the meantime, however, LWFAs have reached a technological maturity that offers a particularly attractive alternative source of potential PWFA drivers. Indeed, state-of-the-art LWFAs nowadays excel in delivering electron beams with femtosecond-scale duration [333] and tens of kiloampere peak currents [41, 277]. Since the accelerated electron population inside a laser-driven plasma wakefield accelerator naturally occupies only a fraction of the blowout volume, they already inherit the spatial dimensions required to themselves drive a subsequent plasma wave at similar, or even higher densities than the wakefield from which they originate. This provides a clear advantage over electron beams accelerated in conventional RF-based metallic cavities, which require additional sophisticated beam optics for transporting, focusing and compressing a high-current electron beam to bridge the vastly different spatial scales and field strengths between RF technology and plasma. Further, the quality requirements on LWFA-generated electron beams for driving a PWFA blowout are much more modest compared to direct light-source applications, and are well within currently

attainable LWFA parameters. In fact, a sizeable energy spread and emittance may even prove beneficial in increasing resilience against driver instabilities in PWFAs [464, 465]. Utilising high-current electron beams from existing LWFAs to drive a strong blowout in a subsequent PWFA stage is therefore not only conceptually feasible, but also promises to exploit and combine the advantages unique to each method while simultaneously addressing their individual challenges. The prospects of such hybrid LWFA-driven PWFA (LPWFA) systems are accordingly manifold.

Realising electron beam-driven wakefield accelerator concepts at widely accessible laser systems increases PWFA R&D capacities substantially, thereby offering a flexible infrastructure with considerably reduced spatial and economic footprint compared to their linac-driven siblings. LPWFA systems can thus provide a complementary research platform for fundamental PWFA studies, for example on driver and wakefield stability, emittance preservation and energy spread control, as well as driver-to-witness energy transfer efficiency and optimising in- and out-coupling of electron beams at the plasma-vacuum interface.

The intrinsic compactness of LWFA-generated beams further enables the exploration of strong-blowout operating modes at high plasma densities above $10^{18}\,\mathrm{cm}^{-3}$ with accelerating gradients beyond $100\,\mathrm{GV/m}$. This not only nurtures prospects of miniaturised PWFAs with GeV energy gains within centimetre-scale accelerating distances, but also facilitates the application of capable optical probing diagnostics [224] already established in LWFA systems operated at similar plasma densities [466–472][473]. Such auxiliary laser pulses with comparatively low power, when derived from the same laser system that drives the LWFA, are intrinsically synchronised to the designated PWFA driver and thus provide convenient means not only for probing, but also for pre-ionisation and injection with femtosecond precision.

A synergistic nexus of laser- and electron-driven plasma accelerator concepts may therefore crucially enhance the capabilities of both PWFAs and LWFAs alike. Augmenting existing LWFAs with a discrete PWFA stage has been conceptualised as a method for overcoming the intrinsic energy limitations of a single-stage LWFA [232], whereby a dual-bunch is generated in consecutive LWFA cavities to form a PWFA driver-witness pair with controlled spatial separation. The energy of the trailing bunch is then efficiently boosted to higher energies in a practically dephasing-free wake driven by the anterior bunch, much akin to the plasma-based "afterburner" concept formulated for RF linacs [17, 474, 475]. The perhaps most impactful prospect of hybrid LPWFAs, however, is to exploit selective ionisation injection methods specifically designed to produce witness beams with ultra-low transverse emittances approaching

the nanometre radian scale, paired with ultra-short, sub-femtosecond duration and multi-kiloampere peak currents. Theoretical studies emphasise the potential of plasma photocathodes and wakefield-induced ionisation injection for generating witness beams with several orders of magnitude superior brightness compared to the original LWFA output [38, 370, 398, 415][174, 371, 399]. The plasma photocathode thereby benefits especially from readily available auxiliary laser pulses inherently synchronised to the electron-driven wakefield. Moreover, the resulting final witness beams may exceed the initial energy of the LWFA-generated electron beams if the appended PWFA stage is driven close to driver depletion while maintaining a transformer ratio of $R_T > 1$.

A subsequent PWFA stage augmenting existing LWFA setups may therefore effectively act as brightness and energy transformer, with the potential of decisively enhancing the currently attainable output from laser-driven wakefield accelerators without compromising their comparatively modest infrastructure and resource demands. Such a hybrid staging concept therefore raises new perspectives on realising truly compact, purely plasma-based electron sources with unprecedentedly low emittance and high brightness at university-scale laboratories and, consequently, their applications.

These prospects strongly motivate dedicated research and development of LPWFA concepts, and the ability of state-of-the-art LWFA systems to generate the required high peak-current beams render such explorations topical. Experimental implementations of hybrid staging schemes are, however, currently in its infancy. Nevertheless, several strategic milestones can already be formulated and are summarised in chapter 11. A first experimental demonstration of electron acceleration in a discrete PWFA stage driven by LWFA-generated electron beams is presented in chapter 12.

11

STRATEGIC MILESTONES

The conceptualisation of hybrid plasma wakefield accelerators has gained significant momentum over the past years. This is reflected by the formation of a dedicated "Hybrid Collaboration" amongst research teams from the UK, France and Germany to coordinate and consolidate their efforts towards experimental realisations of the LPWFA concept. The author has been a core contributor to this collaboration from its inception. Recent developments and prospects of LWFA-driven PWFAs have been extensively discussed in various publications [38, 370, 398][181, 371, 399, 476, 477], from which several strategic milestones can be identified. The following summarises established and future development phases in a rough classification of hybrid LPWFA generations, characterised by key achievements.

0^{th} generation – LWFA-PWFA self-mode transition

Whenever a significant amount of charge is accelerated in a laser-driven plasma wave, the witness will alter the wake structure due to beam loading (see chapter 4.3). The resulting effective wake is thus governed by both the laser driver and the accelerated witness[1]. Upon diffraction and depletion of the driving laser pulse, however, its contribution to the wakefield eventually ceases and a gradual transition to a wake dominated by the previously accelerated electron beam occurs. Such natural transition from beam-loaded to beam-dominated, and ultimately beam-driven regime has initially been studied in simulations [478, 479], followed by first experimental observations indicating such self-mode transitions [167, 480, 481]. A more recent study combines extensive experimental and simulation studies to provide a comprehensive overview and characterisations of such mixed-mode regimes [482]. A transition from laser- to beam-driven wakefields has also been interpreted as the main mechanism in LWFA experiments observing enhanced energy gain of a secondary witness beam in a plasma section elongated beyond the nominal dephasing and depletion limits [483, 484]. In these experiments, an additional energy transfer between the two electron

1 In the linear regime, the effective wake is simply a superposition of laser- and beam driven components (see equation 3.29).

distributions via a beam-driven wake component was identified to assist in attaining the final energies.

While natural self-mode transitions over extended propagation lengths may thus initiate a subsequent PWFA process enabling the acceleration of a secondary electron beam, the implied substantial wakefield alteration is challenging to control [481] and detrimental for beam quality preservation. Moroever, simulations show that the emittance of such secondary witness beams may be substantially deteriorated by the laser remnant as it continues to dephase and slip backwards in the henceforth beam-dominated wake [478]. While it is conceivable to evoke injection of a dedicated PWFA witness beam only after full conversion into a stabilised, purely beam-driven wakefield, reaching such operating mode may be well beyond the depletion length of the PWFA driver, depending on its initial energy obtained during the LWFA process. A clear termination of the LWFA and subsequent controlled conversion into a distinct, pure PWFA mode is therefore vital for enabling the envisaged functionalities of the LPWFA platform.

1st generation – distinct staging and acceleration

Important steps towards a first LPWFA prototype were achieved in several incremental experiments employing individually controlled plasma targets [485, 486][56][57]. The first target provides, and limits, the laser-driven accelerator section, whereas the LWFA-generated electron beams interact with the subsequent plasma stage. A potential laser-driven wakefield in the second target is thereby effectively inhibited by introducing sufficient spatial separation or a laser blocker between the two stages. The progression of these preliminary experiments is characterised by incrementally increasing the charge of the LWFA output, hence enhancing the beam current and interaction strength in the second stage [477].

Among the first observed effects in such two-stage setups was a reduction in divergence of a comparatively low-charge $\lesssim 5\,\mathrm{pC}$ electron beam [485, 486] in an overdense passive plasma lens [487–493]. Upon increasing the LWFA output charge to several tens of picocoulomb, first signatures of longitudinal electron beam-driven wakefields excited in the second plasma stage have been obtained through measuring a collective reduction of the original electron energy [56]. The corresponding decelerating gradients in the second stage were thereby estimated to be on the order of $\sim 10\,\mathrm{GV/m}$. In a further iteration, the LWFA output charge was increased beyond several hundred picocoulomb. This lead to a series of experiments in which electron-driven plasma

waves were directly visualised, characterised and distinguished from laser-driven plasma waves via few-cycle shadowgraphy [233][57]. These remarkable results not only demonstrate the capabilities of LWFAs to generate electron beams capable of driving plasma wakefields at unprecedentedly high plasma densities up to $\sim 10 \times 10^{19}\,\mathrm{cm}^{-3}$, but also showcase that synchronised auxiliary laser pulses can be derived and re-deployed in such hybrid staging setups. They further substantiate the applicability of optical probing tools in high-density LPWFA scenarios and emphasise how hybrid staging concepts can provide valuable insights on fundamental PWFA processes.

The decisive milestone towards establishing compact LWFA-driven PWFAs as an accelerator platform, however, is demonstrating witness beam energy gain in a purely electron-driven plasma wakefield. This break-through was achieved in two complementary experiments, jointly reported in [45]. One of these seminal implementations is presented and discussed in chapter 12. Such a proof-of-principle realisation can be regarded as the first generation of hybrid LPWFAs and leads to the conception of future near-term and long-term developments.

2nd generation – controlled injection, performance optimisations and enhanced witness beams

Establishing a functional prototype of the hybrid LPWFA platform provides the basis for systematic explorations of a broad range of operating modes at numerous LWFA facilities. This encompasses further optimisations of the LWFA performance specifically for generating electron drivers with tunable parameters for various PWFA scenarios, including the generation of driver-witness bunch pairs [232, 233]. A variety of controlled, tunable internal injection schemes may further be realised in the PWFA stage, for example via hydrodynamic [494] and laser-generated [495] density down-ramps. Moreover, the unique operating conditions accessible through high peak-current drivers facilitate the exploration of advanced injection schemes that are currently challenging to realise in linac-driven PWFA scenarios, specifically plasma photocathodes and wakefield-induced ionisation injection.

Fundamental PWFA studies conducted in miniaturised hybrid setups can further complement and assist linac-driven PWFA research and development beyond investigating injection schemes, for example on driver and wakefield stability, driver depletion, charge capture and energy transfer efficiency, as well as witness emittance preservation and energy spread compensation. Such studies benefit from the enhanced flexibility and versatility offered by hybrid configurations, in conjunction with powerful optical probing tools for characterising and monitoring the wake formation [496].

A second generation of hybrid LPWFA systems may thus be characterised by successful implementations of various injection concepts and complementary optimisations of both LWFA and PWFA stages, with the ultimate aim of demonstrating PWFA witness beams with parameters largely superior to the original LWFA output. This may manifest in form of reduced divergence and energy spread, enhanced final energy or combinations thereof.

3rd generation – pathways towards application readiness

A third generation of hybrid LPWFAs may aim for extending their capabilities beyond fundamental PWFA testing environments towards reliable, compact sources of ultra-high brightness beams. To reach this level of maturity, further anticipated studies may address general challenges arising from controlled in- and out-coupling of laser- and electron beams, inter-stage beam transport and matching, as well as emittance-preserving witness extraction from the plasma and subsequent separation from the driver. These challenges are not unique to hybrid LPWFAs, but indeed shared to a large extent with linac-driven PWFAs and LWFAs in general, and in particular with external injection schemes in LWFAs as well as any staging concept of plasma-based accelerators [151]. The advancement of hybrid staging concepts may thus synergistically contribute to the development and testing of purposefully tailored plasma targets, novel plasma-based and conventional beam optics as well as sophisticated diagnostics.

Naturally, LWFA-driven PWFAs also directly benefit from recent developments towards improved LWFA reliability and reproducibility [172, 348, 446]. However, hybrid staging offers a unique approach to not only enhance the final witness beam quality, but also to improve output stability [495], specifically exploiting the intrinsic insensitivity of an electron-driven blowout against variations in the initial driver energy and energy spread. These prospects for a conceptual resilience against LWFA output fluctuations are especially impactful and further extended when combined with decoupled injection offered by the plasma photocathode [399, 497].

Third-generation hybrid LPWFAs may thus ultimately operate simultaneously as brightness, energy and stability transformers of currently existing and future LWFA systems. This development could eventually lead to a new class of application-ready, truly compact and widely accessible sources of highly energetic, ultra-short and ultra-bright electron beams.

4^{th} generation – scalability

While hybrid staging promises to enhance the output brightness of currently existing LWFA systems by several orders of magnitude, in conjunction with the potential for increased final energy and improved stability, the maximum attainable witness energy is, however, ultimately tied to the power of the parent laser system. The final witness beam energy gained in the PWFA stage depends on the realised transformer ratio and the initial energy of the LWFA-generated driver. The latter, in turn, is proportional to the laser pulse power (recall equation 5.13). Consequently, the attainable energy gain in hybrid LPWFAs ultimately depends on the available laser power. High-brightness witness beams from hybrid staging can nonetheless be scaled to several GeV upon approaching petawatt laser powers [371].

Similarly, the average current delivered by hybrid LPWFAs is limited by the repetition rate of the LWFA laser. Current high-power laser systems operate at repetition rates on the order of ~1 Hz, substantially below state-of-the-art conventional linacs which typically operate at a fundamental repetition rate of ~100 Hz and can deliver micro-bunch bursts up to MHz [498]. However, plasmas can, in principle, sustain both laser- and electron-driven wakefields at repetition rates in the kHz to MHz range [499–501].

Future capabilities and capacities of hybrid LPWFA systems hence naturally scale with further advancements in laser technology and an increasing proliferation of high-power laser systems. This is a fortunate correlation, encouraged by a steady trend towards an ever increasing number of such laser systems, alongside continuous development towards higher peak power and repetition rates [442]. Enabled by hybrid LPWFAs, high-brightness electron sources delivering multi-GeV energies may thus become ubiquitous in the near future. Simultaneously reaching repetition rates beyond a kilohertz may, however, still be a long-term goal in comparison. Alternatively, higher LPWFA driver energies may also be achieved through LWFA staging concepts [54, 55], utilising several ~100 TW laser drivers with potentially higher repetition rates. Such staged LWFA concepts may be particularly attractive for generating drivers for a final PWFA stage, as a potential quality degradation between the LWFA stages can be tolerated as long as high charge throughput is maintained. Future laser-wakefield accelerator concepts may hence be designed and optimised explicitly with hybrid staging taken into consideration.

12

REALISATION OF A FIRST-GENERATION HYBRID PLASMA WAKEFIELD ACCELERATOR

Corresponding publication [45]:

T. Kurz, T. Heinemann, M. F. Gilljohann, Y. Y. Chang, J. P. Couperus Cabadağ, A. Debus, O. Kononenko, R. Pausch, S. Schöbel, R. W. Assmann, M. Bussmann, H. Ding, J. Götzfried, A. Köhler, G. Raj, S. Schindler, K. Steiniger, O. Zarini, S. Corde, A. Döpp, B. Hidding, S. Karsch, U. Schramm, A. Martinez de la Ossa and A. Irman. 'Demonstration of a compact plasma accelerator powered by laser-accelerated electron beams'. In: *Nature Communications* 12.1 (May 2021). DOI: 10.1038/s41467-021-23000-7. T. Kurz and T. Heinemann contributed equally to this work

Demonstrating electron acceleration in a discrete PWFA driven by LWFA-generated electron beams constitutes a decisive milestone towards establishing the hybrid LPWFA concept as a platform for research and applications. This was achieved in a joint effort within the Hybrid Collaboration network, with two complementary experimental campaigns conducted at the DRACO laser facility at the Helmholtz-Zentrum Dresden–Rossendorf (HZDR) and the ATLAS laser at the Ludwig-Maximilians-Universität München (LMU). The results of both experiments are reported in [45]. The author has been a primary contributor to the HZDR project throughout its entire duration, from its conception to designing, realising and analysing the experiment. Many aspects of this work were conducted together with Thomas Kurz in the context of a joint Ph.D. project [44].

The conceptual design of the hybrid plasma wakefield accelerator at the DRACO laser facility largely builds upon previously established LWFA capabilities. Preceding experiments explored and optimised an LWFA scheme utilising self-truncated ionisation injection (see chapter 6.3.1), thereby demonstrating reliable generation of high peak-current electron beams with $\gtrsim 10\,\mathrm{kA}$ at central energies of $200 - 300\,\mathrm{MeV}$ and moderate energy spreads of $\sim 15\,\%$ [41–43, 502, 503]. Such LWFA performance provides an excellent foundation for exploring the LPWFA concept. The following introduces the essential components of the hybrid accelerator setup and summarises the main results from this experimental campaign.

12.1 EXPERIMENTAL CONCEPT

A schematic sketch of the hybrid plasma accelerator design is shown in Figure 12.1. To realise hybrid LWFA-PWFA staging with a distinctly separated PWFA section, two consecutive, millimetre-sized and independently controlled gas jet targets [504] are employed. A laser blocker foil positioned at the entrance of the second gas jet reflects the spent LWFA driver, ensuring a pure PWFA process in the subsequent section.

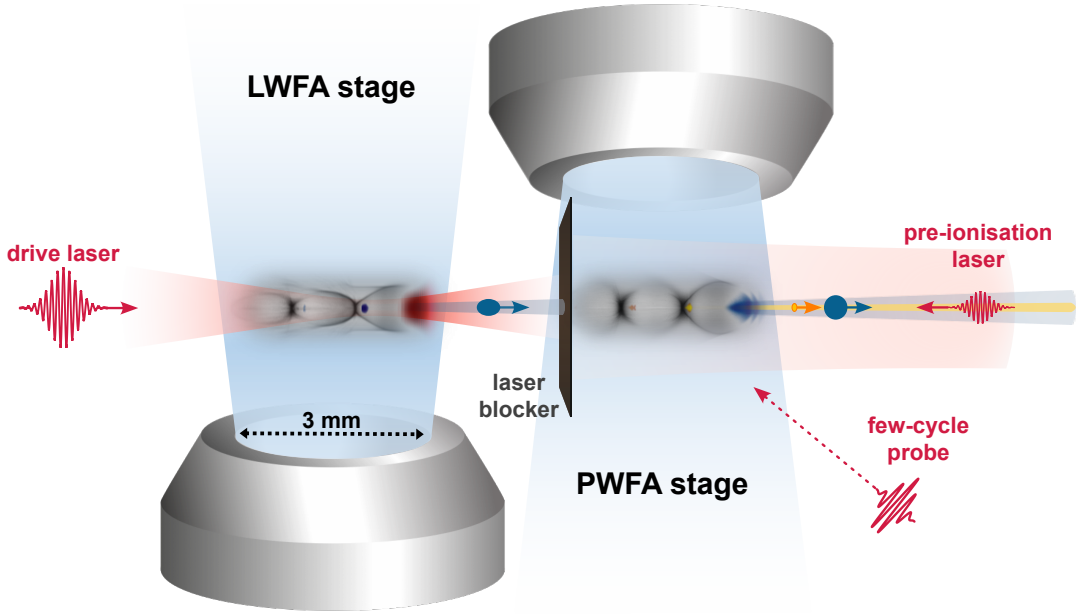

Figure 12.1: **Conceptual design of the hybrid plasma accelerator experiment.** Two consecutive gas jet targets are utilised as discrete LWFA and PWFA stage, respectively. A high-intensity laser pulse (red) drives a plasma wave (greyscale) in the first stage, generating a high peak-current electron beam (blue). After exiting the LWFA stage, the spent LWFA driver is reflected by a blocker foil. The LWFA-generated electron beam passes through the foil and drives a plasma wave in the remaining section of the second gas jet, wherein a witness beam (yellow) is accelerated. An additional counter-propagating laser pulse can be employed for optionally pre-ionising the designated PWFA section downstream of the laser blocker foil. A transverse few-cycle probe pulse enables visualisation of the beam-driven plasma wave. The insets illustrating the laser- and beam-driven plasma waves are obtained from simulations using the PIC code OSIRIS [505], originally conducted and visualised by A. Martinez de la Ossa. Figure adapted from [45] under license CC BY 4.0. Proportions of individual components are sketched not-to-scale.

The LWFA-generated electron beams in this experiment are sufficiently intense to autonomously generate a plasma downstream of the laser blocker via their electric

space-charge field. Nevertheless, a dedicated pre-ionisation laser can optionally be deployed to pre-ionise the designated PWFA section. The compact size of the PWFA stage thereby largely alleviates the requirements on the pre-ionisation setup compared to the E-210 experiment discussed in chapter 9. The hybrid LPWFA experiment can thus be operated in two distinct modes. Characterising and comparing the interaction of the LWFA-generated driver with the self-ionised and pre-ionised PWFA section, in conjunction with the emerging beam-driven plasma waves and resulting witness acceleration, constitutes the main capability of this experiment.

Two centrepiece diagnostics are utilised for this purpose. An electron spectrometer provides essential information about the kinetic energy spectrum, angular divergence and charge of the generated electron beams. Additionally, a few-cycle laser probe is utilised to visualise the electron-driven plasma waves. Further aspects of the main experimental components are detailed below.

12.1.1 *DRACO laser system*

The LWFA driver and the auxiliary pulses are derived from the ~150 TW arm of the DRACO laser system [506]. The DRACO laser is based on a Ti:sapphire double-CPA system, delivering pulses at a central wavelength of 800 nm with a pulse duration of $\tau_{FWHM} \approx 30$ fs after compression. Their spectral shape is characterised via direct electric field reconstruction (SPIDER, A.P.E) in conjunction with a self-referenced spectral interferometer (WIZZLER, Fastlite), dispersion corrections are applied via an acousto-optical dispersive filter (DAZZLER, Fastlite). Several online near- and far field diagnostics are employed along the laser beam line for monitoring the laser stability during operation.

Prior to focusing the laser on target, a small energy fraction of ≈21 mJ is extracted via a 1/2-inch mirror from the central area of the main pulse for powering the counter-propagating pre-ionisation laser and providing a seed for the few-cycle probe. The remaining laser pulse provides the LWFA driver, focused by an f/20 off-axis parabola to a measured FWHM vacuum spot size of 19.5 µm. The vacuum focus is optimised by applying a wavefront correction, utilising a wavefront sensor (SID-4, Phasics) in a closed loop with a deformable mirror. A pulse energy of ≈1.7 J is delivered on target, resulting in an estimated peak intensity of $I_0 \approx 1.0 \times 10^{19}$ W/cm^{-2} and normalised vector potential of $a_0 \approx 2.1$. A dedicated "exit-mode diagnostics", situated at the end of the laser path after traversing the target and electron spectrometer, can be used to characterise the laser profile after its interaction with the LWFA stage.

12.1.2 *Gas targets*

The dedicated LWFA and PWFA stages are formed by two individually controlled super-sonic gas jets of identical design. These two gas jets consist of round de-Laval nozzles with an opening diameter of 3 mm and Mach number of 10.4 , connected to a commercial pulsed valve (Series 9, Parker). Their respective gas density profiles were characterised before the experiment in a dedicated interferometric setup [507]. Reconstructed density profiles along the driver propagation axis are shown in Figure 12.2 , evaluated at a backing pressure of 15 bar . Both gas jets generate a central flat-top region of ≈1.6 mm width with adjacent density ramps of ≈0.6 mm .

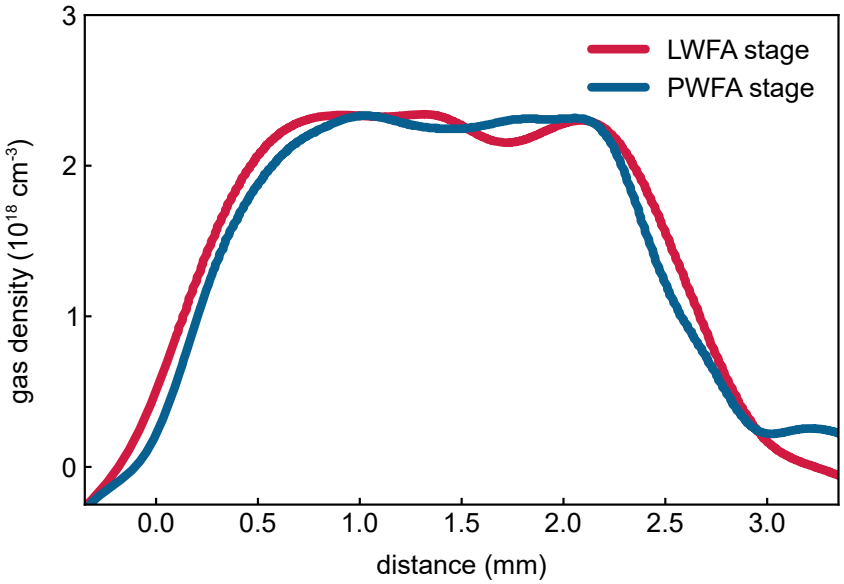

Figure 12.2: **Gas jet density profiles.** Density profiles along the driver propagation axis for both the designated LWFA and PWFA stage, obtained at a backing pressure of 15 bar . Data provided by T. Kurz.

The gas targets are installed together on a 3D translation stage to enable precise alignment to the laser axis. The distance between the two gas jets can be further adjusted remotely to arbitrary close positions. To minimise turbulences between their respective gas flows, they are mounted in a 90° geometry with respect to each other. The default configuration in this experiment was chosen such that the two gas profiles are directly adjoint with no vacuum gap between their respective density ramps. This operating mode of minimum separation between the stages aims to maintain a small transverse size of the diverging electron driver upon entering the PWFA section.

12.1.3 *Laser blocker*

A minimum distance between the two gas targets implies that the remnant of the LWFA laser needs to be extracted before the PWFA section to subsequently ensure a purely electron beam-driven process. For this purpose, a 12.5 µm thin steel foil is implemented into the experimental setup. It can be remotely positioned onto the laser axis with its lower edge slightly above the nozzles, such that its longitudinal location relative to the two gas jets can be freely adjusted. The material of the foil was predominantly chosen for its sturdiness under the influence of the co-located gas flows.

The steel foil effectively blocks the main laser. After its interaction with the first stage, the spent LWFA laser is still sufficiently intense to ionise the foil material, thereby generating an overdense plasma mirror (see chapter 1.3). While the LWFA-generated electron beam is able to pass through the ionised foil, the remaining LWFA driver is thus reflected and cannot penetrate the subsequent PWFA section. This can be empirically confirmed for each shot by the absence of a signal on the "exit mode diagnostic". Damaging back-reflections along the laser beam line are thereby obviated by introducing a shallow angle to the laser blocker foil. During the laser-foil interaction, however, the incident area of the laser on the foil is destroyed and needs to be refreshed prior to a subsequent measurement. This is realised by utilising a disk-shaped foil installed on a rotational mount, which is advanced by a few degrees after each shot. Figure 12.3 shows a close-up photograph of the final target configuration including the laser blocker foil.

Although the laser blocker efficiently separates the laser driver from the LWFA-generated electron beam, the latter is, amongst other processes, affected by the complex magnetic field fluctuations emerging from current filamentation instabilities under the highly intense laser-foil interaction [508]. These significantly deteriorate the divergence of the designated PWFA driver during its passage through the ionised foil. It is therefore sensible to position the laser blocker foil directly in front of the anticipated PWFA section, that is, inside the density plateau region of the second gas jet. On the one hand, extending the distance to the LWFA exit reduces the laser intensity on the foil and thereby the severity of the electron beam divergence growth [508]. On the other hand, the absence of a vacuum drift after the laser blocker mitigates subsequent beam expansion, as the transverse beam dynamics is thereafter largely dominated by its self-generated focusing wakefield. Further, electron beam transport between the LWFA and PWFA section may be assisted by a focusing effect due to a laser-driven

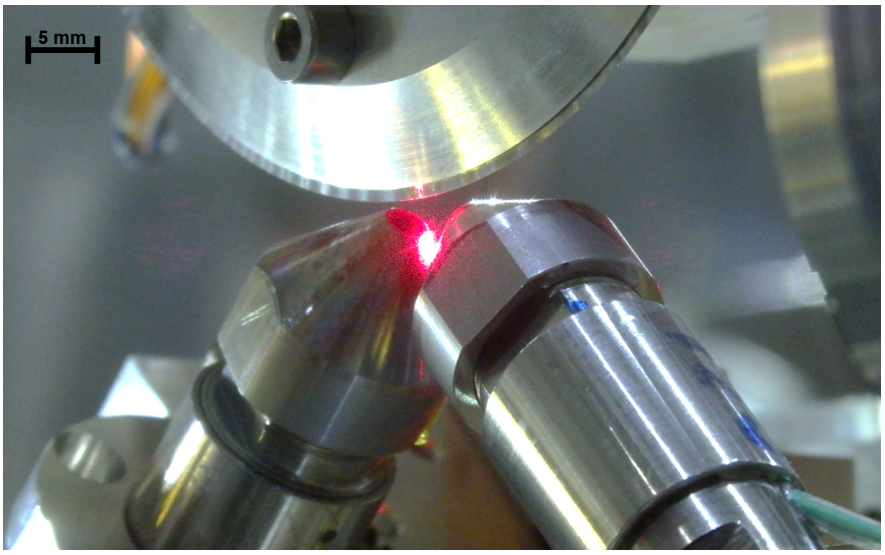

Figure 12.3: **Experimental target configuration.** A photograph of the final target geometry, showing the two gas nozzles and the laser blocker.

plasma lens [509] along the up-ramp section of the second gas jet still exposed to the remnant of the LWFA driver. A side-effect of such configuration is that the presence of the laser blocker perturbs the gas flow of the second jet and introduces substantial shock-fronts around the foil.

12.1.4 *Pre-ionisation laser*

The designated PWFA section downstream of the laser blocker can be optionally ionised prior to the arrival of the electron driver. For this purpose, the majority of the extracted auxiliary laser, about 20 mJ, is transported in a vacuum bypass beam line around the target setup and the electron spectrometer, where it is ultimately focused back on target by curved mirror with 1 m focal length. This curved mirror is positioned slightly below the main laser axis. The pre-ionisation laser thus illuminates the second target from the downstream direction at a shallow angle. With a FWHM focal diameter of about 120 µm, its peak intensity is estimated to $\sim 4 \times 10^{15}\,\mathrm{W/cm^2}$. As illustrated in Figure 12.4, such intensity is suitable to generate a $\gtrsim 160\,\mu\mathrm{m}$ wide plasma channel of ionised hydrogen and the first ionisation level of helium over several centimetres. Its intensity is, however, sufficiently low to not compromise the integrity of the laser blocker foil prior to the main laser arrival. Additional delay sections along the main

laser path are introduced such that the pre-ioniser incides about 1 ps earlier on target than the LWFA laser.

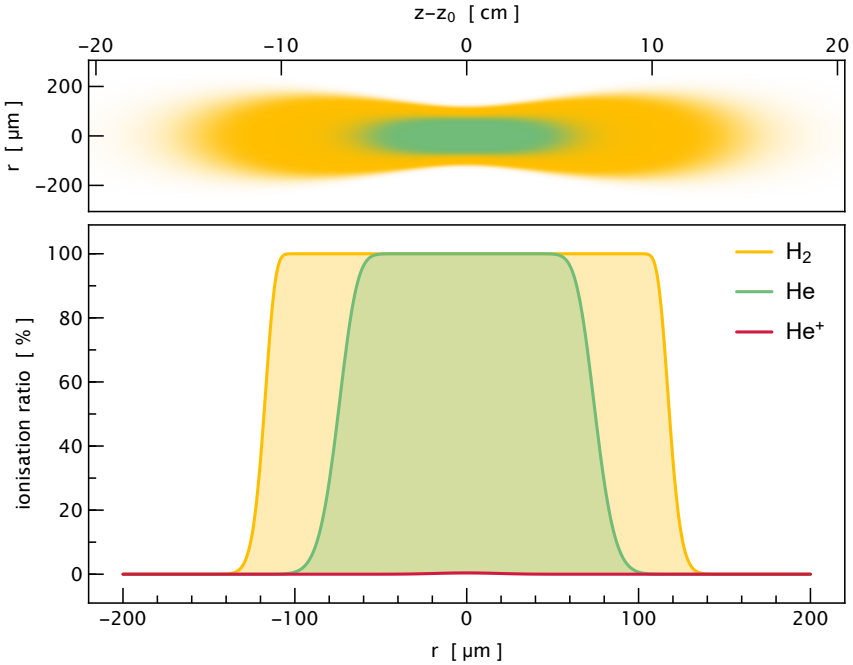

Figure 12.4: **PWFA pre-ionisation.** The top panel shows the calculated plasma channel profile (see chapter 2.2) generated by the pre-ionisation laser with pulse energy of 20 mJ, FWHM pulse duration of 30 fs and FWHM diameter of 120 µm for hydrogen and helium as target gas species. The bottom panel illustrates the corresponding ionisation ratios at its nominal focus position z_0 along the radial dimension. The pre-ionisation laser is thus capable of generating a $\gtrsim$160 µm wide plasma channel over several centimetres.

12.1.5 *Electron spectrometer*

The main diagnostic for online-characterisation of the generated electron beams is a magnetic spectrometer designed by Jurjen P. Couperus Cabadağ, which has been successfully utilised in previous LWFA experiments [42, 506]. Its dispersive section consists of a 0.4 m long permanent dipole magnet with a pole gap of 40 mm and a field strength of 0.9 T. Two scintillating screens (Konica Minolta OG 400) are placed above the magnets in an optimised geometry that enables near point-to-point imaging of divergent electron beams up to 200 MeV. Higher energies up to 550 MeV are projected onto a third screen, with an estimated read-out uncertainty of -1.2 $(+1.6)$ % at 300 MeV

and $-2.5\,(+3.1)\,\%$ at 400 MeV for a 6 mrad pointing error in the dispersive plane [42, 506]. The light emission from the detection screens are imaged onto 12-bit cameras and post-processed to combine and linearise the recorded spectra.

The spectrometer thus provides information about the electron energy distribution, as well as the angular projection of the electron beam perpendicular to the dispersion plane. To further retrieve absolute charge information from the spectrometer images, the charge response of the scintillating screens was calibrated against the Electron Linac for beams with high Brilliance and low Emittance (ELBE) in a dedicated campaign [44, 510]. The results from this measured absolute charge response was subsequently cross-calibrated against a set of secondary light sources in the from of gaseous tritium capsules, which were then installed strategically along the scintillating screens of the spectrometer. With both spectral and charge information obtained from the electron spectrometer, the compound quantity of spectral charge density $S = Q/(\Delta W/\overline{W})$ can be defined as empirical measure for comparing individual electron beams.

12.1.6 *Few-cycle shadowgraphy*

A key capability of this experiment is to directly visualise electron beam-driven plasma wave structures via shadowgraphy. To resolve the short time scale of the plasma density modulations, a few-cycle probe-laser beam line was developed, characterised and integrated into the experimental setup as a Master's project by Susanne Schöbel [511]. The probe setup consists of a hollow-core fibre of 1 m length filled with 2.0 bar of neon gas, utilising the remaining 1 mJ fraction of the auxiliary laser beam line as a seed. After spectral broadening in the fibre [512], the probe is collimated to a beam diameter of 7 mm and further compressed to $\approx$9.2 fs by a set of chirped mirrors. The probe is then directed onto the PWFA stage, transversely illuminating the electron beam-driven plasma wave structures. The resulting shadowgrams are imaged via a microscope objective and recorded with a 14-bit camera.

12.2 LWFA PERFORMANCE

The LWFA stage is operated in a configuration similar to previous, pure LWFA experiments [41, 43], utilising an optimised regime of self-truncated ionisation injection to generate the designated PWFA electron drivers. The LWFA gas target is hereby supplied with a pre-mixed composition of 97 % helium doped with 3 % nitrogen, providing the LIT and HIT media, respectively. The LWFA output is then optimised and characterised while the second gas jet remains disabled. The backing pressure of the LWFA gas target, as well as the spectral phase and vacuum focus position of the laser driver are thereby adjusted to yield a maximum amount of charge in a narrow energy bandwidth measured on the spectrometer. As a result of this optimisation routine, the LWFA gas jet is ultimately operated at a backing pressure of $14 - 16\,\mathrm{bar}$, corresponding to a plateau plasma density of $4.0 - 4.5 \times 10^{18}\,\mathrm{cm}^{-3}$.

A significant difference to previous LWFA experiments is the deployment of the laser blocker foil. In the final hybrid configuration, the foil is located 800 µm downstream of the LWFA exit. Example electron spectra of the LWFA output with and without the laser blocker foil in place are displayed in Figure 12.5 and essential performance parameters summarised in Table 12.1.

	LWFA w/o foil	LWFA w/ foil
$\overline{W}$ [MeV]	263 ± 5	260 ± 9
ΔW [MeV]	27 ± 2	24 ± 4
Q [pC]	103 ± 6	104 ± 12
θ [mrad]	4.2 ± 0.2	6.2 ± 0.4

Table 12.1: **LWFA-beam parameters.** Average parameters of the LWFA-generated electron beams, evaluated within the FWHM energy bandwidth around the high-energy peaks recorded on the spectrometer. Inserting the laser blocker foil does not significantly alter the average energy $\overline{W}$, absolute energy bandwidth ΔW and charge Q, but results in a ≈ 50 % higher divergence θ.

In both configurations, the LWFA electron spectra exhibit distinct peaks in charge density in the range of $200 - 300\,\mathrm{MeV}$, with a FWHM bandwidth of $\sim 10\%$. The integrated charge within this bandwidth amounts to about 100 pC on average. A substantial amount of charge is also detected at lower energies, attributed to additional injection on the density down-ramp transition at the exit of the LWFA gas jet. This observation is consistent with previous measurements [41, 43].

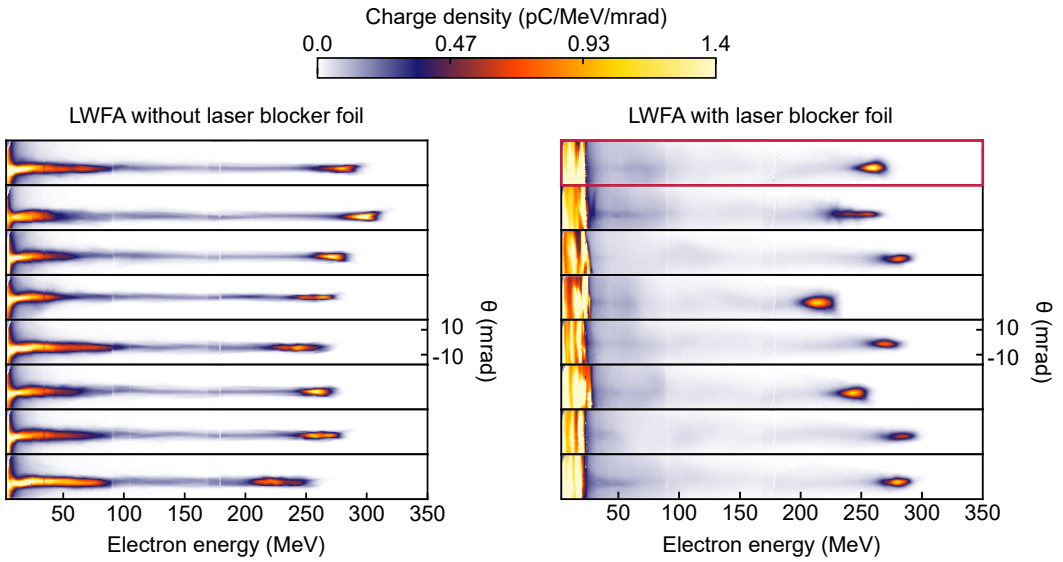

Figure 12.5: **LWFA reference spectra.** Consecutive electron spectra recorded for pure LWFA operation, without the laser blocker foil (left column) and with the foil at its final position (right column). The latter thus provides a reference dataset for characterising the LWFA output before its interaction with the second stage. The spectrum highlighted by the red rectangle is also shown in Figure 12.7. Figure adapted from [45] under license CC BY 4.0.

Introducing the foil does not significantly alter the spectral shape of the high-energy fraction of the LWFA output, however, leads to an increase of $\approx 50\,\%$ in divergence (see Table 12.1). Directly comparing the spectra in Figure 12.5 further reveals that the low-energy fraction of the LWFA spectrum is much more severely affected by the laser blocker foil, leading to a substantial dilution of the angular charge distribution and a visual cut-off of the low-energy background at $\approx 30\,\mathrm{MeV}$. The recorded shots with the laser blocker foil in place serve as a reference dataset for characterising the PWFA driver before its interaction with the second stage.

12.3 PWFA CHARACTERISATION

Once optimisation and characterisation of the LWFA stage is completed, the second gas jet is enabled. For the results presented in the following, the second gas target is supplied with a mixture of 90 % hydrogen and 10 % helium. The backing pressure applied corresponds to a plasma density of $3.5 - 4.2 \times 10^{18}\,\mathrm{cm}^{-3}$, assuming full ionisation of hydrogen and the first level of helium. The location of the laser blocker foil then corresponds to $\sim 100\,\mu\mathrm{m}$ inside the nominal plateau region of the second gas jet. The interaction of the LWFA-generated electron beam with the second stage is then characterised by repeatedly switching between self-ionised and pre-ionised operating modes.

12.3.1 *Drive beam degradation*

In total, a series of 25 shots is recorded without pre-ionisation, complemented by a set of 43 measurements with the pre-ionisation laser engaged. A strong interaction of the LWFA-generated electron beam with the PWFA section is observed in both configurations. This is evidenced by the recorded electron spectra, characterised by spectral broadening and a substantial reduction of the charge density within the FWHM bandwidth of the spectral peak. The electron spectra obtained from both datasets are shown in Figure A3, statistical averages of the electron driver before and after its passage through the second stage are summarised in Table 12.2.

	LWFA reference	PWFA self-ionised	PWFA pre-ionised
$\overline{W}$ [MeV]	260 ± 9	260 ± 5	235 ± 5
ΔW [MeV]	24 ± 4	36 ± 2	51 ± 3
Q [pC]	104 ± 12	48 ± 3	40 ± 2
S [pC/%]	11.3 ± 2.1	3.5 ± 0.3	1.9 ± 0.2

Table 12.2: **PWFA driver parameters.** Average FWHM values of the LWFA-generated electron beam, obtained from the reference dataset and after interaction with second stage in self-ionised and pre-ionised mode. Pre-ionising the PWFA section results in significantly stronger drive beam degradation.

The significant degradation of the electron beam implies that the driver is sufficiently intense to generate a plasma downstream of the laser blocker even without the aid of the pre-ionising laser and transfers energy into the plasma. However, the pre-ionised

and self-ionised modes can be clearly distinguished. Upon traversing a pre-formed plasma section, the driver experiences more severe charge degradation and spectral broadening, accompanied with a substantial reduction in central energy. On average, the measured spectral charge density in the self-ionised mode decreases to $\approx 31\,\%$ compared to the LWFA reference set, whereas pre-ionisation further reduces the remaining spectral charge density of the driver to $\approx 17\,\%$ of the reference.

12.3.2 *Observation of electron-driven plasma waves*

The substantial degradation of the drive beam is a strong indicator of electron-driven plasma waves. The few-cycle probe shadowgraphy diagnostics confirms this hypothesis. Examples of recorded shadowgrams for both self-ionised and pre-ionised mode are shown in Figure 12.6. The shadowgram corresponding to the self-ionised scen-

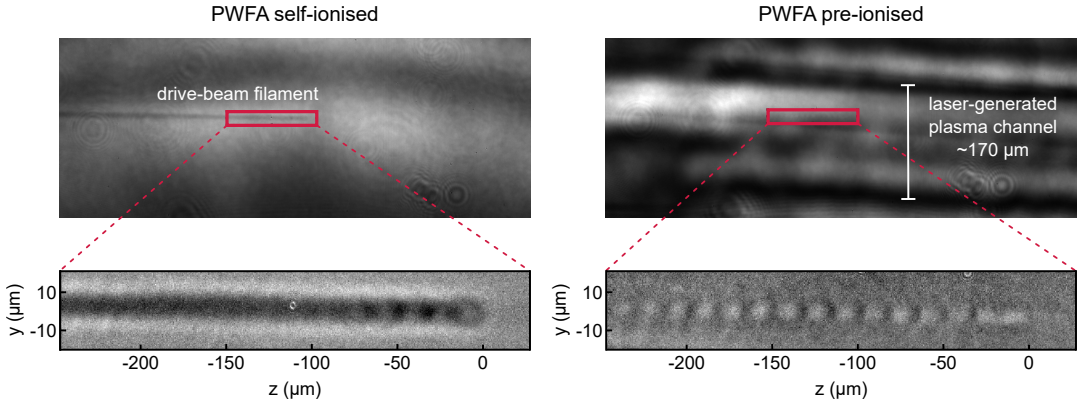

Figure 12.6: **Few-cycle shadowgrams.** Example shadowgraphy images recorded at the centre of the PWFA stage, obtained without (left) and with (right) the pre-ionisation laser engaged. Magnifying and post-processing the highlighted region evidences and visualises beam-driven plasma waves in both scenarios. Pre-ionisation of the PWFA section results in a more pronounced plasma wave structure. Post-processed images provided by S. Schöbel, adapted from [45] under license CC BY 4.0.

ario directly visualises the plasma filament generated by the electron beam. Upon magnifying the region at the front of the filament and applying a noise reduction filter, a few oscillation periods of a plasma wave are clearly visible. The raw shadowgram recorded in pre-ionised mode, in turn, shows the plasma channel generated by the pre-ionising laser. The post-processed and magnified image then reveals a more pronounced plasma wave structure compared to the self-ionised scenario, with

more than 10 consecutive cavities apparent. Despite their different shape, both plasma waves exhibit a similar period length of $\approx 17\,\mu m$, indicating nearly equivalent plasma densities corresponding to $\sim 4 \times 10^{18}\,cm^{-3}$.

The difference in observed plasma wave structures and the stronger driver degradation in pre-ionised mode are consistent with theoretical and numerical predictions; without pre-ionisation, only a fraction of the driver contributes to the wake formation. As further discussed in Appendix A1, this results in a characteristically distinct plasma wave structure and a correspondingly weaker wakefield compared to the pre-ionised scenario. To the author's knowledge, the shadowgrams obtained during this experiment constitute the first direct visual comparison of electron beam-driven plasma waves under self-ionised and pre-ionised conditions.

12.3.3 *Witness acceleration*

The primary finding of this experiment, however, lies in the observation of electron acceleration. Distinct witness beam signatures are detected on the electron spectrometer in $\sim 25\,\%$ of the shots in self-ionised mode, and in about $\sim 40\,\%$ of the shots with the pre-ionising laser engaged. A prominent example electron spectrum of each dataset is presented in Figure 12.7, together with an example of the reference measurements. The lower panel further shows the charge distribution of each spectrum integrated over a divergence angle of $\pm 6\,mrad$. As previously presented in Figure 12.5, the reference driver spectrum features a narrow-band charge density peak at around 260 MeV and a highly diverging low-energy electron background extending up to $\sim 30\,MeV$. With the second jet activated, the driver exhibits substantial degradation in both angular-resolved and integrated spectral charge density, as well as spectral broadening to lower energies. Moreover, a distinct witness beam signature at $\approx 60\,MeV$ is detected in the self-ionised example spectrum, visually extending above the electron background of the low-energy fraction and the spent driver. With the pre-ionisation laser engaged, a similar, but more pronounced witness beam signature is observed at $\approx 130\,MeV$, with peak angular-integrated spectral charge density clearly exceeding the electron background by $\approx 2\,pC/MeV$.

Such a difference in witness energies is also apparent upon evaluating the entire dataset. Figure 12.8 illustrates the individual measured witness beam energies correlated to the corresponding remaining spectral charge density of the spent driver. Consistently higher energies of $100 \pm 5\,MeV$ on average are observed with the PWFA section pre-ionised, compared to $62 \pm 4\,MeV$ in the self-ionised case, accompanied with stronger driver degradation.

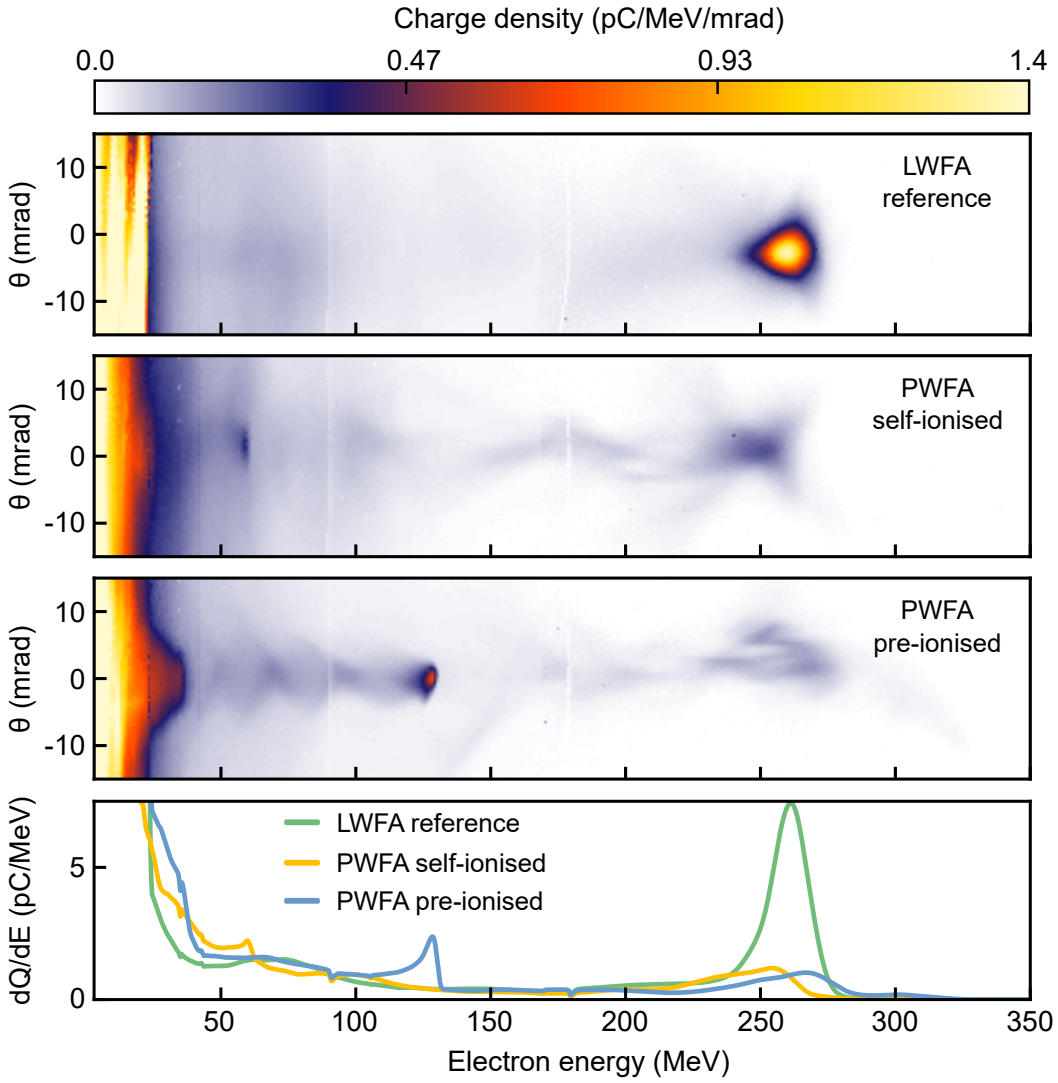

Figure 12.7: **Example LPWFA spectra.** From top to bottom, prominent electron spectra are shown from the LWFA reference dataset (corresponding to the shot highlighted in red in Figure 12.5), with the second stage operated in self-ionised mode, and the PWFA section pre-ionised[1]. The lower panel shows the angular-integrated charge density distribution of the spectra above. With the second stage enabled, the driver is substantially degraded and distinct witness beam signatures are detected above the electron background originating from the spent driver. A significantly higher witness energy is observed in pre-ionised mode. Figure adapted from [45] under license CC BY 4.0.

1 Again, the spectra of the full PWFA datasets are shown in Figure A2.

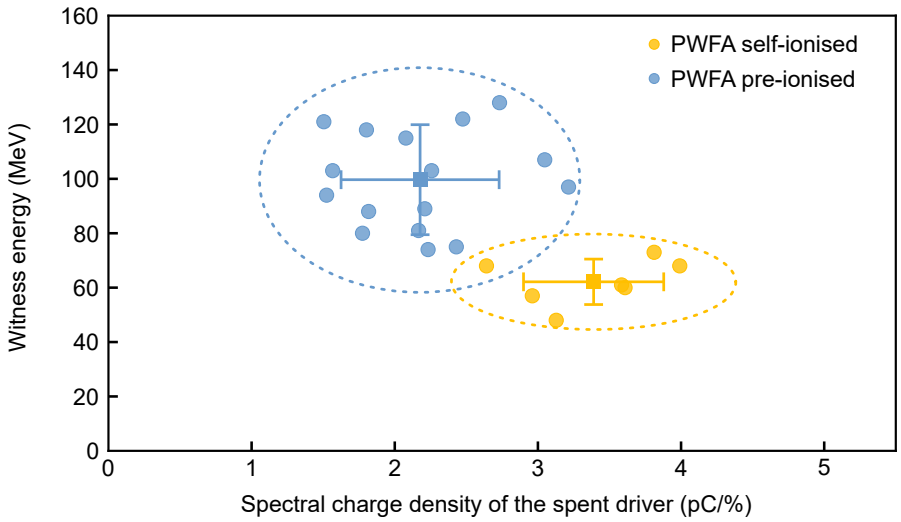

Figure 12.8: **Witness energies against the remaining spectral charge density of the driver.** For all shots exhibiting a distinct witness beam signature, the energy of the observed spectral peak is evaluated against the corresponding spectral charge density of the spent driver. A lower remaining spectral charge density indicates stronger driver degradation during its interaction with the PWFA section. Individual data points correspond to shots recorded in self-ionised (orange) and pre-ionised (blue) operating modes. The squares denote average values, with error bars indicating the standard deviation around the mean. Ellipses encircle the region of two standard deviations. Consistently stronger driver degradation together with higher witness beam energies are observed in the pre-ionised scenario, implying a higher-amplitude wakefield. Figure adapted from [45] under license CC BY 4.0.

Since the pre-ionisation laser only affects the target section downstream of the laser blocker, such increase in witness energy and driver degradation must be attributed to a higher wake amplitude of the purely beam-driven plasma wakefield. Together with the direct observation and qualitative comparison of plasma wave structures in both self-ionised and pre-ionised scenarios, these findings form a conclusive evidence of first electron acceleration in a discrete PWFA stage driven by LWFA-generated electron beams.

12.4 DISCUSSION

In summary, the experiment successfully demonstrates a miniaturised PWFA driven by LWFA-generated electron beams. This prototype of the LPWFA concept is realised in a centimetre-scale target configuration. Two individually controlled gas jet targets comprise the LWFA and PWFA stages, respectively. Propagation of the LWFA laser into the designated PWFA section is unequivocally terminated by means of a laser blocker foil, separating laser-driven and electron-driven processes. The LWFA stage thereby utilises self-truncated ionisation injection, optimised for providing high peak-current electron drivers for the subsequent PWFA section. Before enabling the second stage, the pure LWFA performance is characterised with and without employing the laser blocker to quantify its influence on the LWFA output. With both gas jets in operation, the PWFA section downstream of the foil can be optionally pre-ionised by means of a dedicated auxiliary laser pulse. Comparing these two operating modes leads to the main result of this experiment. Even without engaging the pre-ionisation laser, the electron driver is capable of generating a plasma environment and wakefield, as evidenced by a substantial degradation of the driver spectrum and the direct observation of electron-driven plasma waves via few-cycle shadowgraphy. This further constitutes the first visualisation of beam-driven plasma waves in the self-ionised regime. Enabling the pre-ionisation laser results in significantly stronger driver degradation and more pronounced plasma wave structures, consistent with theoretical and numerical predictions. This shows that self-ionised and pre-ionised operating modes can be clearly distinguished. As a primary finding, distinct signatures of accelerated witness beams are detected on the electron spectrometer in both scenarios, with consistently higher energies attained upon pre-ionising the PWFA section.

The precise origin of the accelerated witness beams, however, cannot be determined unambiguously in this experimental configuration. Several injection processes, or combinations thereof, are conceivable. The choice of a hydrogen-helium mixture in the second gas jet was intended to, in principle, enable injection based on additional ionisation of the helium dopant by either the driver or the wakefield. A significant contribution from ionisation injection, however, can be empirically excluded, as witness beam signatures have also been observed in a similar experimental configuration with pure hydrogen supplied to the second gas jet. Alternatively, a fraction of the low-energy electron reservoir generated on the density down-ramp transition at the end of the LWFA stage may have been captured and further accelerated in the electron beam-driven plasma wake. Start-to-end simulations accompanying the experimental

results reported in in [45] render this process plausible. Moreover, the appearance of witness beam signatures is directly correlated to the laser blocker foil position, as empirically confirmed during initial measurements performed in preparation of the main experiment. Further analysis of these preliminary datasets, combined with auxiliary simulations lead to the conclusion that the observed witness beams are most likely injected via the density shock-fronts caused by the laser blocker foil partially obstructing the gas flow in the second gas jet [44].

Notwithstanding the remaining uncertainty about the witness beam origin, the clear distinction between self-ionised and pre-ionised operating modes conclusively ascertains a PWFA process in the section downstream of the laser blocker, substantiated by systematically stronger driver degradation, the observation of more pronounced plasma wave structures and higher witness beam energies upon pre-ionising the PWFA section. The highest witness energy thereby observed amounts to 128 MeV, compared to an average of 62 MeV in the self-ionised regime. Assuming an effective PWFA acceleration distance of 1.5 mm, from the laser blocker to the end of the flat-top plateau region of the second gas jet, one can thus deduce that the average accelerating gradient in the pre-ionised PWFA was up to ~50 GV/m higher than in self-ionised mode. This provides a conservative lower limit to the actual accelerating gradient. Such acceleration strength is already on par with large-scale PWFAs driven by RF-accelerators [28]. Numerical simulations suggest that the LWFA-generated electron beams in this experiment are capable of driving a wake with a peak accelerating gradient beyond 100 GV/m [45].

While the experiment thus successfully achieved its primary aim of unambiguously demonstrating acceleration in a pure PWFA driven by LWFA-generated electron beams, its conceptual design was not yet optimised specifically for generating high-quality electron beams. Nevertheless, the observed witness beams already exhibit encouraging parameters. The energy, charge and spectral charge density of the five most prominent witness beams from the pre-ionised dataset are illustrated in Figure 12.9, with all parameters evaluated within their spectral FWHM bandwidth after subtracting the driver background. The data point highlighted by the ellipse corresponds to the pre-ionised spectrum shown in Figure 12.7, featuring a witness charge of 12 pC within a bandwidth of 7.8 MeV around its spectral peak at 128 MeV. This corresponds to a relative energy spread of 6 %, nearly a factor of two smaller than the original LWFA output, together with a slightly lower divergence of 3.8 mrad (compared to 4.2 mrad, see Table 12.1), albeit at roughly half the initial driver energy.

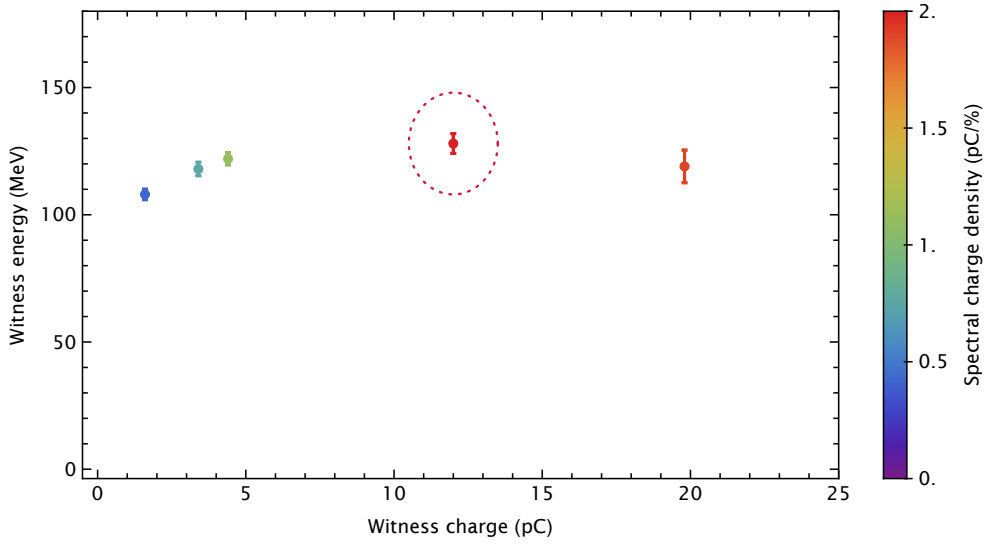

Figure 12.9: **Witness beam parameters in pre-ionised PWFA.** Energy and charge obtained from the spectra of the five most prominent witness beams in the pre-ionised PWFA dataset. Vertical bars indicate the FWHM energy bandwidth, the colour-coding corresponds to spectral charge density. The data point highlighted by the ellipse corresponds to the spectrum shown in Figure 12.7, with $Q = 12\,\mathrm{pC}$, $W = 128\,\mathrm{MeV}$, $\Delta W = 7.8\,\mathrm{MeV}$, and spectral charge density of $2\,\mathrm{pC/\%}$.

Future implementations of the LPWFA concept with improved injection control directly within the PWFA stage are expected to deliver substantially enhanced witness beam quality parameters. This necessitates to place the laser blocker sufficiently upstream of the second gas target. Transporting the driver between the two stages, as well as out-coupling the final witness may then be further assisted by tailored plasma density ramps [148, 156–160] or plasma lenses [509, 513–515][485]. Further adaptions could include elongated gas targets to study driver depletion and facilitate boosting the witness energy beyond the initial LWFA output. Characterising the electron-driven plasma waves and witness beams along the acceleration distance may benefit from additional diagnostics, for example based on polarimetry [468, 469] or multi-plane shadowgraphy [516]. Recently developed diagnostic approaches could provide valuable tools for quantifying the final witness quality parameters [517–519].

Another technical aspect of the laser blocker desires amendments. Due to its specific design, only a limited number of shots is available before the foil is fully depleted, restricting the sample size of consecutive measurements in this experiment. Replacing the rotational wheel-shaped blocker with motorised spools accommodating metres of foil [233, 520, 521], for example, could largely increase the number of measurements

between breaking the vacuum for maintenance, thus facilitating extensive parameter scans with enhanced statistical significance. Ultimately, the laser blocker might be removed from the setup entirely if the divergence of the LWFA output is sufficiently small. In this case, introducing a considerable spatial separation between the LWFA and PWFA targets can be used to ensure a purely beam-driven process in the PWFA stage, thereby specifically exploiting the much larger divergence of the spent laser driver [56][485].

Such a configuration was utilised in the complementary LPWFA campaign conducted at LMU [45]. In this alternative experimental concept, a tailored density shock-front is introduced to the LWFA stage to deliberately inject two electron bunches into consecutive plasma wave cavities. The distance between the two electron populations thus corresponds to approximately one plasma wavelength. This technique effectively utilises the LWFA to provide a driver-witness bunch-pair with controlled spatial separation for the subsequent PWFA stage, as conceptualised in [232]. Similar to the HZDR experiment, several datasets are recorded to characterise the driver and witness spectra before and after interacting with the second stage, albeit each comprising a substantially larger sample size of 200 consecutive measurements. The initial electron driver energy is thereby determined to $244 \pm 1\,\mathrm{MeV}$ on average, together with a FWHM-integrated charge of $120 \pm 5\,\mathrm{pC}$. The trailing witness bunch initially exhibits a distinct spectral peak at $119 \pm 1\,\mathrm{MeV}$, approximately half of the driver energy, and a substantially lower charge of $36 \pm 2\,\mathrm{pC}$. The driver energy and charge are thus comparable to the LWFA-generated electron beams in the HZDR experiment. However, the driver-witness bunch pair in the LMU experiment features a considerably smaller divergence of 1 mrad. The distance between the two stages can therefore be considerably increased, allowing the spent LWFA laser to diverge and diminish its intensity without compromising the ability of the designated PWFA driver to generate a wakefield. After a vacuum propagation distance of 6 mm, the intensity of the laser remnant is sufficiently reduced to no longer drive a significant wakefield, however, is still able to pre-ionise the PWFA stage. This PWFA stage is formed by a 1 mm gas jet, operated initially at a considerably lower plasma density than the LWFA stage, with $n_{0,\mathrm{PWFA}}/n_{0,\mathrm{LWFA}} \approx 0.3$. The nominal plasma wavelength is hence elongated beyond the spatial separation between the bunch pair, such that the trailing witness beam is placed in an accelerating phase of the wake driven by the anterior bunch. Thereby, a similar characteristic degradation of the driver as in the HZDR experiment is observed. At the same time, an energy gain of the witness population by about 14 MeV is detected, signifying energy transfer from the driver to the witness via a

plasma wakefield. This finding is corroborated by repeating the measurement with increased PWFA plasma density, upon which the effective energy transfer is enhanced and the driver and witness spectra start to merge. Further aspects of this experiment are discussed in detail by Max F. Gilljohann in [233].

In conclusion, witness acceleration in discrete PWFAs powered by LWFA-generated electron beams is demonstrated, for the first time, in two independent experiments. Together, they showcase the viability and versatility of the hybrid LPWFA platform and substantiate that a variety of PWFA scenarios can be realised at currently existing LWFA facilities. This achievement can be considered as the first generation of hybrid plasma wakefield accelerators, encouraging and providing the basis for future explorations.

SUMMARY & OUTLOOK

13

SUMMARY & OUTLOOK

Since their conceptualisation almost half a century ago, the research and development of plasma-based particle accelerators has advanced tremendously, with steady refinements in both theory and experiments. Both laser- and particle beam-driven concepts have demonstrated their outstanding capabilities to generate and harness accelerating gradients far beyond the reach of conventional technology.

Especially LWFAs are nowadays commonly realised in numerous university-scale laboratories worldwide, largely enabled by the continuous proliferation of high-intensity laser systems based on of chirped-pulse amplification. This development encourages the conception of miniaturised and economic electron sources for a broad range of applications [1], with the prime example being future compact light sources [19–21]. Prospects of widely accessible, resource-efficient free electron lasers enabled by plasma wakefield accelerators are particularly attractive, in turn empowering new research perspectives in chemistry, biomedical and material science and beyond. Recent experimental advancements towards such plasma-based FELs achieved amplification of radiation in the infrared to extreme-ultraviolet range [31], and plans for a plasma-based FEL user facility are actively being pursued [32]. Nonetheless, electron beams delivered by current plasma wakefield accelerators do not yet fulfil the demanding beam brightness requirements for X-ray FELs. Substantial improvements in electron beam quality are therefore highly desired, specifically in terms of (slice) emittance and energy spread. Addressing this challenge is widely regarded as the primary objective of current and future plasma wakefield accelerator research [31, 33].

This thesis explores two complementary approaches – Plasma photocathode injection and hybrid LWFA-PWFA staging – which, in conjunction, offer a pathway towards compact plasma-based electron sources delivering highest beam brightness.

The injection dynamics in plasma wakefield accelerators largely define the witness beam's residual emittance and energy spread, and hence predetermine the attainable output quality. Plasma photocathodes utilise a synchronised injector laser to release electrons directly inside the plasma wake via selective ionisation, and thus uniquely decouple injection control from the evolution of the driver and the wake structure. Such plasma photocathodes unfold their full potential in particle beam-driven wakefield scenarios, thereby promising the generation of witness beams with unprecedentedly

low emittance, in combination with sub-femtosecond duration and kiloampere peak currents. Plasma photocathodes may thus deliver electron beams exhibiting extreme 5D and 6D brightness values, with prospects of largely surpassing the capabilities of current conventional linacs [399, 407].

The first demonstration of a plasma photocathode, realised during the E-210 experiment in a perpendicular injector geometry, marks an important milestone. Although the experiment was not yet designed to achieve highest witness beam quality, the obtained results substantiate the prospects of plasma photocathodes to operate as highly efficient brightness transformers, and further provide valuable insights regarding experimental strategies and technical improvements for future implementations. Optimisations resulting in significantly enhanced witness beam parameters and reproducibility are anticipated for the successor programme E-310 at FACET-II, including plasma photocathode injection in collinear geometry.

An essential prerequisite to access the full capabilities of plasma photocathodes is a particle beam-driven plasma wake in the blowout regime with adequate trapping conditions, which in turn necessitates short, high-density drivers with sufficient peak current. Delivering such drivers poses considerable challenges for conventional accelerators, and a PWFA operating mode suitable for realising a plasma photocathode could thus far only be achieved at the $\sim 2\,\mathrm{km}$ long FACET facility. In a broader context, the development of PWFA concepts in general is hitherto restricted to a few large-scale conventional accelerator infrastructures.

The second strategy pursued in this thesis is therefore to utilise electron beams generated in a compact laser-driven wakefield accelerator as drivers for a subsequent, individually controlled PWFA stage. The exploration of such hybrid LWFA-PWFA staging concepts is encouraged by recent developments in laser-wakefield accelerators, demonstrating the generation of intrinsically short, multi-kiloampere electron beams in compact LWFA systems. These drivers, in principle, allow stable electron-driven blowouts to be generated at high plasma densities of $\sim 10^{18}\,\mathrm{cm}^{-3}$, enabling practically dephasing-free witness beam acceleration with gradients beyond $\sim 100\,\mathrm{GV/m}$. Hybrid LPWFA systems are thus attractive as a complementary research and development platform for exploring operating modes currently challenging to achieve in conventional linac-driven PWFAs. These prospects are further enhanced by the availability of intrinsically synchronised auxiliary laser pulses for diagnostics, pre-ionisation and, auspiciously, plasma photocathode injection with femtosecond precision. Hybrid staging therefore promises to combine the characteristic advantages unique to laser- and

electron-driven plasma acceleration methods, while simultaneously addressing their individual challenges.

However, the development of hybrid plasma wakefield accelerators is still in its infancy. The first demonstration of witness beam acceleration in a discrete PWFA stage driven by LWFA-generated electron beams marks the decisive milestone to establish the first generation of hybrid LPWFAs. The significance of this seminal achievement is emphasised by a series of subsequent experimental advancements obtained in quick succession after the initial results presented in this thesis. In a similar setup, the laser blocker could be placed upstream of the PWFA stage and controlled injection was achieved upon introducing a wire target generating hydrodynamic shock-fronts [494]. Another subsequent implementation utilised a laser-generated hydrodynamic shock-front to induce injection, showcasing the production of witness beams with improved angular-spectral charge density and enhanced stability compared to the original LWFA output [495]. A detailed investigation of shadowgraphy images obtained in part during the study presented in this thesis provides further valuable insights on the wakefield formation under varying driver parameters [496]. These additional results substantiate the versatility and prospects of the hybrid LPWFA research platform, and may be regarded as first indications of an emerging second generation of hybrid plasma wakefield accelerators.

The first realisation of a plasma photocathode in a linac-driven PWFA, in combination with the demonstration of a first LWFA-driven PWFA, gives rise to new objectives and perspectives for the immediate, near-term and long-term future. Naturally, an immediate objective is to merge these two approaches and explore plasma photocathode injection in a compact, hybrid LPWFA configuration. While this is by no means a straightforward task, all essential components and processes are now already established. The hybrid experiment showcases that auxiliary, comparatively low-power laser pulses can be derived from the parent laser system and steered onto the target under various geometries. The obtained results further indicate that LWFA-generated electron drivers can generate blowout conditions sufficient for plasma photocathode injection, corroborated by the shadowgraphy data and supporting simulations. In the near future, plasma photocathodes may therefore be complementary developed and optimised in both linac-driven and hybrid LPWFA scenarios, thereby mutually benefiting from individual insights. Due to the considerably stronger driver- and wakefields associated with operating a PWFA at high plasma densities, an LPWFA plasma photocathode may, however, target a different HIT species, potentially the second ionisation level of helium.

Another near-term objective specific to the future advancement of hybrid staging concepts is further research on LWFA operating modes delivering optimal PWFA drivers. While self-truncated ionisation injection and shock-front injection have been shown to reliably deliver high peak-current PWFA drivers, further refinements of the LWFA stage and inter-stage transport may yield enhanced driver tunability, reproducibility and stability. In a more forward-oriented outlook, future LWFA concepts may even be designed specifically to be augmented by a subsequent plasma photocathode stage.

Such LPWFA plasma photocathodes are envisaged to operate as highly efficient brightness transformers of the initial LWFA output, with further prospects for enhanced final witness beam energy and stability. The combination of hybrid staging and plasma photocathodes may therefore crucially advance the capabilities of current and future LWFAs without compromising their modest spatial and economic footprint. Employing a secondary plasma photocathode injector may further be utilised to revert the correlated energy spread of a witness beam accumulated during acceleration, thereby substantially increasing the 6D brightness and facilitating emittance-preserving extraction from the plasma and further beam transport [174, 407][403]. Multi-GeV final witness beam energies are in reach upon employing state-of-the-art petawatt-scale laser pulses to drive the initial LWFA. Staged LWFA setups powered by several 100 TW-class laser pulses are conceivable to further increase the initial PWFA driver energy. The steady trajectory of advancements in laser technology towards higher power and repetition rates, together with an increasing number of commercially available high-power laser systems further strengthens the prospects of future LPWFA capabilities and capacities.

Ultimately, these developments could lead to a new class of truly compact, widely accessible plasma-based electron sources with integrated diagnostics, reliably delivering electron beams with unprecedentedly low emittance and exceptionally high 5D and 6D brightness. A variety of light sources based on LPWFA plasma photocathodes may therefore become ubiquitous in the future, ranging from inverse Compton scattering sources [409] to soft X-ray and hard X-ray free electron lasers with substantially reduced gain lengths [403], but also including plasma-based betatron radiation sources and ion channel lasers [399, 405]. Such miniaturised, high-quality electron and light sources could be integrated in university-scale laboratories and, in turn, empower and diversify adjacent research fields across chemistry, biomedical and material science, as well as medical radiation therapies and numerous industrial applications.

Compact LPWFA photocathodes may also provide important contributions to answering open questions in fundamental physics. For example, they could support the development and commissioning of future conventional and plasma-based particle colliders [22] by providing cost-efficient, low-emittance and high-brightness test beams for the corresponding accelerator modules, transport systems and diagnostics, or directly supply the final beam line with electrons. Upon a more courageous look into the future, however, a whole ecosystem comprising high-intensity laser pulses, plasmas, high-brightness electron beams and plasma-based free electron lasers may be provided, all synchronised, in a compact assembly. Such systems could then be either duplicated, or added to existing high-energy physics machines, linac-driven PWFAs and FELs to establish potent infrastructures with colliding geometries. This perspective offers entirely new modalities in generating and co-locating high-density plasmas, highly relativistic electron beams with extreme charge densities, and pulsed high-intensity radiation at infrared, X-ray and γ-ray frequencies. The enormous field strengths attainable in a variety of these configurations would enable innovative experimental pathways for probing condensed matter and vacuum beyond the threshold of non-linear quantum electrodynamics [522–525].

Although a lot of work lies ahead, the prospects of both plasma photocathodes and hybrid plasma wakefield accelerators are manifold individually, and amplified upon their combination. Likewise, the further development of plasma photocathodes and hybrid LWFA-PWFA staging concepts is highly synergistic and mutually reinforcing. The experimental strategies and results presented in this thesis may contribute to laying the foundation for these future advancements.

APPENDIX

A1 ELECTRON-DRIVEN PLASMA WAVES IN THE SELF- AND PRE-IONISED REGIME

In contrast to common LWFA scenarios, PWFAs often rely on a pre-formed plasma environment, due to the substantially lower peak electric field strength of the drivers (see chapter 5). Nevertheless, several experiments at FFTB and FACET have shown that intense electron beams can autonomously generate a plasma and drive a wake in alkali metal vapours with a particularly low ionisation threshold [28, 340, 363, 365, 366, 420], created in a heat-pipe oven [362]. A self-ionised PWFA was also demonstrated at FACET in a less complex target configuration utilising argon with a considerably higher ionisation energy [526]. In this experiment, the driver initially only partially ionised the gas but was rapidly focused to a higher density in the emerging wakefield, thus increasing its field strength and enhancing the ionisation yield. In hybrid plasma wakefield accelerator scenarios, the LWFA-generated electron beams can be sufficiently intense to ionise a broader range of gas species, including hydrogen and helium.

However, tunnel ionisation processes occur over a finite amount of time, and further scale non-linearly with the electric field strength (see chapter 2.2). The self-generated plasma density profile, consequently, varies along the driver in both the longitudinal and transverse dimension. Therefore, only a fraction of the driver interacts with a fully formed plasma and can effectively contribute to the wake formation.

This further implies increased head erosion rates [28, 527, 528], which can lead to premature deterioration of the electron-driven wake before the driver energy is fully depleted. Moreover, simulations show that the trajectories of the expelled plasma electrons differ from a PWFA scenario in a pre-ionised plasma environment, resulting in a more diffuse blowout sheath and a more dilute wake vertex [529]. In a direct simulation comparison to a pre-ionised PWFA with equivalent initial drivers, the self-ionised regime is thus characterised by a weaker peak accelerating field, but also in a collapse of the plasma wake structure after a few oscillation periods [530].

This effect is also observed in the hybrid LPWFA experiment discussed in chapter 12, and visualised directly through the shadowgraphy diagnostic. Ancillary PIC simulations representative of the experimental conditions in the second stage further substantiate this finding. In these simulations, a Gaussian electron driver with central energy of 260 MeV, rms energy spread of 5 % ($\approx$12 % FWHM), total charge of 150 pC ($\approx$114 pC in FWHM bandwidth), peak current of about 7 kA and normalised emittance of 5 µm rad (corresponding to a FWHM divergence of $\theta \approx 5$ mrad) traverses a pure hydrogen gas target with a flat-top plateau length of 1.6 mm and adjacent 0.6 mm long cosine-shaped ramps. Upon full ionisation, the resulting plasma density corresponds

to a nominal plasma wavelength of 17 µm . As in the experiment, the section upstream of the nominal laser blocker position (100 µm into the gas density plateau region) is considered to be pre-ionised by the remnant of the LWFA driver. Other than separating the plasma and neutral gas sections in the self-ionised scenario, no further influence of the laser blocker on the electron driver or the gas density is considered. Figure A1 shows the plasma wave structure obtained from the simulations at the centre of the PWFA gas jet in the pre-ionised and self-ionised regime, respectively.

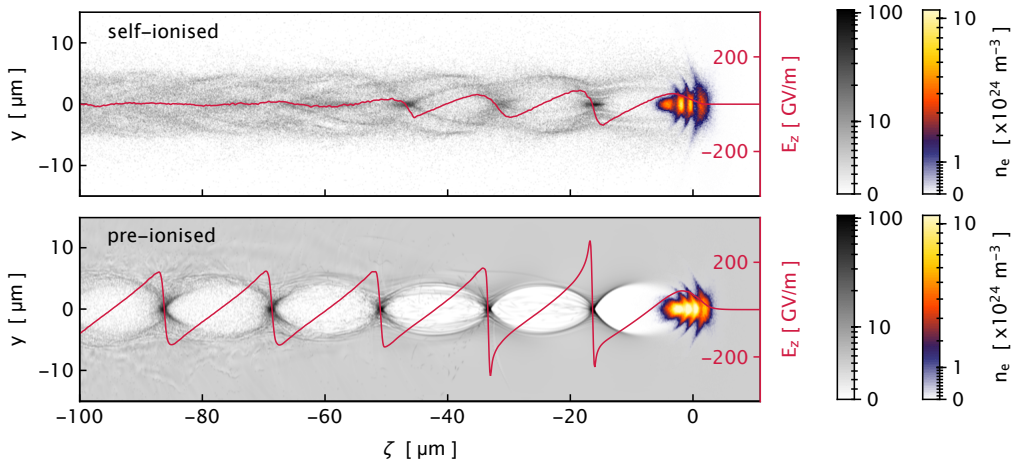

Figure A1: **Electron-driven plasma waves in the self-ionised and pre-ionised regime.** PIC simulations representative of the scenario in the hybrid LPWFA experiment further illustrate the distinct plasma wave structures in the self-ionised and pre-ionised regime. The simulations are visualised at a the approximate centre of the gas jet, corresponding to the shadowgrams shown in Figure 12.6 . The simulations concur with the experimental observations.

As observed in the experiment, the plasma wave is much more pronounced in the pre-ionised regime, whereas the wake structure quickly collapses after a few plasma periods in the self-ionised regime. Further, pre-ionising the PWFA section downstream of the laser blocker results in a substantially stronger wakefield. This also implies a stronger driver deceleration and more severe degradation of its spectral charge density. Corresponding virtual electron spectra of the driver obtained after its passage through the second stage are shown in Figure A2 , again in good agreement with the experimental observations.

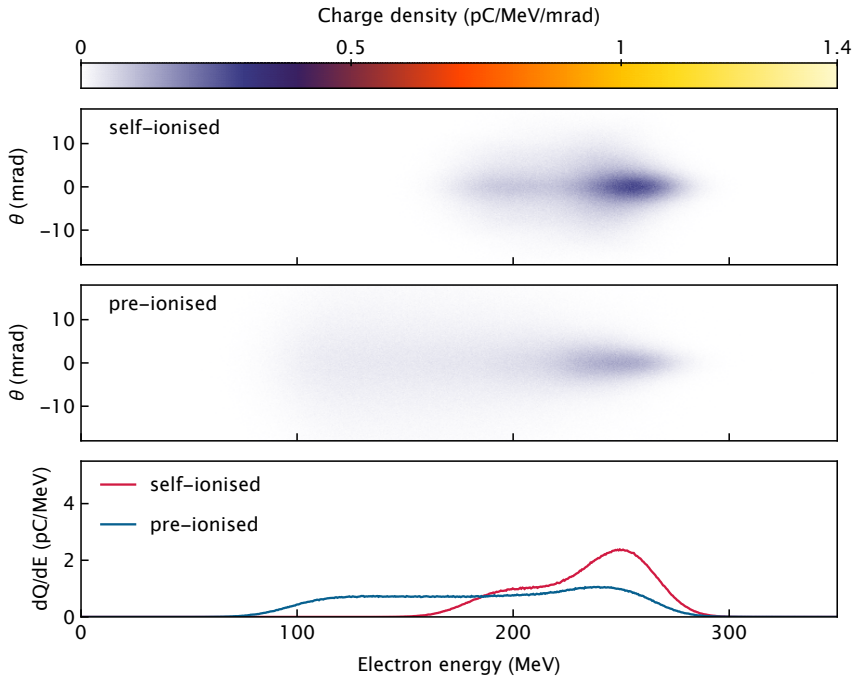

Figure A2: **Virtual driver spectra after the PWFA stage.** To compare the spent driver in the simulations with the experiment, a virtual spectrum of the simulated driver is generated after it has passed through the PWFA stage. Consistent with the experiment, stronger driver degradation is observed in the pre-ionised regime compared to the self-ionised scenario.

A2 ELECTRON SPECTRA RECORDED IN THE HYBRID LPWFA EXPERIMENT

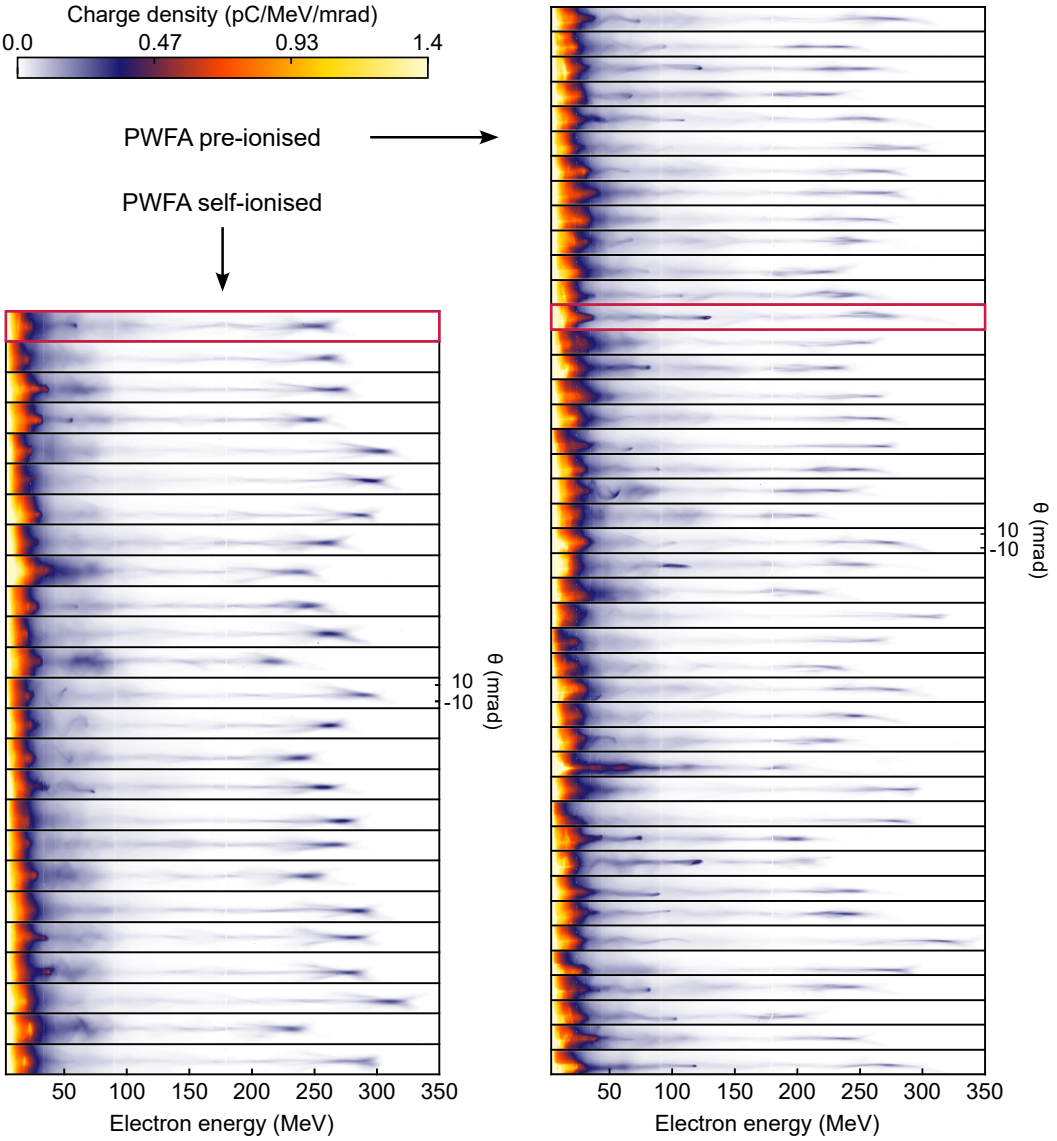

Figure A3: **Recorded LPWFA electron spectra.** The full dataset of electron spectra recorded in the hybrid LPWFA experiment discussed in chapter 12, operated without the pre-ionisation laser engaged (left column) and with the PWFA section ionised prior to the arrival of the LWFA-generated drive beam (right column). Electron spectra highlighted by a red frame correspond to the spectra shown in Figure 12.7. Figure adapted from [45] under license CC BY 4.0.

LIST OF FIGURES

LIST OF TABLES

BIBLIOGRAPHY

[1] The EuCARD-2 Collaboration. *Applications of Particle Accelerators in Europe*. 2017. DOI: 10.17181/CERN.HA4I.UT3N.

[2] S. Sheehy. *Applications of Particle Accelerators*. 2024. DOI: 10.48550/ARXIV.2407.10216. URL: https://arxiv.org/abs/2407.10216.

[3] A. Nassiri et al. 'History and Technology Developments of Radio Frequency (RF) Systems for Particle Accelerators'. In: *IEEE Transactions on Nuclear Science* 63.2 (Apr. 2016), pp. 707–750. DOI: 10.1109/tns.2015.2485164.

[4] T. Behnke et al. *The International Linear Collider Technical Design Report - Volume 1: Executive Summary*. 2013. DOI: 10.48550/ARXIV.1306.6327.

[5] P. Burrows et al. *A Multi-TeV Linear Collider Based on CLIC Technology: CLIC Conceptual Design Report*. en. 2012. DOI: 10.5170/CERN-2012-007.

[6] A. Abada et al. 'FCC-ee: The Lepton Collider: Future Circular Collider Conceptual Design Report Volume 2'. In: *The European Physical Journal Special Topics* 228.2 (June 2019), pp. 261–623. ISSN: 1951-6401. DOI: 10.1140/epjst/e2019-900045-4.

[7] The CEPC Study Group. *CEPC Conceptual Design Report: Volume 1 - Accelerator*. 2018. DOI: 10.48550/ARXIV.1809.00285.

[8] J. M. J. Madey. 'Stimulated Emission of Bremsstrahlung in a Periodic Magnetic Field'. In: *Journal of Applied Physics* 42.5 (Apr. 1971), pp. 1906–1913. DOI: 10.1063/1.1660466.

[9] B. W. J. McNeil and N. R. Thompson. 'X-ray free-electron lasers'. In: *Nature Photonics* 4.12 (Nov. 2010), pp. 814–821. ISSN: 1749-4893. DOI: 10.1038/nphoton.2010.239.

[10] J. Madey, M. O. Scully and P. Sprangle. 'The free electron laser: conceptual history'. In: *Physica Scripta* 91.8 (July 2016), p. 083003. ISSN: 1402-4896. DOI: 10.1088/0031-8949/91/8/083003.

[11] C. Pellegrini. 'X-ray free-electron lasers: from dreams to reality'. In: *Physica Scripta* T169 (Dec. 2016), p. 014004. ISSN: 1402-4896. DOI: 10.1088/1402-4896/aa5281.

[12] C. Pellegrini, A. Marinelli and S. Reiche. 'The physics of x-ray free-electron lasers'. In: *Reviews of Modern Physics* 88.1 (Mar. 2016), p. 015006. DOI: 10.1103/revmodphys.88.015006.

[13] H.-D. Nuhn. *Linac Coherent Light Source (LCLS) Conceptual Design Report*. Tech. rep. SLAC–R–593. SLAC National Accelerator Laboratory, Nov. 2002. DOI: 10.2172/808719.

[14] R. Abela et al. *XFEL: The European X-Ray Free-Electron Laser - Technical Design Report*. en. Tech. rep. Deutsches Elektronen-Synchrotron, 2006. DOI: 10.3204/DESY_06-097.

[15] J. Stohr. *Linac Coherent Light Source II (LCLS-II) Conceptual Design Report*. Tech. rep. SLAC-R-978. SLAC National Accelerator Laboratory, Nov. 2011. DOI: 10.2172/1029479.

[16] T. Tajima and J. M. Dawson. 'Laser Electron Accelerator'. In: *Physical Review Letters* 43.4 (July 1979), pp. 267–270. DOI: 10.1103/physrevlett.43.267.

[17] P. Chen, R. W. Huff and J. M. Dawson. *A Plasma Booster for Linear Accelerators*. Tech. rep. UCLA Report PPG-802. University of California Los Angeles, 1984.

[18] P. Chen, J. M. Dawson, R. W. Huff and T. Katsouleas. 'Acceleration of Electrons by the Interaction of a Bunched Electron Beam with a Plasma'. In: *Physical Review Letters* 54.7 (Feb. 1985), pp. 693–696. DOI: 10.1103/physrevlett.54.693.

[19] S. Corde et al. 'Femtosecond x rays from laser-plasma accelerators'. In: *Reviews of Modern Physics* 85.1 (Jan. 2013), pp. 1–48. DOI: 10.1103/revmodphys.85.1.

[20] F. Albert et al. 'Laser wakefield accelerator based light sources: potential applications and requirements'. In: *Plasma Physics and Controlled Fusion* 56.8 (July 2014), p. 084015. DOI: 10.1088/0741-3335/56/8/084015.

[21] F. Albert and A. G. R. Thomas. 'Applications of laser wakefield accelerator-based light sources'. In: *Plasma Physics and Controlled Fusion* 58.10 (Sept. 2016), p. 103001. DOI: 10.1088/0741-3335/58/10/103001.

[22] B. Foster, R. D'Arcy and C. A. Lindstrøm. 'A hybrid, asymmetric, linear Higgs factory based on plasma-wakefield and radio-frequency acceleration'. In: *New Journal of Physics* 25.9 (Sept. 2023), p. 093037. DOI: 10.1088/1367-2630/acf395.

[23] T. Katsouleas. 'Plasma accelerators race to 10GeV and beyond'. In: *Physics of Plasmas* 13.5 (May 2006). ISSN: 1089-7674. DOI: 10.1063/1.2198172.

[24] C. Joshi. 'The development of laser- and beam-driven plasma accelerators as an experimental field'. In: *Physics of Plasmas* 14.5 (May 2007). ISSN: 1089-7674. DOI: 10.1063/1.2721965.

[25] S. M. Hooker. 'Developments in laser-driven plasma accelerators'. In: *Nature Photonics* 7.10 (Sept. 2013), pp. 775–782. ISSN: 1749-4893. DOI: 10.1038/nphoton.2013.234.

[26] C. Joshi. 'Plasma-based accelerators: then and now'. In: *Plasma Physics and Controlled Fusion* 61.10 (Aug. 2019), p. 104001. DOI: 10.1088/1361-6587/ab396a.

[27] C. Joshi, S. Corde and W. B. Mori. 'Perspectives on the generation of electron beams from plasma-based accelerators and their near and long term applications'. In: *Physics of Plasmas* 27.7 (July 2020), p. 070602. DOI: 10.1063/5.0004039.

[28] I. Blumenfeld et al. 'Energy doubling of 42 GeV electrons in a metre-scale plasma wakefield accelerator'. In: *Nature* 445.7129 (Feb. 2007), pp. 741–744. DOI: 10.1038/nature05538.

[29] A. Gonsalves et al. 'Petawatt Laser Guiding and Electron Beam Acceleration to 8 GeV in a Laser-Heated Capillary Discharge Waveguide'. In: *Physical Review Letters* 122.8 (Feb. 2019), p. 084801. DOI: 10.1103/physrevlett.122.084801.

[30] C. Aniculaesei et al. 'The acceleration of a high-charge electron bunch to 10 GeV in a 10-cm nanoparticle-assisted wakefield accelerator'. In: *Matter and Radiation at Extremes* 9.1 (Nov. 2023). ISSN: 2468-080X. DOI: 10.1063/5.0161687.

[31] M. Galletti et al. 'Prospects for free-electron lasers powered by plasma-wakefield-accelerated beams'. In: *Nature Photonics* 18.8 (Aug. 2024), pp. 780–791. ISSN: 1749-4893. DOI: 10.1038/s41566-024-01474-3.

[32] R. W. Assmann et al. 'EuPRAXIA Conceptual Design Report'. In: *The European Physical Journal Special Topics* 229.24 (Dec. 2020), pp. 3675–4284. DOI: 10.1140/epjst/e2020-000127-8.

[33] C. Emma et al. 'Free electron lasers driven by plasma accelerators: status and near-term prospects'. In: *High Power Laser Science and Engineering* 9 (2021). ISSN: 2052-3289. DOI: 10.1017/hpl.2021.39.

[34] D. Strickland and G. Mourou. 'Compression of amplified chirped optical pulses'. In: *Optics Communications* 55.6 (Oct. 1985), pp. 447–449. DOI: 10.1016/0030-4018(85)90151-8.

[35] S. P. D. Mangles et al. 'Monoenergetic beams of relativistic electrons from intense laser–plasma interactions'. In: *Nature* 431.7008 (Sept. 2004), pp. 535–538. DOI: 10.1038/nature02939.

[36] C. G. R. Geddes et al. 'High-quality electron beams from a laser wakefield accelerator using plasma-channel guiding'. In: *Nature* 431.7008 (Sept. 2004), pp. 538–541. DOI: 10.1038/nature02900.

[37] J. Faure et al. 'A laser–plasma accelerator producing monoenergetic electron beams'. In: *Nature* 431.7008 (Sept. 2004), pp. 541–544. DOI: 10.1038/nature02963.

[38] B. Hidding et al. 'Ultracold Electron Bunch Generation via Plasma Photocathode Emission and Acceleration in a Beam-Driven Plasma Blowout'. In: *Physical Review Letters* 108.3 (Jan. 2012), p. 035001. DOI: 10.1103/physrevlett.108.035001.

[39] B. Hidding et al. 'Beyond injection: Trojan horse underdense photocathode plasma wakefield acceleration'. In: *AIP Conference Proceedings*. Vol. 1507. AIP, 2012, pp. 570–575. DOI: 10.1063/1.4773760.

[40] A. Deng et al. 'Generation and acceleration of electron bunches from a plasma photocathode'. In: *Nature Physics* 15.11 (Aug. 2019), pp. 1156–1160. DOI: 10.1038/s41567-019-0610-9. A. Deng and O. S. Karger contributed equally to this work.

[41] J. P. Couperus et al. 'Demonstration of a beam loaded nanocoulomb-class laser wakefield accelerator'. In: *Nature Communications* 8.1 (Sept. 2017). DOI: 10.1038/s41467-017-00592-7.

[42] J. P. Couperus. 'Optimal Beam Loading In A Nanocoulomb-Class Laser Wakefield Accelerator'. en. PhD thesis. Technische Universität Dresden, 2018. DOI: 10.5281/ZENODO.1463710.

[43] A. Irman et al. 'Improved performance of laser wakefield acceleration by tailored self-truncated ionization injection'. In: *Plasma Physics and Controlled Fusion* 60.4 (Mar. 2018), p. 044015. DOI: 10.1088/1361-6587/aaaef1.

[44] T. Kurz. 'Realization of a compact plasma accelerator for high quality electron beams'. PhD thesis. Technische Universität Dresden, 2021.

[45] T. Kurz et al. 'Demonstration of a compact plasma accelerator powered by laser-accelerated electron beams'. In: *Nature Communications* 12.1 (May 2021). DOI: 10.1038/s41467-021-23000-7. T. Kurz and T. Heinemann contributed equally to this work.

[46] I. Langmuir. 'Oscillations in Ionized Gases'. In: *Proceedings of the National Academy of Sciences* 14.8 (Aug. 1928), pp. 627–637. DOI: 10.1073/pnas.14.8.627.

[47] H. M. Mott-Smith. 'History of "Plasmas"'. en. In: *Nature* 233.5316 (Sept. 1971), pp. 219–219. ISSN: 1476-4687. DOI: 10.1038/233219a0.

[48] F. F. Chen. *Introduction to Plasma Physics and Controlled Fusion*. Springer International Publishing, 2016. DOI: 10.1007/978-3-319-22309-4.

[49] D. J. Griffiths. *Introduction to Electrodynamics*. Pearson Education, 1998. ISBN: 9780139199608.

[50] P. Mulser and D. Bauer. *High Power Laser-Matter Interaction*. Springer Berlin Heidelberg, 2010. DOI: 10.1007/978-3-540-46065-7.

[51] R. Fitzpatrick. *Introduction to Plasma Physics: A graduate level course*. The University of Texas at Austin, 2008.

[52] U. Teubner, U. Wagner and E. Förster. 'Sub-10 fs gating of optical pulses'. In: *Journal of Physics B: Atomic, Molecular and Optical Physics* 34.15 (July 2001), pp. 2993–3002. ISSN: 1361-6455. DOI: 10.1088/0953-4075/34/15/306.

[53] A. Gonoskov. 'Theory of relativistic radiation reflection from plasmas'. In: *Physics of Plasmas* 25.1 (Jan. 2018), p. 013108. DOI: 10.1063/1.5000785.

[54] S. Steinke et al. 'Multistage coupling of independent laser-plasma accelerators'. In: *Nature* 530.7589 (Feb. 2016), pp. 190–193. DOI: 10.1038/nature16525.

[55] S. Steinke et al. 'Staging of laser-plasma accelerators'. In: *Physics of Plasmas* 23.5 (May 2016), p. 056705. DOI: 10.1063/1.4948280.

[56] S. Chou et al. 'Collective Deceleration of Laser-Driven Electron Bunches'. In: *Physical Review Letters* 117.14 (Sept. 2016), p. 144801. ISSN: 1079-7114. DOI: 10.1103/physrevlett.117.144801.

[57] M. F. Gilljohann et al. 'Direct Observation of Plasma Waves and Dynamics Induced by Laser-Accelerated Electron Beams'. In: *Physical Review X* 9.1 (Mar. 2019), p. 011046. DOI: 10.1103/physrevx.9.011046.

[58] W. P. Leemans et al. 'Plasma physics aspects of tunnel-ionized gases'. In: *Physical Review Letters* 68.3 (Jan. 1992), pp. 321–324. DOI: 10.1103/physrevlett.68.321.

[59] S. C. Rae and K. Burnett. 'Possible production of cold plasmas through optical-field-induced ionization'. In: *Physical Review A* 46.4 (Aug. 1992), pp. 2077–2083. ISSN: 1094-1622. DOI: 10.1103/physreva.46.2077.

[60] C. G. Durfee and H. M. Milchberg. 'Light pipe for high intensity laser pulses'. In: *Physical Review Letters* 71.15 (Oct. 1993), pp. 2409–2412. ISSN: 0031-9007. DOI: 10.1103/physrevlett.71.2409.

[61] A. L. Schmeltekopf and H. P. Broida. 'Short-Duration Visible Afterglow in Helium'. In: *The Journal of Chemical Physics* 39.5 (Sept. 1963), pp. 1261–1268. DOI: 10.1063/1.1734425.

[62] V. Lee et al. 'Temporal evolution of the light emitted by a thin, laser-ionized plasma source'. In: *Physics of Plasmas* 31.1 (Jan. 2024). ISSN: 1089-7674. DOI: 10.1063/5.0180416.

[63] L. V. Keldysh. 'Ionization in the field of a strong electromagnetic wave'. In: *Sov. Phys. JETP* 20.5 (1965), pp. 1307–1314.

[64] A. M. Zheltikov. 'Keldysh parameter, photoionization adiabaticity, and the tunneling time'. In: *Physical Review A* 94.4 (Oct. 2016), p. 043412. DOI: 10.1103/physreva.94.043412.

[65] D. Bauer. 'Plasma formation through field ionization in intense laser–matter interaction'. In: *Laser and Particle Beams* 21.4 (Oct. 2003), pp. 489–495. DOI: 10.1017/s0263034603214026.

[66] T. Brabec and F. Krausz. 'Intense few-cycle laser fields: Frontiers of nonlinear optics'. In: *Reviews of Modern Physics* 72.2 (Apr. 2000), pp. 545–591. DOI: 10.1103/revmodphys.72.545.

[67] M. V. Ammosov, N. B. Delone and V. P. Krainov. 'Tunnel ionization of complex atoms and of atomic ions in an alternating electromagnetic field'. In: *Soviet Journal of Experimental and Theoretical Physics* 64.6 (Dec. 1986), p. 1191. URL: https://ui.adsabs.harvard.edu/abs/1986JETP...64.1191A.

[68] A. M. Perelomov, V. S. Popov and M. V. Terent'ev. 'Ionization of Atoms in an Alternating Electric Field'. In: *Soviet Journal of Experimental and Theoretical Physics* 23 (Nov. 1966), p. 924. URL: https://ui.adsabs.harvard.edu/abs/1966JETP...23..924P.

[69] D. Bauer and P. Mulser. 'Exact field ionization rates in the barrier-suppression regime from numerical time-dependent Schrödinger-equation calculations'. In: *Physical Review A* 59.1 (Jan. 1999), pp. 569–577. DOI: 10.1103/physreva.59.569.

[70] V. S. Popov. 'Tunnel and multiphoton ionization of atoms and ions in a strong laser field (Keldysh theory)'. In: *Physics-Uspekhi* 47.9 (Sept. 2004), pp. 855–885. DOI: 10.1070/pu2004v047n09abeh001812.

[71] M. Chen et al. 'Numerical modeling of laser tunneling ionization in explicit particle-in-cell codes'. In: *Journal of Computational Physics* 236 (Mar. 2013), pp. 220–228. DOI: 10.1016/j.jcp.2012.11.029.

[72] F. A. Ilkov, J. E. Decker and S. L. Chin. 'Ionization of atoms in the tunnelling regime with experimental evidence using Hg atoms'. In: *Journal of Physics B: Atomic, Molecular and Optical Physics* 25.19 (Oct. 1992), pp. 4005–4020. DOI: 10.1088/0953-4075/25/19/011.

[73] D. L. Bruhwiler et al. 'Particle-in-cell simulations of tunneling ionization effects in plasma-based accelerators'. In: *Physics of Plasmas* 10.5 (May 2003), pp. 2022–2030. DOI: 10.1063/1.1566027.

[74] S. Augst, D. D. Meyerhofer, D. Strickland and S. L. Chint. 'Laser ionization of noble gases by Coulomb-barrier suppression'. In: *Journal of the Optical Society of America B* 8.4 (Apr. 1991), p. 858. DOI: 10.1364/josab.8.000858.

[75] D. Bauer. 'Ejection energy of photoelectrons in strong-field ionization'. In: *Physical Review A* 55.3 (Mar. 1997), pp. 2180–2185. DOI: 10.1103/physreva.55.2180.

[76] G. L. Yudin and M. Y. Ivanov. 'Nonadiabatic tunnel ionization: Looking inside a laser cycle'. In: *Physical Review A* 64.1 (June 2001), p. 013409. DOI: 10.1103/physreva.64.013409.

[77] V. P. Krainov. 'Ionization rates and energy and angular distributions at the barrier-suppression ionization of complex atoms and atomic ions'. In: *Journal of the Optical Society of America B* 14.2 (Feb. 1997), p. 425. DOI: 10.1364/josab.14.000425.

[78] X. M. Tong and C. D. Lin. 'Empirical formula for static field ionization rates of atoms and molecules by lasers in the barrier-suppression regime'. In: *Journal of Physics B: Atomic, Molecular and Optical Physics* 38.15 (July 2005), pp. 2593–2600. DOI: 10.1088/0953-4075/38/15/001.

[79] X. M. Tong, Z. X. Zhao and C. D. Lin. 'Theory of molecular tunneling ionization'. In: *Physical Review A* 66.3 (Sept. 2002), p. 033402. DOI: 10.1103/physreva.66.033402.

[80] S. Di Mitri. *Fundamentals of Particle Accelerator Physics*. Springer International Publishing, 2022. ISBN: 9783031076626. DOI: 10.1007/978-3-031-07662-6.

[81] W. D. Kilpatrick. 'Criterion for Vacuum Sparking Designed to Include Both rf and dc'. In: *Review of Scientific Instruments* 28.10 (Oct. 1957), pp. 824–826. ISSN: 1089-7623. DOI: 10.1063/1.1715731.

[82] W. Peter, R. J. Faehl, A. Kadish and L. E. Thode. 'Criteria for Vacuum Breakdown in RF Cavities'. In: *IEEE Transactions on Nuclear Science* 30.4 (Aug. 1983), pp. 3454–3456. DOI: 10.1109/tns.1983.4336689.

[83] J. Norem, Z. Insepov and I. Konkashbaev. 'Triggers for RF breakdown'. In: *Nuclear Instruments and Methods in Physics Research Section A: Accelerators, Spectrometers, Detectors and Associated Equipment* 537.3 (Feb. 2005), pp. 510–520. DOI: 10.1016/j.nima.2004.07.289.

[84] A. Grudiev, S. Calatroni and W. Wuensch. 'New local field quantity describing the high gradient limit of accelerating structures'. In: *Physical Review Special Topics - Accelerators and Beams* 12.10 (Oct. 2009), p. 102001. ISSN: 1098-4402. DOI: 10.1103/physrevstab.12.102001.

[85] H. S. Padamsee. 'Superconducting Radio-Frequency Cavities'. In: *Annual Review of Nuclear and Particle Science* 64.1 (Oct. 2014), pp. 175–196. DOI: 10.1146/annurev-nucl-102313-025612.

[86] J. M. Dawson. 'Nonlinear Electron Oscillations in a Cold Plasma'. In: *Physical Review* 113.2 (Jan. 1959), pp. 383–387. DOI: 10.1103/physrev.113.383.

[87] E. Esarey, C. B. Schroeder and W. P. Leemans. 'Physics of laser-driven plasma-based electron accelerators'. In: *Reviews of Modern Physics* 81.3 (Aug. 2009), pp. 1229–1285. DOI: 10.1103/revmodphys.81.1229.

[88] S. Corde et al. 'Multi-gigaelectronvolt acceleration of positrons in a self-loaded plasma wakefield'. In: *Nature* 524.7566 (Aug. 2015), pp. 442–445. DOI: 10.1038/nature14890.

[89] C. A. Lindstrøm et al. 'Measurement of Transverse Wakefields Induced by a Misaligned Positron Bunch in a Hollow Channel Plasma Accelerator'. In: *Physical Review Letters* 120.12 (Mar. 2018), p. 124802. ISSN: 1079-7114. DOI: 10.1103/physrevlett.120.124802.

[90] V. I. Veksler. 'Coherent principle of acceleration of charged particles'. In: CERN Symposium on High Energy Accelerators and Pion Physics (11th–23rd June 1965). CERN Yellow Reports: Conference Proceedings. CERN, 1956, pp. 80–83. DOI: 10.5170/CERN-1956-025.80.

[91] V. I. Veksler. 'The principle of coherent acceleration of charged particles'. In: *The Soviet Journal of Atomic Energy* 2.5 (Sept. 1957), pp. 525–528. DOI: 10.1007/bf01491001.

[92] R. D. Ruth, A. W. Chao, P. L. Morton and P. B. Wilson. 'A plasma wake field accelerator'. In: *Part. Accel.* 17 (1985), pp. 171–189. URL: https://cds.cern.ch/record/157249/files/p171.pdf.

[93] R. Keinigs and M. E. Jones. 'Two-dimensional dynamics of the plasma wakefield accelerator'. In: *Physics of Fluids* 30.1 (1987), p. 252. DOI: 10.1063/1.866183.

[94] A. Caldwell, K. Lotov, A. Pukhov and F. Simon. 'Proton-driven plasma-wakefield acceleration'. In: *Nature Physics* 5.5 (Apr. 2009), pp. 363–367. DOI: 10.1038/nphys1248.

[95] E. Adli et al. 'Acceleration of electrons in the plasma wakefield of a proton bunch'. In: *Nature* 561.7723 (Aug. 2018), pp. 363–367. DOI: 10.1038/s41586-018-0485-4.

[96] S. Gessner et al. 'Demonstration of a positron beam-driven hollow channel plasma wakefield accelerator'. In: *Nature Communications* 7.1 (June 2016). DOI: 10.1038/ncomms11785.

[97] J. D. Lawson. 'Lasers and Accelerators'. In: *IEEE Transactions on Nuclear Science* 26.3 (June 1979), pp. 4217–4219. ISSN: 0018-9499. DOI: 10.1109/tns.1979.4330749.

[98] R. B. Palmer. 'A Laser-Driven Grating Linac'. In: *Particle Accelerators* 11 (1980), pp. 81–90. URL: https://cds.cern.ch/record/1107986.

[99] O. Svelto. *Principles of Lasers*. Springer US, 1998. ISBN: 9781475762662. DOI: 10.1007/978-1-4757-6266-2.

[100] E. Esarey, P. Sprangle, J. Krall and A. Ting. 'Overview of plasma-based accelerator concepts'. In: *IEEE Transactions on Plasma Science* 24.2 (Apr. 1996), pp. 252–288. DOI: 10.1109/27.509991.

[101] E. A. Startsev and C. J. McKinstrie. 'Multiple scale derivation of the relativistic ponderomotive force'. In: *Physical Review E* 55.6 (June 1997), pp. 7527–7535. ISSN: 1095-3787. DOI: 10.1103/physreve.55.7527.

[102] B. Quesnel and P. Mora. 'Theory and simulation of the interaction of ultraintense laser pulses with electrons in vacuum'. In: *Physical Review E* 58.3 (Sept. 1998), pp. 3719–3732. ISSN: 1095-3787. DOI: 10.1103/physreve.58.3719.

[103] O. D. Jefimenko. 'Direct calculation of the electric and magnetic fields of an electric point charge moving with constant velocity'. In: *American Journal of Physics* 62.1 (Jan. 1994), pp. 79–85. ISSN: 1943-2909. DOI: 10.1119/1.17716.

[104] O. Heaviside. 'The electromagnetic effects of a moving charge'. In: *The Electrician* 22 (1888), pp. 147–148.

[105] O. Heaviside. *Electrical Papers*. Cambridge University Press, 2011. ISBN: 9781108028578. DOI: 10.1017/cbo9780511983139.

[106] M. Ferrario, M. Migliorati and L. Palumbo. 'Space Charge Effects'. en. In: *Proceedings of the CAS - CERN Accelerator School: Advanced Accelerator Physics, Trondheim, Norway, 18–29 August 2013, edited by W. Herr, CERN–2014–009 (CERN, Geneva, 2014)*. CERN, 2014, pp. 331–356. DOI: 10.5170/CERN-2014-009.331.

[107] J. B. Rosenzweig. 'Trapping, thermal effects, and wave breaking in the nonlinear plasma wake-field accelerator'. In: *Physical Review A* 38.7 (Oct. 1988), pp. 3634–3642. DOI: 10.1103/physreva.38.3634.

[108] J. B. Rosenzweig, B. Breizman, T. Katsouleas and J. J. Su. 'Acceleration and focusing of electrons in two-dimensional nonlinear plasma wake fields'. In: *Physical Review A* 44.10 (Nov. 1991), R6189–R6192. DOI: 10.1103/physreva.44.r6189.

[109] N. Barov, J. B. Rosenzweig, M. C. Thompson and R. B. Yoder. 'Energy loss of a high-charge bunched electron beam in plasma: Analysis'. In: *Physical Review Special Topics - Accelerators and Beams* 7.6 (June 2004), p. 061301. ISSN: 1098-4402. DOI: 10.1103/physrevstab.7.061301.

[110] J. B. Rosenzweig, N. Barov, M. C. Thompson and R. B. Yoder. 'Energy loss of a high charge bunched electron beam in plasma: Simulations, scaling, and accelerating wakefields'. In: *Physical Review Special Topics - Accelerators and Beams* 7.6 (June 2004), p. 061302. ISSN: 1098-4402. DOI: 10.1103/physrevstab.7.061302.

[111] P. Sprangle, E. Esarey and A. Ting. 'Nonlinear theory of intense laser-plasma interactions'. In: *Physical Review Letters* 64.17 (Apr. 1990), pp. 2011–2014. DOI: 10.1103/physrevlett.64.2011.

[112] T. J. Mehrling. 'Theoretical and numerical studies on the transport of transverse beam quality in plasma-based accelerators'. PhD thesis. Universität Hamburg, 2014.

[113] L. M. Gorbunov and V. I. Kirsanov. 'The excitation of plasma waves by an electromagnetic wave packet'. In: *Zhurnal Eksperimentalnoi i Teoreticheskoi Fiziki* 93 (Aug. 1987), pp. 509–518.

[114] W. Lu et al. 'Limits of linear plasma wakefield theory for electron or positron beams'. In: *Physics of Plasmas* 12.6 (June 2005), p. 063101. DOI: 10.1063/1.1905587.

[115] W. K. H. Panofsky and W. A. Wenzel. 'Some Considerations Concerning the Transverse Deflection of Charged Particles in Radio-Frequency Fields'. In: *Review of Scientific Instruments* 27.11 (Nov. 1956), pp. 967–967. ISSN: 1089-7623. DOI: 10.1063/1.1715427.

[116] J. B. Rosenzweig. 'Nonlinear plasma dynamics in the plasma wake-field accelerator'. In: *Physical Review Letters* 58.6 (Feb. 1987), pp. 555–558. DOI: 10.1103/physrevlett.58.555.

[117] S. V. Bulanov, V. I. Kirsanov and A. S. Sakharov. 'Excitation of ultrarelativistic plasma waves by pulse of electromagnetic radiation'. In: *Soviet Journal of Experimental and Theoretical Physics Letters* 50 (Aug. 1989), p. 198. URL: http://www.jetpletters.ru/ps/1127/article_17078.pdf.

[118] V. I. Berezhiani and I. G. Murusidze. 'Relativistic wake-field generation by an intense laser pulse in a plasma'. In: *Physics Letters A* 148.6–7 (Aug. 1990), pp. 338–340. ISSN: 0375-9601. DOI: 10.1016/0375-9601(90)90813-4.

[119] A. Pukhov and J. Meyer-ter-Vehn. 'Laser wake field acceleration: the highly non-linear broken-wave regime'. In: *Applied Physics B: Lasers and Optics* 74.4-5 (Apr. 2002), pp. 355–361. DOI: 10.1007/s003400200795.

[120] W. Lu et al. 'A nonlinear theory for multidimensional relativistic plasma wave wakefields'. In: *Physics of Plasmas* 13.5 (May 2006), p. 056709. DOI: 10.1063/1.2203364.

[121] I. Kostyukov, A. Pukhov and S. Kiselev. 'Phenomenological theory of laser-plasma interaction in "bubble" regime'. In: *Physics of Plasmas* 11.11 (Nov. 2004), pp. 5256–5264. DOI: 10.1063/1.1799371.

[122] K. V. Lotov. 'Blowout regimes of plasma wakefield acceleration'. In: *Physical Review E* 69.4 (Apr. 2004), p. 046405. DOI: 10.1103/physreve.69.046405.

[123] W. Lu et al. 'Nonlinear Theory for Relativistic Plasma Wakefields in the Blowout Regime'. In: *Physical Review Letters* 96.16 (Apr. 2006), p. 165002. DOI: 10.1103/physrevlett.96.165002.

[124] S. A. Yi, V. Khudik, C. Siemon and G. Shvets. 'Analytic model of electromagnetic fields around a plasma bubble in the blow-out regime'. In: *Physics of Plasmas* 20.1 (Jan. 2013). ISSN: 1089-7674. DOI: 10.1063/1.4775774.

[125] G. Stupakov. 'Short-range wakefields generated in the blowout regime of plasma-wakefield acceleration'. In: *Physical Review Accelerators and Beams* 21.4 (Apr. 2018), p. 041301. ISSN: 2469-9888. DOI: 10.1103/physrevaccelbeams.21.041301.

[126] A. A. Golovanov et al. 'Excitation of strongly nonlinear plasma wakefield by electron bunches'. In: *Plasma Physics and Controlled Fusion* 63.8 (June 2021), p. 085004. ISSN: 1361-6587. DOI: 10.1088/1361-6587/ac0352.

[127] A. Golovanov, I. Y. Kostyukov, A. Pukhov and V. Malka. 'Energy-Conserving Theory of the Blowout Regime of Plasma Wakefield'. In: *Physical Review Letters* 130.10 (Mar. 2023), p. 105001. ISSN: 1079-7114. DOI: 10.1103/physrevlett.130.105001.

[128] C. Nieter and J. R. Cary. 'VORPAL: a versatile plasma simulation code'. In: *Journal of Computational Physics* 196.2 (May 2004), pp. 448–473. ISSN: 0021-9991. DOI: 10.1016/j.jcp.2003.11.004.

[129] M. J. Hogan et al. 'Plasma wakefield acceleration experiments at FACET'. In: *New Journal of Physics* 12.5 (May 2010), p. 055030. ISSN: 1367-2630. DOI: 10.1088/1367-2630/12/5/055030.

[130] B. Cathey, S. Cousineau, A. Aleksandrov and A. Zhukov. 'First Six Dimensional Phase Space Measurement of an Accelerator Beam'. In: *Physical Review Letters* 121.6 (Aug. 2018), p. 064804. ISSN: 1079-7114. DOI: 10.1103/physrevlett.121.064804.

[131] H. Wiedemann. *Particle Accelerator Physics*. Springer International Publishing, 2015. ISBN: 9783319183176. DOI: 10.1007/978-3-319-18317-6.

[132] K. Floettmann. 'Some basic features of the beam emittance'. In: *Physical Review Special Topics - Accelerators and Beams* 6.3 (Mar. 2003), p. 034202. DOI: 10.1103/physrevstab.6.034202.

[133] E. D. Courant and H. S. Snyder. 'Theory of the alternating-gradient synchrotron'. In: *Annals of Physics* 3.1 (Jan. 1958), pp. 1–48. DOI: 10.1016/0003-4916(58)90012-5.

[134] G. Ha et al. 'Bunch shaping in electron linear accelerators'. In: *Reviews of Modern Physics* 94.2 (May 2022), p. 025006. DOI: 10.1103/revmodphys.94.025006.

[135] M. Migliorati et al. 'Intrinsic normalized emittance growth in laser-driven electron accelerators'. In: *Physical Review Special Topics - Accelerators and Beams* 16.1 (Jan. 2013), p. 011302. DOI: 10.1103/physrevstab.16.011302.

[136] A. Cianchi et al. 'Observations and diagnostics in high brightness beams'. In: *Nuclear Instruments and Methods in Physics Research Section A: Accelerators, Spectrometers, Detectors and Associated Equipment* 829 (Sept. 2016), pp. 343–347. DOI: 10.1016/j.nima.2016.03.076.

[137] P. W. Hawkes and E. Kasper. *Principles of Electron Optics Volume Two: Applied Geometrical Optics. Applied Geometrical Optics*. Elsevier, 2018, p. 770. ISBN: 9780128133699. DOI: 10.1016/c2015-0-06653-9.

[138] M. Reiser. *Theory and Design of Charged Particle Beams*. 2nd ed. Wiley-VCH, 2008, p. 660. ISBN: 9783527407415.

[139] S. Di Mitri. 'On the Importance of Electron Beam Brightness in High Gain Free Electron Lasers'. In: *Photonics* 2.2 (Mar. 2015), pp. 317–341. ISSN: 2304-6732. DOI: 10.3390/photonics2020317.

[140] S. Di Mitri and M. Cornacchia. 'Electron beam brightness in linac drivers for free-electron-lasers'. In: *Physics Reports* 539.1 (June 2014), pp. 1–48. ISSN: 0370-1573. DOI: 10.1016/j.physrep.2014.01.005.

[141] S. G. Anderson, J. B. Rosenzweig, G. P. LeSage and J. K. Crane. 'Space-charge effects in high brightness electron beam emittance measurements'. In: *Physical Review Special Topics - Accelerators and Beams* 5.1 (Jan. 2002), p. 014201. ISSN: 1098-4402. DOI: 10.1103/physrevstab.5.014201.

[142] J. B. Rosenzweig et al. 'Effects of Ion Motion in Intense Beam-Driven Plasma Wakefield Accelerators'. In: *Physical Review Letters* 95.19 (Oct. 2005), p. 195002. ISSN: 1079-7114. DOI: 10.1103/physrevlett.95.195002.

[143] C. A. Lindstrøm and M. Thévenet. 'Emittance preservation in advanced accelerators'. In: *Journal of Instrumentation* 17.05 (May 2022), P05016. DOI: 10.1088/1748-0221/17/05/p05016.

[144] P. G. O'Shea. 'Reversible and irreversible emittance growth'. In: *Physical Review E* 57.1 (Jan. 1998), pp. 1081–1087. ISSN: 1095-3787. DOI: 10.1103/physreve.57.1081.

[145] K. A. Marsh et al. 'Beam Matching to a Plasma Wake Field Accelerator using a Ramped Density Profile at the Plasma Boundary'. In: *Proceedings of the 2005 Particle Accelerator Conference*. IEEE, 2005. DOI: 10.1109/pac.2005.1591234.

[146] Y. Glinec et al. 'Direct observation of betatron oscillations in a laser-plasma electron accelerator'. In: *EPL (Europhysics Letters)* 81.6 (Feb. 2008), p. 64001. ISSN: 1286-4854. DOI: 10.1209/0295-5075/81/64001.

[147] T. Mehrling et al. 'Transverse emittance growth in staged laser-wakefield acceleration'. In: *Physical Review Special Topics - Accelerators and Beams* 15.11 (Nov. 2012), p. 111303. DOI: 10.1103/physrevstab.15.111303.

[148] R. Ariniello et al. 'Transverse beam dynamics in a plasma density ramp'. In: *Physical Review Accelerators and Beams* 22.4 (Apr. 2019), p. 041304. ISSN: 2469-9888. DOI: 10.1103/physrevaccelbeams.22.041304.

[149] R. Ariniello. 'Emittance Preservation in a Plasma Wakefield Accelerator'. PhD thesis. University of Colorado, 2022.

[150] P. Michel et al. 'Radiative damping and electron beam dynamics in plasma-based accelerators'. In: *Physical Review E* 74.2 (Aug. 2006), p. 026501. ISSN: 1550-2376. DOI: 10.1103/physreve.74.026501.

[151] C. A. Lindstrøm. 'Staging of plasma-wakefield accelerators'. In: *Physical Review Accelerators and Beams* 24.1 (Jan. 2021), p. 014801. ISSN: 2469-9888. DOI: 10.1103/physrevaccelbeams.24.014801.

[152] R. L. Williams and T. Katsouleas. 'Numerical studies on the ramped density plasma lens'. In: *AIP Conference Proceedings*. AIP, 1992. DOI: 10.1063/1.44073.

[153] M. Sands. *A Beta Mismatch Parameter*. Tech. rep. SLAC-AP-85. Stanford Linear Accelerator Center, 1991. URL: https://www.slac.stanford.edu/cgi-bin/getdoc/slac-ap-085.pdf.

[154] B. W. Montague. *Linear optics for improved chromaticity correction*. Tech. rep. LEP Note 165. LEP Notes - 1979. CERN, 1979. URL: https://cds.cern.ch/record/67243.

[155] C. A. Lindstrøm and E. Adli. 'Design of general apochromatic drift-quadrupole beam lines'. In: *Physical Review Accelerators and Beams* 19.7 (July 2016), p. 071002. ISSN: 2469-9888. DOI: 10.1103/physrevaccelbeams.19.071002.

[156] I. Dornmair, K. Floettmann and A. Maier. 'Emittance conservation by tailored focusing profiles in a plasma accelerator'. In: *Physical Review Special Topics - Accelerators and Beams* 18.4 (Apr. 2015), p. 041302. DOI: 10.1103/physrevstab.18.041302.

[157] X. Xu et al. 'Physics of Phase Space Matching for Staging Plasma and Traditional Accelerator Components Using Longitudinally Tailored Plasma Profiles'. In: *Physical Review Letters* 116.12 (Mar. 2016), p. 124801. DOI: 10.1103/physrevlett.116.124801.

[158] X. Li, A. Chancé and P. A. P. Nghiem. 'Preserving emittance by matching out and matching in plasma wakefield acceleration stage'. In: *Physical Review Accelerators and Beams* 22.2 (Feb. 2019), p. 021304. DOI: 10.1103/physrevaccelbeams.22.021304.

[159] M. D. Litos et al. 'Beam emittance preservation using Gaussian density ramps in a beam-driven plasma wakefield accelerator'. In: *Philosophical Transactions of the Royal Society A: Mathematical, Physical and Engineering Sciences* 377.2151 (June 2019), p. 20180181. ISSN: 1471-2962. DOI: 10.1098/rsta.2018.0181.

[160] Y. Zhao et al. 'Emittance preservation through density ramp matching sections in a plasma wakefield accelerator'. In: *Physical Review Accelerators and Beams* 23.1 (Jan. 2020), p. 011302. ISSN: 2469-9888. DOI: 10.1103/physrevaccelbeams.23.011302.

[161] A. Ferran Pousa, A. Martinez de la Ossa and R. W. Assmann. 'Intrinsic energy spread and bunch length growth in plasma-based accelerators due to betatron motion'. In: *Scientific Reports* 9.1 (Nov. 2019). DOI: 10.1038/s41598-019-53887-8.

[162] T. C. Katsouleas et al. 'Beam Loading in Plasma Accelerators'. In: *Particle Accelerators* 22 (1987), pp. 81–99.

[163] S. Wilks et al. 'Beam Loading in Plasma Waves'. In: *IEEE Transactions on Plasma Science* 15.2 (1987), pp. 210–217. DOI: 10.1109/tps.1987.4316687.

[164] S. Van der Meer. *Improving the power efficiency of the plasma wakefield accelerator*. Tech. rep. CERN-PS-85-65-AA, CLIC-Note-3. CERN, 1985. URL: https://cds.cern.ch/record/163918.

[165] S. Gordienko and A. Pukhov. 'Scalings for ultrarelativistic laser plasmas and quasimonoenergetic electrons'. In: *Physics of Plasmas* 12.4 (Apr. 2005), p. 043109. DOI: 10.1063/1.1884126.

[166] W. Lu et al. 'Generating multi-GeV electron bunches using single stage laser wakefield acceleration in a 3D nonlinear regime'. In: *Physical Review Special Topics - Accelerators and Beams* 10.6 (June 2007), p. 061301. DOI: 10.1103/physrevstab.10.061301.

[167] E. Guillaume et al. 'Physics of fully-loaded laser-plasma accelerators'. In: *Physical Review Special Topics - Accelerators and Beams* 18.6 (June 2015), p. 061301. DOI: 10.1103/physrevstab.18.061301.

[168] M. Tzoufras et al. 'Beam Loading in the Nonlinear Regime of Plasma-Based Acceleration'. In: *Physical Review Letters* 101.14 (Sept. 2008), p. 145002. DOI: 10.1103/physrevlett.101.145002.

[169] M. Tzoufras et al. 'Beam loading by electrons in nonlinear plasma wakes'. In: *Physics of Plasmas* 16.5 (May 2009), p. 056705. DOI: 10.1063/1.3118628.

[170] M. Litos et al. '9 GeV energy gain in a beam-driven plasma wakefield accelerator'. In: *Plasma Physics and Controlled Fusion* 58.3 (Feb. 2016), p. 034017. DOI: 10.1088/0741-3335/58/3/034017.

[171] G. Li et al. 'Control of electron beam energy-spread by beam loading effects in a laser-plasma accelerator'. In: *Plasma Physics and Controlled Fusion* 62.5 (Mar. 2020), p. 055004. DOI: 10.1088/1361-6587/ab7c50.

[172] M. Kirchen et al. 'Optimal Beam Loading in a Laser-Plasma Accelerator'. In: *Physical Review Letters* 126.17 (Apr. 2021), p. 174801. DOI: 10.1103/physrevlett.126.174801.

[173] C. Lindstrøm et al. 'Energy-Spread Preservation and High Efficiency in a Plasma-Wakefield Accelerator'. In: *Physical Review Letters* 126.1 (Jan. 2021), p. 014801. DOI: 10.1103/physrevlett.126.014801.

[174] G. G. Manahan et al. 'Single-stage plasma-based correlated energy spread compensation for ultrahigh 6D brightness electron beams'. In: *Nature Communications* 8.1 (June 2017). DOI: 10.1038/ncomms15705.

[175] G. G. Manahan et al. 'Advanced schemes for underdense plasma photocathode wakefield accelerators: pathways towards ultrahigh brightness electron beams'. In: *Philosophical Transactions of the Royal Society A: Mathematical, Physical and Engineering Sciences* 377.2151 (June 2019), p. 20180182. DOI: 10.1098/rsta.2018.0182.

[176] A. Koehler et al. 'Restoring betatron phase coherence in a beam-loaded laser-wakefield accelerator'. In: *Physical Review Accelerators and Beams* 24.9 (Sept. 2021), p. 091302. DOI: 10.1103/physrevaccelbeams.24.091302.

[177] D. H. Whittum et al. 'Electron-hose instability in the ion-focused regime'. In: *Physical Review Letters* 67.8 (Aug. 1991), pp. 991–994. ISSN: 0031-9007. DOI: 10.1103/physrevlett.67.991.

[178] V. E. Balakin, A. V. Novokhatsky and V. P. Smirnov. 'VLEPP: TRANSVERSE BEAM DYNAMICS'. In: *Conf. Proc. C* 830811 (1983). Ed. by F. T. Cole and R. Donaldson, pp. 119–120.

[179] G. V. Stupakov. *BNS damping of beam breakup instability*. Tech. rep. SLAC-AP-108. Stanford Linear Accelerator Center, Aug. 1997.

[180] C. L. Bohn and K.-Y. Ng. 'Preserving High Multibunch Luminosity in Linear Colliders'. In: *Physical Review Letters* 85.5 (July 2000), pp. 984–987. ISSN: 1079-7114. DOI: 10.1103/physrevlett.85.984.

[181] B. Hidding et al. 'Fundamentals and Applications of Hybrid LWFA-PWFA'. In: *Applied Sciences* 9.13 (June 2019), p. 2626. DOI: 10.3390/app9132626.

[182] C. B. Schroeder, C. Benedetti, E. Esarey and W. P. Leemans. 'Nonlinear Pulse Propagation and Phase Velocity of Laser-Driven Plasma Waves'. In: *Physical Review Letters* 106.13 (Mar. 2011), p. 135002. DOI: 10.1103/physrevlett.106.135002.

[183] D. Cardenas et al. 'Electron bunch evolution in laser-wakefield acceleration'. In: *Physical Review Accelerators and Beams* 23.11 (Nov. 2020), p. 112803. DOI: 10.1103/physrevaccelbeams.23.112803.

[184] W. B. Mori. 'The physics of the nonlinear optics of plasmas at relativistic intensities for short-pulse lasers'. In: *IEEE Journal of Quantum Electronics* 33.11 (1997), pp. 1942–1953. ISSN: 0018-9197. DOI: 10.1109/3.641309.

[185] T. Katsouleas. 'Physical mechanisms in the plasma wake-field accelerator'. In: *Physical Review A* 33.3 (Mar. 1986), pp. 2056–2064. DOI: 10.1103/physreva.33.2056.

[186] W. Rittershofer et al. 'Tapered plasma channels to phase-lock accelerating and focusing forces in laser-plasma accelerators'. In: *Physics of Plasmas* 17.6 (June 2010). ISSN: 1089-7674. DOI: 10.1063/1.3430638.

[187] E. Guillaume et al. 'Electron Rephasing in a Laser-Wakefield Accelerator'. In: *Physical Review Letters* 115.15 (Oct. 2015), p. 155002. ISSN: 1079-7114. DOI: 10.1103/physrevlett.115.155002.

[188] A. Döpp et al. 'Energy boost in laser wakefield accelerators using sharp density transitions'. In: *Physics of Plasmas* 23.5 (Apr. 2016). ISSN: 1089-7674. DOI: 10.1063/1.4946018.

[189] A. Debus et al. 'Circumventing the Dephasing and Depletion Limits of Laser-Wakefield Acceleration'. In: *Physical Review X* 9.3 (Sept. 2019), p. 031044. DOI: 10.1103/physrevx.9.031044.

[190] K. G. Miller et al. 'Dephasingless laser wakefield acceleration in the bubble regime'. In: *Scientific Reports* 13.1 (Dec. 2023). ISSN: 2045-2322. DOI: 10.1038/s41598-023-48249-4.

[191] H. L. Buchanan. 'Electron beam propagation in the ion-focused regime'. In: *The Physics of Fluids* 30.1 (Jan. 1987), pp. 221–231. ISSN: 0031-9171. DOI: 10.1063/1.866173.

[192] R. G. Hemker, W. B. Mori, S. Lee and T. Katsouleas. 'Dynamic effects in plasma wakefield excitation'. In: *Physical Review Special Topics - Accelerators and Beams* 3.6 (June 2000), p. 061301. DOI: 10.1103/physrevstab.3.061301.

[193] A. Butler, D. J. Spence and S. M. Hooker. 'Guiding of High-Intensity Laser Pulses with a Hydrogen-Filled Capillary Discharge Waveguide'. In: *Physical Review Letters* 89.18 (Oct. 2002), p. 185003. ISSN: 1079-7114. DOI: 10.1103/physrevlett.89.185003.

[194] C. G. R. Geddes et al. 'Production of high-quality electron bunches by dephasing and beam loading in channeled and unchanneled laser plasma accelerators'. In: *Physics of Plasmas* 12.5 (May 2005), p. 056709. DOI: 10.1063/1.1882352.

[195] W. P. Leemans et al. 'GeV electron beams from a centimetre-scale accelerator'. In: *Nature Physics* 2.10 (Sept. 2006), pp. 696–699. DOI: 10.1038/nphys418.

[196] K. Nakamura et al. 'GeV electron beams from a centimeter-scale channel guided laser wakefield accelerator'. In: *Physics of Plasmas* 14.5 (May 2007), p. 056708. DOI: 10.1063/1.2718524.

[197] A. J. Goers et al. 'Laser wakefield acceleration of electrons with ionization injection in a pure N5+ plasma waveguide'. In: *Applied Physics Letters* 104.21 (May 2014), p. 214105. DOI: 10.1063/1.4880102.

[198] R. J. Shalloo et al. 'Low-density hydrodynamic optical-field-ionized plasma channels generated with an axicon lens'. In: *Physical Review Accelerators and Beams* 22.4 (Apr. 2019), p. 041302. ISSN: 2469-9888. DOI: 10.1103/physrevaccelbeams.22.041302.

[199] B. Miao et al. 'Optical Guiding in Meter-Scale Plasma Waveguides'. In: *Physical Review Letters* 125.7 (Aug. 2020), p. 074801. ISSN: 1079-7114. DOI: 10.1103/physrevlett.125.074801.

[200] K. Oubrerie et al. 'Controlled acceleration of GeV electron beams in an all-optical plasma waveguide'. In: *Light: Science & Applications* 11.1 (June 2022). DOI: 10.1038/s41377-022-00862-0.

[201] B. Miao et al. 'Multi-GeV Electron Bunches from an All-Optical Laser Wakefield Accelerator'. In: *Physical Review X* 12.3 (Sept. 2022), p. 031038. ISSN: 2160-3308. DOI: 10.1103/physrevx.12.031038.

[202] P. Sprangle, C.-M. Tang and E. Esarey. 'Relativistic Self-Focusing of Short-Pulse Radiation Beams in Plasmas'. In: *IEEE Transactions on Plasma Science* 15.2 (1987), pp. 145–153. ISSN: 0093-3813. DOI: 10.1109/tps.1987.4316677.

[203] E. Esarey, P. Sprangle, J. Krall and A. Ting. 'Self-focusing and guiding of short laser pulses in ionizing gases and plasmas'. In: *IEEE Journal of Quantum Electronics* 33.11 (1997), pp. 1879–1914. ISSN: 0018-9197. DOI: 10.1109/3.641305.

[204] G.-Z. Sun, E. Ott, Y. C. Lee and P. Guzdar. 'Self-focusing of short intense pulses in plasmas'. In: *Physics of Fluids* 30.2 (1987), p. 526. DOI: 10.1063/1.866349.

[205] J. E. Ralph et al. 'Self-Guiding of Ultrashort, Relativistically Intense Laser Pulses through Underdense Plasmas in the Blowout Regime'. In: *Physical Review Letters* 102.17 (Apr. 2009), p. 175003. DOI: 10.1103/physrevlett.102.175003.

[206] O. Jakobsson et al. 'Tailored plasma-density profiles for enhanced energy extraction in passive plasma beam dumps'. In: *Plasma Physics and Controlled Fusion* 61.12 (Oct. 2019), p. 124002. ISSN: 1361-6587. DOI: 10.1088/1361-6587/ab4cfb.

[207] F. Peña et al. 'Energy depletion and re-acceleration of driver electrons in a plasma-wakefield accelerator'. In: *Physical Review Research* 6.4 (Nov. 2024), p. 043090. ISSN: 2643-1564. DOI: 10.1103/physrevresearch.6.043090.

[208] K. L. F. Bane, P. Chen and P. B. Wilson. 'On Collinear Wake Field Acceleration'. In: *IEEE Transactions on Nuclear Science* 32.5 (Oct. 1985), pp. 3524–3526. ISSN: 0018-9499. DOI: 10.1109/tns.1985.4334416.

[209] K. L. F. Bane, P. B. Wilson and T. Weiland. 'Wake fields and wake field acceleration'. In: *AIP Conference Proceedings*. Vol. 127. AIP, 1985, pp. 875–928. DOI: 10.1063/1.35182.

[210] P. Chen et al. 'Energy Transfer in the Plasma Wake-Field Accelerator'. In: *Physical Review Letters* 56.12 (Mar. 1986), pp. 1252–1255. DOI: 10.1103/physrevlett.56.1252.

[211] M. Litos et al. 'High-efficiency acceleration of an electron beam in a plasma wakefield accelerator'. In: *Nature* 515.7525 (Nov. 2014), pp. 92–95. DOI: 10.1038/nature13882.

[212] P. B. Wilson. *Transient beam loading in electron-positron storage rings*. Tech. rep. CERN-ISR-TH-78-23-rev, ISR-TH-78-23-rev. Geneva: CERN, 1978. URL: https://cds.cern.ch/record/119634.

[213] C. Joshi et al. 'High energy density plasma science with an ultrarelativistic electron beam'. In: *Physics of Plasmas* 9.5 (May 2002), pp. 1845–1855. ISSN: 1089-7674. DOI: 10.1063/1.1455003.

[214] K. V. Lotov. 'Efficient operating mode of the plasma wakefield accelerator'. In: *Physics of Plasmas* 12.5 (May 2005). ISSN: 1089-7674. DOI: 10.1063/1.1889444.

[215] F. Lemery and P. Piot. 'Tailored electron bunches with smooth current profiles for enhanced transformer ratios in beam-driven acceleration'. In: *Physical Review Special Topics - Accelerators and Beams* 18.8 (Aug. 2015), p. 081301. ISSN: 1098-4402. DOI: 10.1103/physrevstab.18.081301.

[216] G. Loisch et al. 'Observation of High Transformer Ratio Plasma Wakefield Acceleration'. In: *Physical Review Letters* 121.6 (Aug. 2018), p. 064801. DOI: 10.1103/physrevlett.121.064801.

[217] R. Roussel et al. 'Single Shot Characterization of High Transformer Ratio Wakefields in Nonlinear Plasma Acceleration'. In: *Physical Review Letters* 124.4 (Jan. 2020), p. 044802. DOI: 10.1103/physrevlett.124.044802.

[218] S. V. Bulanov et al. 'Nonlinear depletion of ultrashort and relativistically strong laser pulses in an underdense plasma'. In: *Physics of Fluids B: Plasma Physics* 4.7 (Mar. 1992), pp. 1935–1942. DOI: 10.1063/1.860046.

[219] J. Faure et al. 'Observation of Laser-Pulse Shortening in Nonlinear Plasma Waves'. In: *Physical Review Letters* 95.20 (Nov. 2005), p. 205003. ISSN: 1079-7114. DOI: 10.1103/physrevlett.95.205003.

[220] B. A. Shadwick, C. B. Schroeder and E. Esarey. 'Nonlinear laser energy depletion in laser-plasma accelerators'. In: *Physics of Plasmas* 16.5 (May 2009). ISSN: 1089-7674. DOI: 10.1063/1.3124185.

[221] N. E. Andreev et al. 'Analysis of laser wakefield dynamics in capillary tubes'. In: *New Journal of Physics* 12.4 (Apr. 2010), p. 045024. ISSN: 1367-2630. DOI: 10.1088/1367-2630/12/4/045024.

[222] S. Shiraishi et al. 'Laser red shifting based characterization of wakefield excitation in a laser-plasma accelerator'. In: *Physics of Plasmas* 20.6 (June 2013), p. 063103. DOI: 10.1063/1.4810802.

[223] C. D. Decker, W. B. Mori, K.-C. Tzeng and T. Katsouleas. 'The evolution of ultra-intense, short-pulse lasers in underdense plasmas'. In: *Physics of Plasmas* 3.5 (May 1996), pp. 2047–2056. ISSN: 1089-7674. DOI: 10.1063/1.872001.

[224] M. C. Downer et al. 'Diagnostics for plasma-based electron accelerators'. In: *Reviews of Modern Physics* 90.3 (Aug. 2018), p. 035002. ISSN: 1539-0756. DOI: 10.1103/revmodphys.90.035002.

[225] J. B. Rosenzweig et al. 'Experimental Observation of Plasma Wake-Field Acceleration'. In: *Physical Review Letters* 61.1 (July 1988), pp. 98–101. DOI: 10.1103/physrevlett.61.98.

[226] J. B. Rosenzweig et al. 'Experimental measurement of nonlinear plasma wake fields'. In: *Physical Review A* 39.3 (Feb. 1989), pp. 1586–1589. DOI: 10.1103/physreva.39.1586.

[227] K. Nakajima et al. 'Plasma wake-field accelerator experiments at KEK'. In: *Nuclear Instruments and Methods in Physics Research Section A: Accelerators, Spectrometers, Detectors and Associated Equipment* 292.1 (June 1990), pp. 12–20. DOI: 10.1016/0168-9002(90)91729-u.

[228] E. Kallos et al. 'High-Gradient Plasma-Wakefield Acceleration with Two Subpicosecond Electron Bunches'. In: *Physical Review Letters* 100.7 (Feb. 2008), p. 074802. DOI: 10.1103/physrevlett.100.074802.

[229] S. Schröder et al. 'Tunable and precise two-bunch generation at FLASHForward'. In: *Journal of Physics: Conference Series* 1596.1 (July 2020), p. 012002. DOI: 10.1088/1742-6596/1596/1/012002.

[230] R. Pompili et al. 'Energy spread minimization in a beam-driven plasma wakefield accelerator'. In: *Nature Physics* 17.4 (Jan. 2021), pp. 499–503. DOI: 10.1038/s41567-020-01116-9.

[231] R. Pompili et al. 'Free-electron lasing with compact beam-driven plasma wakefield accelerator'. In: *Nature* 605.7911 (May 2022), pp. 659–662. DOI: 10.1038/s41586-022-04589-1.

[232] B. Hidding et al. 'Monoenergetic Energy Doubling in a Hybrid Laser-Plasma Wakefield Accelerator'. In: *Physical Review Letters* 104.19 (May 2010), p. 195002. DOI: 10.1103/physrevlett.104.195002.

[233] M. F. Gilljohann. 'Towards Hybrid Wakefield Acceleration'. PhD thesis. Ludwig-Maximilians-Universität München, 2021.

[234] A. Doche et al. 'Acceleration of a trailing positron bunch in a plasma wakefield accelerator'. In: *Scientific Reports* 7.1 (Oct. 2017). DOI: 10.1038/s41598-017-14524-4.

[235] C. E. Clayton et al. 'Ultrahigh-gradient acceleration of injected electrons by laser-excited relativistic electron plasma waves'. In: *Physical Review Letters* 70.1 (Jan. 1993), pp. 37–40. DOI: 10.1103/physrevlett.70.37.

[236] M. Everett et al. 'Trapped electron acceleration by a laser-driven relativistic plasma wave'. In: *Nature* 368.6471 (Apr. 1994), pp. 527–529. DOI: 10.1038/368527a0.

[237] N. A. Ebrahim. 'Optical mixing of laser light in a plasma and electron acceleration by relativistic electron plasma waves'. In: *Journal of Applied Physics* 76.11 (Dec. 1994), pp. 7645–7647. DOI: 10.1063/1.357937.

[238] F. Amiranoff et al. 'Observation of Laser Wakefield Acceleration of Electrons'. In: *Physical Review Letters* 81.5 (Aug. 1998), pp. 995–998. DOI: 10.1103/physrevlett.81.995.

[239] E. N. Svystun et al. 'Two-stage laser-driven plasma acceleration with external injection for EuPRAXIA'. In: *Journal of Physics: Conference Series* 1067 (Sept. 2018), p. 042011. DOI: 10.1088/1742-6596/1067/4/042011.

[240] E. Svystun et al. 'Beam quality preservation studies in a laser-plasma accelerator with external injection for EuPRAXIA'. In: *Nuclear Instruments and Methods in Physics Research Section A: Accelerators, Spectrometers, Detectors and Associated Equipment* 909 (Nov. 2018), pp. 90–94. DOI: 10.1016/j.nima.2018.02.060.

[241] B. Marchetti et al. 'Electron-beam manipulation techniques in the SINBAD Linac for external injection in plasma wake-field acceleration'. In: *Nuclear Instruments and Methods in Physics Research Section A: Accelerators, Spectrometers, Detectors and Associated Equipment* 829 (Sept. 2016), pp. 278–283. DOI: 10.1016/j.nima.2016.03.041.

[242] A. R. Rossi et al. 'The External-Injection experiment at the SPARC_LAB facility'. In: *Nuclear Instruments and Methods in Physics Research Section A: Accelerators, Spectrometers, Detectors and Associated Equipment* 740 (Mar. 2014), pp. 60–66. DOI: 10.1016/j.nima.2013.10.063.

[243] B. Marchetti, R. Assmann, U. Dorda and J. Zhu. 'Conceptual and Technical Design Aspects of Accelerators for External Injection in LWFA'. In: *Applied Sciences* 8.5 (May 2018), p. 757. DOI: 10.3390/app8050757.

[244] Y. Wu et al. 'High-throughput injection–acceleration of electron bunches from a linear accelerator to a laser wakefield accelerator'. In: *Nature Physics* 17.7 (Mar. 2021), pp. 801–806. DOI: 10.1038/s41567-021-01202-6.

[245] A. Ferran Pousa, R. Assmann, R. Brinkmann and A. Martinez de la Ossa. 'External injection into a laser-driven plasma accelerator with sub-femtosecond timing jitter'. In: *Journal of Physics: Conference Series* 874 (July 2017), p. 012032. DOI: 10.1088/1742-6596/874/1/012032.

[246] A. Ferran Pousa, A. Martinez de la Ossa, R. Brinkmann and R. W. Assmann. 'Compact Multistage Plasma-Based Accelerator Design for Correlated Energy Spread Compensation'. In: *Physical Review Letters* 123.5 (July 2019), p. 054801. DOI: 10.1103/physrevlett.123.054801.

[247] A. I. Akhiezer and R. V. Polovin. 'Theory of wave motion of an electron plasma'. In: *Soviet Phys. JETP* 3 (1956), pp. 696–705.

[248] W. B. Mori and T. Katsouleas. 'Wavebreaking of longitudinal plasma oscillations'. In: *Physica Scripta* T30 (Jan. 1990), pp. 127–133. DOI: 10.1088/0031-8949/1990/t30/018.

[249] E. Esarey and M. Pilloff. 'Trapping and acceleration in nonlinear plasma waves'. In: *Physics of Plasmas* 2.5 (May 1995), pp. 1432–1436. DOI: 10.1063/1.871358.

[250] T. P. Coffey. 'Breaking of Large Amplitude Plasma Oscillations'. In: *The Physics of Fluids* 14.7 (July 1971), pp. 1402–1406. DOI: 10.1063/1.1693620.

[251] T. Katsouleas and W. B. Mori. 'Wave-Breaking Amplitude of Relativistic Oscillations in a Thermal Plasma'. In: *Physical Review Letters* 61.1 (July 1988), pp. 90–93. ISSN: 0031-9007. DOI: 10.1103/physrevlett.61.90.

[252] Z. M. Sheng and J. Meyer-ter-Vehn. 'Relativistic wave breaking in warm plasmas'. In: *Physics of Plasmas* 4.2 (Feb. 1997), pp. 493–495. DOI: 10.1063/1.872116.

[253] C. B. Schroeder, E. Esarey and B. A. Shadwick. 'Warm wave breaking of nonlinear plasma waves with arbitrary phase velocities'. In: *Physical Review E* 72.5 (Nov. 2005), p. 055401. DOI: 10.1103/physreve.72.055401.

[254] C. B. Schroeder, E. Esarey, B. A. Shadwick and W. P. Leemans. 'Trapping, dark current, and wave breaking in nonlinear plasma waves'. In: *Physics of Plasmas* 13.3 (Mar. 2006), p. 033103. DOI: 10.1063/1.2173960.

[255] S. V. Bulanov, F. Pegoraro, A. M. Pukhov and A. S. Sakharov. 'Transverse-Wake Wave Breaking'. In: *Physical Review Letters* 78.22 (June 1997), pp. 4205–4208. DOI: 10.1103/physrevlett.78.4205.

[256] S. Bulanov, F. Pegoraro and J.-i. Sakai. 'Variety of nonlinear wave-breaking'. In: *Nuclear Instruments and Methods in Physics Research Section A: Accelerators, Spectrometers, Detectors and Associated Equipment* 410.3 (June 1998), pp. 477–487. ISSN: 0168-9002. DOI: 10.1016/s0168-9002(98)00155-7.

[257] S. V. Bulanov et al. 'Electron bunch acceleration in the wake wave breaking regime'. In: *Plasma Physics Reports* 32.4 (Apr. 2006), pp. 263–281. ISSN: 1562-6938. DOI: 10.1134/s1063780x06040015.

[258] S. V. Bulanov, F. Pegoraro and A. M. Pukhov. 'Two-Dimensional Regimes of Self-Focusing, Wake Field Generation, and Induced Focusing of a Short Intense Laser Pulse in an Underdense Plasma'. In: *Physical Review Letters* 74.5 (Jan. 1995), pp. 710–713. DOI: 10.1103/physrevlett.74.710.

[259] W. Lu. 'Nonlinear Plasma Wakefield Theory and Optimum Scaling for Laser WakefieldAccelerator (LWFA) in the Blowout Regime'. PhD thesis. University of California Los Angeles, 2006.

[260] H. Xu et al. 'Electron self-injection and acceleration driven by a tightly focused intense laser beam in an underdense plasma'. In: *Physics of Plasmas* 12.1 (Jan. 2005), p. 013105. DOI: 10.1063/1.1827625.

[261] A. Oguchi et al. 'Multiple self-injection in the acceleration of monoenergetic electrons by a laser wake field'. In: *Physics of Plasmas* 15.4 (2008), p. 043102. DOI: 10.1063/1.2833593.

[262] S. Kalmykov, S. A. Yi, V. Khudik and G. Shvets. 'Electron Self-Injection and Trapping into an Evolving Plasma Bubble'. In: *Physical Review Letters* 103.13 (Sept. 2009), p. 135004. DOI: 10.1103/physrevlett.103.135004.

[263] A. Zhidkov et al. 'Characterization of electron self-injection in laser wake field acceleration due to the parametric resonance'. In: *Physics of Plasmas* 17.8 (Aug. 2010). ISSN: 1089-7674. DOI: 10.1063/1.3458669.

[264] S. Y. Kalmykov et al. 'Electron self-injection into an evolving plasma bubble: Quasi-monoenergetic laser-plasma acceleration in the blowout regime'. In: *Physics of Plasmas* 18.5 (May 2011), p. 056704. DOI: 10.1063/1.3566062.

[265] S. A. Yi, V. Khudik, S. Y. Kalmykov and G. Shvets. 'Hamiltonian analysis of electron self-injection and acceleration into an evolving plasma bubble'. In: *Plasma Physics and Controlled Fusion* 53.1 (Dec. 2010), p. 014012. ISSN: 1361-6587. DOI: 10.1088/0741-3335/53/1/014012.

[266] C. Benedetti et al. 'Numerical investigation of electron self-injection in the nonlinear bubble regime'. In: *Physics of Plasmas* 20.10 (Oct. 2013), p. 103108. DOI: 10.1063/1.4824811.

[267] J. Faure, Y. Glinec, G. Gallot and V. Malka. 'Ultrashort laser pulses and ultrashort electron bunches generated in relativistic laser-plasma interaction'. In: *Physics of Plasmas* 13.5 (May 2006), p. 056706. DOI: 10.1063/1.2180727.

[268] D. H. Froula et al. 'Measurements of the Critical Power for Self-Injection of Electrons in a Laser Wakefield Accelerator'. In: *Physical Review Letters* 103.21 (Nov. 2009), p. 215006. DOI: 10.1103/physrevlett.103.215006.

[269] S. P. D. Mangles et al. 'Self-injection threshold in self-guided laser wakefield accelerators'. In: *Physical Review Special Topics - Accelerators and Beams* 15.1 (Jan. 2012), p. 011302. ISSN: 1098-4402. DOI: 10.1103/physrevstab.15.011302.

[270] T. N. Dalichaouch et al. 'Generating high quality ultrarelativistic electron beams using an evolving electron beam driver'. In: *Physical Review Accelerators and Beams* 23.2 (Feb. 2020), p. 021304. ISSN: 2469-9888. DOI: 10.1103/physrevaccelbeams.23.021304.

[271] A. Modena et al. 'Electron acceleration from the breaking of relativistic plasma waves'. In: *Nature* 377.6550 (Oct. 1995), pp. 606–608. DOI: 10.1038/377606a0.

[272] V. Malka et al. 'Electron Acceleration by a Wake Field Forced by an Intense Ultrashort Laser Pulse'. In: *Science* 298.5598 (Nov. 2002), pp. 1596–1600. DOI: 10.1126/science.1076782.

[273] S. Kneip et al. 'Near-GeV Acceleration of Electrons by a Nonlinear Plasma Wave Driven by a Self-Guided Laser Pulse'. In: *Physical Review Letters* 103.3 (July 2009), p. 035002. ISSN: 1079-7114. DOI: 10.1103/physrevlett.103.035002.

[274] N. A. M. Hafz et al. 'Stable generation of GeV-class electron beams from self-guided laser–plasma channels'. In: *Nature Photonics* 2.9 (Aug. 2008), pp. 571–577. DOI: 10.1038/nphoton.2008.155.

[275] X. Wang et al. 'Quasi-monoenergetic laser-plasma acceleration of electrons to 2 GeV'. In: *Nature Communications* 4.1 (June 2013). DOI: 10.1038/ncomms2988.

[276] H. T. Kim et al. 'Enhancement of Electron Energy to the Multi-GeV Regime by a Dual-Stage Laser-Wakefield Accelerator Pumped by Petawatt Laser Pulses'. In: *Physical Review Letters* 111.16 (Oct. 2013), p. 165002. DOI: 10.1103/physrevlett.111.165002.

[277] Y. F. Li et al. 'Generation of 20 kA electron beam from a laser wakefield accelerator'. In: *Physics of Plasmas* 24.2 (Feb. 2017), p. 023108. DOI: 10.1063/1.4975613.

[278] S. Corde et al. 'Observation of longitudinal and transverse self-injections in laser-plasma accelerators'. In: *Nature Communications* 4.1 (Feb. 2013). DOI: 10.1038/ncomms2528.

[279] S. Bulanov, N. Naumova, F. Pegoraro and J. Sakai. 'Particle injection into the wave acceleration phase due to nonlinear wake wave breaking'. In: *Physical Review E* 58.5 (Nov. 1998), R5257–R5260. DOI: 10.1103/physreve.58.r5257.

[280] G. Fubiani, E. Esarey, C. B. Schroeder and W. P. Leemans. 'Improvement of electron beam quality in optical injection schemes using negative plasma density gradients'. In: *Physical Review E* 73.2 (Feb. 2006), p. 026402. ISSN: 1550-2376. DOI: 10.1103/physreve.73.026402.

[281] A. Martinez de la Ossa et al. 'Optimizing density down-ramp injection for beam-driven plasma wakefield accelerators'. In: *Physical Review Accelerators and Beams* 20.9 (Sept. 2017), p. 091301. DOI: 10.1103/physrevaccelbeams.20.091301.

[282] R. G. Hemker, N. M. Hafz and M. Uesaka. 'Computer simulations of a single-laser double-gas-jet wakefield accelerator concept'. In: *Physical Review Special Topics - Accelerators and Beams* 5.4 (Apr. 2002), p. 041301. DOI: 10.1103/physrevstab.5.041301.

[283] P. Tomassini et al. 'Production of high-quality electron beams in numerical experiments of laser wakefield acceleration with longitudinal wave breaking'. In: *Physical Review Special Topics - Accelerators and Beams* 6.12 (Dec. 2003), p. 121301. DOI: 10.1103/physrevstab.6.121301.

[284] A. V. Brantov et al. 'Controlled electron injection into the wake wave using plasma density inhomogeneity'. In: *Physics of Plasmas* 15.7 (July 2008). ISSN: 1089-7674. DOI: 10.1063/1.2956989.

[285] S. A. Samant, A. K. Upadhyay and S. Krishnagopal. 'High brightness electron beams from density transition laser wakefield acceleration for short-wavelength free-electron lasers'. In: *Plasma Physics and Controlled Fusion* 56.9 (July 2014), p. 095003. DOI: 10.1088/0741-3335/56/9/095003.

[286] H. Ekerfelt et al. 'A tunable electron beam source using trapping of electrons in a density down-ramp in laser wakefield acceleration'. In: *Scientific Reports* 7.1 (Sept. 2017). DOI: 10.1038/s41598-017-12560-8.

[287] H. Suk, N. Barov, J. B. Rosenzweig and E. Esarey. 'Plasma Electron Trapping and Acceleration in a Plasma Wake Field Using a Density Transition'. In: *Physical Review Letters* 86.6 (Feb. 2001), pp. 1011–1014. DOI: 10.1103/physrevlett.86.1011.

[288] M. C. Thompson, J. B. Rosenzweig and H. Suk. 'Plasma density transition trapping as a possible high-brightness electron beam source'. In: *Physical Review Special Topics - Accelerators and Beams* 7.1 (Jan. 2004), p. 011301. DOI: 10.1103/physrevstab.7.011301.

[289] R. J. England, J. B. Rosenzweig and N. Barov. 'Plasma electron fluid motion and wave breaking near a density transition'. In: *Physical Review E* 66.1 (July 2002), p. 016501. ISSN: 1095-3787. DOI: 10.1103/physreve.66.016501.

[290] J. Grebenyuk, A. Martinez de la Ossa, T. Mehrling and J. Osterhoff. 'Beam-driven plasma-based acceleration of electrons with density down-ramp injection at FLASHForward'. In: *Nuclear Instruments and Methods in Physics Research Section A: Accelerators, Spectrometers, Detectors and Associated Equipment* 740 (Mar. 2014), pp. 246–249. DOI: 10.1016/j.nima.2013.10.054.

[291] X. Xu et al. 'High quality electron bunch generation using a longitudinal density-tailored plasma-based accelerator in the three-dimensional blowout regime'. In: *Physical Review Accelerators and Beams* 20.11 (Nov. 2017), p. 111303. DOI: 10.1103/physrevaccelbeams.20.111303.

[292] C. Zhang et al. 'Effect of fluctuations in the down ramp plasma source profile on the emittance and current profile of the self-injected beam in a plasma wakefield accelerator'. In: *Physical Review Accelerators and Beams* 22.11 (Nov. 2019), p. 111301. DOI: 10.1103/physrevaccelbeams.22.111301.

[293] H. Suk, H. J. Lee and I. S. Ko. 'Generation of high-energy electrons by a femtosecond terawatt laser propagating through a sharp downward density transition'. In: *Journal of the Optical Society of America B* 21.7 (July 2004), p. 1391. ISSN: 1520-8540. DOI: 10.1364/josab.21.001391.

[294] C. G. R. Geddes et al. 'Plasma-Density-Gradient Injection of Low Absolute-Momentum-Spread Electron Bunches'. In: *Physical Review Letters* 100.21 (May 2008), p. 215004. DOI: 10.1103/physrevlett.100.215004.

[295] A. J. Gonsalves et al. 'Tunable laser plasma accelerator based on longitudinal density tailoring'. In: *Nature Physics* 7.11 (Aug. 2011), pp. 862–866. DOI: 10.1038/nphys2071.

[296] M. Hansson et al. 'Down-ramp injection and independently controlled acceleration of electrons in a tailored laser wakefield accelerator'. In: *Physical Review Special Topics - Accelerators and Beams* 18.7 (July 2015), p. 071303. DOI: 10.1103/physrevstab.18.071303.

[297] W. Wang et al. 'High-Brightness High-Energy Electron Beams from a Laser Wakefield Accelerator via Energy Chirp Control'. In: *Physical Review Letters* 117.12 (Sept. 2016), p. 124801. DOI: 10.1103/physrevlett.117.124801.

[298] K. Schmid et al. 'Density-transition based electron injector for laser driven wakefield accelerators'. In: *Physical Review Special Topics - Accelerators and Beams* 13.9 (Sept. 2010), p. 091301. DOI: 10.1103/physrevstab.13.091301.

[299] A. Buck et al. 'Shock-Front Injector for High-Quality Laser-Plasma Acceleration'. In: *Physical Review Letters* 110.18 (May 2013), p. 185006. DOI: 10.1103/physrevlett.110.185006.

[300] M. Burza et al. 'Laser wakefield acceleration using wire produced double density ramps'. In: *Physical Review Special Topics - Accelerators and Beams* 16.1 (Jan. 2013), p. 011301. DOI: 10.1103/physrevstab.16.011301.

[301] S. Barber et al. 'Measured Emittance Dependence on the Injection Method in Laser Plasma Accelerators'. In: *Physical Review Letters* 119.10 (Sept. 2017), p. 104801. DOI: 10.1103/physrevlett.119.104801.

[302] K. K. Swanson et al. 'Control of tunable, monoenergetic laser-plasma-accelerated electron beams using a shock-induced density downramp injector'. In: *Physical Review Accelerators and Beams* 20.5 (May 2017), p. 051301. DOI: 10.1103/physrevaccelbeams.20.051301.

[303] H.-E. Tsai et al. 'Control of quasi-monoenergetic electron beams from laser-plasma accelerators with adjustable shock density profile'. In: *Physics of Plasmas* 25.4 (Apr. 2018), p. 043107. DOI: 10.1063/1.5023694.

[304] L. Ke et al. 'Near-GeV Electron Beams at a Few Per-Mille Level from a Laser Wakefield Accelerator via Density-Tailored Plasma'. In: *Physical Review Letters* 126.21 (May 2021), p. 214801. DOI: 10.1103/physrevlett.126.214801.

[305] W. Wang et al. 'Free-electron lasing at 27 nanometres based on a laser wakefield accelerator'. In: *Nature* 595.7868 (July 2021), pp. 516–520. DOI: 10.1038/s41586-021-03678-x.

[306] P. Volfbeyn, E. Esarey and W. P. Leemans. 'Guiding of laser pulses in plasma channels created by the ignitor-heater technique'. In: *Physics of Plasmas* 6.5 (May 1999), pp. 2269–2277. ISSN: 1089-7674. DOI: 10.1063/1.873503.

[307] R. J. Shalloo et al. 'Hydrodynamic optical-field-ionized plasma channels'. In: *Physical Review E* 97.5 (May 2018), p. 053203. ISSN: 2470-0053. DOI: 10.1103/physreve.97.053203.

[308] H. Jang et al. 'Plasma Channel Generation for Electron Acceleration with a Laser-Induced Density Gradient'. In: *Journal of the Korean Physical Society* 50.95 (May 2007), p. 1466. DOI: 10.3938/jkps.50.1466.

[309] T.-Y. Chien et al. 'Spatially Localized Self-Injection of Electrons in a Self-Modulated Laser-Wakefield Accelerator by Using a Laser-Induced Transient Density Ramp'. In: *Physical Review Letters* 94.11 (Mar. 2005), p. 115003. DOI: 10.1103/physrevlett.94.115003.

[310] C.-T. Hsieh et al. 'Tomography of Injection and Acceleration of Monoenergetic Electrons in a Laser-Wakefield Accelerator'. In: *Physical Review Letters* 96.9 (Mar. 2006), p. 095001. ISSN: 1079-7114. DOI: 10.1103/physrevlett.96.095001.

[311] J. Kim et al. 'Quasi-Monoenergetic Electron-Beam Generation Using a Laser Accelerator for Ultra-Short X-ray Sources'. In: *Journal of the Korean Physical Society* 51.91 (July 2007), p. 397. DOI: 10.3938/jkps.51.397.

[312] J. Faure et al. 'Injection and acceleration of quasimonoenergetic relativistic electron beams using density gradients at the edges of a plasma channel'. In: *Physics of Plasmas* 17.8 (Aug. 2010). DOI: 10.1063/1.3469581.

[313] P. Brijesh et al. 'Tuning the electron energy by controlling the density perturbation position in laser plasma accelerators'. In: *Physics of Plasmas* 19.6 (June 2012), p. 063104. DOI: 10.1063/1.4725421.

[314] S. Fourmaux et al. 'Quasi-monoenergetic electron beams production in a sharp density transition'. In: *Applied Physics Letters* 101.11 (Sept. 2012), p. 111106. DOI: 10.1063/1.4752114.

[315] K. v. Grafenstein et al. 'Laser-accelerated electron beams at 1 GeV using optically-induced shock injection'. In: *Scientific Reports* 13.1 (July 2023). ISSN: 2045-2322. DOI: 10.1038/s41598-023-38805-3.

[316] G. Wittig et al. 'Optical plasma torch electron bunch generation in plasma wakefield accelerators'. In: *Physical Review Special Topics - Accelerators and Beams* 18.8 (Aug. 2015), p. 081304. DOI: 10.1103/physrevstab.18.081304.

[317] G. Wittig et al. 'Electron beam manipulation, injection and acceleration in plasma wakefield accelerators by optically generated plasma density spikes'. In: *Nuclear Instruments and Methods in Physics Research Section A: Accelerators, Spectrometers, Detectors and Associated Equipment* 829 (Sept. 2016), pp. 83–87. DOI: 10.1016/j.nima.2016.02.027.

[318] D. Umstadter, J. K. Kim and E. Dodd. 'Laser Injection of Ultrashort Electron Pulses into Wakefield Plasma Waves'. In: *Physical Review Letters* 76.12 (Mar. 1996), pp. 2073–2076. DOI: 10.1103/physrevlett.76.2073.

[319] R. G. Hemker et al. 'Computer simulations of cathodeless, high-brightness electron-beam production by multiple laser beams in plasmas'. In: *Physical Review E* 57.5 (May 1998), pp. 5920–5928. ISSN: 1095-3787. DOI: 10.1103/physreve.57.5920.

[320] E. Esarey et al. 'Electron Injection into Plasma Wakefields by Colliding Laser Pulses'. In: *Physical Review Letters* 79.14 (Oct. 1997), pp. 2682–2685. DOI: 10.1103/physrevlett.79.2682.

[321] C. B. Schroeder et al. 'Generation of ultrashort electron bunches by colliding laser pulses'. In: *Physical Review E* 59.5 (May 1999), pp. 6037–6047. ISSN: 1095-3787. DOI: 10.1103/physreve.59.6037.

[322] G. Fubiani, E. Esarey, C. B. Schroeder and W. P. Leemans. 'Beat wave injection of electrons into plasma waves using two interfering laser pulses'. In: *Physical Review E* 70.1 (July 2004), p. 016402. DOI: 10.1103/physreve.70.016402.

[323] H. Kotaki et al. 'Head-on injection of a high quality electron beam by the interaction of two laser pulses'. In: *Physics of Plasmas* 11.6 (June 2004), pp. 3296–3302. DOI: 10.1063/1.1751171.

[324] V. Malka et al. 'Laser-driven accelerators by colliding pulses injection: A review of simulation and experimental results'. In: *Physics of Plasmas* 16.5 (May 2009), p. 056703. DOI: 10.1063/1.3079486.

[325] Z. M. Sheng et al. 'Mechanisms of electron injection into laser wakefields by a weak counter-propagating pulse'. In: *The European Physical Journal Special Topics* 175.1 (Aug. 2009), pp. 49–55. ISSN: 1951-6401. DOI: 10.1140/epjst/e2009-01116-5.

[326] R. Lehe et al. 'Optical Transverse Injection in Laser-Plasma Acceleration'. In: *Physical Review Letters* 111.8 (Aug. 2013), p. 085005. DOI: 10.1103/physrevlett.111.085005.

[327] J. Faure et al. 'Controlled injection and acceleration of electrons in plasma wakefields by colliding laser pulses'. In: *Nature* 444.7120 (Dec. 2006), pp. 737–739. DOI: 10.1038/nature05393.

[328] J. Faure et al. 'Controlled electron injection in a laser-plasma accelerator'. In: *Plasma Physics and Controlled Fusion* 49.12B (Nov. 2007), B395–B402. ISSN: 1361-6587. DOI: 10.1088/0741-3335/49/12b/s36.

[329] C. Toth et al. 'Colliding pulse injection experiments in non-collinear geometry for controlled laser plasma wakefield acceleration of electrons'. In: *2007 IEEE Particle Accelerator Conference (PAC)*. IEEE, June 2007. DOI: 10.1109/pac.2007.4440639.

[330] H. Kotaki et al. 'Improvement of the Quality and Stability of Electron Bunch Using Countercrossing Laser Beam'. In: *IEEE Transactions on Plasma Science* 36.4 (Aug. 2008), pp. 1760–1764. DOI: 10.1109/tps.2008.927944.

[331] G. R. Plateau et al. 'Colliding Laser Pulses for Laser-Plasma Accelerator Injection Control'. In: *AIP Conference Proceedings*. AIP, 2010. DOI: 10.1063/1.3520310.

[332] H. Kotaki et al. 'Electron Optical Injection with Head-On and Countercrossing Colliding Laser Pulses'. In: *Physical Review Letters* 103.19 (Nov. 2009), p. 194803. ISSN: 1079-7114. DOI: 10.1103/physrevlett.103.194803.

[333] O. Lundh et al. 'Few femtosecond, few kiloampere electron bunch produced by a laser–plasma accelerator'. In: *Nature Physics* 7.3 (Jan. 2011), pp. 219–222. ISSN: 1745-2481. DOI: 10.1038/nphys1872.

[334] C. G. R. Geddes et al. 'High energy, low energy spread electron bunches produced via colliding pulse injection'. In: *AIP Conference Proceedings*. 2016. DOI: 10.1063/1.4965605.

[335] C. Rechatin et al. 'Controlling the Phase-Space Volume of Injected Electrons in a Laser-Plasma Accelerator'. In: *Physical Review Letters* 102.16 (Apr. 2009), p. 164801. DOI: 10.1103/physrevlett.102.164801.

[336] C. Rechatin et al. 'Observation of Beam Loading in a Laser-Plasma Accelerator'. In: *Physical Review Letters* 103.19 (Nov. 2009), p. 194804. DOI: 10.1103/physrevlett.103.194804.

[337] C. Rechatin et al. 'Quasi-monoenergetic electron beams produced by colliding cross-polarized laser pulses in underdense plasmas'. In: *New Journal of Physics* 11.1 (Jan. 2009), p. 013011. ISSN: 1367-2630. DOI: 10.1088/1367-2630/11/1/013011.

[338] N. H. Matlis et al. 'Controlling electron injection in laser plasma accelerators using multiple pulses'. In: *AIP Conference Proceedings*. AIP, 2013. DOI: 10.1063/1.4773786.

[339] E. Oz. 'Physics of particle trapping in ultrarelativistic plasma wakes'. PhD thesis. University of Southern California, 2007.

[340] E. Oz et al. 'Ionization-Induced Electron Trapping in Ultrarelativistic Plasma Wakes'. In: *Physical Review Letters* 98.8 (Feb. 2007), p. 084801. DOI: 10.1103/physrevlett.98.084801.

[341] A. Knetsch. 'Acceleration of laser-injected electron beams in an electron-beam driven plasma wakefield accelerator'. PhD thesis. Universität Hamburg, 2017.

[342] M. Ferrario, T. C. Katsouleas, L. Serafini and I. B. Zvi. 'Adiabatic plasma buncher'. In: *IEEE Transactions on Plasma Science* 28.4 (2000), pp. 1152–1158. DOI: 10.1109/27.893295.

[343] L. Serafini. 'Velocity bunching in photo-injectors'. In: *AIP Conference Proceedings*. AIP, 2001. DOI: 10.1063/1.1401564.

[344] C. McGuffey et al. 'Ionization Induced Trapping in a Laser Wakefield Accelerator'. In: *Physical Review Letters* 104.2 (Jan. 2010), p. 025004. DOI: 10.1103/physrevlett.104.025004.

[345] A. Pak et al. 'Injection and Trapping of Tunnel-Ionized Electrons into Laser-Produced Wakes'. In: *Physical Review Letters* 104.2 (Jan. 2010), p. 025003. DOI: 10.1103/physrevlett.104.025003.

[346] C. E. Clayton et al. 'Self-Guided Laser Wakefield Acceleration beyond 1 GeV Using Ionization-Induced Injection'. In: *Physical Review Letters* 105.10 (Sept. 2010), p. 105003. DOI: 10.1103/physrevlett.105.105003.

[347] M. Chen et al. 'Theory of ionization-induced trapping in laser-plasma accelerators'. In: *Physics of Plasmas* 19.3 (Mar. 2012), p. 033101. DOI: 10.1063/1.3689922.

[348] S. Bohlen et al. 'Stability of ionization-injection-based laser-plasma accelerators'. In: *Physical Review Accelerators and Beams* 25.3 (Mar. 2022), p. 031301. DOI: 10.1103/physrevaccelbeams.25.031301.

[349] M. Z. Mo et al. 'Quasimonoenergetic electron beams from laser wakefield acceleration in pure nitrogen'. In: *Applied Physics Letters* 100.7 (Feb. 2012), p. 074101. DOI: 10.1063/1.3685464.

[350] P. Lee et al. 'Dynamics of electron injection and acceleration driven by laser wakefield in tailored density profiles'. In: *Physical Review Accelerators and Beams* 19.11 (Nov. 2016), p. 112802. DOI: 10.1103/physrevaccelbeams.19.112802.

[351] J. S. Liu et al. 'All-Optical Cascaded Laser Wakefield Accelerator Using Ionization-Induced Injection'. In: *Physical Review Letters* 107.3 (July 2011), p. 035001. DOI: 10.1103/physrevlett.107.035001.

[352] B. B. Pollock et al. 'Demonstration of a Narrow Energy Spread, ~ 0.5 GeV Electron Beam from a Two-Stage Laser Wakefield Accelerator'. In: *Physical Review Letters* 107.4 (July 2011), p. 045001. DOI: 10.1103/physrevlett.107.045001.

[353] M. Vargas et al. 'Improvements to laser wakefield accelerated electron beam stability, divergence, and energy spread using three-dimensional printed two-stage gas cell targets'. In: *Applied Physics Letters* 104.17 (Apr. 2014). ISSN: 1077-3118. DOI: 10.1063/1.4874981.

[354] G. Golovin et al. 'Tunable monoenergetic electron beams from independently controllable laser-wakefield acceleration and injection'. In: *Physical Review Special Topics - Accelerators and Beams* 18.1 (Jan. 2015), p. 011301. DOI: 10.1103/physrevstab.18.011301.

[355] G. Golovin et al. 'Control and optimization of a staged laser-wakefield accelerator'. In: *Nuclear Instruments and Methods in Physics Research Section A: Accelerators, Spectrometers, Detectors and Associated Equipment* 830 (Sept. 2016), pp. 375–380. ISSN: 0168-9002. DOI: 10.1016/j.nima.2016.06.022.

[356] Z. Qin et al. 'Multi-GeV cascaded laser wakefield acceleration in a hybrid capillary discharge waveguide'. In: *New Journal of Physics* 24.7 (July 2022), p. 073048. ISSN: 1367-2630. DOI: 10.1088/1367-2630/ac81e2.

[357] C. Xia et al. 'Effects of self-focusing on tunnel-ionization-induced injection in a laser wakefield accelerator'. In: *Physics of Plasmas* 18.11 (Nov. 2011), p. 113101. DOI: 10.1063/1.3656958.

[358] B. S. Rao et al. 'Quasi-monoenergetic electron beams from a few-terawatt laser driven plasma acceleration using a nitrogen gas jet'. In: *Plasma Physics and Controlled Fusion* 59.6 (Apr. 2017), p. 065006. DOI: 10.1088/1361-6587/aa69f3.

[359] M. Zeng et al. 'Self-truncated ionization injection and consequent monoenergetic electron bunches in laser wakefield acceleration'. In: *Physics of Plasmas* 21.3 (Mar. 2014), p. 030701. DOI: 10.1063/1.4868404.

[360] F. Li et al. 'Low-energy-spread laser wakefield acceleration using ionization injection with a tightly focused laser in a mismatched plasma channel'. In: *Plasma Physics and Controlled Fusion* 58.3 (Jan. 2016), p. 034004. DOI: 10.1088/0741-3335/58/3/034004.

[361] M. Mirzaie et al. 'Demonstration of self-truncated ionization injection for GeV electron beams'. In: *Scientific Reports* 5.1 (Oct. 2015). DOI: 10.1038/srep14659.

[362] P. Muggli et al. 'Photo-ionized lithium source for plasma accelerator applications'. In: *IEEE Transactions on Plasma Science* 27.3 (June 1999), pp. 791–799. DOI: 10.1109/27.774685.

[363] N. Kirby et al. 'Transverse emittance and current of multi-GeV trapped electrons in a plasma wakefield accelerator'. In: *Physical Review Special Topics - Accelerators and Beams* 12.5 (May 2009), p. 051302. DOI: 10.1103/physrevstab.12.051302.

[364] N. Vafaei-Najafabadi et al. 'Evidence for high-energy and low-emittance electron beams using ionization injection of charge in a plasma wakefield accelerator'. In: *Plasma Physics and Controlled Fusion* 58.3 (Feb. 2016), p. 034009. DOI: 10.1088/0741-3335/58/3/034009.

[365] N. Vafaei-Najafabadi et al. 'Beam Loading by Distributed Injection of Electrons in a Plasma Wakefield Accelerator'. In: *Physical Review Letters* 112.2 (Jan. 2014), p. 025001. DOI: 10.1103/physrevlett.112.025001.

[366] N. Vafaei-Najafabadi et al. 'Limitation on the accelerating gradient of a wakefield excited by an ultrarelativistic electron beam in rubidium plasma'. In: *Physical Review Accelerators and Beams* 19.10 (Oct. 2016), p. 101303. DOI: 10.1103/physrevaccelbeams.19.101303.

[367] N. Vafaei-Najafabadi et al. 'Producing multi-coloured bunches through beam-induced ionization injection in plasma wakefield accelerator'. In: *Philosophical Transactions of the Royal Society A: Mathematical, Physical and Engineering Sciences* 377.2151 (June 2019), p. 20180184. DOI: 10.1098/rsta.2018.0184.

[368] L. D. Amorim and N. Vafaei-Najafabadi. 'Ionization injection of 'inception' beams in plasma wakefield accelerators'. In: *Plasma Physics and Controlled Fusion* 61.10 (Sept. 2019), p. 105015. DOI: 10.1088/1361-6587/ab4005.

[369] A. Martinez de la Ossa et al. 'High-Quality Electron Beams from Beam-Driven Plasma Accelerators by Wakefield-Induced Ionization Injection'. In: *Physical Review Letters* 111.24 (Dec. 2013), p. 245003. DOI: 10.1103/physrevlett.111.245003.

[370] A. Martinez de la Ossa et al. 'Wakefield-induced ionization injection in beam-driven plasma accelerators'. In: *Physics of Plasmas* 22.9 (Sept. 2015), p. 093107. DOI: 10.1063/1.4929921.

[371] A. Martinez de la Ossa et al. 'Hybrid LWFA–PWFA staging as a beam energy and brightness transformer: conceptual design and simulations'. In: *Philosophical Transactions of the Royal Society A: Mathematical, Physical and Engineering Sciences* 377.2151 (June 2019), p. 20180175. DOI: 10.1098/rsta.2018.0175.

[372] Y. Wan et al. 'Colliding ionization injection in a plasma wakefield accelerator'. In: *Plasma Physics and Controlled Fusion* 58.3 (Feb. 2016), p. 034015. DOI: 10.1088/0741-3335/58/3/034015.

[373] F. Li et al. 'Generating High-Brightness Electron Beams via Ionization Injection by Transverse Colliding Lasers in a Plasma-Wakefield Accelerator'. In: *Physical Review Letters* 111.1 (July 2013), p. 015003. DOI: 10.1103/physrevlett.111.015003.

[374] M. Zeng, A. Martinez de la Ossa and J. Osterhoff. 'Ponderomotively assisted ionization injection in plasma wakefield accelerators'. In: *New Journal of Physics* 22.12 (Dec. 2020), p. 123003. DOI: 10.1088/1367-2630/abc9ee.

[375] M. Chen, Z.-M. Sheng, Y.-Y. Ma and J. Zhang. 'Electron injection and trapping in a laser wakefield by field ionization to high-charge states of gases'. In: *Journal of Applied Physics* 99.5 (Mar. 2006), p. 056109. DOI: 10.1063/1.2179194.

[376] M. Chen et al. 'Electron injection and emittance control by transverse colliding pulses in a laser-plasma accelerator'. In: *Physical Review Special Topics - Accelerators and Beams* 17.5 (May 2014), p. 051303. ISSN: 1098-4402. DOI: 10.1103/physrevstab.17.051303.

[377] N. Bourgeois, J. Cowley and S. M. Hooker. 'Two-Pulse Ionization Injection into Quasilinear Laser Wakefields'. In: *Physical Review Letters* 111.15 (Oct. 2013), p. 155004. DOI: 10.1103/physrevlett.111.155004.

[378] M. von der Leyen et al. 'Observation of Monoenergetic Electrons from Two-Pulse Ionization Injection in Quasilinear Laser Wakefields'. In: *Physical Review Letters* 130.10 (Mar. 2023), p. 105002. DOI: 10.1103/physrevlett.130.105002.

[379] L.-L. Yu et al. 'Two-Color Laser-Ionization Injection'. In: *Physical Review Letters* 112.12 (Mar. 2014), p. 125001. DOI: 10.1103/physrevlett.112.125001.

[380] X. Xu et al. 'Low emittance electron beam generation from a laser wakefield accelerator using two laser pulses with different wavelengths'. In: *Physical Review Special Topics - Accelerators and Beams* 17.6 (June 2014), p. 061301. DOI: 10.1103/physrevstab.17.061301.

[381] C. B. Schroeder et al. 'Thermal emittance from ionization-induced trapping in plasma accelerators'. In: *Physical Review Special Topics - Accelerators and Beams* 17.10 (Oct. 2014), p. 101301. ISSN: 1098-4402. DOI: 10.1103/physrevstab.17.101301.

[382] M. Zeng et al. 'Multichromatic Narrow-Energy-Spread Electron Bunches from Laser-Wakefield Acceleration with Dual-Color Lasers'. In: *Physical Review Letters* 114.8 (Feb. 2015), p. 084801. ISSN: 1079-7114. DOI: 10.1103/physrevlett.114.084801.

[383] M. Zeng et al. 'High quality electron beam acceleration by ionization injection in laser wakefields with mid-infrared dual-color lasers'. In: *Physics of Plasmas* 23.6 (June 2016). ISSN: 1089-7674. DOI: 10.1063/1.4953895.

[384] T. Hosokai et al. 'Effect of External Static Magnetic Field on the Emittance and Total Charge of Electron Beams Generated by Laser-Wakefield Acceleration'. In: *Physical Review Letters* 97.7 (Aug. 2006), p. 075004. ISSN: 1079-7114. DOI: 10.1103/physrevlett.97.075004.

[385] J. Vieira et al. 'Magnetic Control of Particle Injection in Plasma Based Accelerators'. In: *Physical Review Letters* 106.22 (May 2011), p. 225001. DOI: 10.1103/physrevlett.106.225001.

[386] Q. Zhao et al. 'Ionization injection in a laser wakefield accelerator subject to a transverse magnetic field'. In: *New Journal of Physics* 20.6 (June 2018), p. 063031. ISSN: 1367-2630. DOI: 10.1088/1367-2630/aac926.

[387] Q. Zhao et al. 'Sub-femtosecond electron bunches in laser wakefield acceleration via injection suppression with a magnetic field'. In: *Plasma Physics and Controlled Fusion* 61.8 (June 2019), p. 085015. ISSN: 1361-6587. DOI: 10.1088/1361-6587/ab249c.

[388] F. Y. Li et al. 'Dense Attosecond Electron Sheets from Laser Wakefields Using an Up-Ramp Density Transition'. In: *Physical Review Letters* 110.13 (Mar. 2013), p. 135002. ISSN: 1079-7114. DOI: 10.1103/physrevlett.110.135002.

[389] M. K. Weikum et al. 'Generation of attosecond electron bunches in a laser-plasma accelerator using a plasma density upramp'. In: *Nuclear Instruments and Methods in Physics Research Section A: Accelerators, Spectrometers, Detectors and Associated Equipment* 829 (Sept. 2016), pp. 33–36. ISSN: 0168-9002. DOI: 10.1016/j.nima.2016.01.003.

[390] B. Shen et al. 'Electron injection by a nanowire in the bubble regime'. In: *Physics of Plasmas* 14.5 (May 2007). ISSN: 1089-7674. DOI: 10.1063/1.2728773.

[391] M. H. Cho, V. B. Pathak, H. T. Kim and C. H. Nam. 'Controlled electron injection facilitated by nanoparticles for laser wakefield acceleration'. In: *Scientific Reports* 8.1 (Nov. 2018). ISSN: 2045-2322. DOI: 10.1038/s41598-018-34998-0.

[392] C. Aniculaesei et al. 'Proof-of-Principle Experiment for Nanoparticle-Assisted Laser Wakefield Electron Acceleration'. In: *Physical Review Applied* 12.4 (Oct. 2019), p. 044041. ISSN: 2331-7019. DOI: 10.1103/physrevapplied.12.044041.

[393] J. Xu et al. 'Nanoparticle-insertion scheme to decouple electron injection from laser evolution in laser wakefield acceleration'. In: *Scientific Reports* 12.1 (July 2022). ISSN: 2045-2322. DOI: 10.1038/s41598-022-15125-6.

[394] J. Wenz et al. 'Dual-energy electron beams from a compact laser-driven accelerator'. In: *Nature Photonics* 13.4 (Feb. 2019), pp. 263–269. ISSN: 1749-4893. DOI: 10.1038/s41566-019-0356-z.

[395] C. Thaury et al. 'Shock assisted ionization injection in laser-plasma accelerators'. In: *Scientific Reports* 5.1 (Nov. 2015). DOI: 10.1038/srep16310.

[396] M. Hansson et al. 'Localization of ionization-induced trapping in a laser wakefield accelerator using a density down-ramp'. In: *Plasma Physics and Controlled Fusion* 58.5 (Mar. 2016), p. 055009. DOI: 10.1088/0741-3335/58/5/055009.

[397] Y. Xi et al. 'Hybrid modeling of relativistic underdense plasma photocathode injectors'. In: *Physical Review Special Topics - Accelerators and Beams* 16.3 (Mar. 2013), p. 031303. ISSN: 1098-4402. DOI: 10.1103/physrevstab.16.031303.

[398] B. Hidding et al. 'Ultrahigh brightness bunches from hybrid plasma accelerators as drivers of 5th generation light sources'. In: *Journal of Physics B: Atomic, Molecular and Optical Physics* 47.23 (Nov. 2014), p. 234010. DOI: 10.1088/0953-4075/47/23/234010.

[399] A. F. Habib et al. 'Plasma Photocathodes'. In: *Annalen der Physik* 535.10 (Sept. 2023). ISSN: 1521-3889. DOI: 10.1002/andp.202200655. A. F. Habib, T. Heinemann and B. Hidding contributed equally to this work.

[400] K.-J. Kim. 'Rf and space-charge effects in laser-driven rf electron guns'. In: *Nuclear Instruments and Methods in Physics Research Section A: Accelerators, Spectrometers, Detectors and Associated Equipment* 275.2 (Feb. 1989), pp. 201–218. ISSN: 0168-9002. DOI: 10.1016/0168-9002(89)90688-8.

[401] I. V. Bazarov, B. M. Dunham and C. K. Sinclair. 'Maximum Achievable Beam Brightness from Photoinjectors'. In: *Physical Review Letters* 102.10 (Mar. 2009), p. 104801. DOI: 10.1103/physrevlett.102.104801.

[402] K. Moon, S. Kumar, M. Hur and M. Chung. 'Longitudinal phase space dynamics of witness bunch during the Trojan Horse injection for plasma-based particle accelerators'. In: *Physics of Plasmas* 26.7 (July 2019). ISSN: 1089-7674. DOI: 10.1063/1.5108928.

[403] A. F. Habib. 'Towards Plasma-Based Attosecond-Ångstrom Class Free-Electron Laser'. PhD thesis. University of Strathclyde, 2024. DOI: https://doi.org/10.48730/wccd-8k95.

[404] X. Xu et al. 'Phase-Space Dynamics of Ionization Injection in Plasma-Based Accelerators'. In: *Physical Review Letters* 112.3 (Jan. 2014), p. 035003. DOI: 10.1103/physrevlett.112.035003.

[405] F. Habib et al. 'Plasma accelerator-based ultrabright x-ray beams from ultrabright electron beams'. In: *Advances in Laboratory-based X-Ray Sources, Optics, and Applications VII*. Ed. by A. Murokh and D. Spiga. SPIE, Sept. 2019. DOI: 10.1117/12.2530976.

[406] G. G. Manahan et al. 'Hot spots and dark current in advanced plasma wakefield accelerators'. In: *Physical Review Accelerators and Beams* 19.1 (Jan. 2016), p. 011303. DOI: 10.1103/physrevaccelbeams.19.011303.

[407] A. F. Habib et al. 'Attosecond-Angstrom free-electron-laser towards the cold beam limit'. In: *Nature Communications* 14.1 (Feb. 2023). DOI: 10.1038/s41467-023-36592-z.

[408] B. Hidding et al. *Tunable Electron Multibunch Production in Plasma Wakefield Accelerators*. 2014. DOI: 10.48550/ARXIV.1403.1109.

[409] P. Scherkl. 'High-brightness plasma-based Compton backscattering source for high energy physics'. PhD thesis. University of Strathclyde, 2019. DOI: https://doi.org/10.48730/e7nv-ek71.

[410] G. Zhu et al. 'Simultaneous spatial and temporal focusing of femtosecond pulses'. In: *Optics Express* 13.6 (2005), p. 2153. ISSN: 1094-4087. DOI: 10.1364/opex.13.002153.

[411] M. Clerici et al. 'Space–time focusing of Bessel-like pulses'. In: *Optics Letters* 35.19 (Sept. 2010), p. 3267. ISSN: 1539-4794. DOI: 10.1364/ol.35.003267.

[412] M. Stumpf, M. Melchger, S. Montag and G. Pretzler. 'Multiparameter-controlled laser ionization within a plasma wave for wakefield acceleration'. In: *Journal of Physics B: Atomic, Molecular and Optical Physics* 55.1 (Jan. 2022), p. 015401. ISSN: 1361-6455. DOI: 10.1088/1361-6455/ac489b.

[413] M. Stumpf. 'Optimierte lasergetriebene Elektroneninjektion in einen Plasma-Wakefield-Beschleuniger'. PhD thesis. Heinrich-Heine-Universität Düsseldorf, 2022.

[414] X. Xu et al. 'Generation of topologically complex three-dimensional electron beams in a plasma photocathode'. In: *Physical Review Accelerators and Beams* 25.1 (Jan. 2022), p. 011302. DOI: 10.1103/physrevaccelbeams.25.011302.

[415] G. Wittig. 'Start-to-end simulations of hybrid laser- and beam-driven plasma wakefield acceleration and free electron lasers'. PhD thesis. Universität Hamburg, 2017. URL: https://ediss.sub.uni-hamburg.de/handle/ediss/7487.

[416] D. Ullmann et al. 'All-optical density downramp injection in electron-driven plasma wakefield accelerators'. In: *Physical Review Research* 3.4 (Dec. 2021), p. 043163. DOI: 10.1103/physrevresearch.3.043163.

[417] D. Ullmann. 'Laser generated plasma torch injectors for beam-driven plasma wakefield accelerators'. PhD thesis. University of Strathclyde, 2021. DOI: https://doi.org/10.48730/7xv9-k025.

[418] A. Knetsch et al. 'Stable witness-beam formation in a beam-driven plasma cathode'. In: *Physical Review Accelerators and Beams* 24.10 (Oct. 2021), p. 101302. DOI: 10.1103/physrevaccelbeams.24.101302.

[419] B. E. Blue et al. 'Plasma-Wakefield Acceleration of an Intense Positron Beam'. In: *Physical Review Letters* 90.21 (May 2003), p. 214801. ISSN: 1079-7114. DOI: 10.1103/physrevlett.90.214801.

[420] C. L. O'Connell et al. 'Plasma production via field ionization'. In: *Physical Review Special Topics - Accelerators and Beams* 9.10 (Oct. 2006), p. 101301. DOI: 10.1103/physrevstab.9.101301.

[421] P. Scherkl et al. 'Plasma photonic spatiotemporal synchronization of relativistic electron and laser beams'. In: *Physical Review Accelerators and Beams* 25.5 (May 2022), p. 052803. ISSN: 2469-9888. DOI: 10.1103/physrevaccelbeams.25.052803.

[422] B. Hidding et al. 'First Measurements of Trojan Horse Injection in a Plasma Wakefield Accelerator'. In: *Proceedings of the 8th Int. Particle Accelerator Conf.* IPAC2017 (Denmark). JACoW, Geneva, Switzerland, 2017. DOI: 10.18429/JACOW-IPAC2017-TUYB1.

[423] Y. Xi. 'Ionization injection plasma wakefield acceleration'. PhD thesis. University of California Los Angeles (UCLA), 2016.

[424] O. S. Karger. 'Pathways towards ultra-high brightness electron beams'. PhD thesis. Universität Hamburg. in preparation.

[425] S. J. Gessner. 'Demonstration of the hollow channel plasma wakefield accelerator'. PhD thesis. Stanford University, 2016. URL: https://purl.stanford.edu/rm116jm0173.

[426] S. Z. Green et al. 'Laser ionized preformed plasma at FACET'. In: *Plasma Physics and Controlled Fusion* 56.8 (July 2014), p. 084011. ISSN: 1361-6587. DOI: 10.1088/0741-3335/56/8/084011.

[427] N. Davidson, A. A. Friesem and E. Hasman. 'Holographic axilens: high resolution and long focal depth'. In: *Optics Letters* 16.7 (Apr. 1991), p. 523. ISSN: 1539-4794. DOI: 10.1364/ol.16.000523.

[428] P. Muggli et al. 'Collective refraction of a beam of electrons at a plasma-gas interface'. In: *Physical Review Special Topics - Accelerators and Beams* 4.9 (Sept. 2001), p. 091301. ISSN: 1098-4402. DOI: 10.1103/physrevstab.4.091301.

[429] E. Oz. 'Optical Diagnostics for Plasma Wakefield Accelerators'. In: *AIP Conference Proceedings*. Vol. 737. AIP, 2004, pp. 708–714. DOI: 10.1063/1.1842612.

[430] X. Yan et al. 'Subpicosecond Electro-optic Measurement of Relativistic Electron Pulses'. In: *Physical Review Letters* 85.16 (Oct. 2000), pp. 3404–3407. ISSN: 1079-7114. DOI: 10.1103/physrevlett.85.3404.

[431] A. L. Cavalieri et al. 'Clocking Femtosecond X Rays'. In: *Physical Review Letters* 94.11 (Mar. 2005), p. 114801. ISSN: 1079-7114. DOI: 10.1103/physrevlett.94.114801.

[432] G. Berden et al. 'Benchmarking of Electro-Optic Monitors for Femtosecond Electron Bunches'. In: *Physical Review Letters* 99.16 (Oct. 2007), p. 164801. ISSN: 1079-7114. DOI: 10.1103/physrevlett.99.164801.

[433] B. Steffen et al. 'Electro-optic time profile monitors for femtosecond electron bunches at the soft x-ray free-electron laser FLASH'. In: *Physical Review Special Topics - Accelerators and Beams* 12.3 (Mar. 2009), p. 032802. ISSN: 1098-4402. DOI: 10.1103/physrevstab.12.032802.

[434] T. Heinemann et al. *Particle-Driven Wakefield Dynamics in a Confined Plasma Channel*. 3rd European Advanced Accelerator Concepts Workshop. 2017.

[435] S. Diederichs et al. 'Positron transport and acceleration in beam-driven plasma wakefield accelerators using plasma columns'. In: *Physical Review Accelerators and Beams* 22.8 (Aug. 2019), p. 081301. DOI: 10.1103/physrevaccelbeams.22.081301.

[436] S. Diederichs et al. 'Self-stabilizing positron acceleration in a plasma column'. In: *Physical Review Accelerators and Beams* 25.9 (Sept. 2022), p. 091304. ISSN: 2469-9888. DOI: 10.1103/physrevaccelbeams.25.091304.

[437] D. H. Whittum, A. M. Sessler and J. M. Dawson. 'Ion-channel laser'. In: *Physical Review Letters* 64.21 (May 1990), pp. 2511–2514. DOI: 10.1103/physrevlett.64.2511.

[438] M. Litos et al. 'Experimental Opportunities for the Ion Channel Laser'. In: *2018 IEEE Advanced Accelerator Concepts Workshop (AAC)*. IEEE, Aug. 2018. DOI: 10.1109/aac.2018.8659422.

[439] M. Hogan. *Preliminary Conceptual Design Report for the FACET-II Project at SLAC National Accelerator Laboratory*. Tech. rep. SLAC National Accelerator Laboratory, Apr. 2016. DOI: 10.2172/1248537.

[440] *Technical Design Report for the FACET-II Project at SLAC National Accelerator Laboratory*. Tech. rep. SLAC National Accelerator Laboratory, Aug. 2016. DOI: 10.2172/1340171.

[441] V. Yakimenko et al. 'FACET-II facility for advanced accelerator experimental tests'. In: *Physical Review Accelerators and Beams* 22.10 (Oct. 2019), p. 101301. ISSN: 2469-9888. DOI: 10.1103/physrevaccelbeams.22.101301.

[442] C. N. Danson et al. 'Petawatt and exawatt class lasers worldwide'. In: *High Power Laser Science and Engineering* 7 (2019). ISSN: 2052-3289. DOI: 10.1017/hpl.2019.36.

[443] E. Brookner. 'Phased-Array Radars'. In: *Scientific American* 252.2 (1985), pp. 94–103.

[444] *The Nobel Prize in Physics 2018*. NobelPrize.org. URL: https://www.nobelprize.org/prizes/physics/2018/summary/.

[445] W. P. Leemans et al. 'Multi-GeV Electron Beams from Capillary-Discharge-Guided Subpetawatt Laser Pulses in the Self-Trapping Regime'. In: *Physical Review Letters* 113.24 (Dec. 2014), p. 245002. ISSN: 1079-7114. DOI: 10.1103/physrevlett.113.245002.

[446] A. R. Maier et al. 'Decoding Sources of Energy Variability in a Laser-Plasma Accelerator'. In: *Physical Review X* 10.3 (Aug. 2020), p. 031039. ISSN: 2160-3308. DOI: 10.1103/physrevx.10.031039.

[447] S. Kneip et al. 'Bright spatially coherent synchrotron X-rays from a table-top source'. In: *Nature Physics* 6.12 (Oct. 2010), pp. 980–983. ISSN: 1745-2481. DOI: 10.1038/nphys1789.

[448] J. Wenz et al. 'Quantitative X-ray phase-contrast microtomography from a compact laser-driven betatron source'. In: *Nature Communications* 6.1 (July 2015). ISSN: 2041-1723. DOI: 10.1038/ncomms8568.

[449] V. Tomkus et al. 'Laser wakefield accelerated electron beams and betatron radiation from multijet gas targets'. In: *Scientific Reports* 10.1 (Oct. 2020). DOI: 10.1038/s41598-020-73805-7.

[450] N. D. Powers et al. 'Quasi-monoenergetic and tunable X-rays from a laser-driven Compton light source'. In: *Nature Photonics* 8.1 (Nov. 2013), pp. 28–31. ISSN: 1749-4893. DOI: 10.1038/nphoton.2013.314.

[451] K. Khrennikov et al. 'Tunable All-Optical Quasimonochromatic Thomson X-Ray Source in the Nonlinear Regime'. In: *Physical Review Letters* 114.19 (May 2015), p. 195003. ISSN: 1079-7114. DOI: 10.1103/physrevlett.114.195003.

[452] K. Ta Phuoc et al. 'All-optical Compton gamma-ray source'. In: *Nature Photonics* 6.5 (Apr. 2012), pp. 308–311. ISSN: 1749-4893. DOI: 10.1038/nphoton.2012.82.

[453] S. Chen et al. 'MeV-Energy X Rays from Inverse Compton Scattering with Laser-Wakefield Accelerated Electrons'. In: *Physical Review Letters* 110.15 (Apr. 2013), p. 155003. ISSN: 1079-7114. DOI: 10.1103/physrevlett.110.155003.

[454] H.-E. Tsai et al. 'Compact tunable Compton x-ray source from laser-plasma accelerator and plasma mirror'. In: *Physics of Plasmas* 22.2 (Feb. 2015). ISSN: 1089-7674. DOI: 10.1063/1.4907655.

[455] C. Yu et al. 'Ultrahigh brilliance quasi-monochromatic MeV γ-rays based on self-synchronized all-optical Compton scattering'. In: *Scientific Reports* 6.1 (July 2016). ISSN: 2045-2322. DOI: 10.1038/srep29518.

[456] Y. Wu et al. 'Dual-color γ-rays via all-optical Compton scattering from a cascaded laser-driven wakefield accelerator'. In: *Plasma Physics and Controlled Fusion* 61.8 (July 2019), p. 085030. DOI: 10.1088/1361-6587/ab29d9.

[457] H.-P. Schlenvoigt et al. 'A compact synchrotron radiation source driven by a laser-plasma wakefield accelerator'. In: *Nature Physics* 4.2 (Dec. 2007), pp. 130–133. ISSN: 1745-2481. DOI: 10.1038/nphys811.

[458] M. Fuchs et al. 'Laser-driven soft-X-ray undulator source'. In: *Nature Physics* 5.11 (Sept. 2009), pp. 826–829. DOI: 10.1038/nphys1404.

[459] M. P. Anania et al. 'An ultrashort pulse ultra-violet radiation undulator source driven by a laser plasma wakefield accelerator'. In: *Applied Physics Letters* 104.26 (June 2014), p. 264102. DOI: 10.1063/1.4886997.

[460] A. R. Maier et al. 'Water-Window X-Ray Pulses from a Laser-Plasma Driven Undulator'. In: *Scientific Reports* 10.1 (Mar. 2020). DOI: 10.1038/s41598-020-62401-4.

[461] M. Labat et al. 'Seeded free-electron laser driven by a compact laser plasma accelerator'. In: *Nature Photonics* 17.2 (Dec. 2022), pp. 150–156. DOI: 10.1038/s41566-022-01104-w.

[462] C. P. J. Barty. *Map of all ultra-high intensity laser systems in the world that are known to ICUIL*. ICUIL. URL: https://www.easymapmaker.com/map/ICUIL_World_Map_v3.

[463] B. Hidding et al. 'Plasma Wakefield Accelerator Research 2019 - 2040: A community-driven UK roadmap compiled by the Plasma Wakefield Accelerator Steering Committee (PWASC)'. In: *ArXiv* (19th Apr. 2019). DOI: 10.48550/ARXIV.1904.09205. arXiv: 1904.09205 [physics.acc-ph].

[464] T. J. Mehrling, R. A. Fonseca, A. Martinez de la Ossa and J. Vieira. 'Mitigation of the Hose Instability in Plasma-Wakefield Accelerators'. In: *Physical Review Letters* 118.17 (Apr. 2017), p. 174801. ISSN: 1079-7114. DOI: 10.1103/physrevlett.118.174801.

[465] A. Martinez de la Ossa, T. Mehrling and J. Osterhoff. 'Intrinsic Stabilization of the Drive Beam in Plasma-Wakefield Accelerators'. In: *Physical Review Letters* 121.6 (Aug. 2018), p. 064803. DOI: 10.1103/physrevlett.121.064803.

[466] N. H. Matlis et al. 'Snapshots of laser wakefields'. In: *Nature Physics* 2.11 (Oct. 2006), pp. 749–753. ISSN: 1745-2481. DOI: 10.1038/nphys442.

[467] P. Dong et al. 'Holographic visualization of laser wakefields'. In: *New Journal of Physics* 12.4 (Apr. 2010), p. 045016. ISSN: 1367-2630. DOI: 10.1088/1367-2630/12/4/045016.

[468] M. C. Kaluza et al. 'Measurement of Magnetic-Field Structures in a Laser-Wakefield Accelerator'. In: *Physical Review Letters* 105.11 (Sept. 2010), p. 115002. ISSN: 1079-7114. DOI: 10.1103/physrevlett.105.115002.

[469] A. Buck et al. 'Real-time observation of laser-driven electron acceleration'. In: *Nature Physics* 7.7 (Mar. 2011), pp. 543–548. ISSN: 1745-2481. DOI: 10.1038/nphys1942.

[470] M. B. Schwab et al. 'Few-cycle optical probe-pulse for investigation of relativistic laser-plasma interactions'. In: *Applied Physics Letters* 103.19 (Nov. 2013), p. 191118. ISSN: 1077-3118. DOI: 10.1063/1.4829489.

[471] A. Sävert et al. 'Direct Observation of the Injection Dynamics of a Laser Wakefield Accelerator Using Few-Femtosecond Shadowgraphy'. In: *Physical Review Letters* 115.5 (July 2015), p. 055002. ISSN: 1079-7114. DOI: 10.1103/physrevlett.115.055002.

[472] H. Ding et al. 'Nonlinear plasma wavelength scalings in a laser wakefield accelerator'. In: *Physical Review E* 101.2 (Feb. 2020), p. 023209. DOI: 10.1103/physreve.101.023209.

[473] M. B. Schwab et al. 'Visualization of relativistic laser pulses in underdense plasma'. In: *Physical Review Accelerators and Beams* 23.3 (Mar. 2020), p. 032801. ISSN: 2469-9888. DOI: 10.1103/physrevaccelbeams.23.032801.

[474] S. Lee et al. 'Energy doubler for a linear collider'. In: *Physical Review Special Topics - Accelerators and Beams* 5.1 (Jan. 2002), p. 011001. DOI: 10.1103/physrevstab.5.011001.

[475] C. Joshi and T. Katsouleas. 'Plasma Accelerators at the Energy Frontier and on Tabletops'. In: *Physics Today* 56.6 (June 2003), pp. 47–53. DOI: 10.1063/1.1595054.

[476] T. Heinemann et al. 'Investigating the Key Parameters of a Staged Laser- and Particle Driven Plasma Wakefield Accelerator Experiment'. In: *Proceedings of the 8th Int. Particle Accelerator Conf.* IPAC2017. JACoW, Geneva, Switzerland, 2017. DOI: 10.18429/JACOW-IPAC2017-TUPIK010.

[477] B. Hidding et al. 'Progress in Hybrid Plasma Wakefield Acceleration'. In: *Photonics* 10.2 (Jan. 2023), p. 99. DOI: 10.3390/photonics10020099.

[478] F. S. Tsung et al. 'Near-GeV-Energy Laser-Wakefield Acceleration of Self-Injected Electrons in a Centimeter-Scale Plasma Channel'. In: *Physical Review Letters* 93.18 (Oct. 2004), p. 185002. DOI: 10.1103/physrevlett.93.185002.

[479] K. H. Pae, I. W. Choi and J. Lee. 'Self-mode-transition from laser wakefield accelerator to plasma wakefield accelerator of laser-driven plasma-based electron acceleration'. In: *Physics of Plasmas* 17.12 (Dec. 2010). ISSN: 1089-7674. DOI: 10.1063/1.3522757.

[480] S. Corde et al. 'Mapping the X-Ray Emission Region in a Laser-Plasma Accelerator'. In: *Physical Review Letters* 107.21 (Nov. 2011), p. 215004. ISSN: 1079-7114. DOI: 10.1103/physrevlett.107.215004.

[481] M. Heigoldt et al. 'Temporal evolution of longitudinal bunch profile in a laser wakefield accelerator'. In: *Physical Review Special Topics - Accelerators and Beams* 18.12 (Dec. 2015), p. 121302. ISSN: 1098-4402. DOI: 10.1103/physrevstab.18.121302.

[482] J. Götzfried et al. 'Physics of High-Charge Electron Beams in Laser-Plasma Wakefields'. In: *Physical Review X* 10.4 (Oct. 2020), p. 041015. DOI: 10.1103/physrevx.10.041015.

[483] P. E. Masson-Laborde et al. 'Giga-electronvolt electrons due to a transition from laser wakefield acceleration to plasma wakefield acceleration'. In: *Physics of Plasmas* 21.12 (Dec. 2014), p. 123113. ISSN: 1089-7674. DOI: 10.1063/1.4903851.

[484] Y. Wu et al. 'Energy Enhancement and Energy Spread Compression of Electron Beams in a Hybrid Laser-Plasma Wakefield Accelerator'. In: *Applied Sciences* 9.12 (June 2019), p. 2561. ISSN: 2076-3417. DOI: 10.3390/app9122561.

[485] S. Kuschel et al. 'Demonstration of passive plasma lensing of a laser wakefield accelerated electron bunch'. In: *Physical Review Accelerators and Beams* 19.7 (July 2016), p. 071301. DOI: 10.1103/physrevaccelbeams.19.071301.

[486] T. Heinemann. 'On the Applications of Plasma Lenses towards Hybrid Plasma Wakefield Accelerators'. MA thesis. Universität Hamburg, 2015.

[487] P. Chen. 'A possible final focusing mechansim for linear colliders'. In: *Particle Accelerators* 20 (1987), pp. 171–182.

[488] J. B. Rosenzweig et al. 'Demonstration of electron beam self-focusing in plasma wake fields'. In: *Physics of Fluids B: Plasma Physics* 2.6 (June 1990), pp. 1376–1383. ISSN: 0899-8221. DOI: 10.1063/1.859559.

[489] H. Nakanishi et al. 'Direct observation of plasma-lens effect'. In: *Physical Review Letters* 66.14 (Apr. 1991), pp. 1870–1873. ISSN: 0031-9007. DOI: 10.1103/physrevlett.66.1870.

[490] G. Hairapetian et al. 'Experimental demonstration of dynamic focusing of a relativistic electron bunch by an overdense plasma lens'. In: *Physical Review Letters* 72.15 (Apr. 1994), pp. 2403–2406. ISSN: 0031-9007. DOI: 10.1103/physrevlett.72.2403.

[491] G. Hairapetian et al. 'Transverse dynamics of a short, relativistic electron bunch in a plasma lens'. In: *Physics of Plasmas* 2.6 (June 1995), pp. 2555–2561. ISSN: 1089-7674. DOI: 10.1063/1.871217.

[492] R. Govil, W. P. Leemans, E. Y. Backhaus and J. S. Wurtele. 'Observation of Return Current Effects in a Passive Plasma Lens'. In: *Physical Review Letters* 83.16 (Oct. 1999), pp. 3202–3205. ISSN: 1079-7114. DOI: 10.1103/physrevlett.83.3202.

[493] J. S. T. Ng et al. 'Observation of Plasma Focusing of a 28.5 GeV Positron Beam'. In: *Physical Review Letters* 87.24 (Nov. 2001), p. 244801. ISSN: 1079-7114. DOI: 10.1103/physrevlett.87.244801.

[494] J. P. Couperus Cabadağ et al. 'Gas-dynamic density downramp injection in a beam-driven plasma wakefield accelerator'. In: *Physical Review Research* 3.4 (Oct. 2021), p. l042005. DOI: 10.1103/physrevresearch.3.l042005.

[495] F. M. Foerster et al. 'Stable and High-Quality Electron Beams from Staged Laser and Plasma Wakefield Accelerators'. In: *Physical Review X* 12.4 (Nov. 2022), p. 041016. DOI: 10.1103/physrevx.12.041016.

[496] S. Schöbel et al. 'Effect of driver charge on wakefield characteristics in a plasma accelerator probed by femtosecond shadowgraphy'. In: *New Journal of Physics* 24.8 (Aug. 2022), p. 083034. DOI: 10.1088/1367-2630/ac87c9.

[497] D. Campbell et al. 'Self-Adaptive Stabilization and Quality Boost for Electron Beams from all-optical Plasma Wakefield Accelerators'. 2025. in preparation.

[498] R. D'Arcy et al. 'FLASHForward: plasma wakefield accelerator science for high-average-power applications'. In: *Philosophical Transactions of the Royal Society A: Mathematical, Physical and Engineering Sciences* 377.2151 (June 2019), p. 20180392. ISSN: 1471-2962. DOI: 10.1098/rsta.2018.0392.

[499] J. Faure et al. 'A review of recent progress on laser-plasma acceleration at kHz repetition rate'. In: *Plasma Physics and Controlled Fusion* 61.1 (Nov. 2018), p. 014012. ISSN: 1361-6587. DOI: 10.1088/1361-6587/aae047.

[500] L. Rovige et al. 'Demonstration of stable long-term operation of a kilohertz laser-plasma accelerator'. In: *Physical Review Accelerators and Beams* 23.9 (Sept. 2020), p. 093401. ISSN: 2469-9888. DOI: 10.1103/physrevaccelbeams.23.093401.

[501] R. D'Arcy et al. 'Recovery time of a plasma-wakefield accelerator'. In: *Nature* 603.7899 (Mar. 2022), pp. 58–62. DOI: 10.1038/s41586-021-04348-8.

[502] O. Zarini. 'Measuring sub-femtosecond temporal structures in multi-ten kiloampere electron beams'. PhD thesis. Technische Universität Dresden, 2019. URL: https://www.hzdr.de/publications/Publ-29222.

[503] O. Zarini et al. 'Multioctave high-dynamic range optical spectrometer for single-pulse, longitudinal characterization of ultrashort electron bunches'. In: *Physical Review Accelerators and Beams* 25.1 (Jan. 2022), p. 012801. ISSN: 2469-9888. DOI: 10.1103/physrevaccelbeams.25.012801.

[504] K. Schmid and L. Veisz. 'Supersonic gas jets for laser-plasma experiments'. In: *Review of Scientific Instruments* 83.5 (May 2012). ISSN: 1089-7623. DOI: 10.1063/1.4719915.

[505] R. A. Fonseca et al. 'OSIRIS: A Three-Dimensional, Fully Relativistic Particle in Cell Code for Modeling Plasma Based Accelerators'. In: *Computational Science — ICCS 2002*. Springer Berlin Heidelberg, 2002, pp. 342–351. ISBN: 9783540477891. DOI: 10.1007/3-540-47789-6_36.

[506] U. Schramm et al. 'First results with the novel petawatt laser acceleration facility in Dresden'. In: *Journal of Physics: Conference Series* 874 (July 2017), p. 012028. ISSN: 1742-6596. DOI: 10.1088/1742-6596/874/1/012028.

[507] J. P. Couperus et al. 'Tomographic characterisation of gas-jet targets for laser wakefield acceleration'. In: *Nuclear Instruments and Methods in Physics Research Section A: Accelerators, Spectrometers, Detectors and Associated Equipment* 830 (Sept. 2016), pp. 504–509. ISSN: 0168-9002. DOI: 10.1016/j.nima.2016.02.099.

[508] G. Raj et al. 'Probing ultrafast magnetic-field generation by current filamentation instability in femtosecond relativistic laser-matter interactions'. In: *Physical Review Research* 2.2 (May 2020), p. 023123. DOI: 10.1103/physrevresearch.2.023123.

[509] C. Thaury et al. 'Demonstration of relativistic electron beam focusing by a laser-plasma lens'. In: *Nature Communications* 6.1 (Apr. 2015). DOI: 10.1038/ncomms7860.

[510] T. Kurz et al. 'Calibration and cross-laboratory implementation of scintillating screens for electron bunch charge determination'. In: *Review of Scientific Instruments* 89.9 (Sept. 2018). ISSN: 1089-7623. DOI: 10.1063/1.5041755.

[511] S. Schöbel. 'Development and Characterization and of a Few-Cycle and Probe-Beam setup'. MA thesis. Technische Universität Dresden, 2018.

[512] C. Vozzi et al. 'Optimal spectral broadening in hollow-fiber compressor systems'. In: *Applied Physics B* 80.3 (Dec. 2004), pp. 285–289. ISSN: 1432-0649. DOI: 10.1007/s00340-004-1721-1.

[513] J. van Tilborg et al. 'Active Plasma Lensing for Relativistic Laser-Plasma-Accelerated Electron Beams'. In: *Physical Review Letters* 115.18 (Oct. 2015), p. 184802. ISSN: 1079-7114. DOI: 10.1103/physrevlett.115.184802.

[514] C. Doss et al. 'Underdense plasma lens with a transverse density gradient'. In: *Physical Review Accelerators and Beams* 26.3 (Mar. 2023), p. 031302. DOI: 10.1103/physrevaccelbeams.26.031302.

[515] R. Pompili et al. 'Plasma lens-based beam extraction and removal system for plasma wakefield acceleration experiments'. In: *Physical Review Accelerators and Beams* 22.12 (Dec. 2019), p. 121302. ISSN: 2469-9888. DOI: 10.1103/physrevaccelbeams.22.121302.

[516] H. Ding. 'LWFA Diagnostics Development for ATLAS-300 and Nonlinear Plasma Wavelength Scalings'. PhD thesis. Ludwig-Maximilians-Universität München, 2021.

[517] K. Huang et al. 'Electro-optic 3D snapshot of a laser wakefield accelerated kilo-ampere electron bunch'. In: *Light: Science & Applications* 13.1 (Apr. 2024). ISSN: 2047-7538. DOI: 10.1038/s41377-024-01440-2.

[518] F. C. Salgado et al. 'All-optical source size and emittance measurements of laser-accelerated electron beams'. In: *Physical Review Accelerators and Beams* 27.5 (May 2024), p. 052803. ISSN: 2469-9888. DOI: 10.1103/physrevaccelbeams.27.052803.

[519] M. LaBerge et al. 'Revealing the three-dimensional structure of microbunched plasma-wakefield-accelerated electron beams'. In: *Nature Photonics* (July 2024). ISSN: 1749-4893. DOI: 10.1038/s41566-024-01475-2.

[520] T. Sokollik et al. 'Tape-Drive Based Plasma Mirror'. In: *AIP Conference Proceedings*. AIP, 2010. DOI: 10.1063/1.3520320.

[521] B. H. Shaw, S. Steinke, J. van Tilborg and W. P. Leemans. 'Reflectance characterization of tape-based plasma mirrors'. In: *Physics of Plasmas* 23.6 (June 2016). ISSN: 1089-7674. DOI: 10.1063/1.4954242.

[522] V. Yakimenko et al. 'Prospect of Studying Nonperturbative QED with Beam-Beam Collisions'. In: *Physical Review Letters* 122.19 (May 2019), p. 190404. ISSN: 1079-7114. DOI: 10.1103/physrevlett.122.190404.

[523] T. G. Blackburn. 'Radiation reaction in electron–beam interactions with high-intensity lasers'. In: *Reviews of Modern Plasma Physics* 4.1 (Mar. 2020). ISSN: 2367-3192. DOI: 10.1007/s41614-020-0042-0.

[524] P. Zhang et al. 'Relativistic plasma physics in supercritical fields'. In: *Physics of Plasmas* 27.5 (May 2020). ISSN: 1089-7674. DOI: 10.1063/1.5144449.

[525] A. Matheron et al. 'Probing strong-field QED in beam-plasma collisions'. In: *Communications Physics* 6.1 (June 2023). ISSN: 2399-3650. DOI: 10.1038/s42005-023-01263-4.

[526] S. Corde et al. 'High-field plasma acceleration in a high-ionization-potential gas'. In: *Nature Communications* 7.1 (June 2016). ISSN: 2041-1723. DOI: 10.1038/ncomms11898.

[527] M. Zhou et al. 'Beam head erosion in self-ionized plasma wakefield accelerators'. In: *2007 IEEE Particle Accelerator Conference (PAC)*. IEEE, 2007. DOI: 10.1109/pac.2007.4440669.

[528] S. Z. Li et al. 'Head erosion with emittance growth in PWFA'. In: *AIP Conference Proceedings*. AIP, 2013. DOI: 10.1063/1.4773762.

[529] W. An et al. 'Strategies for mitigating the ionization-induced beam head erosion problem in an electron-beam-driven plasma wakefield accelerator'. In: *Physical Review Special Topics - Accelerators and Beams* 16.10 (Oct. 2013), p. 101301. ISSN: 1098-4402. DOI: 10.1103/physrevstab.16.101301.

[530] S. Deng et al. 'Plasma wakefield acceleration in self-ionized gas or plasmas'. In: *Physical Review E* 68.4 (Oct. 2003), p. 047401. ISSN: 1095-3787. DOI: 10.1103/physreve.68.047401.

ACKNOWLEDGEMENTS

Pursuing the projects that resulted in this thesis has been a great journey, which, beyond doing some interesting physics, has lead me through some welcome detours and a lot of hilarious moments. I am grateful to have met and worked with many talented people and to have developed new friendships along the way.

Realising the E-210 experiment has been an incredible endeavour. I want to express a wholehearted thank you to all members of the E-210 collaboration, and to everyone who, in one way or the other, contributed to the success of this experiment.

I want to thank Brendon O'Shea, Mike Litos, Spencer Gessner, Rafal Zgadzaj and Carl Linstrøm for the tremendous support inside and outside the depths of the tunnel, but also Mark Hogan, Vitaly Yakimenko and Christine Clarke for their constant push forwards.

I want to especially thank Oliver Karger, Alexander Knetsch, Aihua Deng, Paul Scherkl and Grace Manahan, who all worked relentlessly to prepare, develop and ultimately accomplish the E-210 experiment. It's been a great team!
Olli and Alex, your undeterred spirit and immense passion has always been an inspiration.
Paul, you are an even wiser man since you've become a parent.

I want to thank Daniel Ullmann, Andrew Beaton, Andrew Sutherland and Fahim Habib for contributing with simulations and for investigating things further.
Fahim, I continue to enjoy our lively discussions, which sometimes even involve physics, and thanks for teaching me a thing or two about free electron lasers.

Exploring hybrid plasma wakefield accelerators would not have been possible without the combined effort and the dedication of many people. I would like to thank the entire Hybrid Collaboration, for all the fruitful discussions, the open knowledge exchange and the joint effort across several laboratories.

I want to especially thank Thomas Kurz.
Sharing this journey with you has been an immense pleasure. Also, bats and fire-alarms in French castles will never be the same fun without you.

Likewise, a special thank you to Alberto Martinez de la Ossa, Arie Irman, Jurjen Couperus Cabadağ and Susanne Schöbel for all the passionate hard work.

Jurjen and Arie, thank you for building this nice laser-wakefield accelerator. I remember when you two first presented some of your results during a workshop that Alberto and I attended, and we both knew immediately that we want to try turning this into a hybrid experiment.
Alberto, thank you for pursuing and promoting this project from the very beginning, and for all your support and teachings along the way. I learned a lot from you.
Thank you Susanne for becoming the expert on few-cycle probe shadowgraphy, but also for guiding us through our own labyrinth of controls and settings.

Many other people have contributed to realising this project, to whom I wish to express my gratitude. I want to explicitly thank Max Gilljohann, Maxwell LaBerge, Vincent Chang, Olena Kononenko and Sébastien Corde for their experimental support and all the additional work across several labs.

Richard Pausch, Alexander Debus, Klaus Steiniger and Michael Bussmann provided immensely helpful simulations. Thank you all.

Many thanks to the DRACO laser team, René Gebhart, Uwe Helbig, Thomas Püschel and Stefan Bock.

Thank you Alastair Nutter, Patrick Ufer, Moritz Foerster, David Campbell and Thomas Wilson for exploring things further in experiments and theory.

I further want to thank Bernhard Hidding for being my main supervisor throughout all these projects, Zheng-Ming Sheng for taking the role as my second supervisor at the University of Strathclyde, and Ralph Aßmann for supervising me during my time at DESY. I am sincerely grateful to Bernhard Hidding and Ralph Aßmann for their tremendous support, encouragement and plenty of good advice (although I may have not followed all of them).

Bernhard Hidding has involved me in the E-210 project while I was still a graduate student. His mentoring has incredibly enhanced my scientific and personal abilities. Thank you for fiercely inspiring and pushing your students and entrusting them with exciting endeavours!

I also want to thank all members and students in Bernhard Hidding's research groups across the University of Strathclyde and Heinrich Heine University Düsseldorf for their tremendous support.

Ralph Aßmann welcomed me in his working group during my time at DESY and supported me to pursue the idea of the hybrid experiment. Thank you very much for the encouragement and guidance!

Many thanks also to my office mates Elena Svystun and Ángel Ferran Pousa, but also Sonja Jaster-Merz and Daniel Marx, who all made my time at DESY an especially joyful experience.

I am immensely grateful for my family.
Thank you for your infinite encouragement and love.

My friends helped me along the way much more than they might know. Although they sometimes get tired of hearing about physics, they have been nothing but supportive. Some of them welcomed me in their homes during my plenty trips to Dresden.
Thank you all!

Finally, I want to address a very special thank you to Harriet.
Thank you for, well, just about everything, and above all, for being you.

Prof. Farnsworth: And, now that I've found all the answers, I realise that what I was living for were the questions!

Fry: That stinks, Professor. Too bad the universe made it turn out that way and not some other way. I wonder why it did that.

Hawking's head: Probably magnets.

Prof. Farnsworth: Shut up, Hawking. Fry, you idiot – you're a genius! Why are the laws of physics what they are? Instead of some other laws? To find out, we'd have to recreate the conditions before the Big Bang.

It would take decades of work by thousands of scientists in a particle accelerator powered by dump trucks of flaming grant money.

Of course, there'd be no guarantee of success. And, in any case, I'd never live to see it.

Leela: I'm surprised you lived through that sentence.

Hermes: Sorry you wasted your life, Professor. I guess you never know everything after all.

Prof. Farnsworth: Indeed. The pursuit of knowledge is hopeless and eternal. *Hooray!*

text overlay:

LEVEL

COMPLETE

Insert coin to continue

— Futurama, *S6 E26* "Reincarnation"